Infrared limb-emission observations of the upper troposphere, lower stratosphere with high spatial resolution

Dissertation

for the acquisition of the doctor degree (Dr. rer. nat.)

of the Faculty C: Mathematics and Natural Sciences

University of Wuppertal

submitted by

Katja Weigel

March 2009

prepared at the

Institute for Chemistry and Dynamics of the Geosphere 1: Stratosphere

Forschungszentrum Jülich

JÜLICH FORSCHUNGSZENTRUM

Universität Wuppertal

Abstract

The Cryogenic Infrared Spectrometers and Telescopes for the Atmosphere - New Frontiers (CRISTA-NF) instrument has successfully taken part in the African Monsoon Multidisciplinary Analyses - Stratospheric-Climate Links with Emphasis on the Upper Troposphere and Lower Stratosphere (AMMA-SCOUT-O3) measurement campaign in July and August 2006. Deployed on the high-altitude aircraft M55-Geophysica radiance measurements in the mid infrared are taken between about 5 and 21 km altitude with a vertical and horizontal sampling of up to 250 m and 15 km, respectively.

The Juelich Rapid Spectral Simulation Code (JURASSIC) was used to retrieve the composition of the atmosphere from the radiance in the spectral range between about 776 to 868 cm^{-1}. A new retrieval setup and improvements of the forward model used for the retrieval allowed to obtain temperature, altitude and the volume mixing ratios of water vapor (H_2O), ozone (O_3), nitric acid (HNO_3), peroxyacetyl nitrate (PAN), carbon tetrachloride (CCl_4) as well as aerosol extinction and a radiometric offset.

Intercomparisons between CRISTA-NF data and in situ measurements from the Fast in situ Stratospheric Hygrometer (FISH) and the Fast Ozone Analyzer (FOZAN), respectively, show a good agreement.

The retrieved variables are available on a grid with 500 m vertical spacing with a vertical resolution of about 500 m to 3 km below the flight altitude. Hence, information about different atmospheric trace gases and temperature are available in the upper troposphere, lower stratosphere (UTLS) region with a higher spacial resolution than today's satellites and a better coverage than in situ measurements can provide. The simultaneous observation of trace gases mainly originating from the troposphere (like H_2O and PAN) and from the stratosphere (like O_3 and HNO_3), respectively, allows to determine the origin of air masses and detect mixing.

The results for the test flight on 29 of July 2006 are discussed in detail. This flight started in Verona and went to the south of Italy and back, crossing twice over the subtropical jet. The CRISTA-NF observations over Italy and the Mediterranean Sea indicated that a tropopause fold was located on the northern side of the jet. Tracer-tracer correlation between O_3 and PAN showed the presence of mixed tropospheric and lowermost stratospheric air at this fold and around the lapsrate tropopause north of it.

The structures seen in connection with this tropopause fold in the O_3 mixing ratios of CRISTA-NF were reproduced by a Chemical Lagrangian Model of the Stratosphere (CLaMS) simulation but were not found in such detail in ECMWF analysis data. These results emphasize that CRISTA-NF provides and excellent tool to observe and analyze mesoscale processes in the UTLS.

Kurzzusammenfassung

Das CRISTA-NF Instrument hat im Juli und August 2006 erfolgreich an der AMMA-SCOUT-O3 Meßkampagne teilgenommen. An Bord des hochlfliegenden Forschungsflugzeuges M55-Geophysica wurden Strahlungsmessungen im mittleren Infrarot zwischen 5 und 21 km Höhe mit einer vertikalen und horizontalen Abtastung von bis zu 250 m, bzw 15 km durchgeführt.

Die in Jülich entwickelte JURASSIC Programbibliothek wurde genutzt, um die atmosphärische Zusammensetzung aus den Strahldichten im Spektralbereich zwischen 776 to 868 cm^{-1} herzuleiten. Eine neue Konfiguration für dieses sogenannte Retrieval und Verbesserungen des dabei genutzten Vorwärtsmodells haben es ermöglicht, Temperatur, Höhe und die Volumenmischungsverhältnisse von Wasserdampf (H_2O), Ozon (O_3), Salpertersäure (HNO_3), Peroxyacetylnitrat (PAN), Tetrachlormethan (CCl_4) sowie die Aerosolextinktion und einen Strahlungsuntergrund zu erhalten.

Vergleiche zwischen CRISTA-NF Daten und in situ Messungen von dem Hygrometer FISH bzw dem Ozonmessgerät FOZAN zeigen eine gute Übereinstimmung.

Die abgeleiteten Variablen liegen unterhalb der Flughöhe auf einem vertikalen 500 m Gitter mit einer vertikalen Auflösung von etwa 500 m bis 3 km vor. Somit sind die Informationen über die verschiedenen atmosphärischen Spurengase und die Temperatur für die Region der unteren Stratosphäre und oberen Troposphäre (UTLS) mit einer höheren räumlichen Auflösung als sie heutige Satelliten und einer besseren Abdeckung als sie in situ Instruments bieten können verfügbar. Die gleichzeitige Beobachtung von Spurengasen die ihre Hauptquellen in der Troposphäre (wie H_2O and PAN) bzw. in der Stratosphäre (wie HNO_3 and O_3) haben erlaubt es, die Herkunft der Luftmassen und Vermischungen nachzuweisen.

Die Ergebnisse für den Testflug am 29. Juli 2006 werden detailliert diskutiert. Dieser Flug startete in Verona und führte nach Süditalien und zurück, wobei er zweimal den subtropische Strahlstrom kreuzte. Die CRISTA-NF Beobachtungen über Italien und dem Mittelmeer zeigen, dass eine Tropopausenfalte an der nördlichen Seite des Strahlstroms lag. Spurengaskorrelationen zwischen O_3 und PAN zeigen das Vorhandensein von vermischter Luft aus Troposphäre und unterer Stratosphäre bei dieser Falte und nördlich davon rund um die Tropopause (definiert duch den Temperaturgradienten).

Die Strukturen des O_3 Mischungsverhältnisses im Zusammenhang mit dieser Tropopausenfalte wurden auch mit einer CLaMS Modellrechnung reproduziert, wurden aber nicht mit derselben Detailfülle in der ECMWF Analyse gefunden. Diese Ergebnisse heben hervor, dass CRISTA-NF ein hervoragendes Instrument zur Beobachtung und Analyse mesoskaliger Prozesse in der UTLS darstellt.

Contents

1 Introduction **1**

2 Instrument and measurement description **7**

2.1 Calibrations and data corrections 12

2.2 Cloud index 14

3 JURASSIC **17**

3.1 Forward model 17

3.1.1 Emissivity tables 18

3.1.2 Continuum 22

3.1.3 EGA and CGA 22

3.1.4 Regression 23

3.2 Retrieval 24

3.2.1 Retrieval setup 25

3.2.2 χ^2-test 33

3.2.3 Retrieval result for one profile 34

3.2.4 Averaging kernel, resolution and measurement contribution 39

3.2.5 Retrieval errors 45

3.2.6 Temperature and altitude 50

3.2.7 Sequential retrieval 62

3.2.8 Filter and grid for the retrieval result 63

4 The AMMA-SCOUT-O3 Campaign **67**

4.1 Overview of the Campaign 67

4.2 Comparison to in situ measurements 68

4.3 Comparison to CLaMS model results 70

4.4 AMMA test flight on 29 July 2006 73

4.4.1 Results and intercomparisons 73

4.4.2 Discussion 92

5 Summary and Outlook **103**

A Appendix **I**

A.1 CRISTA-NF I

A.1.1 Black body calibration III

A.1.2 Spectral resolution IV

A.1.3 In-flight wavelength calibration V

A.1.4 LOS calibration IX

A.1.5 The attitude monitoring system IX
A.1.6 Correcting the internal clock XII
A.1.7 Correction of the pointing measurements XIII
A.1.8 Offset angles XX
A.1.9 Active attitude system XXII

B Appendix **XXV**
B.1 The forward model XXV
B.2 JURASSIC XXIX

C Appendix **XXX**
C.1 AMMA transfer and fifth local flight XXX
C.1.1 AMMA T1 XXX
C.1.2 AMMA T2 XXXIV
C.1.3 AMMA L5 XXXVIII
C.1.4 AMMA T3 XLII
C.1.5 AMMA T4 XLVI
C.2 ECMWF data L

D Acknowledgments **3**

List of Figures

1 CRISTA-NF in the front bay of M55-Geophysica 2
2 Scheme of exchange processes across the dynamical tropopause 3
3 Limb sounding geometry without refraction. 7
4 Schematic drawing of CRISTA-NF (from Kullmann, 2006). 8
5 Spectra from detector L5 and L6 10
6 CRISTA-NF spectra from detector L6 and RFM calculation 11
7 Cloud index calculation for spectra measured during AMMA TF2, profile 32. . 14
8 Altitude cross section for the cloud Index during AMMA T2 16
9 Percentage radiance difference between JFM and RFM calculation for different correction methods 21
10 Percentage radiance difference between JFM and RFM calculations for atmospheric conditions of flight T3 25
11 View point and tangent point without refraction. 31
12 Histogram of normalized χ^2/m for all profiles of AMMA flights TF2, T1, T2, L5, T3 and T4 34
13 Retrieval results for forward and backward spectra, Profile 94, AMMA T3 . . 36
14 Averaging Kernels (AVKs) for AMMA T3, Profile 94 for a) altitude, b) temperature, c) H_2O , d) aerosol 40
15 Like Figure 14 for a) O_3 , b) HNO_3 , c) CCl_4 and d) PAN. 41
16 CRISTA-NF O3 Retrieval for AMMA TF2 subtracted from CLaMS O3 without and with applying the AVK to the CLaMS data 44
17 Estimated retrieval error components for AMMA T3, Profile 94. For a) altitude, b) temperature, c) H_2O, and d) aerosol retrieval. 45
18 Like Figure 17, for a) O_3, b) HNO_3, c) CCl_4, and d) PAN retrieval 46
19 Altitude retrieval for three different Setups 53
20 Temperature retrieval for three different Setups 54
21 CFC-11 a priori profile for AMMA TF2 55
22 Comparison of measured CRISTA-NF spectra for AMMA T3, Profile 94 and RFM calculations for the results of the three different setups 57
23 Retrieval results for three different setups for a) aerosol, b) CCl_4, c) H_2O, d) O_3, e) PAN, and f) offset 58
24 Offset angles for AMMA TF2 60
25 Results for two different sequential retrievals in comparison to Setup C 64
26 Overview over cloud index along flight tracks of all AMMA flights used for the trace gas retrieval. 67

27 Cross section of CRISTA-NF O_3 mixing ratios and FOZAN measurements on 2006/08/13 . . . 70
28 Profiles of measured O_3 on 2006/08/13 . . . 71
29 PAN as retrieved for the AMMA test flight on 29 of July 2006 . . . 73
30 Cross section of CRISTA-NF temperatures together with M55-Geophysicas in situ avionic temperatures . . . 75
31 CRISTA-NF temperature, in situ temperature during ascent, descent and dive together with ECMWF temperature for the test flight on 29 of July 2006 . . . 76
32 CRISTA-NF and CLaMS H_2O during the test flight on 29 of July 2006 . . . 77
33 ECMWF H_2O during the test flight on 29 of July 2006 . . . 79
34 Profiles of H_2O during the dive of the test flight on 29 of July 2006 . . . 80
35 Scatter plot of CRISTA-NF and CLaMS water vapor for the test flight on 29 of July 2006. . . . 81
36 CRISTA-NF O_3 during the test flight on 29 of July 2006 . . . 83
37 CLaMS and ECMWF O_3 during the test flight on 29 of July 2006 . . . 85
38 Scatter plot of retrieved CRISTA-NF and modeled CLaMS O_3 mixing ratios during the test flight on 29 of July 2006. . . . 86
39 Map of the CRISTA-NF O_3 during the test flight on 29 of July 2006 . . . 87
40 Horizontal distribution of CLaMS O_3 on the $\zeta = 350K$ (about 13 km altitude) level during the test flight on 29 of July 2006 . . . 88
41 Cross section of CRISTA-NF HNO_3 and PAN for the test flight on 29 of July 2006 . . . 89
42 Cross section of CRISTA-NF CCl_4 and aerosol for the test flight on 29 of July 2006 . . . 90
43 Scatter plot of CRISTA-NF O_3 versus PAN . . . 92
44 Scatter plot of CRISTA-NF HNO_3 versus O_3 . . . 94
45 Excerpt of the CRISTA-NF O_3 cross section from Figure 36 with lapsrate tropopause from CRISTA-NF measurements, cold-point tropopause from ECMWF temperatures and ECMWF wind speed . . . 95
46 Map with 10 day backward trajectories from the TF2 CRISTA-NF grid positions between 350 and 360 K ζ. Color coding shows the CLaMS O_3 . . . 98
47 Vertical motion in ζ space of the backward trajectories from in Figure 46 plotted versus time. . . . 98
48 As Figure 46 but 10 day forward trajectories . . . 99
49 Cross section of mean age of air from the climatological CLaMS run interpolated on CRISTA-NF grid points. . . . 100

50 Effect on separate wavelength calibration on the difference between forward and backward profile VII
51 Attitude angles roll Φ, pitch Θ and yaw Ψ following DIN 9300 X
52 GPS altitude - pressure altitude for all AMMA flights. XI
53 Vector of total acceleration measured from an aircraft during a) straight flight with constant velocity and b) a turn. XIV
54 UCSE roll angle, CRISTA-NF AMS accelerometer, inclinometer and normalized gyro x-angle and their differences XIV
55 UCSE roll pitch, CRISTA-NF AMS accelerometer and normalized gyro x-angle and their differences XV
56 Scheme of the roll angle correction. XVII
57 Spikes in gyro Ω_y and Ω_z during the AMMA flight on 2006/08/16. XVIII
58 UCSE roll and corrected roll angle for an interval of about 20 seconds with a reliable correction. XVIII
59 As Figure 58 for an interval of about 1.5 minutes. XIX
60 As figure 58 overview of the whole flight AMMA T3. XIX
61 Inclinometer and UCSE roll angle and offset angle for the AMMA flight on 2006/08/16 XXI
62 Combined angle out of airplane roll and primary mirror XXIII
63 Spectra with an without active attitude system XXIV
64 Percentage radiance difference between JFM and RFM calculation for 163 example atmospheres for all ISBs XXVII
65 Estimated retrieval error components as in Figure 17 and 18 in percent XXIX
66 CRISTA-NF altitude and temperature retrieval results for T1 XXX
67 CRISTA-NF Retrieval results of H_2O , Aerosol, O_3 , HNO_3 , CCl_4 , and PAN for T1 XXXI
68 CLaMS results of H_2O , O_3 and mean age of air for AMMA T1 XXXII
69 CRISTA-NF Retrieval results compared to in situ data, CLaMs and ECMWF analysis data for T1 XXXIII
70 CRISTA-NF altitude and temperature retrieval results for T2 XXXIV
71 CRISTA-NF Retrieval results of H_2O , Aerosol, O_3 , HNO_3 , CCl_4 , and PAN for T2 XXXV
72 CLaMS results of H_2O , O_3 and mean age of air for AMMA T2 XXXVI
73 CRISTA-NF Retrieval results compared to in situ data, CLaMs and ECMWF analysis data for T2 XXXVII
74 CRISTA-NF altitude and temperature retrieval results for L5 XXXVIII

75 CRISTA-NF Retrieval results of H_2O , Aerosol, O_3 , HNO_3 , CCl_4 , and PAN for L5 XXXIX
76 CLaMS results of H_2O , O_3 and mean age of air for AMMA L5 XL
77 CRISTA-NF Retrieval results compared to in situ data, CLaMs and ECMWF analysis data for L5 XLI
78 CRISTA-NF altitude and temperature retrieval results for T3 XLII
79 CRISTA-NF Retrieval results of H_2O , Aerosol, O_3 , HNO_3 , CCl_4 , and PAN for T3 XLIII
80 CLaMS results of H_2O , O_3 and mean age of air for AMMA T3 XLIV
81 CRISTA-NF Retrieval results compared to in situ data, CLaMs and ECMWF analysis data for T3 XLV
82 CRISTA-NF altitude and temperature retrieval results for T4 XLVI
83 CRISTA-NF Retrieval results of H_2O , Aerosol, O_3 , HNO_3 , CCl_4 , and PAN for T4 XLVII
84 CLaMS results of H_2O , O_3 and mean age of air for AMMA T4 XLVIII
85 CRISTA-NF Retrieval results compared to in situ data, CLaMs and ECMWF analysis data for T4 XLIX
86 Cross section of ECMWF data on CRISTA-NF tangent points for TF2 on 2006/07/29 LI
87 Cross section of ECMWF data on CRISTA-NF tangent points for T1 on 2006/07/31 LII
88 Cross section of ECMWF data on CRISTA-NF tangent points for T2 on 2006/08/01 LIII
89 Cross section of ECMWF data on CRISTA-NF tangent points for L5 on 2006/08/13 LIV
90 Cross section of ECMWF data on CRISTA-NF tangent points for T3 on 2006/08/16 LV
91 Cross section of ECMWF data on CRISTA-NF tangent points for T4 on 2006/08/17 LVI

List of Tables

1 Integrated spectral bands (ISBs) used and main target variables. 26
2 Retrieved gases, aerosol and temperature. 27
3 Forward model parameters. 28
4 A priori radiance uncertainties. 32
5 Retrieval setups. 52
6 AMMA flights analyzed in this work 68
7 Detectors and spectral ranges available in level-1A data. II
8 Black body calibration errors for detector L5 and L6 IV
9 Fit parameters and their standard deviation for the in flight wavelength calibration for AMMA T3, detector L6 VIII
10 Errors for in flight wavelength calibration for AMMA T3, detector L6 for forward and backward spectra VIII
11 Overview of time offsets and offset angles for all AMMA flights. XX
12 Overview of time offsets and offset angles for the Testcampaign (TC5) and SCOUT-O3 flights. XXI

List of Abbreviations

ACE-FTS Atmospheric Chemistry Experiment - Fourier Transform Spectrometer

AMMA African Monsoon Multidisciplinary Analyses

AMS Attitude monitoring system

C_2H_6 Ethane

CCl_4 Carbon tetrachloride

CGA Curtis-Godson Approximation

CI Cloud index

CLaMS Chemical Lagrangian Model of the Stratosphere

CRISTA-NF CRyogenic Infrared Spectrometers and Telescopes for the Atmosphere - New Frontiers

ECMWF European Centre for Medium-Range Weather Forecasts

EGA Emissivity Growth Approximation

ESA European Space Agency

FISH Fast In situ Stratospheric Hygrometer

FOZAN Fast OZone ANalyzer

GLORIA GLObal Limb Radiance Imager of the Atmosphere

H1, H2, H3, H4, H5, H5R, H6, H7 Detector names HRS

H_2O Water

HAGAR High Altitude Gas AnalyzeR

HALOE HALogen Occultation Experiment

HIRDLS HIgh Resolution Dynamics Limb Sounder

HITRAN2004 HIgh-resolution TRANsmission molecular absorption database 2004

HNO_3 Nitric acid

HNO_4 Pernitric acid

HRS High Resolution Spectrometer

ISB Integrated Spectral Band

JFM JURASSIC Forward Model

JRP JURASSIC Retrieval Processor

JURASSIC JUelich RApid Spectral Simulation Code

L1, L2, L3, L4, L5 Local flights

L1, L2, L3, L5, L6, L7, L8 Detector names LRS

LOS Line Of Sight

LRS Low Resolution Spectrometer

MDB Myasishchev Design Bureau

MIPAS Michelson Interferometer for Passive Atmospheric Sounding

MSL Mean Sea Level

O_3 Ozone

OCS Carbonyl sulfide

PAN Peroxyacetyl nitrate

ppmV, ppbV, pptV Volume mixing ratios: parts per million, parts per billion, parts per trillion

PREMIER PRocess Exploration through Measurements of Infrared and millimetrewave Emitted Radiation

PVU Potential Vorticity Unit [$10^{-6}\mathrm{Km^2kg^{-1}s^{-1}}$]

RFM Reference Forward Model

SCOUT-O3 Stratospheric-Climate links with emphasis On the UTLS - O3

SF_6 Sulfur hexafluoride

(Si:Ga) Gallium-doped silicium

T1, T2, T3, T4 Transfer flights

TF2 Test flight 2

UCSE Unit for Connection with Scientific Equipment

UTC Universal Time Coordinated

UTLS Upper Troposphere Lower Stratosphere

FOV Field Of View

WMO World Meteorological Organization

ZnSe Zinc Selenid

1 Introduction

The Upper Troposphere Lower Stratosphere (UTLS) is the transition layer between the stratosphere and the troposphere and is important for the exchange of trace gases (e.g. Holton et al., 1995). At the same time it is an atmospheric layer which is even today sparsely covered by in situ measurements and not well resolved by satellite observations (e.g. Engel et al., 2003). Therefore a lot of questions concerning the processes behind transport and exchange of trace gases through the UTLS and its magnitude are still unanswered. Further, it is known that the temperature structure of the stratosphere and thus the vertical circulation within it can have effects on the climate and the weather in the troposphere. However, the underlying mechanisms are still not sufficiently understood (WMO, 2006). This makes measurements which can improve the knowledge about the UTLS, its structure, dynamics, and chemistry especially valuable. Such measurements can be provided by the CRyogenic Infrared Spectrometers and Telescopes for the Atmosphere - New Frontiers (CRISTA-NF) onboard the high-altitude research aircraft M55-Geophysica.

CRISTA-NF was developed in a cooperation between Forschungszentrum Jülich and the University of Wuppertal. It is based on the satellite instrument CRISTA, which was measuring twice, in November 1994 and August 1997, from a platform deployed and retrieved by a space shuttle (e.g. Offermann et al., 1999; Riese et al., 1999a; Grossmann et al., 2002). Its central telescope and spectrometers were reused for the development of the aircraft instrument CRISTA-NF.

Deployed on the high-altitude aircraft M55-Geophysica, which reaches a maximum altitude of up to 21 km (Stefanutti et al., 1999), CRISTA-NF measurements cover an altitude range from 5 km to the flight altitude with a sampling of about 250 m (Kullmann et al., 2004). Figure 1 shows the CRISTA-NF instrument inside M55-Geophysica during service in the hangar. It is situated at the front of the aircraft. The bay is closed during the flight, leaving just an opening at the position of the window at the upper left side of CRISTA-NF. This allows remote sensing of the UTLS with a high resolution and dense coverage.

CRISTA-NF performed its first successful measurements during the SCOUT-O3 campaign

Figure 1: CRISTA-NF in the front bay of M55-Geophysica, photograph: Fred Stroh.

in autumn 2005 (Hoffmann et al., 2009; Kullmann, 2006). This work concentrates on the results of the AMMA-SCOUT-O3 Campaign in Summer 2006, with a particular focus on the test flight, on 29 July 2006. The AMMA campaign included ten flights: The test flight (TF2), four transfer flights (T1-T4) and five local flights (L1-L5). During TF2, there were nearly cloud free conditions and the active attitude system was in operation, providing ideal conditions for the trace gas retrieval. In addition, this flight was chosen because it passed over the subtropical jet, observing both, air from the lowermost stratosphere in the north and the upper tropical troposphere in the south, as well as the transition between these air-masses (see Figure 2).

Figure 2 shows a schematic drawing of various exchange processes through the tropopause. The green shaded area shows the latitude range explored by CRISTA-NF measurements during the test flight mentioned above. The thick black line indicates the position of the dynamical tropopause, blue lines show the isentropes and the position of the subtropical jet is marked by a pink shading. Isentropic mixing across the tropopause can take place in the subtropics (indicated as red arrows). In the tropics tropospheric air can enter the stratosphere by overshooting convection. The lowermost stratosphere is marked by a blue shading, and the Brewer-Dobson circulation is indicated by orange arrows.

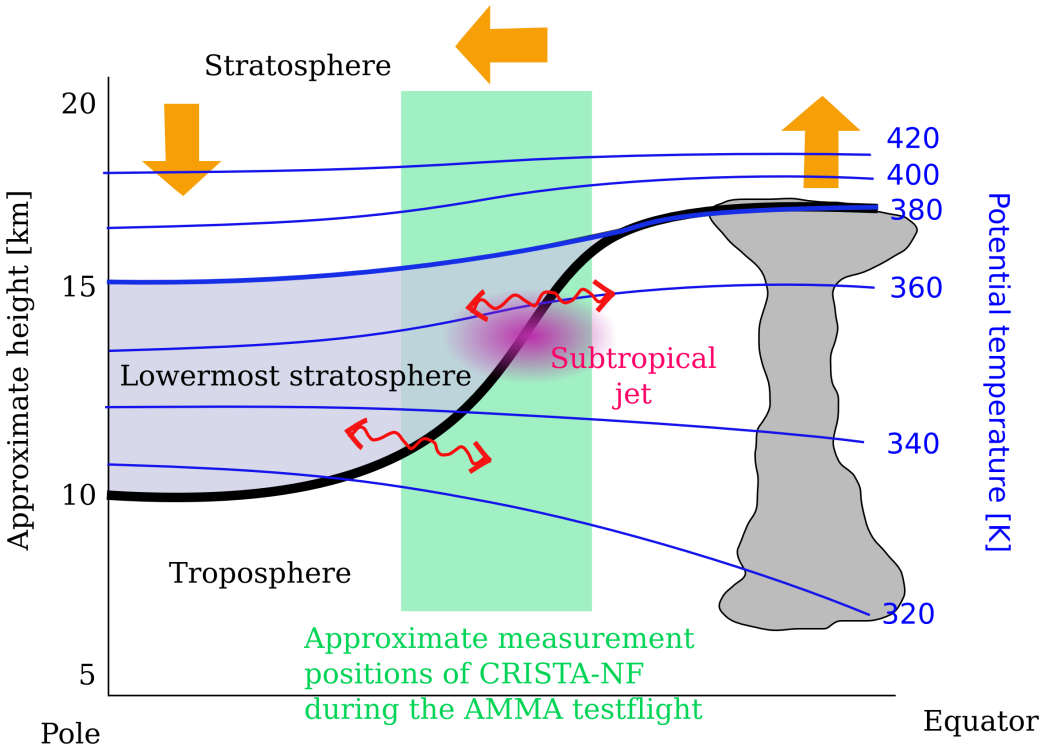

Figure 2: Scheme of exchange processes across the dynamical tropopause (thick black line). Drawing based on Holton et al. (1995) and Hoor et al. (2002). Thin blue lines display the potential temperature. The pink shaded area indicates the position of the subtropical jet, the blue shaded area highlights the lowermost stratosphere. Possible exchange processes are indicated as arrows, the approximate setting of the CRISTA-NF measurements during the AMMA test flight are displayed as green shading.

Measurements are taken with two mid infrared spectrometers, detecting radiance between 4 and 15 μm with 15 detector channels in total (Kullmann et al., 2004). From the radiance measured the composition of the atmosphere ("level-2 data") is derived. This "retrieval" requires calculations based on inverse mathematical methods. Here, the Juelich Spectral Simulation Code (JURASSIC) (Hoffmann, 2006) was applied and adopted to the requirements of CRISTA-NF.

Simulations from the Chemical Lagrangian Model for the Stratosphere (CLaMS) were used for scientific data interpretation. In situ measurements of water vapor, O_3, and temperature taken onboard M55-Geophysica are used for comparison in order to establish the reliability of the retrieved data.

This work concentrates mainly on the analysis of the Lower Resolution Spectrometer (LRS)

detector between 776 and 868 cm^{-1}, because it provides the possibility to derive temperature and altitude, which are a basic requirement for all trace gas retrievals, together with water vapor (H_2O), ozone (O_3), nitric acid (HNO_3), peroxyacetyl nitrate (PAN), carbon tetrachloride (CCl_4) and an estimate of the aerosol extinction from the same detector channel. These are important trace gases for the following reasons:

- H_2O:

  Water vapor is the most important natural greenhouse gas and plays an important role in the formation of clouds and the chemistry of both troposphere and stratosphere (WMO, 2006). Its main source in the atmosphere is the evapotranspiration at the earth surface. Few H_2O enters from the troposphere into the stratosphere due to dehydration in connection with freezing of ice crystals (e.g. Danielsen, 1982). An increase in upper tropospheric water vapor has been observed and is linked to increasing temperatures therefore providing a major positive feedback process to climate change (Trenberth et al., 2007)

- O_3:

  Additionally to its well known role to shield the earth surface from ultraviolet radiation, O_3 plays an important role for the temperature structure of the stratosphere and thus for the circulation within it. It is mainly originated in the lower tropical stratosphere. The exchange of O_3 between stratosphere and troposphere is still not well quantified (e.g. Denman et al., 2007).

- HNO_3:

  Nitric acid belongs to the NOy (reactive odd nitrogen) species and plays a main role in the formation of Polar Stratospheric Clouds (Toon et al., 1986) and cirrus clouds (e.g. Krämer et al., 2006). Like for O_3, the highest HNO_3 mixing ratios are found in the lower stratosphere (Murcray et al., 1968).

- PAN:

  Peroxyacetyl nitrate is a tropospheric NOy constituent mainly originating from pollution and hence in the troposphere. Its lifetime is longest (in the order of few month) in the upper troposphere. There, the only sink for PAN is photolysis (Talukdar et al., 1995). Therefore it is an indicator for long range transport of pollutants. Allen et al. (2005) showed that it has a important infrared emission band at about 794 cm^{-1}. It was first observed with infrared remote sensing in the upper troposphere by the Michelson Interferometer for Passive Atmospheric Sounding (MIPAS) balloon instrument (Remedios et al., 2007a) and its global distribution was described by Glatthor et al. (2007).

- CCl_4:

  Carbon tetrachloride belongs to the ozone depleting species and is originated in the production process of chlorofluorocarbons (CFCs) (WMO, 2006), i.e. in the troposphere and has its main sink in the stratosphere. Thus its total amount decreases since the production of CFCs is reduced. Its lifetime is relatively long (20 to 30 years, e.g. Volk et al., 1997 and Happell and Roche, 2003), therefore its mixing ratio is almost constant in the troposphere but decreases with altitude in the stratosphere.

Overall, CRISTA-NF can provide information about both, stratospheric and tropospheric trace gases. This enables to distinguish tropospheric and stratospheric air-masses and to identify transport and mixing among them. Together with its high resolution and coverage this provides the possibility for a detailed analysis of mesoscale processes in the UTLS.

Chapter 2 presents the CRISTA-NF instrument and radiance measurements. Details of the retrieval, necessary modifications of the forward model and the retrieval setup can be found in Chapter 3. In Chapter 4 the results from the test flight on the 29 of July 2006 are presented and discussed in detail. A summary and outlook is given in the final Section 5.

2 Instrument and measurement description

This Section gives a short introduction to the instrument and describes important steps in the processing of the radiance data. Detailed descriptions of the CRISTA-NF instrument can be found in Kullmann et al. (2004) and Kullmann (2006).

CRISTA-NF is a limb sounding instrument. Thus, the measured radiance originates along a line of sight (LOS), see e.g Gille and House (1971). For CRISTA-NF, the LOS is positioned orthogonally to the flight direction to the right of the aircraft. The emitted radiance is dependent on the density of the emitting gases. The density of the atmosphere increases exponentially towards the earth surface. Therefore it can be assumed in first order that most of the radiance originates from the point where the LOS is closest to the earth surface, the tangent point. The altitude of the tangent point ("tangent altitude") is usually lower or equal to the aircraft altitude.

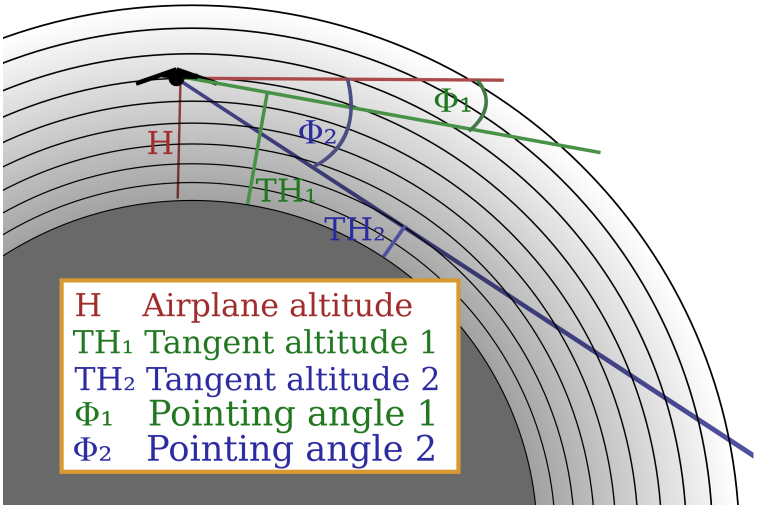

Figure 3: Limb sounding geometry without refraction.

Figure 3 shows a scheme of the limb sounding geometry for different LOSs. It is obvious from this geometry that a lower tangent point means at the same time a larger horizontal distance of the measurement from the aircraft. This implies that vertical profiles shown later are slant rather than vertical. A limb sounding geometry implies a moderate horizontal but a high vertical resolution. Due to the density gradient in the atmosphere the tangent point is lowered additionally by refraction. This effect is included in the radiative transfer model.

A schematic drawing of CRISTA-NF is shown in Figure 4. The atmospheric radiance enters the spectrometers trough a zinc selenide (ZnSe) window, a deflection mirror, a Herschel telescope, and several stray light baffles (telescopes and baffles are not drawn in detail and summarized as "optics" in Figure 4). A field stop and a Lyot stop constrain the LOS to a beam of 30" in the horizontal and 5" in the vertical. The primary mirror is turned to focus onto 60 different pointing angles. This leads to measurements of radiance from 60 LOSs with different tangent altitudes. Such a profile of radiance covers an altitude range between about 5 and 21 km.

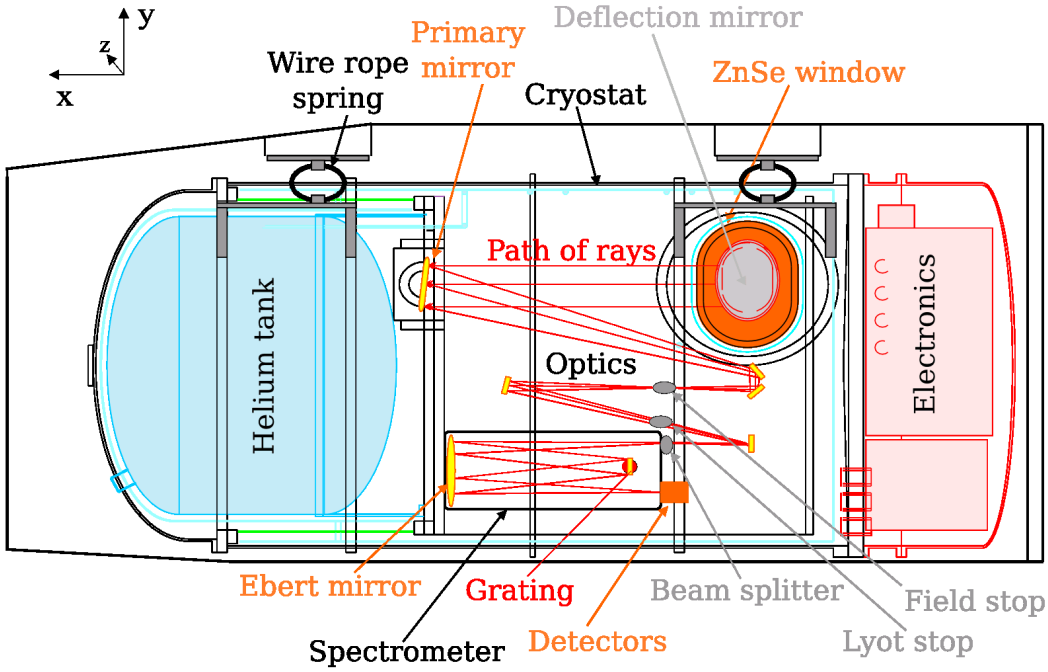

Figure 4: Schematic drawing of CRISTA-NF (from Kullmann, 2006).

CRISTA-NF contains two mid infrared Ebert-Fastie grating spectrometers (see e.g. Fastie, 1991). The Ebert-Fastie spectrometer type is used because it is especially robust against vibrations (Barthol, 1994) and hence well suited for measurements onboard satellites and aircraft. The beam splitter distributes the radiance among the two spectrometers. The "High Resolution Spectrometer" (HRS) has a resolution of about $\lambda/d\lambda = 1000$ (at a wavelength λ around 12.5 μm). The resolution of the "Low Resolution Spectrometer" (LRS) for $\lambda \approx 12.5\mu$m is about $\lambda/d\lambda = 500$. Figure 4 displays only one spectrometer containing the Ebert mirror

and the grating. Gallium-doped silicium (Si:Ga) semiconductor detectors are used to sample a broad wavelength interval during a short measurement time of about 1.2 s. These detectors need to be cooled with liquid helium to a temperature of about 12 K. A profile of atmospheric radiance measured by varying pointing angles of the primary mirror consists of 60 spectra, so it is recorded within about 70 s.

The whole instrument apart from the electronics is embedded in a cryostat, because the optical system needs to be cooled to minimize infrared emission from the instrument itself. This assures that also the relative low atmospheric radiance can be measured with a good signal to noise ratio. A more detailed description of the optical system of the satellite instrument CRISTA is presented by Barthol (1994) and the modifications for CRISTA-NF are discussed by Kullmann (2006).

The spectrometer setup used during the AMMA campaign and the spectral ranges of the detectors are listed in Table 7 in Appendix A.1. There are eight detectors for the HRS (H1-H7 and H5R) and seven detectors for the LRS (L1-L3 and L5-L8)[1] covering the spectral range of their spectrometers. This work concentrates on the analysis of the detectors L6 (776-868 cm^{-1}) and L5 (849-963 cm^{-1}). Figure 5 shows a profile of spectra measured with theses two detectors during the test flight of the AMMA campaign. Note that the spectra overlap between the two detector channels at about 849 to 868 cm^{-1}.

Figure 6 shows which trace gases cause the spectral features in the spectral range of detector L6 at four different altitudes. The black line in each Panel is a spectrum measured by CRISTA-NF, the black, dashed line results from the reference forward model (RFM; Dudhia, 2004, see Section 3.1 for details), which calculates the radiance for a given atmospheric composition and LOS based on the High-resolution transmission molecular absorption database (HITRAN)2004 spectroscopic data base (Rothman et al., 2005). The contribution of the different trace gases to the total radiance is calculated with RFM, too. The most distinct spectral features are the CO_2 Q branch at about 792 cm^{-1} and a CFC-11 band emission between about 840 and 860 cm^{-1}. The relative contributions of several other emitters vary with

[1]The detector names refer to the exit slit of the spectrometers. Slit 5 is occupied with two detectors for the HRS, there is no detector in slit 4 for the LRS. For details see Appendix A.1.

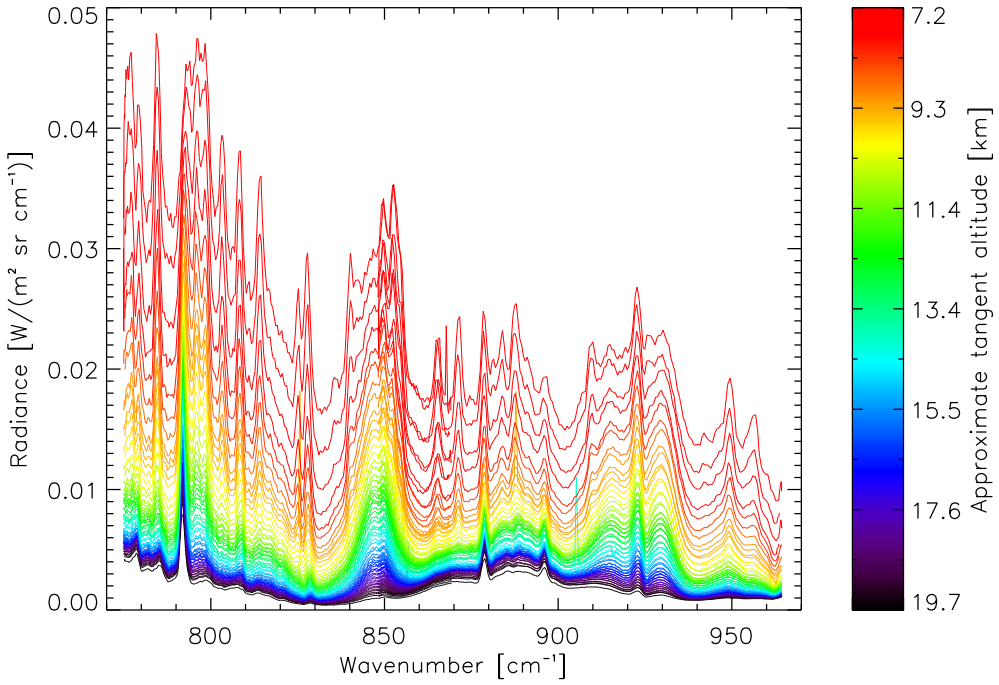

Figure 5: Spectra from detector L5 (849-963 cm^{-1}) and L6(776-868 cm^{-1}) from profile 172 during the AMMA test flight. Color coding shows the approximate tangent altitude (without corrections and refraction).

altitude: There are several H_2O peaks in the spectra at 9.4 and 12.2 km, but they are hardly visible above. The magnitude of the aerosol and PAN emissions decrease with altitude, too. In contrast, the largest emissions originating from O_3 and HNO_3 relative to the total radiance are found for the upper tangent altitudes.

In order to retrieve atmospheric data, radiance values integrated over selected spectral bands (ISBs) are used in this work (see e.g. Hoffmann, 2006). They are described in detail in Section 3.2.1. No ISBs are defined in the spectral region between about 800 and 825 cm^{-1} because of spectral cross talks, which are caused by reflections inside the spectrometer (Preusse, 1995; Riese et al., 1999a). Additionally, the abundance of CFC-22 and some other minor emitters effecting the spectral region between about 800 and 825 cm^{-1} are not well known, but they have few influence outside this region. Therefore most differences between the simulation and the measured spectra are found between 800 and 825 cm^{-1} in Figure 6.

CRISTA-NF was developed from parts of the original satellite instrument CRISTA. CRISTA

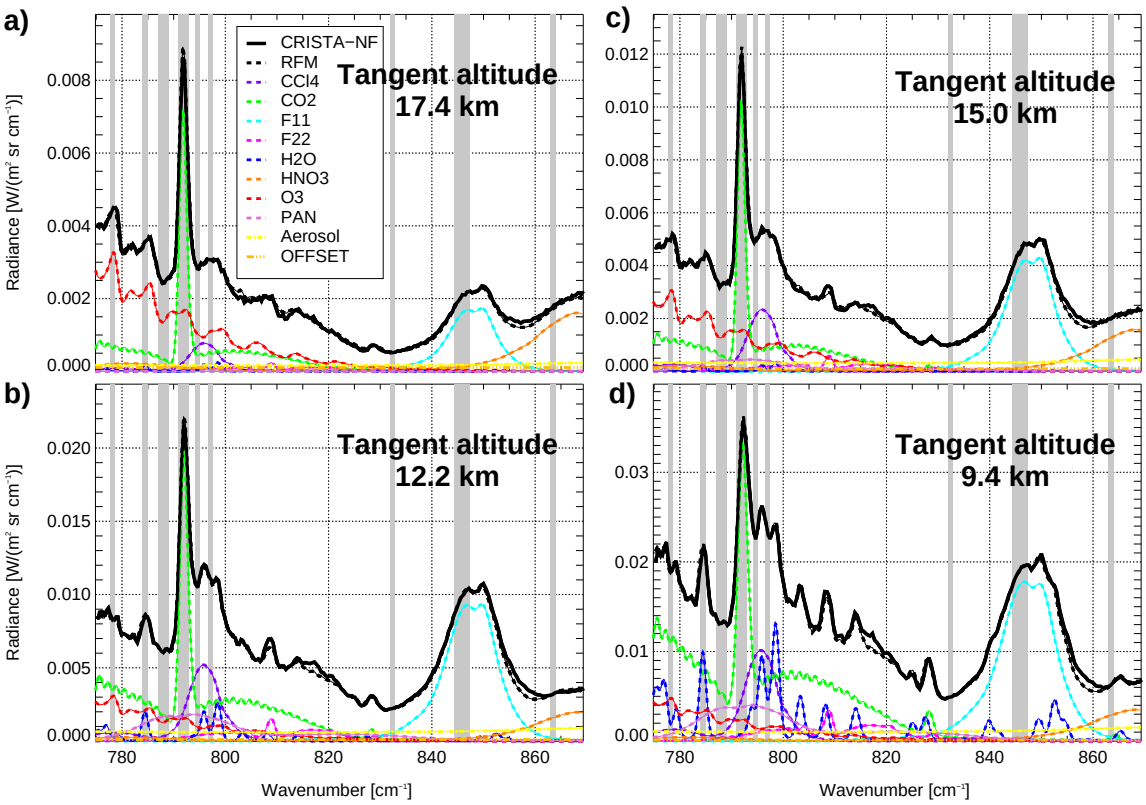

Figure 6: CRISTA-NF spectra from detector L6, flight TF2, profile 76 (black line). RFM calculation for the retrieval result is shown as black dashed line (the RFM calculation is based on an atmosphere including all emitters listed in Table 2 and 3). Colored lines show the contribution of the most relevant trace gases to the result: CO_2 (green), O_3 (red), H_2O (blue), CFC-11 (cyan), CFC-22 (pink), HNO_3 (orange), CCl_4 (violet) and PAN (orchid). The contribution of Aerosol is shown as yellow, the instruments radiance offset as gold line. Grey bars indicate the position of the ISBs used for the retrieval.

took part in two successful space missions in November 1994 and August 1997 for measurement periods of about ten days, where it was deployed and returned to Earth by a space shuttle. CRISTA measured thermal radiance of the atmosphere with unprecedented vertical and horizontal resolution. Trace gas concentrations and temperatures were retrieved by an onion peeling retrieval (Riese et al., 1999a). The results gave insight into the atmospheric composition covering an altitude range from the upper troposphere and stratosphere where various small and mesoscale structures were observed (e.g. Riese et al., 1999b; Preusse et al., 2002) up to the lower thermosphere (e.g. Kaufmann et al., 2002). Additionally, due to the marked influence of clouds on mid infrared spectra, clouds were identified and information about

their distribution gained (e.g. Spang et al., 2002). For the deployment on M55-Geophysica the central CRISTA Herschel telescope and twin spectrometer were integrated into a smaller cryostat. Because of the lower observer altitude of CRISTA-NF on M55-Geophysica compared to CRISTA, measurements with an even higher vertical resolution in the UTLS region are possible.

2.1 Calibrations and data corrections

Before it is possible to use the CRISTA-NF radiance measurements to retrieve atmospheric properties several corrections and calibrations are necessary. Three calibrations are performed to translate the instrument output (usually recorded as voltages) into physical values:

- The **black body calibration** translates the detector signals into radiance, see Appendix A.1.1 for details including radiance errors for the detectors L5 and L6.
- For each detector the wavelength corresponding to the voltage monitoring the grating position is determined by the **wavelength calibration**. This is done by comparing measured spectra to spectra modeled with RFM. To do so, it is necessary to know the spectral resolution, which could not be determined within the wavelength calibration. Therefore the resolution measured for the satellite instrument CRISTA was used, see Appendix A.1.2. In-flight data were used for the wavelength calibration, see Section A.1.3. It is important to note that spectra recorded during different turning directions of the grating (forward and backward spectra) must be separated in advance of the wavelength calibration.
- The alignment of the primary mirror is determined within the **line of sight (LOS) calibration** to better than $40'' = 0.011°$, see Appendix A.1.4.

In a moving aircraft, the pointing of CRISTA-NF is not only governed by the alignment of the primary mirror but also by the instrument and hence the aircraft attitude. The attitude monitoring system (AMS, see Appendix A.1.5) of CRISTA-NF has a high time resolution of 28Hz during AMMA but is not sufficient to ascertain the absolute attitude, see Appendix A.1.7. Therefore data from M55-Geophysicas avionic system, recorded within the Unit for Connection with Scientific Equipment (UCSE, MDB, 2002, see Appendix A.1.5) was used with a time resolution of only 1Hz but better absolute accuracy.

To make use of the high time resolution of the AMS and the better absolute accuracy of the UCSE data, it is advantageous to combine both information. To do so, the time of the internal clock of CRISTA-NF needs to be synchronized with UCSE time. Time deviations of more than one hour where observed for CRISTA-NF. The accuracy of the corrected time is usually better than 0.5 seconds, see Appendix A.1.6 for details.

Additionally, it is necessary to know the offset angles between CRISTA-NF and the aircraft. CRISTA-NF is connected by wire rope springs to the aircraft, which are stiff enough to ensure constant offset angles during each flight. Nevertheless, these offset angles have a relatively large uncertainty compared to the LOS calibration, see Appendix A.1.8.

The pointing corrections is described in detail in Appendix A.1.7. Most important for the pointing are the roll (Φ) and pitch (Θ) angles. The standard deviation of these angles measured by the M55-Geophysicas avionic system is according to MDB (2002) $\sigma = 0.05°$. For the trace gas retrieval a standard deviation of the same order as the error of the LOS calibration is required ($\approx 0.01°$). Since the absolute accuracy is despite the corrections dependent on the M55-Geophysicas avionic system and an additional systematic error results from the offset angles, the resulting error is too large. Therefore, the pointing must be determined within the trace gas retrieval, see Section 3.2.

During some flights, for example during the AMMA test flight on 29 of July 2006 (discussed in Section 4.4), an active attitude system was used. This means that the alignment of the primary mirror is adjusted to compensates for the aircraft movements. The active attitude system does not influence the knowledge of the pointing, but did improve the pointing stability during the measurements significantly, see Appendix A.1.9.

2.2 Cloud index

In contrast to spectra measured by microwave instruments like e.g. the Millimetre-wave Airborne Receiver for Spectroscopic CHaracterisation of Atmospheric Limb-Sounding (MARSCHALS) (Dinelli et al., 2009) mid infrared spectra are strongly influenced by clouds. This prevents a trace gas retrieval in the vicinity of clouds but does on the other hand provide a possibility to identify the LOSs influenced by clouds and gain information about cloud distribution and properties (Spang et al., 2002).

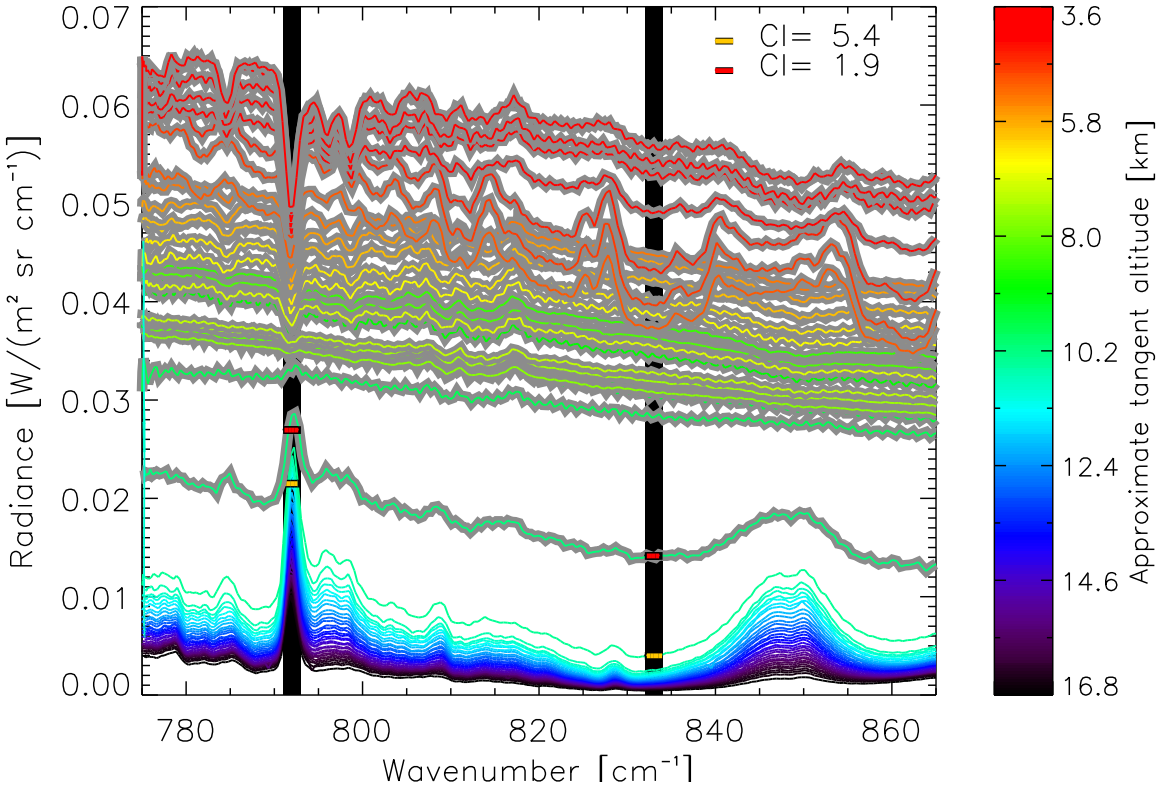

Figure 7: Spectra measured during AMMA TF2, profile 32. Colors shows the approximated (uncorrected) tangent altitude. Black bars in the background mark the ISBs used to calculate the CI. Red and yellow rectangles mark the ISBs used to calculate the CI for one spectrum with a CI < 3.5 (red) and one spectrum with a CI > 3.5 (yellow). Colored lines framed by gray lines indicate a CI < 3.5.

Figure 7 shows a profile of radiance spectra measured with CRISTA-NF during the test flight containing both, spectra measured under cloud free conditions and spectra influenced by clouds or optically dense conditions. Clouds emit a nearly continuous radiance spectrum

in the infrared. The radiance it thereby generally higher radiance values than in the case of a cloud free spectrum at the same temperature with partly optically thin spectral features caused by emission of gases. Along the LOS the radiance emitted by clouds can be modified due to the absorptions by trace gases, causing absorptions signals as the structures on the spectra from below about 5 km in Figure 7.

Because the shape of the spectra differs between clear air and clouds or optically dense conditions, they can be identified through color ratios, the so-called cloud index (CI). Here the ratio between two ISBs at $\mathrm{ISB_A} = 832 - 834\,\mathrm{cm^{-1}}$ and $\mathrm{ISB_B} = 791 - 793\,\mathrm{cm^{-1}}$ is used. If the ratio $\mathrm{CI} = \mathrm{ISB_A}/\mathrm{ISB_B} < 3.5$, the spectrum is considered to be influenced by clouds or optically dense conditions (see red bars in Figure 7) and is excluded from the trace gas retrieval.

One altitude step above, yellow bars mark one spectrum with a CI larger than 3.5, which would be identified to imply cloud free conditions. Nevertheless, this spectrum has a clearly higher radiance difference to the one at the next altitude above (i.e. lower radiance) than usual for the cloud free spectra. The approximated tangent altitudes show no indication that this is caused by a altitude difference. Therefore, it is likely that there is still some influence from of clouds although the cloud index is larger than 3.5. Hence, always one spectrum in an altitude above all spectra with a cloud index below 3.5 is excluded from the retrieval, too.

Figure 8 shows a cross section of the cloud index for the flight AMMA T2. During the first half of the flight the atmosphere is optically thin down to 8-10 km altitude. Single points with lower CI between 8 and 15 km altitude are in most cases artifacts recorded while the primary mirror is reset to its initial position for the next profile. They can be recognized because they occur only in the last spectra of a profile. After 13:00 UTC CIs smaller than 3.5 are found up to an altitude of 15-16 km, indicating a dense cloud layer.

The altitudes are corrected for refraction and the offset angles detected during the altitude retrieval (see Section 3.2.6). Nevertheless, the true altitude of the cloud can be higher, because it can be situated at any position along the LOS, not necessarily at the tangent point, see e.g. Adams et al. (2009). Anyhow, in addition to provide a filter to prevent the influence

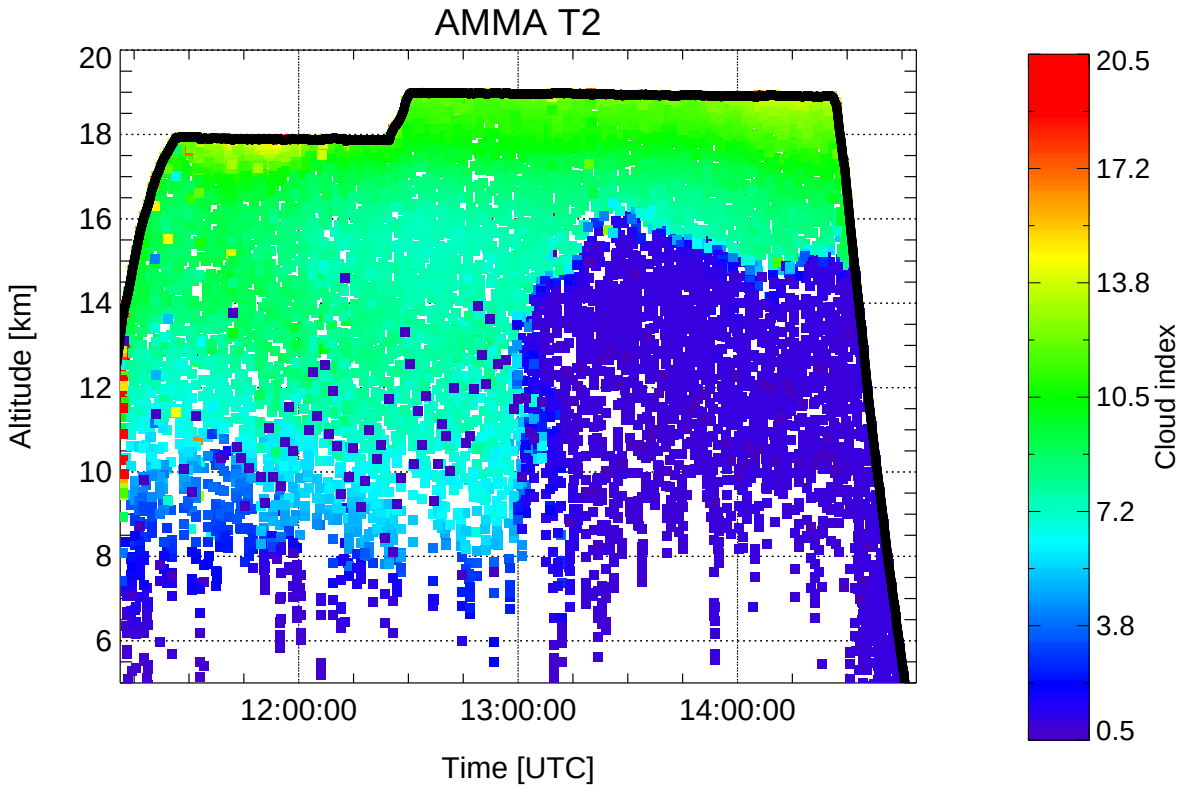

Figure 8: Altitude cross section for the cloud Index during AMMA T2, altitudes corrected for refraction and offset angle from the altitude retrieval. The black line shows the flight height of M55-Geophysica.

of clouds on the retrieval, the CI provides information about the distribution of clouds along the flight track.

3 JURASSIC

The Juelich Rapid Spectral Simulation Code (JURASSIC) (Hoffmann, 2006) is applied to retrieve atmospheric data from CRISTA-NF radiance measurements. JURASSIC was previously used to analyze stratospheric observations (e.g. Hoffmann et al., 2008; Hoffmann and Alexander, 2009). For this work, it was adapted to the requirements of CRISTA-NF, including tropospheric conditions. JURASSIC contains, among others, the JURASSIC forward model (JFM), a radiative transfer model based on pre-calculated emissivity tables, and the JURASSIC retrieval processor (JRP). This Chapter outlines the improvements applied to JFM and presents the setup used for retrieval of the data from the AMMA campaign.

3.1 Forward model

A radiative transfer model calculates the radiance emitted by and transferred trough an atmosphere of given chemical and microphysical composition prescribed for an observation geometry. The general equation for the radiative transfer through the atmosphere is according to Chandrasekhar (1960):

$$I(\nu, x) = I(\nu, 0)\tau(\nu, 0, x) + \int_0^x J(\nu, x', x)dx', \tag{1}$$

where ν is the wavenumber, x the coordinate along the LOS, $I(\nu, x)$ the radiance emerging from the ray path at the location of the instrument, $I(\nu, 0)$ the incident radiance entering at the end of the LOS opposite to the instrument, $\tau(\nu, 0, x)$ the transmission of the atmosphere and $J(\nu, x', x)$ the source function along the LOS consisting of thermal emission and scattering. Neglecting scattering and assuming local thermal equilibrium the source function corresponds to the Planck function $B[\nu, T(x')]$. The forward model combines a radiative transfer model and the instrument model. Taking into account the finite spectral resolution of the instruments the radiative transfer equation transforms to:

$$I = \int_{\nu_0}^{\nu_1} f(\nu) \int_0^{\infty} B[\nu, T(x')] \frac{d}{dx'} \epsilon(\nu, x', 0) dx' d\nu, \tag{2}$$

with emissivity $\epsilon(\nu, x', 0) = 1 - \tau(\nu, x', 0)$, and instrument function $f(\nu)$. The incoming radiance $I(\nu, 0)$ is zero because the instrument is pointing through the atmosphere towards cold space.

3.1.1 Emissivity tables

In order to calculate $\epsilon(\nu, x', 0)$, all spectral lines in the mid infrared region of interest for all relevant species have to be taken into account. This can be done with a line-by-line model, which calculates the radiance with a high accuracy but is rather time-consuming due to the large number of emission lines that may be involved. Since the retrieval requires a large number of forward model calculations, a fast forward model based on pre-calculated emissivity look-up tables implemented in JURASSIC is used. For each trace gas and ISB, the look-up tables list the emissivity integrated over a given spectral range as a function of pressure (p), temperature (T) and column density (u). The column density is calculated by:

$$u = q * p/(k_B * T) * dx, \tag{3}$$

with the volume mixing ratio (q), the path length (dx) and the Boltzmann constant k_B. The emissivity look-up tables are pre-computed with the line-by-line model RFM version 4.27 (Dudhia, 2004) with emissivity depending on p, T, q and dx. Line data or absorption cross-sections are taken from the HITRAN2004 spectroscopic database (Rothman et al., 2005)[2]

To reduce the table size and the computation time, the emissivity tables depend only on u instead of both, q and dx. For the calculation of the emissivity it usually makes a difference if q or dx is varied because the fraction of self- and air-broadening depends on the partial pressure and therefore on the volume mixing ratio of the emitter.

For practical reasons these dependence on q cannot be considered in the look-up tables, i.e. the self-broadening effect needs to be neglected[3]. This approximation is acceptable for typical atmospheric pressures and mixing ratios with exception of the H_2O and CO_2 continua.

[2]A conversion tool from Anu Dudhia allows to include also the CO_2 line mixing into RFM version 4.27.

[3]Inside the RFM Code, the self-broadening is disabled by setting the partial pressure to zero for the pressure broadening.

Therefore continua were not included in the look-up tables. Instead, to solve this an explicit H_2O continuum was included directly into JURASSIC (see Section 3.1.2).

For the look-up tables, the line-by-line emissivities obtained with RFM are convoluted with the instrument function, which has a Gaussian shape for CRISTA-NF and integrated over the given wavenumber interval. If integrated emissivities are used like line-by-line emissivities, two approximations are implicitly made (e.g. Hoffmann, 2006):

1. Band Transmittance Approximation

   Look-up tables contain spectrally integrated values which means that the spectral mean of the emissivity and the spectral mean of Planck's function are used. Their product is then integrated along the LOS. The band transmittance approximation leads to an error (Rodgers, 2000).

2. Continuum Approximation

   For each segment of the ray path the total emissivity is calculated from the total transmission ($\tau = 1 - \epsilon$). The total transmission is obtained by multiplying the mean transmission of each emitter. This neglects possible spectral correlations between emitters, i.e. their transmittance is treated like a continuum. If two or more emitters have a spectral correlation, this can lead to significant errors.

There are multiple approaches to correct for errors introduced by these approximations. For the BANDPACK model (Marshall et al., 1994) additional tables are included to account for the correlation between each pair of emitters to minimize the effect of the Continuum Approximation for the analysis of the radiance from the CRISTA satellite instrument. To minimize the error caused by the Band Transmittance Approximation, the Emissivity-Growth Approximation (EGA) and the Curtis-Godson Approximation (CGA) are applied for CRISTA.

In the current work different methods were tested to correct for the errors caused by the Band Transmittance Approximation and the Continuum Approximation: EGA, CGA, a linear regression and the combination of all those (see Section 3.1.4). Figure 9 shows the effect of the H_2O continuum and the methods mentioned above on the differences between JFM and RFM for the 787–790 cm^{-1} ISB for about 160 different example atmospheres (for the other ISBs see Appendix B.1, Figure 64). The JFM results applying neither EGA nor CGA differ with a standard deviation of more than 10% from the RFM result. EGA and CGA both

significantly reduce this difference and the combination of the two methods leads to an even better result, as already observed by Marshall et al. (1994). Both methods combined with a regression lead to a bias of less than 0.01% with a standard deviation $< 1\%$, see Figure 9f. The H_2O continuum included in all but the first column is most important for the lower altitudes, where the amount of water vapor in the atmosphere is high.

The same comparison for all ISBs used in the retrieval setup (Section 3.2) can be seen in Appendix B.1, Figure 64. The ISBs below 800 cm^{-1} show a similar deviation of JFM to RFM to the one shown in Figure 9. In contrast, the JFM result for ISBs with higher wavenumbers agree much better to the RFM result even without the correction (832-832.9 cm^{-1} and 844.3–847.3 cm^{-1}) or only corrected by EGA (863–864 cm^{-1}). This underlines the special importance of the corrections applied to the forward model for wavenumbers in the interval 775 to 800 cm^{-1}. The standard deviation of the difference between the RFM and JFM calculations for the test atmospheres (red dashed line in Figures 9 and Figure 64) is used for computing the forward model covariance for the retrieval (see Table 4).

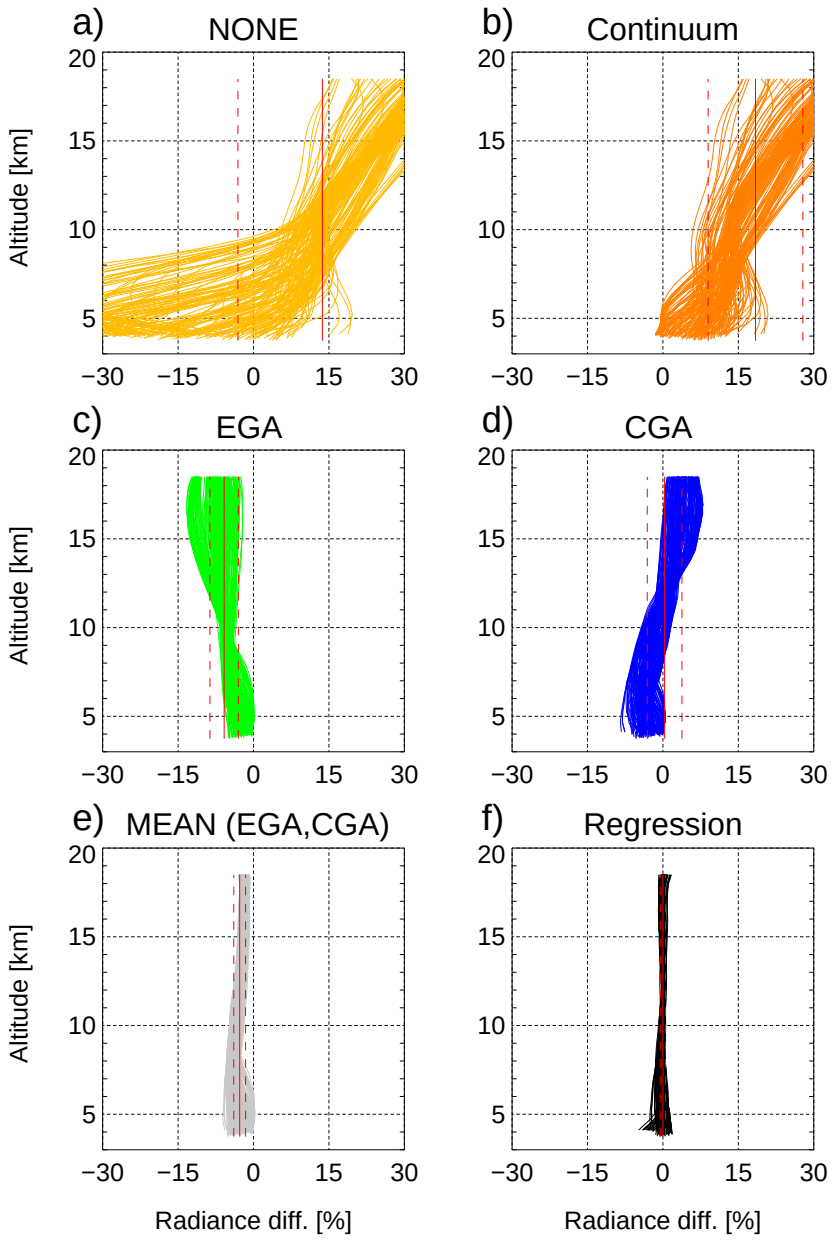

Figure 9: Percentage radiance difference between JFM and RFM calculation for 163 example atmospheres for the 787-790 cm^{-1} ISB for a) JFM without corrections and without H_2O continuum b) with H_2O continuum, c) with EGA and H_2O continuum, d) with CGA and H_2O continuum, e) mean of CGA and EGA including H_2O continuum, f) with regression (including EGA, CGA and continuum). Red solid lines: Average over all profiles and altitudes, red dashed lines: standard deviation.

3.1.2 Continuum

Molecules with strong emission bands in the mid infrared, like H_2O and CO_2 have continua which result from the superposition of line wings of these bands. The effect of self broadening is not negligible for these continua because they are very sensitive to the line shape of the lines they originate from. Since the effect of self-broadening cannot be included in the JURASSIC emissivity tables (see Section 3.1.1), it became necessary to calculate continuum contributions explicitly to analyze CRISTA-NF observations.

The H_2O continuum was directly implemented into JFM (based on the algorithms and coefficients used in RFM, see Clough et al., 2005). It is calculated based on both column density and partial pressure preventing further approximation errors. The CO_2 continuum is neglected here, because resulting contributions are smaller and effectively compensated by the regression (see Section 3.1.4). All emissivity tables are computed excluding the continua.

3.1.3 EGA and CGA

EGA and CGA are two methods to minimize the errors caused by the Band Transmission Approximation.

EGA

The Emissivity Growth Approximation (EGA) was proposed by Gordley and Russell (1981) based on a technique developed by Weinreb and Neuendorfer (1973). It assumes that the emissivity always increases along the LOS. Instead of calculating the emissivity for the total path, the growth of emissivity for each segment dx is calculated, using a pseudo mass path. The pseudo mass path is chosen to give the correct composite emissivity for the total path including the new segment based on its pressure and temperature. For details about the implementation of EGA into JFM see Hoffmann (2006).

CGA

The Curtis-Godson approximation (CGA) is based on Curtis (1952) and Godson (1981). For a detailed description see e.g. Marshall et al. (1994). It calculates the emissivity for the whole

path like for a homogeneous cell using an averaged temperature and pressure weighed with the column density. The CGA was implemented into JURASSIC in the frame of this work, see also Appendix B.1.

Combining EGA and CGA

Marshall et al. (1994) noted that a combination of EGA and CGA often decreases the errors of a band model further than each method alone. This empirical result is also observed for most JFM ISBs used in this work (see Figure 9e and Figure 64 Column 5 in Appendix B.1). For the sequential HNO_3 retrieval (see Section 3.2.7) this correction is sufficient. However, for the spectral region with wavenumbers smaller than 800 cm^{-1} even this combination leads to forward model errors in excess of 1%. Hence, further corrections are necessary for this spectral region.

3.1.4 Regression

Corrections based on a linear regression are a common method to improve fast radiative transfer models (see e.g. Francis et al., 2006). Such a correction is applied here to minimize the deviation of JFM from RFM (see Figure 9 and Figure 64 in Appendix B.1) for each ISB. The regression coefficients are obtained by least squares fitting of JFM to RFM computations for about 160 training atmospheres. These atmospheres are composed of ECMWF data for H_2O , O_3 , and temperatures and climatological data for the other emitters taken from Remedios et al. (2007b). Nine regression coefficients a_i with $i = [0, ..., 8]$ are calculated for each ISB, according to the regression equation:

$$\begin{aligned} I_{reg} = a_0 + a_1 * I_{EGA} + a_2 * I_{CGA} + \\ a_3 * T_{CGA} + a_4 * p_{CGA} + \\ a_5 * u_{C_2H_6} + a_6 * u_{CO_2} + a_7 * u_{H_2O} + a_8 * u_{O_3} \end{aligned} \tag{4}$$

Regression coefficients are calculated for:

- Constant radiance offset a_0

- Weighing factors for the amount of radiance from EGA I_{EGA} and CGA I_{CGA} (a_1,a_2)
- Curtis-Godson temperature T_{CGA} and pressure p_{CGA}, see Appendix B.1, Equation 18 (a_3,a_4)
- The column densities of along the LOS C_2H_6 ($u_{C_2H_6}$), CO_2 (u_{CO_2}), H_2O (u_{H_2O}) and O_3 (u_{O_3}), see Appendix B.1, Equation 12 (a_5,a_6,a_7,a_8)

In this way the regression combines the radiance from EGA and CGA and provides an additional radiance corrections dependent on the atmospheric conditions. The other retrieved gases and forward model parameters are not included into the regression, because to little is known about their variability a priori to the retrieval. Multiple regression schemes were tested and the one given above provided the best correction.

Furthermore, the regression turned out to depend on the observer altitude. Therefore regression coefficients are calculated for 12 different observer altitudes: 14.6 km to 20.1 km with 0.5 km spacing. These altitudes where chosen, because the most frequent observer altitudes during the AMMA transfer flights are about 18.1 km and 19.1 km. Additionally to the regression coefficients the JURASSIC regression tool calculates the forward model errors and their correlation lengths (see Section 3.2) from the remaining difference between the JFM with regression to the RFM radiance.

Figure 10 shows the difference between final radiance values and respective RFM calculations for the profiles of atmospheric variables obtained from the retrieval of the AMMA flight T3. In this way the regression is tested on an independent data set to confirm that the variability of the training atmospheres is adequately chosen for the regression. Figure 10 shows that there are still some systematic differences, but the mean differences are smaller than 1% for all ISBs, which is sufficient for the retrieval.

3.2 Retrieval

A forward model calculates the radiance received along an LOS in the atmosphere, but to analyze the CRISTA-NF data the received radiance has to be inverted into an atmospheric state. Since the forward model is non-linear, there is no direct analytical way to calculate

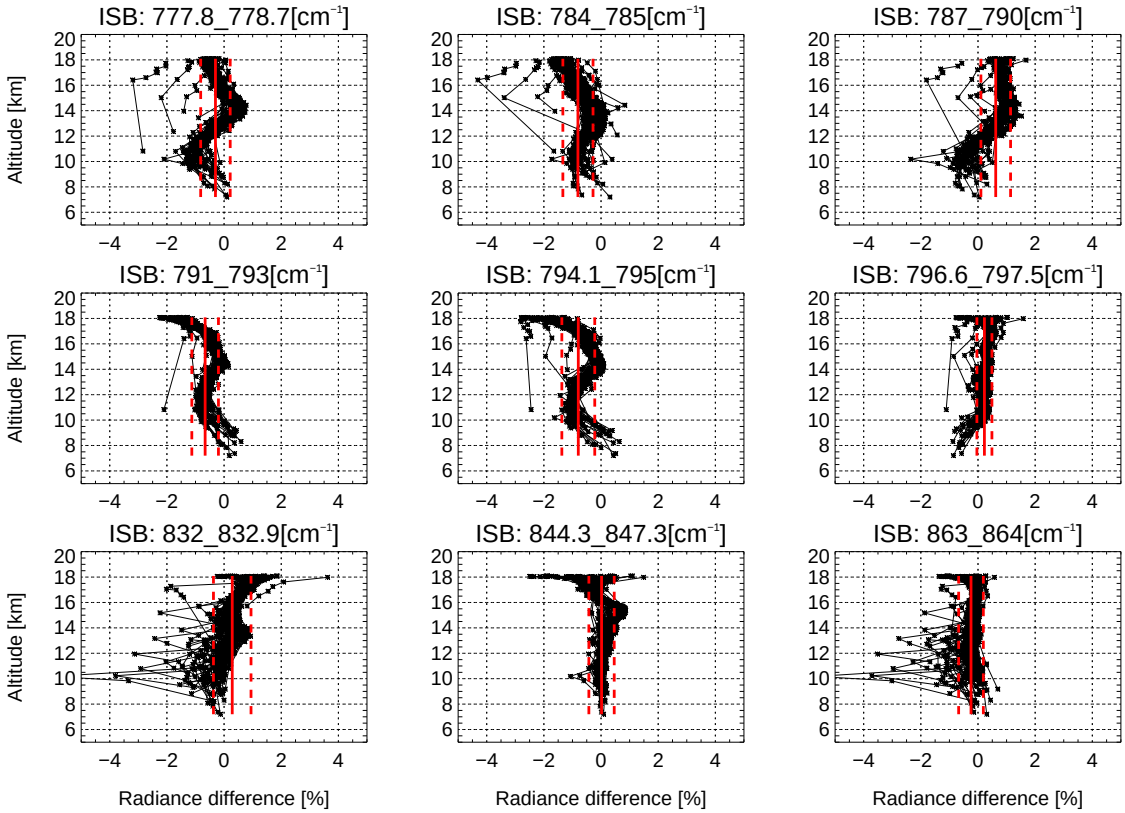

Figure 10: Percentage radiance difference between JFM and RFM calculations for atmospheric conditions of flight T3. Black lines with crosses: All Profiles of AMMA T3; red solid line: Mean; red dashed line: Standard deviation.

the composition of the atmosphere from the measured radiance. Hence, inverse methods must be used. This is done with the JURASSIC retrievals processor (JRP). JRP is based on the optimal estimation approach and provides the maximum a posteriori solution (Rodgers, 2000) of the inverse problem. The choice of the retrieval setup is important to gain as much information about the atmosphere as possible for the given measurement.

3.2.1 Retrieval setup

Choice of spectral bands

The main retrieval setup used in this work is based on 9 ISBs in the spectral range of detector L6. Measurements from this detector are used because its data quality is high and because it covers a wide spectral range containing absorptions of various trace gases. The spectral

position and the main targets for each ISB are presented in Table 1 (see also Figure 6 for the contributions of different emitters to the total radiance). Most ISBs are chosen because they contain characteristic emissions of targeted trace gases. However, it is important to keep in mind that JRP fits the radiance on all ISBs simultaneously by varying all retrieved variables. Hence, not only changes of the main target influence the radiance of each ISB.

Table 1: Integrated spectral bands (ISBs) used and main target variables.

ISB [cm $^{-1}$]	Main target
777.8–778.7	O_3
784–785	H_2O
787–790	Offset
791–793	CO_2 (Temperature)
794.1–795	PAN
796.6–797.5	CCl_4
832–832.9	Aerosol
844.3-847.3	CFC-11 (Altitude)
863–864	HNO_3

The widths of the ISBs are between 0.9 and 3 cm^{-1}. At least 0.9 cm^{-1} to use two or more measured radiance values for each ISB (the spectral sampling for detector L6 is about 0.4 cm^{-1}), but also not too wide, in order to focus on selected spectral features.

The 787–790 cm^{-1} and 832–832.9 cm^{-1} ISB are situated in spectral regions with rather low emissions to obtain information about aerosol (which has an almost continuum like emission) and the radiometric offset, which is a background radiance not completely removed by applying the black body calibration.

Retrieved variables and forward model parameters

Trace gas volume mixing ratios, temperature, and aerosol extinction, which are varied during the retrieval process are called "retrieved" variables or emitters. Trace gas mixing ratios, which are kept constant are called "forward model parameters" further on. Table 2 lists the retrieved variables and Table 3 the forward model parameters and pressure. The pressure is not varied by the retrieval in the actual sense but is calculated from temperature and altitude

assuming hydrostatic conditions. Tables 2 and 3 give the references to a priori values, a priori standard deviation and the uncertainty of the spectroscopic data. The spectroscopic data are taken from the HITRAN2004 spectroscopic database (Rothman et al., 2005). Errors are included in HITRAN2004 for emitters whose line data are available. If emissions are defined through cross-sections[4] the errors are not given within the data base or Rothman et al. (2005). Hence, the original references to the cross-sections and their errors are included in Table 2 and 3.

Table 2: Retrieved gases, aerosol and temperature.

Emitter	A priori state	Altitude dependent dependent a priori standard deviation	Minimum a priori standard deviation	Uncertainty of spectroscopic data
CCl_4	global [1]	midlat./tropical[1]	1%	2%[3]
H_2O	midlatitude[1]	200 ppmV under, 2 ppmV over 17 km	50%	5%[2]
HNO_3	tropical[1]	800 pptV under 25km tropical[1] above	20%	4.5%[2]
O_3	ECMWF	300 ppbV	5%	5%[2]
PAN	set to zero	100% of approximated profile from (Glatthor et al., 2007)	100%	4%[4]
Aerosol	HALOE[5]	-	500%	-
Temperature	ECMWF	-	5 K	-

[1]Remedios et al. (2007b), [2]Rothman et al. (2005), [3]Nemtchinov and Varanasi (2003), [4]Allen et al. (2005)
[5]HALogen Occultation Experiment (Hervig et al., 1993)

Most a priori values for the trace gases are taken from the MIPAS reference atmospheres (Remedios et al., 2007b). The CO_2 value is adjusted for the increased amount in 2006 compared to the 2001 value given in the reference atmospheres. CFC-113 is increased by a factor of 3.7 to achieve a better agreement to more recent measurements, e.g. Dufour et al. (2005) and Laube et al. (2008). This also improves the residuals in spectral regions where CFC-113 emits. For HNO_3 only the tropical value is used, while the values are altered between

[4]Different to line data, which calculate a spectrum based on the shape of each line, cross-sections describe the whole spectrum dependent on temperature and pressure. They are used if there are two many lines or the line data are not known well enough.

Table 3: Forward model parameters.

Parameter	A priori state	Altitude dependent a priori standard deviation	Minimum a priori standard deviation	Uncertainty of spectroscopic data
C_2H_6	midlat./tropical[1]	midlat./tropical[1]	5%	10%[2]
$ClONO_2$	tropical[1]	tropical[1]	5%	3.5%[3]
CO_2	modified global[1]	global[1]	5%	5%[2]
CFC-11	HAGAR, midlat./tropical[1]	HAGAR, midlat./tropical[1]	5%	3%
CFC-113	modified global[1]	-	10%	5%[4]
CFC-114	global[1]	-	5%	5%[4]
CFC-12	HAGAR midlat./tropical[1]	HAGAR, midlat./tropical[1]	5%	1%[5]
HCFC-22	ACE-FTS or global[1]	global[1]	5%	4%[6]
HNO_4	midlat./tropical[1]	midlat./tropical[1]	5%	10%[7]
OCS	global[1]	global[1]	5%	10%[2]
Pressure	ECMWF	-	1%	-

[1]Remedios et al. (2007b), [2]Rothman et al. (2005), [3]Wagner and Birk (2003), [4]McDaniel et al. (1991), [5]Varanasi and Nemtchinov (2003), [6]Ballard et al. (2000), [7]May and Friedl (1993)

tropical and mid latitude values for other gases. A priori profiles for O_3 and temperature are taken from interpolated European Centre for Medium-Range Weather Forecasts (ECMWF) operational analysis data with 0.5 degrees horizontal resolution on 28 pressure levels interpolated on the retrieval grid and position for each profile. Annual mean HCFC-22 values from the Atmosphere Chemistry Experiment Fourier Transform Spectrometer (ACE-FTS; see e.g. Bernath et al., 2005) are used for the tropical flights (L5, T2, T3). CFC-11 and CFC-12 profiles are combined from the High Altitude Gas Analyser (HAGAR) measurements up to the flight altitude and values from Remedios et al. (2007b) above (see Figure 21, Section 3.2.6).

A priory standard deviations can be set in the control file and/or altitude dependent on the same grid as the a priori data. If both exist, the maximum of them is used for each grid point in the retrieval, the standard deviation from the control file can therefore be regarded as the minimum standard deviation. Rather large values are chosen for the standard deviation of

the retrieved variables to give a greater weight to the measurements compared to the a priori data. For forward model parameters the best estimate available for the standard deviation is used.

A priori covariance and correlation lengths

The a priori covariance for retrieved variables is determined by a first-order autoregressive model (Hoffmann, 2006):

$$S_{ij} = \sigma_i \sigma_j * \exp \frac{-\Delta z}{c_z}, \tag{5}$$

where σ_i and σ_j are the standard deviations for the row and the column (given in Tables 2 and 3), Δz is the vertical grid spacing, and c_z is the vertical correlation length. The correlation length determines the strength of the decay of the correlations in the a priori covariance (e.g. Hoffmann et al., 2008). For each retrieved variable the vertical correlation lengths can be set individually. Its choice may influences the retrieval error and characteristics (e.g. resolution) significantly.

Especially for O_3 and HNO_3 long vertical correlation lengths are necessary to stabilize the retrieval result. The reason is presumably, that the highest abundance of these emitters is located above the measurement altitudes. Uncertainties in trace gas mixing ratios at upper altitudes may effect the retrieval results. Due to the lack of proper measurement information the retrieval needs to be constrained stronger. In contrast, for the other retrieved trace gases the concentration usually decreases with altitude. For CCl_4 and PAN a vertical correlation length of one kilometer is chosen, for H_2O and temperature the vertical correlation length is set to 5 km and to 25 km for aerosol. It is important to note that the vertical resolution is influenced by the correlation length but can still become much finer than the given correlation length, dependent on how much information is provided by the measurements (see Section 3.2.4). The effect was studied carefully by analyzing the retrieval diagnostics to chose ideal correlation lengths.

Retrieval grid

The retrieval is run on a vertical grid varying with altitude:

- 500 m spacing for altitudes between 3-20 km
- 1 km spacing for altitudes between 1-3 km and between 20-30 km
- 2 km spacing for altitudes between 30-50 km
- 2.5 km spacing for altitudes between 50-65 km

Tests performed in the frame of this work showed the best retrieval performance regarding measurement content, resolution and retrieval errors for a spacing of the retrieval grid similar to the tangent altitude spacing. Since forward and backward spectra are separated in advance of the retrieval (see Appendix A.1.3), the vertical spacing distance between two measured spectra used in the retrieval is approximately 500 m. It is necessary to include information about the atmosphere above the measurement altitudes because these layers contribute to the radiance along the LOS. A coarser grid is sufficient there and saves computation time.

A 1D-retrieval is run for each profile independently. This means that for each profile no horizontal grid is used and no horizontal structures are resolved. Information on the horizontal structures in the atmospheres is obtained from changes between successive profiles. The horizontal distance between two profiles is about 15 km, depending on the speed of the aircraft. In addition, it can be assumed that the information at a grid point is originated mainly close to the horizontal position of the vertically nearest tangent point (respecting refraction). Using a 1D-retrieval is a reasonable approach because vertical structures are generally dominant in the atmosphere and exhibit a much stronger influence on the retrieval result than horizontal structures.

Tangent point and offset

As discussed in Appendix A.1.7 the tangent altitude could not be determined accurately enough based on the attitude system alone. Hence, it is retrieved together with the trace gases, temperature and the radiometric offset. The a priori error for the altitude retrieval

is given as standard deviation of the pointing angle of 0.5^o. In the setup used the tangent altitude is varied keeping all other variables and atmospheric parameters on a fixed vertical grid[5]. The term "tangent altitude retrieval" is used, even though the changes of the radiance are caused by the differences of variables and parameters (including pressure, but not pressure alone) along the perturbed LOS. This concept was also used e.g. by Kiefer et al. (2007) for MIPAS. No vertical a priori correlation length is set for the tangent altitudes. This ensures that all tangent altitudes are retrieved independently. The retrieval of the radiance offset is restricted to one value for all ISBs and altitudes.

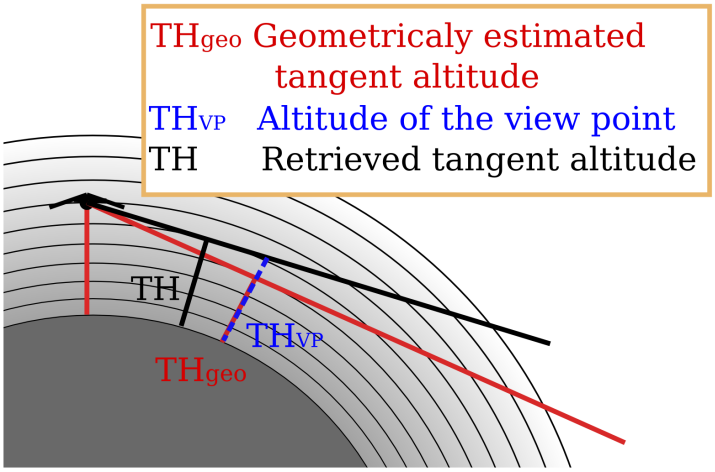

Figure 11: View point and tangent point without refraction.

The result of the tangent altitude retrieval with JURASSIC is not directly the tangent altitude but the altitude of the point on the line of sight at the horizontal position of the first guess for the tangent point, the so-called view point (see Figure 11)[6].

However, differences between the altitude of the view point and tangent altitude can amount to more than 200 m, therefore a correction is necessary. The real tangent point without refraction is calculated through raytracing as the altitude and geographic position of the point closest to the earth surface omitting refraction. All figures displaying retrieved tangent points without refraction are corrected in this way. The refraction is omitted when

[5]I.e. there are two independent grids: One for the atmosphere and one for the instrument related variables like tangent altitude and offset.

[6]This provides the possibility to define not only limb sounding geometries but geometries without defined tangent points, like nadir or upward looking LOS, too.

displaying the tangent altitude to focus on effects caused by the aircraft and instruments alignment. The retrieval grid for trace gases and other atmospheric variables does take the refraction into account.

Radiance uncertainties

The a priori error assumed for the offset and the other radiance errors for each ISB is given in Table 4. There are two sources for radiance uncertainties, the instrument and the forward model. The standard deviation of the forward model is estimated during the determination of the regression parameters (see Section 3.1.4). Like the regression coefficients it is varying with the observer altitude, but only to a small amount. The values given in Table 4 are valid for an observer altitude of 19.1 km.

The radiance uncertainties of CRISTA-NF are estimated in the frame of the black body calibration. The values used for the retrieval can be found in Table 4.

They are divided in

- Offset: A systematic, absolute radiance error.
- Gain: A systematic, relative radiance error.
- Absolute and relative noise: Random error.

Table 4: A priori radiance uncertainties.

ISB [cm^{-1}]	Forward Model standard deviation [%]	Offset [$W/m^2sr\ cm^{-1}$]	Gain [%]	Absolute noise [$W/m^2sr\ cm^{-1}$]	Relative noise [%]
777.8-778.7	0.70	0.0009	1	0.00005	1
784-785	0.82	0.0009	1	0.00005	1
787-790	0.51	0.0009	1	0.00005	1
791-793	0.35	0.0009	1	0.00005	1
794.1-795	0.45	0.0009	1	0.00005	1
796.6-797.5	0.42	0.0009	1	0.00005	1
832-832.9	0.25	0.0009	1	0.00005	1
844.3-847.3	0.21	0.0009	1	0.00005	1
863-864	0.18	0.0009	1	0.00005	1

The aim of an optimal estimation retrieval is to find the best representation of the real atmospheric state taking into account a priori knowledge as well as the full error characterization of the instrument. However, the best result is only obtained, if the a priori and error covariances are known exactly. In reality, the covariances are often less accurately known. Therefore it was decided to tune the covariances to closely reproduce the measured radiance in the retrieval procedure. However, an exact fit of the measured radiance is not desired at this point since such a approach typically leads to significant retrieval error amplifications and would contradict the idea of the optimal estimation method. Reproducing the measured radiance exactly could even favor unrealistic solutions, i.e. strong oscillations of trace gases, due to the measurement noise.

In the chosen retrieval setup only the absolute and relative noise are considered in the measurement error covariance. The relative and absolute radiance noise (see Table 4) were set just high enough to enable to fit the resulting radiance to the measured ones within the noise. Nevertheless, all uncertainties are considered when computing the error budget of the retrieval result.

3.2.2 χ^2-test

The consistency of the retrieval with the measurements and a priori data can be validated by a χ^2-test (e.g. Rodgers, 2000). A histogram of normalized χ^2/m (m is the number of radiance measurements for each profile) is shown in Figure 12. It contains all profiles of the AMMA flights TF2, T1, T2, L5, T3 and T4 (1506 profiles, if forward and backward spectra are separated).

Like for the CRISTA-NF H_2O retrieval for SCOUT-O3 (Hoffmann et al., 2009), most values of χ^2/m for the retrieval result are smaller or close to 1.0 indicating that these retrievals are consistent with the measured and a priori data within their errors. This can only be achieved by using larger noise than estimated from the black body calibration. This may be due to the forward model uncertainty or other nearly random errors such as the error of the in flight wavelength calibration (see Appendix A.1.3).

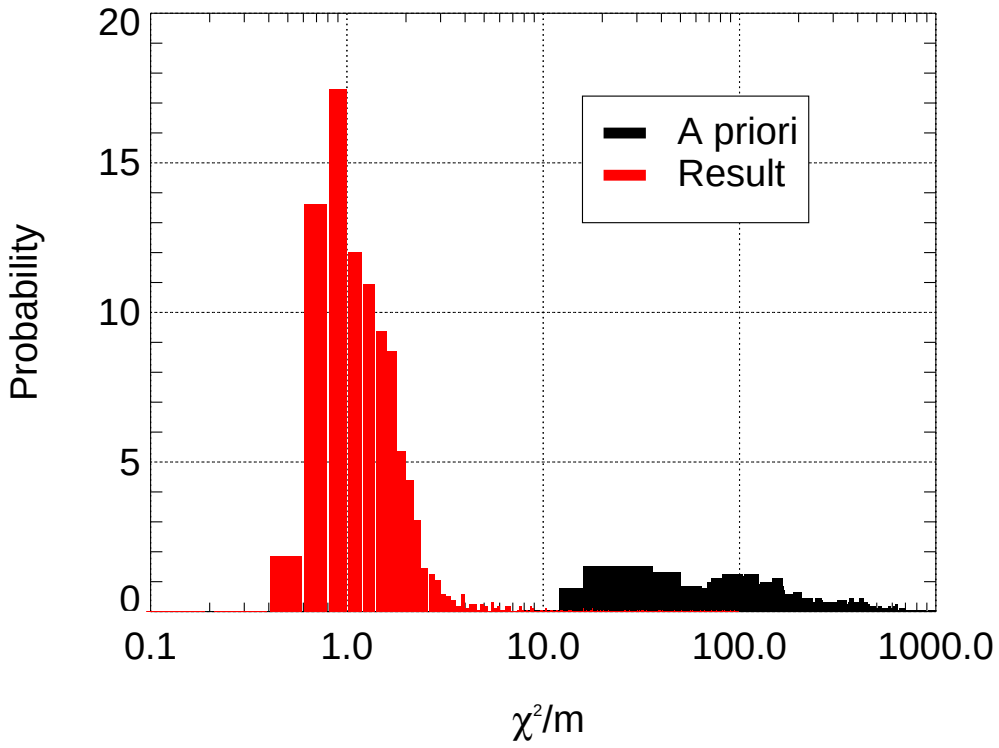

Figure 12: Histogram of normalized χ^2/m for all profiles of AMMA flights TF2, T1, T2, L5, T3 and T4, black bars: a priori, red bars: result. Bin size for the result is 0.2, for the a priori 20.

3.2.3 Retrieval result for one profile

In the following, the result of the setup presented above is discussed in detail for AMMA T3, profile 94. Figure 13 shows the resulting altitude, temperature and trace gases retrieved from forward and backward spectra separately

Panel a) shows the difference between the retrieved and a priori tangent altitudes calculated geometrically from the attitude system (both without refraction). Error bars show the total error including smoothing (see Section 3.2.5 for a detailed discussion of the retrieval errors). The tangent altitudes are very similar for forward and backward spectra. The absolute value of the difference is largest (up to 1.8 km) for the lowest altitudes and smallest close to the observer altitude. The angular difference resulting for this profile is about 0.25-0.3° for all altitudes, indicating that the reason for the difference to the geometric tangent points is a constant angular pointing offset. For backward spectra there are no radiance measurements between about 11 and 13 km, because these spectra are filtered out due to spikes detected

before the retrieval.

Panel b) shows the retrieved temperatures from forward and backward spectra compared to the a priori temperature from interpolated ECMWF operational analysis data. The largest differences below the flight altitude are found around the tropopause, where the CRISTA-NF temperatures are up to 3 K lower, and between 10 and 13 km where the CRISTA-NF temperatures are up to 5 K higher than the ones from ECMWF. Generally they agree well below the flight altitude. Above, starting at about 19 km larger differences can be seen. Variables above the flight altitude and the highest tangent point can be retrieved in principle, because the LOS also intersects these altitudes. However, for most species there is not enough information for a reliable retrieval there. Whether this is the case, can be estimated by the quality measures presented in Section 3.2.4. Above 25 km the a priori temperature is not altered by the retrieval.

Panel c) shows the retrieved water vapor volume mixing ratio in comparison to its a priori (midlatitude case of the MIPAS reference atmospheres from Remedios et al. (2007b)). The water vapor mixing ratio is only altered up to an altitude of 17 km during the retrieval. The reason not to retrieve water vapor at higher altitudes is that it can only be detected for mixing ratios above about 10 to 15 ppmV in the spectral range of detector L6. For lower mixing ratios the spectral signatures of interfering emissions from other gases like O_3 and CO_2 are much stronger than the emission from the H_2O lines (see Figure 6). Depending on the location and the observed air masses the H_2O mixing ratio falls below 10 ppmV above 10 to 16 km altitude. This causes also a water vapor mixing ratio of zero at 16.5 km in this profile (not displayed due to the logarithmic x-axis). Below 9 km it is close to but slightly lower than the a priori. Between 10 and 15 km the retrieved water vapor is higher and shows large variability. Between 10.5 and 12.5 km the differences of the water vapor for backward spectra and forward spectra is largest. The mixing ratios from backward spectra stay closer to the a priori value and have larger error bars than the ones from forward spectra. This is most probably caused by the low number of measurements for backward spectra between 11 and 13 km (see Panel a)).

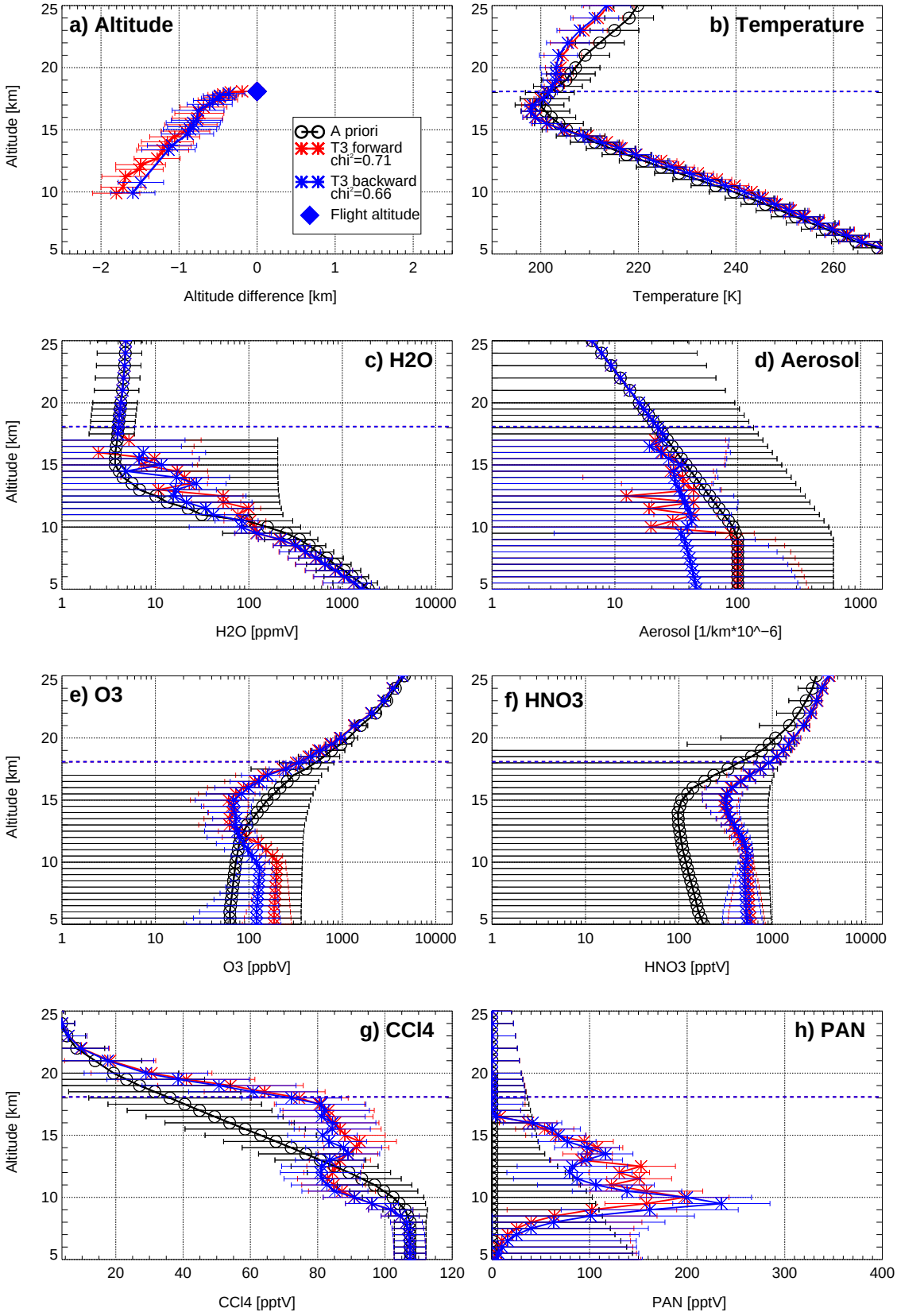

Figure 13: Retrieval results for forward and backward spectra, Profile 94, AMMA T3 for a) altitude, b) temperature, c) H_2O, d) aerosol, e) O_3, f) HNO_3, g) CCl_4, and h) PAN. The dotted horizontal lines in Panel b) to h) show the observer altitude.

Panel d) shows the retrieved aerosol extinction. As for water vapor the maximum altitude where aerosol is retrieved is 17 km. Aerosol is the most uncertain of all retrieved variables. This manifests itself in Figure 13d by the large error bars and the big differences between forward and backward spectra both in absolute values and in the structure of the profiles.

Panel e) shows the retrieved O_3 volume mixing ratio from forward and backward spectra compared to the a priori O_3 from interpolated ECMWF data. Above 12 km and below the observer altitude, results for forward and backward spectra agree well and are somewhat lower compared to the a priori value. Under 12 km forward and backward spectra are higher than the a priori and differ from each other. In the process of the retrieval O_3 is alternated up to 60 km altitude using a vertical correlation length of 100 km (see Table 2). Values retrieved above 25 km are most often not fulfilling the requirements of quality checks presented within Section 3.2.4, Figure 15, but the large altitude range chosen increases the stability of the retrieval also for altitudes below. In this way it is possible to obtain reliable information about O_3 (see also Section 4.2) even though the measurements take place below the O_3 maximum at 30 to 40 km altitude. The long vertical correlation length causes the retrieved values not to return to the a priori underneath 9 km, where no measurements exist for this profile. Instead, they remain on the value retrieved for the grid point close to the altitude of the lowest existing measurement for a profile, while their error bars increase.

Panel f) shows the retrieved HNO_3 volume mixing ratio from forward and backward spectra compared to its a priori (tropical profile of the MIPAS reference atmospheres from Remedios et al. (2007b)). Forward and backward spectra agree well. Both are significantly higher than the a priori value. This is probably because a too low tropical profile was used as a priori, but profile 94 was recorded in the subtropics where the real atmospheric HNO_3 and hence the retrieval result is higher. The MIPAS reference atmospheres contain profiles for tropic, mid-latitude, and polar summer and winter conditions. The a priori profile was chosen to represent the conditions during the flight best. The selection of the case is not necessarily the same for all gases: For AMMA T3 (Ouagadougou to Marrakesh) the midlatitude mixing ratios for water vapor were chosen because the main part of the flight was situated above the

Sahara, where the water vapor values were clearly lower than in the tropics. However, the tropical profile for HNO_3 was used, because the midlatitude value rather represents profiles typical for Latitudes higher than about 45° N. If not taken from interpolated ECMWF data, the a priori was kept constant during each flight to assure that all gradients and structures along the flight track are resulting from measurements and are not caused by the choice of a priori. This is also the reason why a climatological profile was chosen for H_2O even though ECMWF data is available. The results for HNO_3 for this profile are, as expected, in between the tropical and the midlatitude profiles. Like O_3, HNO_3 is varied up to 60 km altitude with a correlation length of 100 km.

Panel g) shows the retrieved CCl_4 volume mixing ratio from forward and backward spectra compared to its a priori (profile of the MIPAS reference atmospheres from Remedios et al. (2007b), for CCl_4 only one global profile is given). The profiles of forward and backward spectra agree well, but differ significantly from the a priori profile. This is probably the case because the global profile is not a good representation for the local conditions, especially the tropopause altitude seems to be too low in the a priori profile. Below 9 km the retrieved profiles return to the a priori values because no measurements are available there (see Panel a)). Due to the employed vertical correlation length of 1 km values relax smoothly to the a priori above and below the altitudes where measurements are present. Like temperature, CCl_4 is varied up to an altitude of 25 km during the retrieval.

Panel h) shows the retrieved PAN volume mixing ratio from forward and backward spectra. The a priori value is set to zero in this case, but an assumption for the amount of PAN expected is included with choosing 100% of a profile approximated from Glatthor et al. (2007) as a priori standard deviation. This provides some constrain to the PAN retrieval but the influence of the a priori on the result is presumably lower than with an explicit a priori profile. The profiles from forward and backward spectra agree well apart from the values between 11 and 13 km where no radiance measurements are available for the backward spectra. At these altitudes PAN tends to lower values because of the increasing influence of the zero a priori profile. PAN is, as CCl_4 and temperature, varied up to an altitude of 25 km with a correlation

length of 1 km. Below the lowest measurement altitude the PAN amount relaxes towards the zero a priori profile. That no PAN is found above 16.5 km (i.e. below the flight altitude) shows that there is less PAN than CRISTA-NF can detect.

3.2.4 Averaging kernel, resolution and measurement contribution

For the scientific interpretation of the results it is important to have measures indicating whether a retrieved value represents a real state of the atmosphere or is biased by the a priori or other effects. Such measures can be derived from the Averaging Kernel (AVK) matrix. The AVK matrix describes the sensitivity of the retrieval to the true state (Rodgers, 2000):

$$\hat{\mathbf{x}} = \mathbf{A}\mathbf{x} + (\mathbf{I} - \mathbf{A})\mathbf{x_a} + \mathbf{G}\epsilon, \tag{6}$$

where $\mathbf{A}$ is the AVK matrix, $\mathbf{I}$ the identity matrix, $\mathbf{x_a}$ the a priori data, $\hat{\mathbf{x}}$ the retrieval result, $\mathbf{x}$ is the true state and $\mathbf{G}\epsilon$ is the retrieval error.

The AVKs (rows of the AVK matrix) are displayed in Figure 14 and 15 (colored line) for the retrieval results of the profiles for forward spectra of profile 94 of AMMA flight T3 (corresponding to the retrieval results displayed as red lines in Figure 13). In all cases only the part of the AVK matrix considering the influence of the retrieved variable itself is regarded, the effect of correlation between different variables to the AVKs is neglected. Reduced to one variable, the AVK matrix gives the sensitivity of the vector of the retrieved variable on the given altitude grid (row) to changes in the true state vector (column). Ideally and without correlation lengths this matrix would be diagonal, that means the retrieval result for one variable at one altitude would not be influence by results from other altitudes or variables.

In addition, two retrieval characteristics derived from the AVK matrix are shown: The retrieval resolution and the measurement contribution. Following Purser and Huang (1993) the resolution is given as information density (reciprocal of the trace of the AVK matrix) multiplied by the grid spacing. The measurement contribution is calculated as the integral over the AVKs. The measurement contribution is an approximate measure of the proportion to which measurements and a priori contribute to the retrieval results (Rodgers, 2000). In

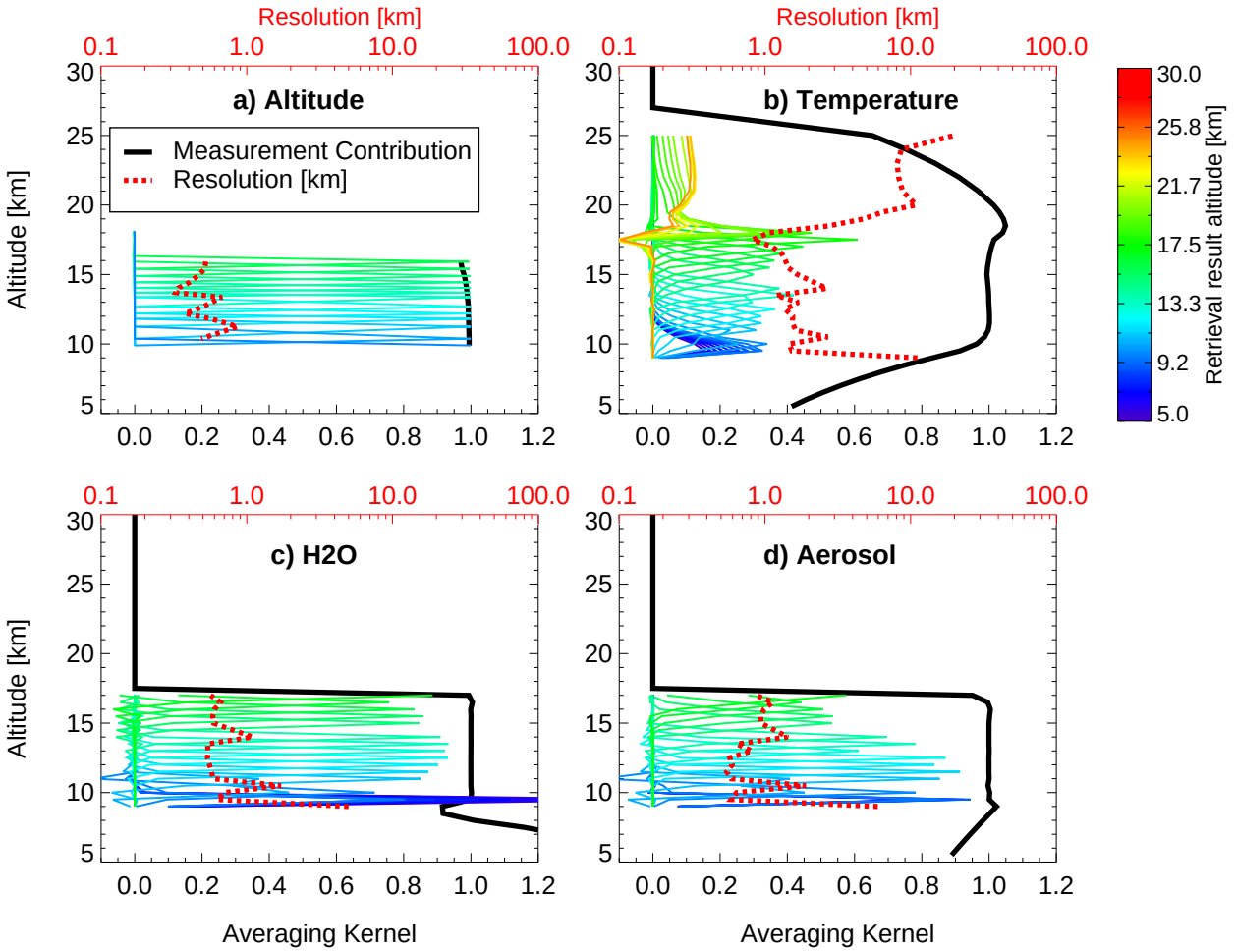

Figure 14: Averaging Kernels (AVKs) for AMMA T3, Profile 94 for a) altitude, b) temperature, c) H_2O , d) aerosol. The AVKs (colored line) displays the influence of the elements of the state vector on the result at the retrieval grid point of the altitude (color code). The red dotted line shows the resolution, the black line the measurement contribution in relative units (0-1).

an idealized case, a value of 0.0 for the measurement contribution means, that the result is only containing a priori information. A value of 1.0 means that the result contains only measurement information and is independent of the a priori. However, the measurement contribution can exceed the value of one in case of non-linearities and large retrieval errors.

Panel a) of Figure 14 shows the AVKs for the altitude retrieval. The AVKs reach a value of nearly 1.0 for each retrieved altitude and they are very narrow. This indicates that the retrieved altitudes are mainly influenced by measurements at the resulting altitudes. Also, the influence of the a priori (i.e. the geometrically calculated tangent altitude) is low, since

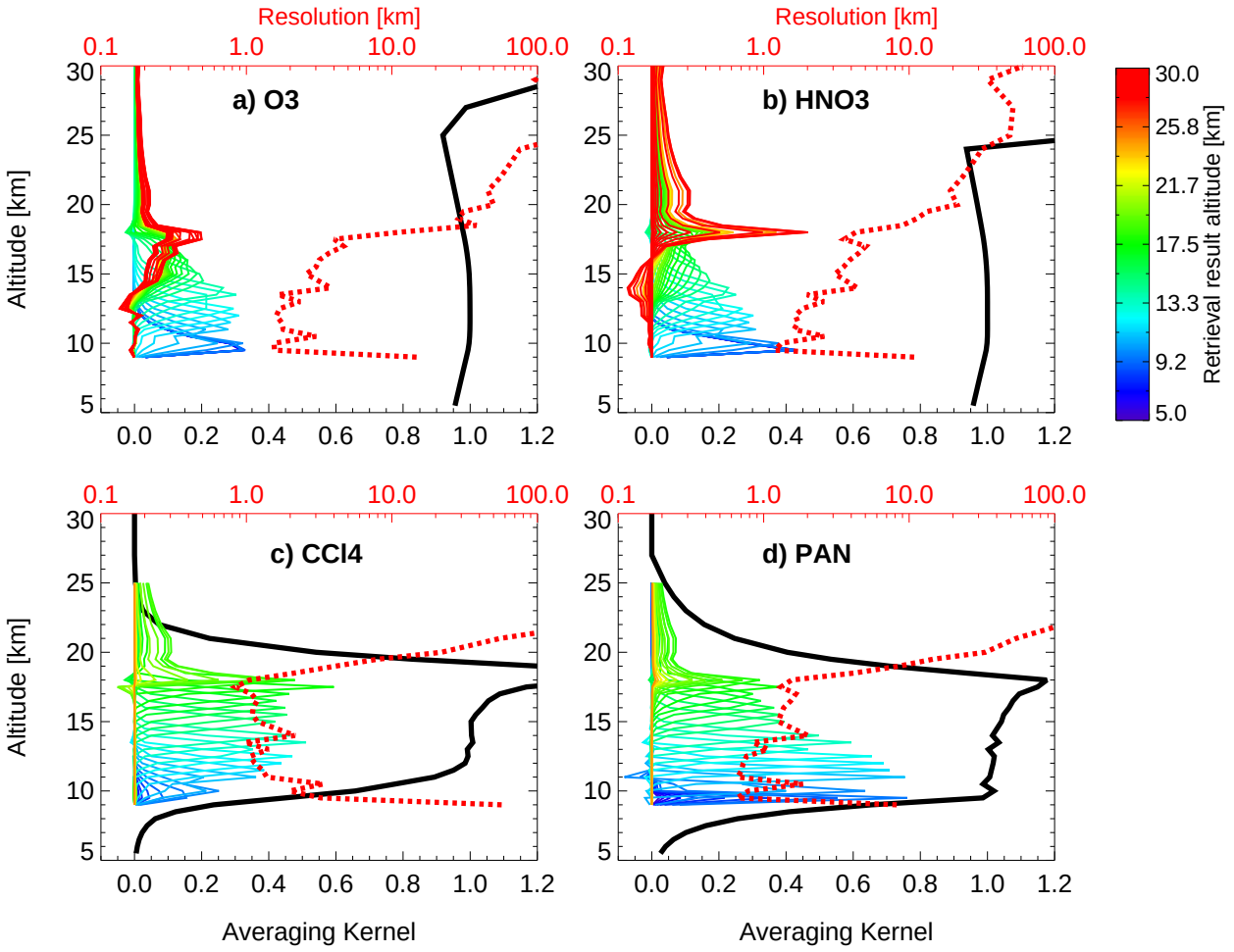

Figure 15: Like Figure 14 for a) O_3 , b) HNO_3 , c) CCl_4 and d) PAN.

the measurement contribution stays close to 1.0. Weak a priori influence can be found at the highest altitudes. In case of the altitude retrieval, the resolution matches the spacing of the retrieved tangent point altitudes of about 500 m.

The AVKs for temperature, CCl_4 and PAN are shown in Figure 14b), and Figure 15 c) and d). They have somewhat wider AVK peaks as the retrieved altitude and typically peak values are between 0.3 and 0.8. This indicates that some information contributing to the result originates either from other altitudes than the regarded grid point or from the a priori. In order to separate these two effects the retrieval resolution and the measurement contribution have to be considered. The vertical resolution for temperature, CCl_4 and PAN is usually between 1 and 2 km, implying that two to four neighboring grid points influence each other. The measurement contribution reveals that the contribution of the a priori value to the result

is small within the altitude range of the measurements. Above and below the altitudes with radiance measurements the result is, as expected, dominated by the a priori. The measurement contribution provides information to filter out data which is clearly influenced by the a priori, like the ones below about 10 km for CCl_4 and PAN (Figure 13). Also, very high measurement contribution over 1.2 (e.g. for CCl_4 between 17.5 and 19 km) are a sign of questionable data quality. One should notice that hardly any information enters the retrieval below the lowest measurement altitude (as expected) but clear peaks of the AVK can be found above the highest one. This is due to the fact that along the LOS radiance from above, but not below the tangent point is contributing to the corresponding measurement.

Figures 14c) and d) show the AVKs, vertical resolution and measurement content for water vapor and aerosol. The AVK peaks are more narrow than for temperature, CCl_4, and PAN and reach higher values. For aerosol they get somewhat broader for altitudes above 15 km indicating that the data quality is better at the lower part of the profile. The resolution, especially for H_2O, nearly reaches the grid spacing for most altitudes. The measurement contribution is close to 1.0 from the lowest measurement altitude up to 17 km. No information is used from above this altitude, since these variables are only varied up to 17 km altitude during the retrieval (see Section 3.2.1).

Figures 15 a) and b) show the AVKs, vertical resolution and measurement contribution for O_3 and HNO_3. The AVK peaks are broadest for these two gases and rarely reach higher values than 0.4. The measurement contribution is close to 1.0 below 25 km indicating a minor influence of a priori data on the retrieval result. As for CCl_4, results with very high measurement content found e.g. above 25 km are not reliable. At altitudes above 25 km also the vertical resolution is worse. For HNO_3 and O_3 the vertical resolution for all altitudes is rarely better than 1.5 km. It is important to keep in mind that the measurements contributing to the result are not necessarily (only) from altitudes close to the retrieval grid point regarded. It is even possible that most of the measurement information originates at a lower or higher altitude. This is the case for O_3 and HNO_3 above 20 km in Figure 15a) and b). Both have a measurement contribution close to one, but the AVK reveals that most of this information

comes from an altitude of about 17-18 km. Hence, always measurement contribution and resolution need to be regarded for the interpretation of the retrieval results.

Comparison with independent data

When retrieved data is compared to data from other sources, e.g. the Chemical Lagrangian Model of the Stratosphere (CLaMS, see Section 4.3), the AVK needs to be considered. The retrieval result can be regarded as a combination of the unknown real state, the a priori and the retrieval errors (Rodgers, 2000), see also Equation 6. Therefore the independent data need to be convoluted with the AVK as well, to be comparable to the CRISTA-NF retrieval result, following e.g. von Clarmann (2006). Hence, the CLaMS data for comparison results from:

$$\mathbf{x}_{\mathrm{CLaMS(AVK)}} = \mathbf{A}\mathbf{x}_{\mathrm{CLaMS}} + (\mathbf{I} - \mathbf{A})\mathbf{x}_{\mathbf{a}} \tag{7}$$

Where $\mathbf{x}_{\mathrm{CLaMS}}$ are the CLaMS data (interpolated onto the retrieval grid) and $\mathbf{x}_{\mathrm{CLaMS(AVK)}}$ are the resulting, convoluted CLaMS data.

Figure 16 shows the difference between O_3 from CLaMS and the result of the CRISTA-NF O_3 for AMMA flight TF2. For a detailed discussion of these results see Section 4. In Panel a) the CLaMS results are interpolated onto the grid of the CRISTA-NF retrieval results. In Panel b) CLaMS data is additionally convoluted with the AVK following Equation 7. Obviously the differences to the CRISTA-NF data are much larger, when omitting the AVK as in Panel a), especially above about 17 km. Hence, the largest differences are found above the measurement altitudes where the resolution of the CRISTA-NF data decreases (see Figure 15). This indicates that it is necessary to apply the AVK to other data sets, if comparing O_3 data, because the CRISTA-NF retrieval results are notably smoothed above about 16km due to their decreasing vertical resolution at these altitudes. The same comparison for CLaMS water vapor and ECMWF temperatures reveals nearly no influence of the AVKs on the comparison (not shown), since these variables can be retrieved with a vertical resolution much better than for O_3 from CRISTA-NF measurements.

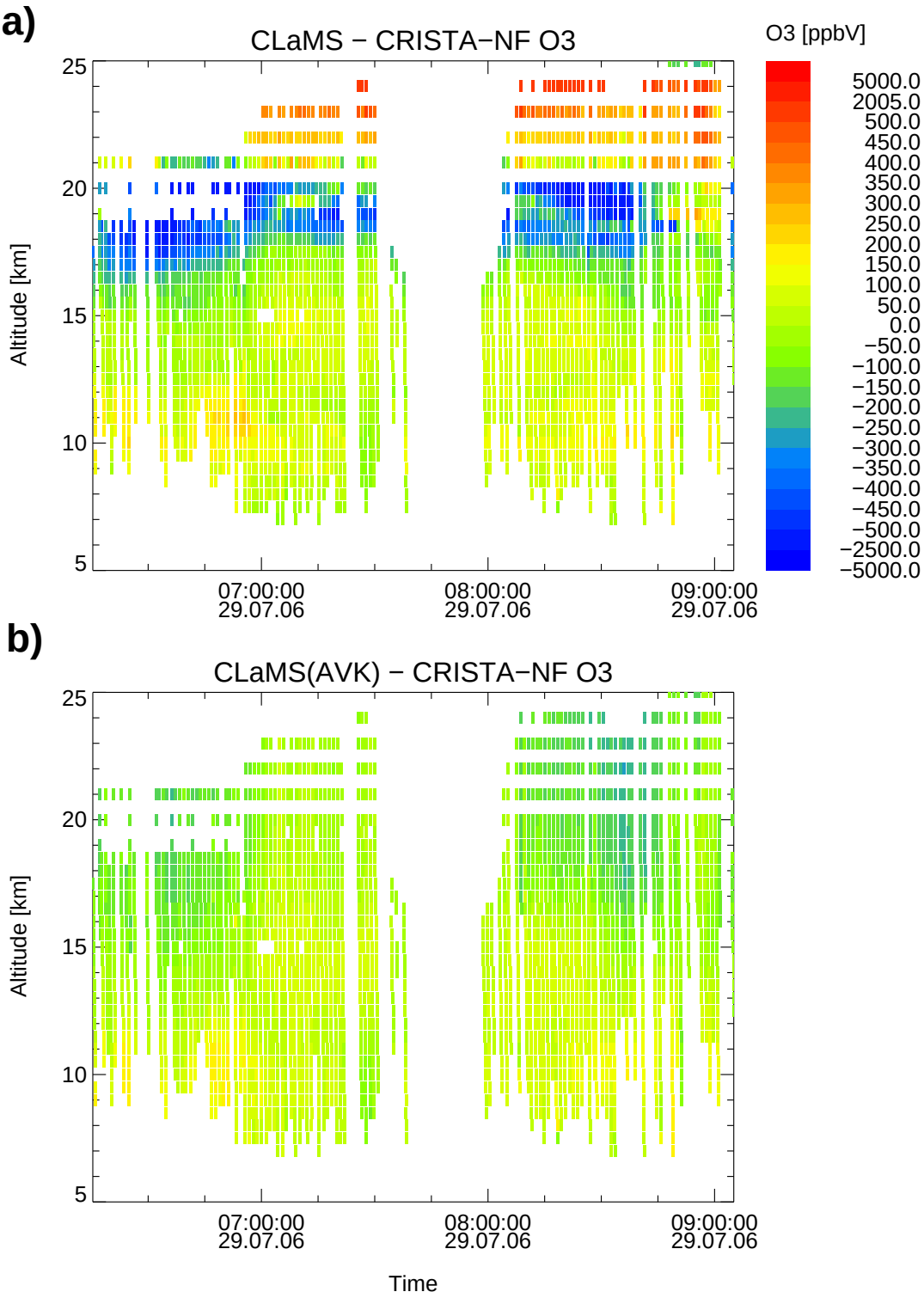

Figure 16: CRISTA-NF O3 Retrieval for AMMA TF2 (see Section 4.4) subtracted from CLaMS O3 a) without and b) with applying the AVK to the CLaMS data. Note nonlinear color scale.

3.2.5 Retrieval errors

Another measure to assess the quality of the retrieved data are the retrieval errors. In Figure 13c the result of the water vapor mixing ratio drops to zero at 16 km, which is not realistic (e.g. Silva dos Santos, 2008). That means that CRISTA-NF is not able to detect the small mixing ratios (below 10 ppmV) correctly in this altitude. It can not be explained by resolution and the measurement content (Figure 14c), but is consistent within the large H_2O error obtained for this altitude.

The overall errors of the retrieval results are displayed for each variable in Figure 13. The corresponding detailed error analysis is shown in Figures 17 and 18. The retrieval errors consists of several components:

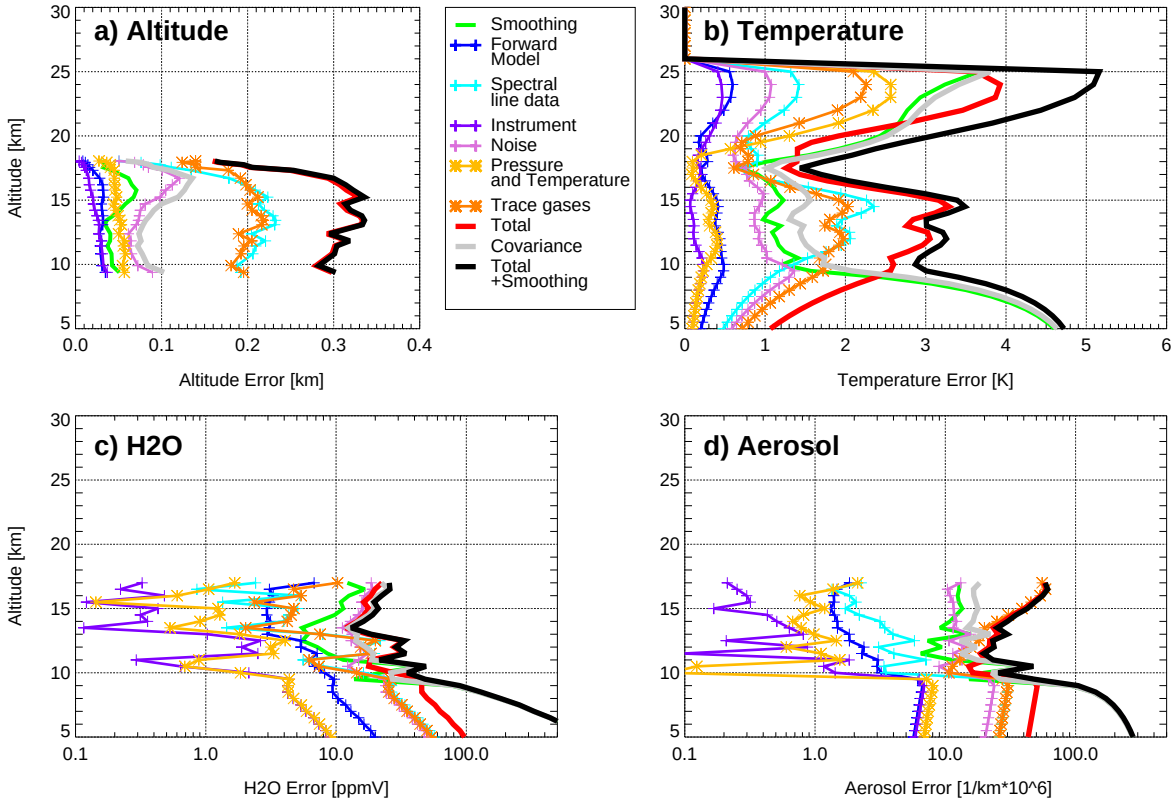

Figure 17: Estimated retrieval error components for AMMA T3, Profile 94. For a) altitude, b) temperature, c) H_2O, and d) aerosol retrieval.

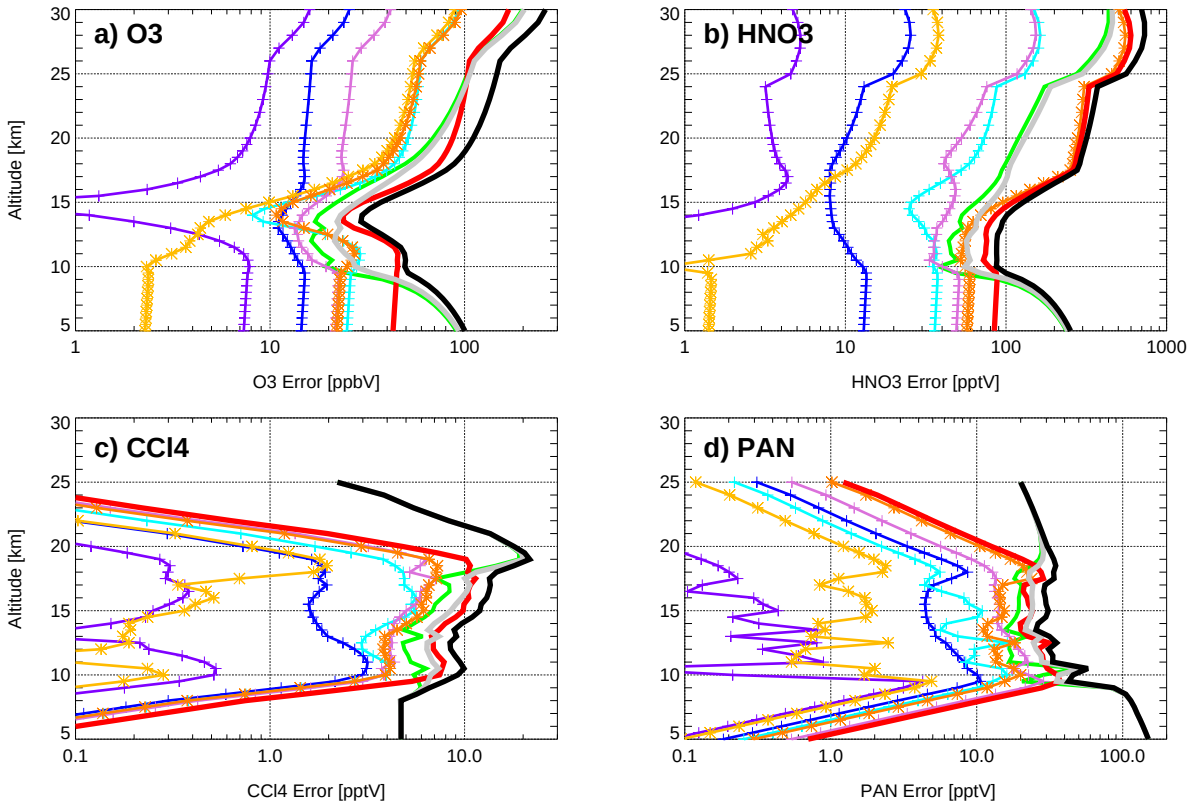

Figure 18: Estimated retrieval error components as in Figure 17. For a) O_3, b) HNO_3, c) CCl_4, and d) PAN retrieval. Colors as in Figure 17

- Smoothing error:

  The smoothing error is shown as green line in Figures 17 and 18. It is caused by the a priori covariance and depends on the measurement contribution. However, often the exact covariance of the a priori is not known exactly and a higher, conservative estimate is used for the retrievals in order to increase the weight of the measurements. In these cases, the smoothing error is overestimated and results in an overestimated error of the retrieval result, if included in the total error. On the other hand, the total error without smoothing error tends to underestimate the real error with respect to the unknown real state of the atmosphere. The total error without smoothing can be regarded as the error of the smoothed state, i.e. it does describe the error compared to data smoothed on the retrieval grid but does not take larger variations which might occur on smaller vertical scales into account. This means, when comparing the retrieval result to an estimate of the real state (e.g. high resolution in situ observations) the smoothing error should be included, when comparing to an estimate after applying the AVK (like for CLaMS data) it should be omitted.

- Forward model error:
  The forward model error (blue line in Figures 17 and 18) is the part of the retrieval error caused be the standard deviation of JFM (see Table 4). This is determined by comparing the fast forward model JFM with the line-by-line model RFM during the regression (see Section 3.1.4).

- Spectral line data error:
  The errors caused by uncertainties of the spectral line data (see Table 2 and 3) are shown as a cyan line in Figures 17 and 18.

- Model parameter error:
  Errors caused by the standard deviations of the forward model parameters (see Table 2 and 3). These include not retrieved emitters and pressure. But also temperature and retrieved emitters contribute to this error through the altitudes where they are not varied in the retrieval and therefore act as forward model parameters. In Figures 17 and 18 this error is divided into contributions from temperature and pressure (gold line) and the one from the trace gases (orange line).

- Instrument error:
  The instrument error comprises the instrument offset and gain (violet line).

- Noise:
  This is the error caused by measurement noise (orchid line).

The total error (red line) is the square root of the sum of the squares of all components mentioned above except for the smoothing error. The total+smoothing error (black line) also contains the smoothing part. The "covariance error" (gray line) contains all errors of quantities considered for the retrieval fit (see Section 3.2.1), i.e. for the setup used a combination of the noise and the smoothing error.

The leading terms of the total error for most of the retrieved variables are the errors due to the non-retrieved emitters, the spectral line data and the noise. The instrumental errors, forward model errors and pressure and temperature play a minor role. For the altitude retrieval CO_2 and CFC-11 contribute most to the errors caused by forward model parameters (not shown), even though in situ data are used to improve the knowledge about CFC-11, implying a smaller standard deviation (see Section 3.2.6). This underlines the sensitivity of the altitude retrieval to these emitters. The error components of profile 94 shown in Figures 17

and 18 can be considered to be representative for the errors of most profiles. The error analyze clearly shows:

- A good spectral data base is important.
- Improving JFM with a linear regression (see Section 3.1.4) decreased the forward model errors sufficiently for the retrieval.
- The black body calibration (Appendix A.1.1), i.e. the instrument and noise error, is sufficiently accurate for the retrieval.
- The retrieval result could be improved, if
    1. it would be possible to fit the retrieved radiance to the measured ones inside the limits of the noise error. An improved in-flight wavelength calibration may contribute to this.
    2. improved data for emitters, which cannot be retrieved (e.g. CO_2, $ClONO_2$, CFC-11), would be implemented, e.g. from satellite measurements.

It should be noted that especially for aerosol and H_2O the errors are rather large compared to the absolute value of the variables. For H_2O relative errors often exceed 100% for low H_2O mixing ratios below about 10 ppmV in the higher altitudes, for aerosol high relative errors do occur more often (see Appendix B.2, Figure 65). This can explain unexpected values of H_2O even if χ^2/m, resolution and measurement contribution indicate a high data quality and underlines that a retrieval of H_2O mixing ratios under about 10–15 ppmV is not possible with the setup used.

Further sources of errors

Calibrations and the comparison to a line by line forward model cannot assess all possible errors. Errors not accounted for are:

- Aerosol extinction and thin clouds:

  Aerosol extinctions have a rather continuous spectral signature, but its shape can change with the composition of aerosols. For the retrieval one fixed spectral shape is assumed, (75% of H_2SO_4 approximated from Massie et al., 1994; Spang pers. com.) and applied as

scaling factors. Especially for tropospheric conditions the real spectral shape can differ significantly. For wavenumbers smaller than about 850 cm^{-1} the aerosol extinction has few structures and is relatively low, resulting in a low influence on the retrieval result. For the ISBs above about 850 cm^{-1} and the sequential HNO_3 retrieval (see Section 3.2.7) its influence could be important.

Thin clouds or clouds entering the field of view while one spectrum is measured may not be detected by the cloud index and can influence the retrieval. Presumably thin clouds would be mistaken as aerosol layers. Compared to most limb measurements these errors caused by clouds are relatively small for CRISTA-NF because of the narrow field of view.

- Relaxations:

  For the satellite instrument CRISTA so called relaxations, which are short-term, non-linear sensitivity changes of the detectors, up to 10% were observed (Offermann et al., 1999). For the Satellite instrument CRISTA an empirical correction model was developed (Ern et al., 2003). Due to the changes in the spectrometers and the different observation geometry, it is not possible to use this correction without modifications for CRISTA-NF. There are presumably some relaxations which do also contribute to the difference between forward and backward spectra.

- Stray light:

  Several baffles are used to filter the incoming radiance for stray light (Barthol, 1994). Nevertheless, some stray light might enter the spectrometer and influence the result.

- Undetected spikes:

  Spikes are filtered before the retrieval according to Arndt (2006). If spikes are overlooked they could be misinterpreted for spectral features. There are relatively few spikes for the detectors L5 and L6 and most of them are identified and removed by the filter. Therefore the remaining spikes would, if at all, only influence single retrieved grid points and have only minor effects on the result.

- Errors of the line-by-line forward model:

  Through the emissivity tables RFM directly influences the result of the retrieval. Since it is also used to check the final data, errors in connection with RFM itself, e.g. because of missing emitters, underestimated errors of the spectral line data or problems with line mixing are difficult to quantify. In comparison with other forward models it has shown to be very reliable (von Clarmann et al., 2003). Nevertheless, there is a systematic difference between the measured spectra and RFM calculations around 855 and 860 cm^{-1}, in the order of 10% for all altitudes present in most spectra (see e.g. Figures 6 and 22). No general explanation could be found and comparisons to MIPAS spectra for the fifth local flight of AMMA (not shown) indicate, that it is not caused by an instrumental error of CRISTA-NF. Also for the satellite instrument CRISTA problems to fit the measured spectra to the modeled ones are known for this wavenumber region (Küll, 2006 and Olschewsky pers. com.). This could indicate that an unknown spectral signature is present at this point.

To exclude that any of these errors has a substantial influence, the retrieval result is compared to other data, e.g. in situ measurements performed simultaneously on M55-Geophysica (see Section 4.2).

3.2.6 Temperature and altitude

For trace gas retrievals, information about the temperature of the atmosphere and the measurement altitude are important (e.g. Riese et al., 1999a). There are different ways to determine both, temperature and altitude (see Section 3.2.1 for the explanation of the altitude retrieval), in addition to the emitter mixing ratios:

1. Temperature and/or altitude can be taken from external sources.
2. At one spectral point it is not possible to distinguish the influence of temperature and altitude, but their behavior varies spectrally. This makes it possible to use either:
   (a) the shape of one spectral peak or
   (b) two different spectral regions with known major emitters.

On the temporal and spacial scales observed by CRISTA-NF, the atmosphere can be assumed to be in hydrostatic equilibrium, allowing to calculate pressure from altitude and temperature. To do so it is sufficient to know the reference pressure at one altitude. The required reference pressure is taken from ECMWF analysis data at an altitude of 15 km.

Temperature, pressure and altitude determine the shape and relative intensities of the observed spectral signatures. If the mixing ratios of all relevant emitters, their vertical distribution, their spectral lines, the pressure and the LOS are known the radiance at a given wavelength depends only on the temperature (see Section 3.1). Given an accurate pointing information, it is therefore possible to retrieve the temperature in a wavenumber range, where the radiation is mainly emitted by one gas with known mixing ratio. An ideal gas for this purpose is CO_2 , because it is well mixed in the troposphere and lower stratosphere, its mixing ratio is frequently measured by various instruments, and because it is the dominant emitter in the wavenumber region around 792 cm^{-1}, covered by the CRISTA-NF channels H5, H5R and L6. The CO_2 Q branch at 792 cm^{-1} was also used for the temperature retrieval for the CRISTA satellite instrument, see Riese et al. (1999a).

However, due to problems with the CRISTA-NF attitude system (see Appendix A.1.7) the altitude has to be retrieved. Hence, a potential retrieval setup for CRISTA-NF must retrieve both altitude and temperature or use temperatures from an external data source.

The retrieval setup presented before in Section 3.2.1 uses 9 ISBs and therefore it requires relatively large computational effort. The setup was the result of a thorough selection process. This Section describes the reason for choosing the particular ISBs and compares the setup with 9 ISBs (Setup C) to two faster setups using just 6 ISBs. Table 5 summarizes the employed setups.

Setup A

Instead of retrieving the temperature, this setup uses ECMWF temperatures. It is based on 6 ISBs, omitting the spectral range above 800 cm^{-1}. Hence, HNO_3 can not be retrieved, see Figure 6. A similar approach, but with only 3 ISBs was applied for the measurements of CRISTA-NF during several SCOUT-O3 transfer flights by Hoffmann et al. (2009).

Table 5: Retrieval setups.

Setup A	Setup B	Setup C
6 ISBs $[cm^{-1}]$	6 ISBs $[cm^{-1}]$	9 ISBs $[cm^{-1}]$
777.8–778.7, 784–785 787–790, 791–793 794.1–795, 796.6–797.5	777.8–778.7, 784-785 787–790, 791–793 794.1–795, 796.6–797.5	777.8–778.7, 784–785 787–790, 791–793 794.1–795, 796.6–797.5 832–832.9, 844.3–847.3 863–864
Retrieved variables	Retrieved variables	Retrieved variables
Altitude CCl_4, H_2O O_3, PAN Aerosol and offset	Temperature, altitude CCl_4, H_2O O_3, PAN Aerosol and offset	Temperature, altitude CCl_4, H_2O, HNO_3 O_3, PAN Aerosol and offset

Sources for a priori mixing ratios of the different emitters, their covariances and the retrieval grid are the same as in Section 3.2.1 apart from the a priori covariance of temperature, which is set to 2 K and for the one for HNO_3 , which is set to 10% for all altitudes. The influence of all three different setups (see Table 5) on the altitude and temperature retrieval is presented in Figures 19 and 20 exemplary for the forward spectra of profile 94 during the AMMA flight T3.

The retrieved altitude from Setup A is shown in green in these Figures. Figure 19 shows the difference between the retrieved tangent altitudes and geometrically calculated tangent altitudes. Obviously, the errors of the retrieved altitude become large for the upper tangent altitudes because there small temperature changes correspond to relatively large altitude changes. For the same reason the measurement contribution, shown in Panel c), decreases. Figure 20 shows the retrieved temperature for three different setups together with the a priori temperature from ECMWF operational analysis data. The temperature of Setup A is not varied but remains on the ECMWF value.

Setup B

Here the same variables as in Setup C are retrieved from only 6 ISBs, except HNO_3 . The result of the altitude retrieval from Setup B (blue line in Figure 19) differs a lot from the one

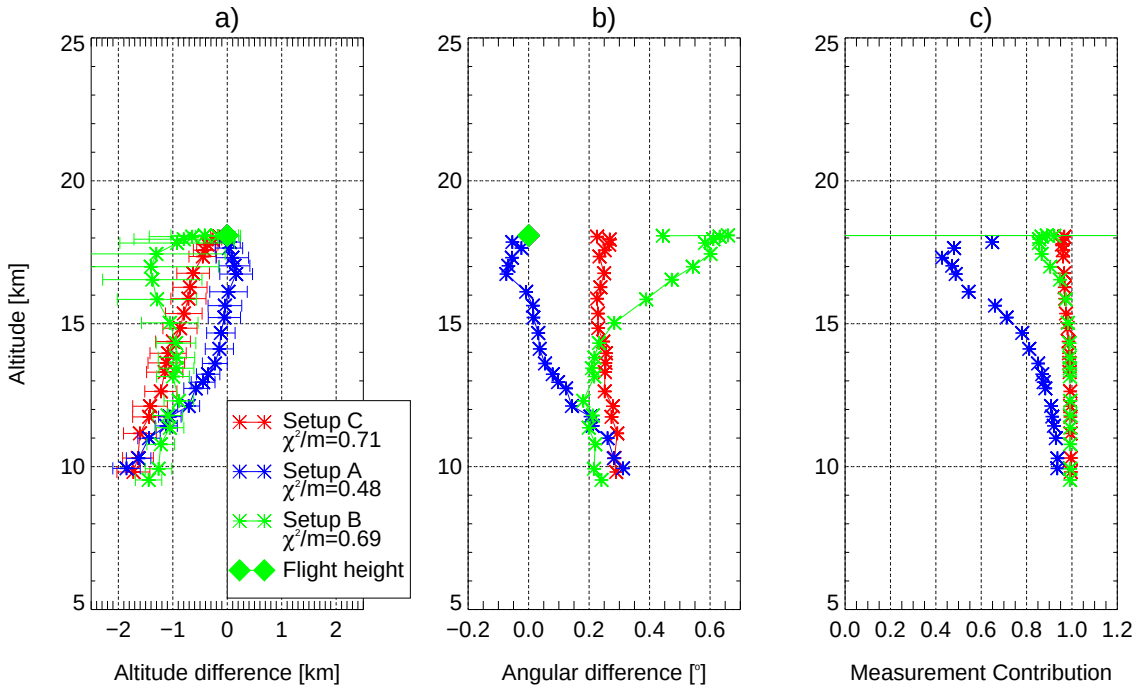

Figure 19: Altitude retrieval for three different Setups A (green), B (blue) and C (red) explained in the text. Panel a) shows the altitude differences between the retrieved altitude and the geometrically calculated altitude the with the total error (including smoothing), Panel b) shows the angular difference and Panel c) the measurement contribution.

of Setup A. The measurement contribution indicates that insufficient information is provided to retrieve both, temperature and altitude. This is due to the small number of ISBs providing not enough information.

Around the tropopause, the retrieved temperature is much lower than the ECMWF temperature and higher below 11 km (Figure 20). The deviations from the ECMWF temperature appear too large and are probably due to a systematic error in the retrieved altitude.

Setup C

Setup C was already explained in detail in Section 3.2.1. From Setup B it is obvious that more information is necessary. Setups with several ISBs at the CO_2 Q branch were tested, but resulted only in small improvements compared to Setup B. Even the higher spectral resolution

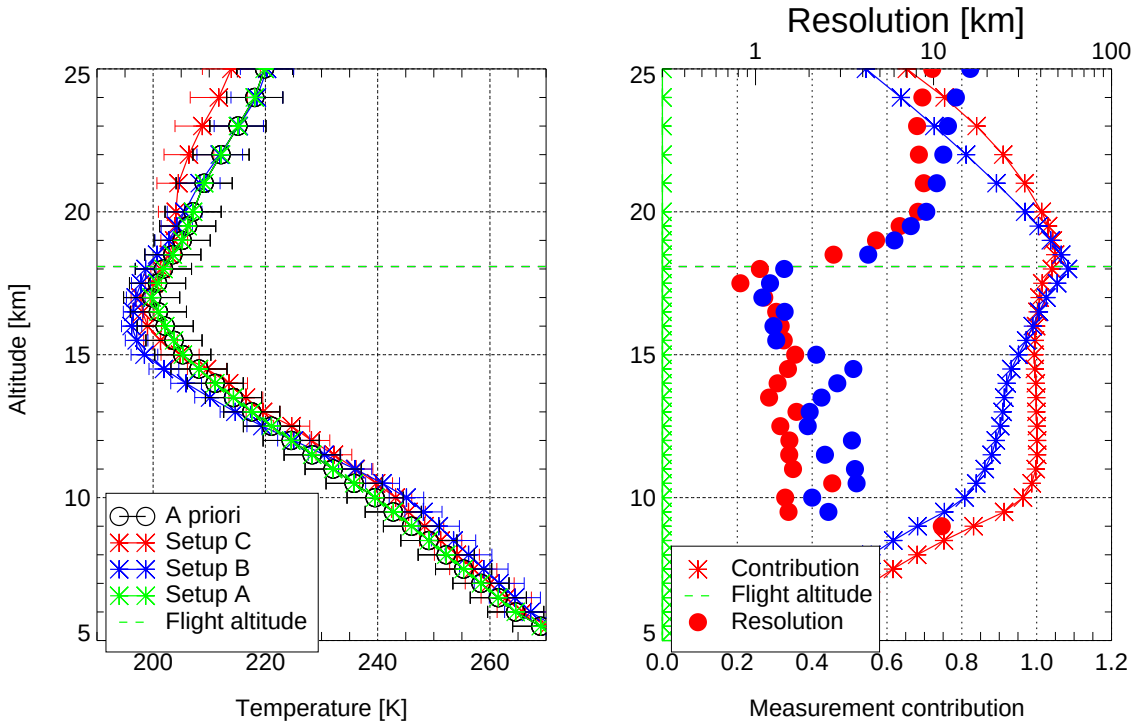

Figure 20: Temperature retrieval for the same setups as Figure 19. Panel a) shows the retrieved temperature and the a priori (ECMWF) temperature. Panel b) shows the resolution and measurement contribution.

of detector H5R was not sufficient to clearly separate temperature and altitude. Therefore a different spectral region with a known dominant emitter was added with the 845 cm^{-1} CFC-11 emission band.

Like CO_2 , the amount of CFC-11 in the troposphere is relatively well known. In addition, it was measured by the in situ instrument HAGAR (see e.g. Werner et al., 2009 for a description of the HAGAR instrument) on M55-Geophysica during the AMMA campaign. The profiles measured during ascent and descent of M55-Geophysica are combined with CFC-11 values above the flight altitude from the MIPAS reference atmosphere scaled to the measured values and smoothed at the transition (see Figure 21). The CFC-11 a priori covariance is a combination of the climatological error and the difference between the HAGAR ascent and descent profiles. For CFC-12 HAGAR measurements were combined with CFC-12 from the reference atmosphere the same way, allowing to retrieve also HNO_3 . CFC-12 has some

spectral signature between 860 and 865 cm^{-1}, where HNO_3 is the main emitter.

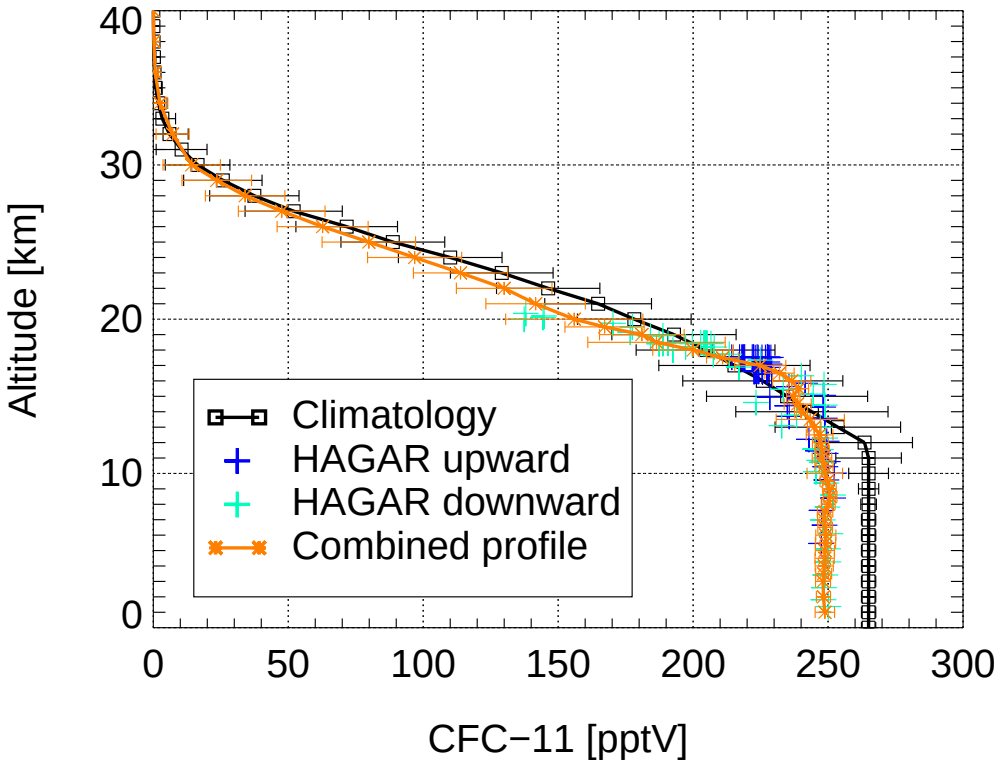

Figure 21: CFC-11 a priori profile for AMMA TF2 (orange). Blue and green crosses show the HAGAR measurements, the MIPAS reference atmosphere is given in black.

The result of the altitude retrieval compared to Setup A and B is shown as red line[7] in Figure 19. The retrieved altitudes show a constant angular offset with respect to the geometrically calculated altitudes. Such a constant offset might be explained by a misalignment between CRISTA-NF and the aircraft axes, which are the reference for the attitude of the M55-Geophysicas avionic system, see Appendix A.1.8. In Setup C the measurement contribution is the highest of all three setups.

The temperature retrieved with Setup C(Figure 20) is again lower than the ECMWF temperature close to the tropopause and higher below 14 km, but the differences are smaller than for Setup B. The measurement contribution is close to 1.0, the resolution better than 2 km for all altitudes between 10 km and the flight altitude.

[7]This is identically to the retrieval result for forward spectra presented in Figure 13, red line

The main disadvantage of Setup C is that it needs more computation time than the setups with 6 ISBs. In addition, a profound a priori knowledge of CFC-11 is necessary, implying that it is not possible to retrieve CFC-11. However, Setup C provides the possibility to retrieve temperature and altitude simultaneously. Therefore it does not rely on an external source of temperature data. By this approach it is possible to determine temperature with about the same spatial resolution as retrieved trace gases like CCl_4 and PAN. Additionally, using the complete spectral range of detector L6 allows to retrieve HNO_3, too.

Comparison with RFM spectra

The χ^2/m values given for the different setups are all smaller than 1.0, see legend in Figure 19. This indicates that the measured radiance in each setup is reproduced well for the ISBs used. But how well do the retrieved values describe the whole radiance spectrum measured? Which spectral information is responsible for the largely improved performance of Setup C? In order to investigate this, the measured radiance is compared to a line-by-line calculation with RFM for the results for the three retrieved profiles. Figure 22 compares the results of the three setups for two different tangent altitudes at 17.9 and 9.4 km. The upper panels show the measured spectrum together with the respective RFM spectra, the lower panels show their differences in percent.

All RFM calculations show a good agreement for wavenumbers below 800 cm^{-1} but only the RFM result for Setup C agrees well inside the whole wavelength range of L6 for both altitudes. This confirms that the wavelength region around the 792 cm^{-1} CO_2 peak does not provide sufficient information to distinguish the effects of temperature and altitude on the radiance for the moderate spectral resolution of CRISTA-NF. The uncertainty of CRISTA-NFs spectral resolution (see Appendix A.1.2) provides an additional difficulty when relying on the shape of one isolated spectral feature.

Additional ISBs below 800 cm^{-1} would not provide much more information because the residuals of the three setups do not differ much there. Tests with the detector H5R covering the wavenumber interval between 770 - 815 cm^{-1} with higher spectral resolution compared to L6 do confirm this.

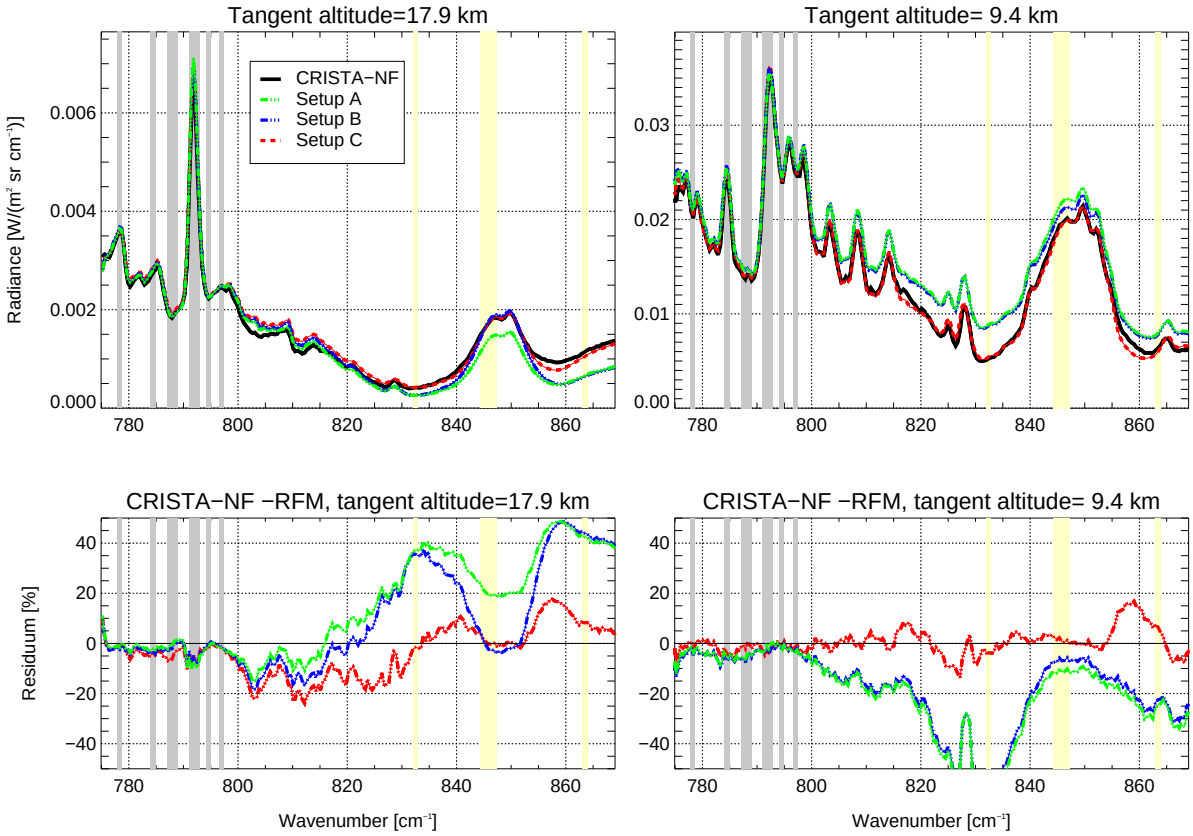

Figure 22: Comparison of measured CRISTA-NF spectra for AMMA T3, Profile 94 and RFM calculations for the results of the three different setups (Table 5). The tangent altitudes include refraction and refer to the Setup C. Gray bars mark ISBs used in all three setups, light yellow bars the ones used only in Setup C. The upper Panels shows the spectra, the lower the percentage difference between the measured spectra and RFM results for each setup.

In summary, the additional information which allows to retrieve temperature and altitude simultaneously in Setup C is provided by the ISBs above 832 cm^{-1}. In this spectral range there are obvious differences between the three setups and only Setup C can reproduce the measured spectra well as shown in Figure 22.

Simultaneously retrieved variables

Simultaneously with altitude and temperature, aerosol, CCl_4, H_2O, O_3, PAN, and a radiometric offset are retrieved for all three setups presented in Table 5. The results are shown in Figure 23. There are significant differences between the results for the different setups, too. Hence the choice of the ISBs does not only influence temperature and altitude but

also the other retrieved variables. The largest improvement is found for O_3 (Panel d). A O_3 retrieval is possible only with 9 ISBs. Otherwise O_3 drops to zero below about 16 km altitude. H_2O (Panel c)is least sensitive to the different setups. About all retrieved variables, namely CCl_4, aerosol, and especially PAN show the best result, i.e. the highest measurement content and the best resolution for Setup C.

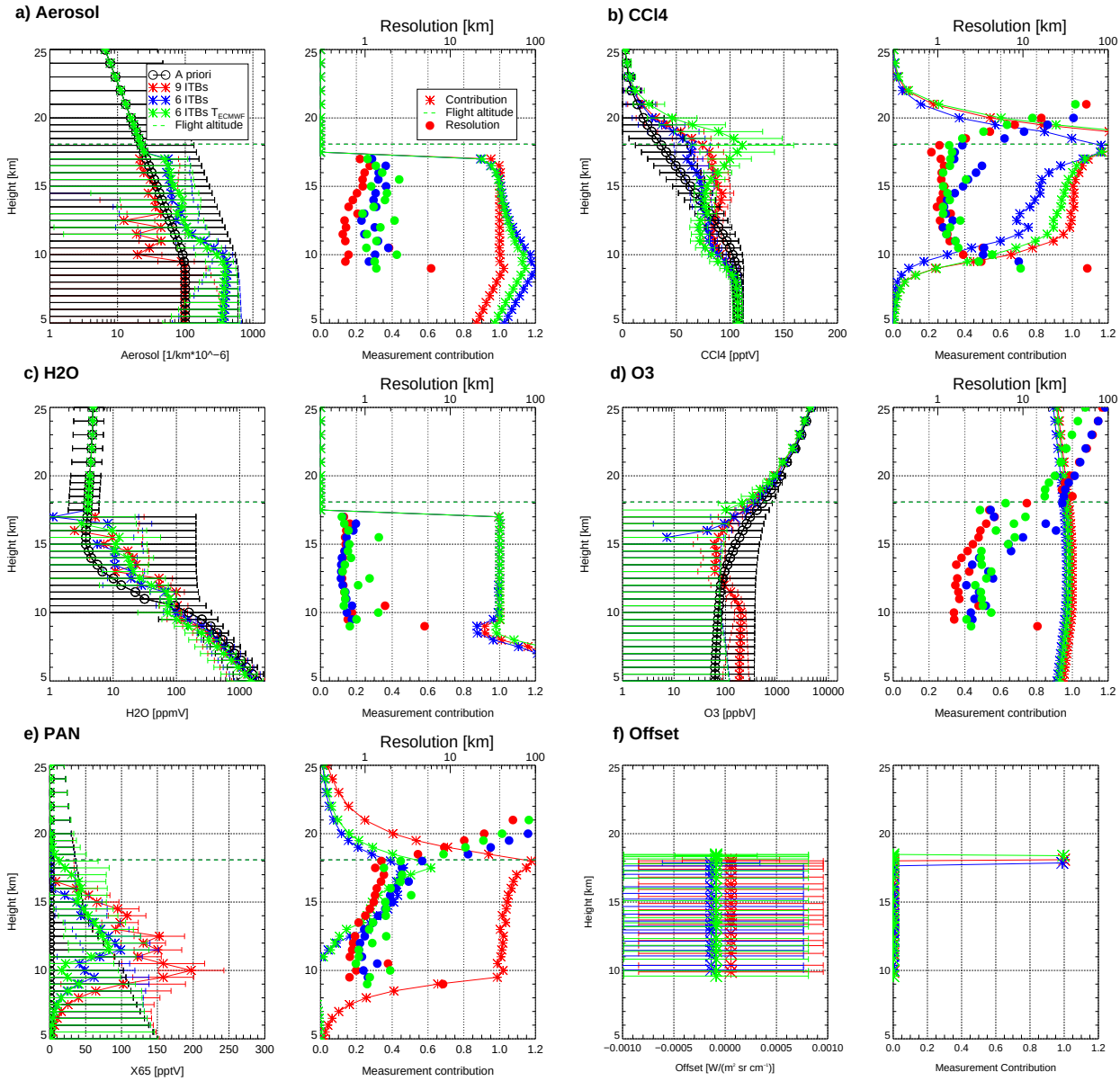

Figure 23: Retrieval results for the same setups as Figure 19 for a) aerosol, b) CCl_4, c) H_2O, d) O_3, e) PAN, and f) offset.

In total, the comparison shows that only a retrieval of H_2O is possible with a setup with ISBs only below 800 cm^{-1} and predefined temperatures. For midlatitude flights as TF2 (see Chapter 4) there are somewhat smaller differences between the retrieved temperature and the ECMWF temperatures facilitating a retrieval based on fixed ECMWF temperatures like in Hoffmann et al. (2009). That the retrieved temperatures differ less from ECMWF during TF2 might be due to a higher accuracy of the ECMWF data for this flights. Setup C will be used further on because it performs better for all retrieved trace gases, temperature and altitude and allows to retrieve HNO_3, additionally.

Accuracy of the altitude

The accuracy of the roll angle of the airplane, which has the largest influence on the pointing, is supposed to be better than $\sigma = 0.05^o$ (see Appendix A.1.7). However, the retrieved altitude in Figure 19 shows a large difference of about 0.25° from the one calculated geometrically from the attitude angles. Since an exact altitude information is essential for the trace gas retrieval it is tried to identify the source of the difference. The first guess would be that the difference is caused by the alignment of the instrument in the airplane which is known less accurately (see Appendix A.1.8).

A misalignment of the instrument around the aircrafts x-axis would have the largest impact on the pointing and cause a constant offset during the whole flight. Figure 24 shows the result of an altitude retrieval with Setup C for the complete flight AMMA TF2. Panel a) displays the difference of the retrieved altitude to the geometric altitude and the corresponding angular difference versus time. Panel b) shows the same versus altitude and Panel c) shows only the angular difference versus the aircrafts yaw angle. Different legs of the flight are colored differently to recognize them in all panels. The retrieved angles vary systematically over the flight with maximum values of up to 0.5°. These variations seem to be connected to different yaw direction of the aircraft.

The differences between offset angles resulting from the altitude retrieval are much larger than the stated uncertainty of the roll angle from the M55-Geophysica avionic system (UCSE roll angle). Since the average corrected roll angle is normalized on the UCSE roll it can not

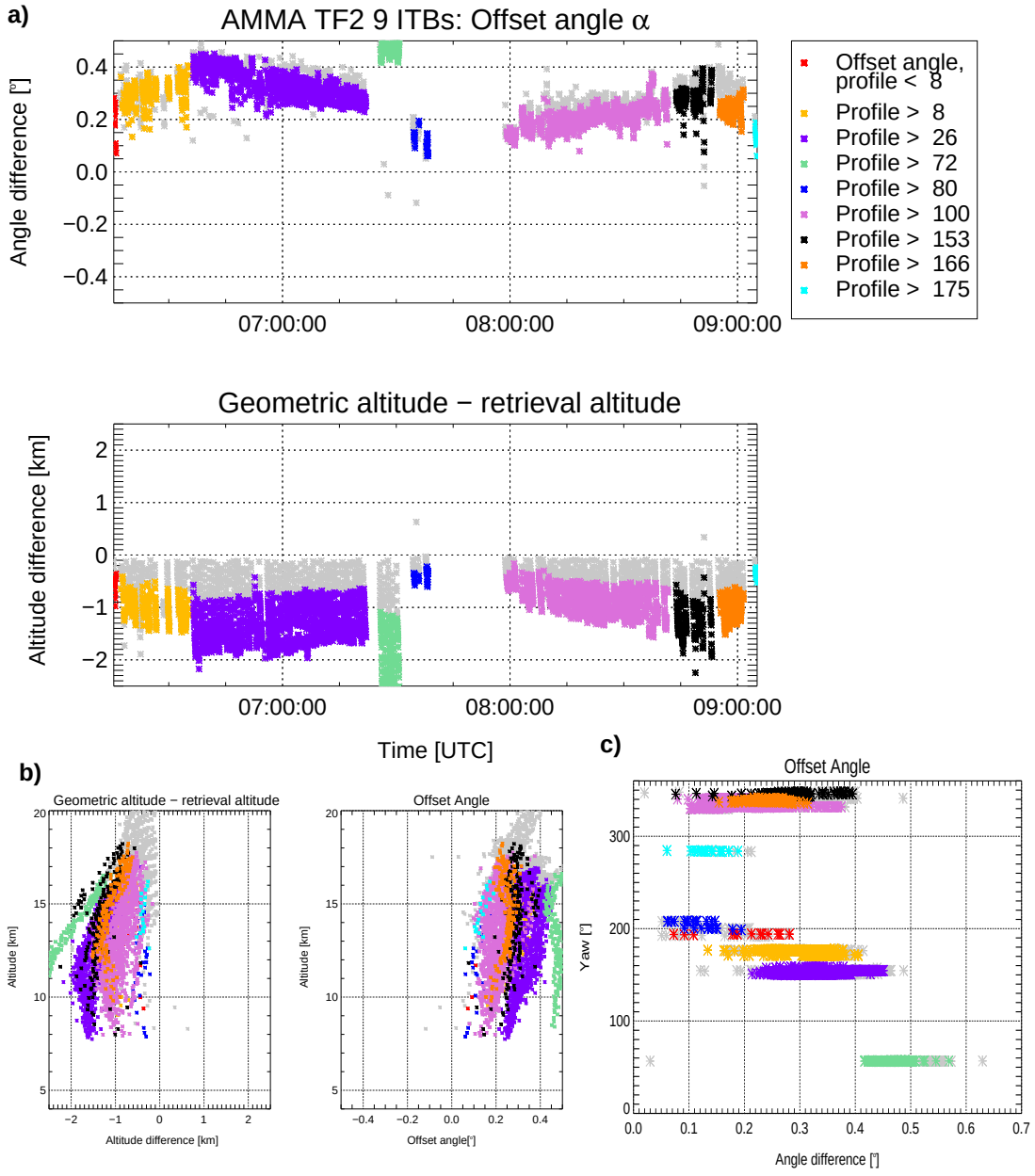

Figure 24: Offset angles vs. time for AMMA TF2. Grey stars indicate spectra with a $\chi^2/m > 2$ or a measurement content $< 98\%$, which are not included in the calculation of the average offset angle. Colored stars mark spectra included in the calculation from different parts of the flight track.

be caused by the pointing correction. A misalignment of the instrument can as well not be the reason, because it could only explain a constant offset over the whole flight.

A systematic variation in CFC-11 could have a significant influence on the retrieved altitude and would be likely to cause some systematic error because a constant CFC-11 profile is used for each flight. However, a clear dependence of the CFC-11 influence on the flight direction is not very likely, as was tested with CLaMS CFC-11 data for TF2 (not shown). Further the altitude differences are larger than the error of the retrieved altitude (see Figures 17a and 19) which includes an error component caused by the CFC-11 uncertainty. Other systematic errors in the retrieval due to differences in cloud cover, stray light, mixing ratios of not retrieved emitters or aerosol extinction can not be totally excluded as reason for the altitude differences. Indication of the influence of a high cloud cover on the resulting altitudes can be seen for flight T2 (see Appendix C.1, Figure 70), but is only observed if profiles can not be retrieved lower than about 10 km due to clouds. The flight TF2, where the largest differences between retrieved altitude and geometrically calculated altitude occur, took place in nearly cloud free conditions.

Systematic differences between the UCSE and the MIPAS pointing in the same magnitude were observed by Keim (2002). Also in this case the differences were connected with changes of the flight direction. This indicates that differences in pointing might be caused by the UCSE attitude angles. The differences exceed 2km for the lowest altitudes in some profiles of TF2, and underline the importance of applying an altitude retrieval simultaneous to or before the trace gas retrieval.

3.2.7 Sequential retrieval

Instead of retrieving all variables simultaneously, it is also possible to retrieve them sequentially, i.e. after each other. For such a sequential retrieval one should note that correlations between the variables and non-linearities can lead to errors.

The retrieval of HNO_3 with Setup C (simultaneous with the other retrieved variables) relies on the information from the spectral range between 863 and 864 cm^{-1} where HNO_3 is the primary emitter. For this ISB, situated close the upper limit of the detector L6, the wavelength calibration is less accurate (see Appendix A.1, Table 10). In addition, the measured radiance cannot be well reproduced by RFM for unknown reasons close to this ISB (see Figure 6, 22, and Section 3.2.5)

Therefore, to confirm the HNO_3 mixing ratio resulting from Setup C, a sequential retrieval for HNO_3 (simultaneous with aerosol and a radiance offset varying with altitude) is performed. Detector L5 is used for the sequential retrieval, because it covers a spectral region where HNO_3 is the dominant emitter and shows more distinct spectral features as within the spectral range of L6.

The setups for the sequential retrieval use three ISBs at 876–876.9, 878.1–879 and 880.2–881.1 cm^{-1}, i.e. next to and in the center of a relative strong HNO_3 band. A combination of EGA and CGA is used for the forward model, but no regression. The forward model error is estimated to be 0.5% for all ISBs. Temperature, CCl_4, H_2O, O_3, and PAN from Setup C are used as forward model parameters. The geometric altitude is adjusted by the average correction angle obtained from the altitude retrieval. The other forward model parameters and radiance errors are the same as the ones from Section 3.2. The aerosol extinction is more important for wavenumbers greater than about 850 cm^{-1}. Therefore two different setups for sequential retrievals are used with different aerosol extinction scaling factors:

- Setup CS1 (green line in Figure 25): Scaling factors from Massie et al. (1994) as in Section 3.2.5.
- Setup CS2 (purple line in Figure 25): The same scaling factor (100%) is used for all three ISBs.

Figure 25 shows the result of the sequential retrieval for the two different setups in comparison to the result of Setup C from Section 3.2.6 for aerosol, HNO_3 and offset for flight AMMA T3, profile 94, forward spectra. The results of the aerosol (Panel a)) and offset retrieval (Panel c)) differ clearly between the three setups, but agree well for HNO_3 . This underlines the robustness of the HNO_3 retrieval with respect to the spectral range and aerosol extinction.

The aerosol retrieval seems to be more difficult, especially for Setup CS1. In this setup also the normalized χ^2 value is relatively high ($\chi^2/m = 1.73$), indicating that the radiance is not reproduced as good as for Setup C and CS2. This is also confirmed by a comparison to RFM spectra (not shown). Hence, it is questionable if the extinction scaling factors from Massie et al. (1994) (derived for stratospheric conditions) can be used for wavenumbers between 850 and 900 cm^{-1} within the troposphere. Instead, a spectrally constant aerosol extinction like in Setup CS2 is preferable, where the normalized χ^2 is much closer to 1.0 (see Figure 25). Setup CS2 was used for a retrieval for the whole flight AMMA T3 confirming that HNO_3 structures along the flight path are similar to Setup C (not shown).

A sequential retrieval could be used further to determine trace gases with spectral features outside the spectral range of detector L6, for instance stratospheric water vapor between 1500 and 1600 cm^{-1} and SF_6 at about 950 cm^{-1}.

3.2.8 Filter and grid for the retrieval result

Together with the χ^2-test, which indicates the quality of the radiance fit, measurement contribution and resolution provide measures for the quality of the retrieved variables (see Section 3.2.2 and 3.2.4). Therefore, if not mentioned otherwise, all retrieval results displaced hereafter are filtered for the following thresholds:

- $\chi^2/m < 2$
- Resolution: $< 60 * \Delta z$ for O_3 and HNO_3 ; $< 6 * \Delta z$ for all other variables, where Δz is the grid spacing in km
- Measurement Content: > 0.8 and < 1.2

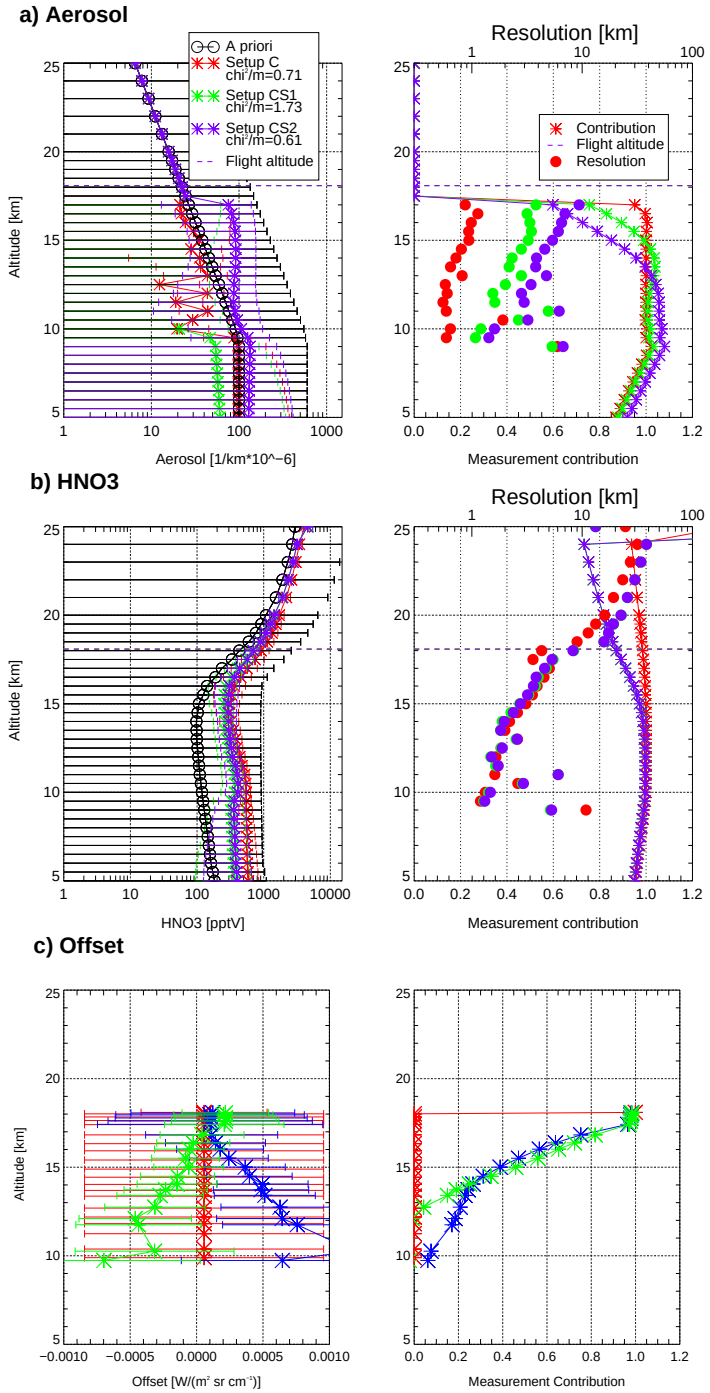

Figure 25: Results for two different sequential retrievals (green and purple line, details see text) in comparison to Setup C (red line, see Section 3.2, Figure 23). The panels show: a) Aerosol, b) HNO_3, and c) radiance offset. Right panels show the appropriate measurement contribution and resolution.

Results with a total error (without smoothing) larger than 90% are marked in the following 2D-images of retrieval results but are not excluded. To present the results, the retrieved data

from forward and backward spectra are combined onto the same grid:

- Vertical: retrieval grid
- Horizontal: position of the refracted tangent point closest to the vertical grid point
- Usually the vertical position and errors for forward or backward spectra are interpolated, only one result is used if
  - only one of them exists or passes the filtering mentioned above
  - one χ^2/m value is more than 20% lower
  - one measurement contribution is 2% higher on the absolute scale
  - one vertical resolution is less than 50% of the other

The vertical grid position is kept and not interpolated to the tangent point positions because resolution and measurement contribution are only valid for the grid positions. The 1D-retrieval used does not contain information on the horizontal structure along the LOS. It is assumed that the position of the vertically nearest, refracted tangent altitude best represents the real horizontal position. The tangent point is therefore chosen as horizontal coordinate for interpolating the CLaMS data and for displaying the CRISTA-NF data on maps.

- The CLaMS results are convoluted with the AVK (according to Equation 7) before the comparison.
- CLaMS data convoluted with the AVK are filters the same way as the corresponding CRISTA-NF data.
- CLaMS data of properties not retrieved and hence not convoluted with the AVK (e.g. mean age of air) are presented on the unfiltered grid.

4 The AMMA-SCOUT-O3 Campaign

4.1 Overview of the Campaign

The African Monsoon Multidisciplinary Analyses (AMMA) campaign had the aim to obtain a better understanding of the West African Monsoon and its implications on local and global processes by combining field measurements, satellite observation and modeling studies (Redelsperger et al., 2006).

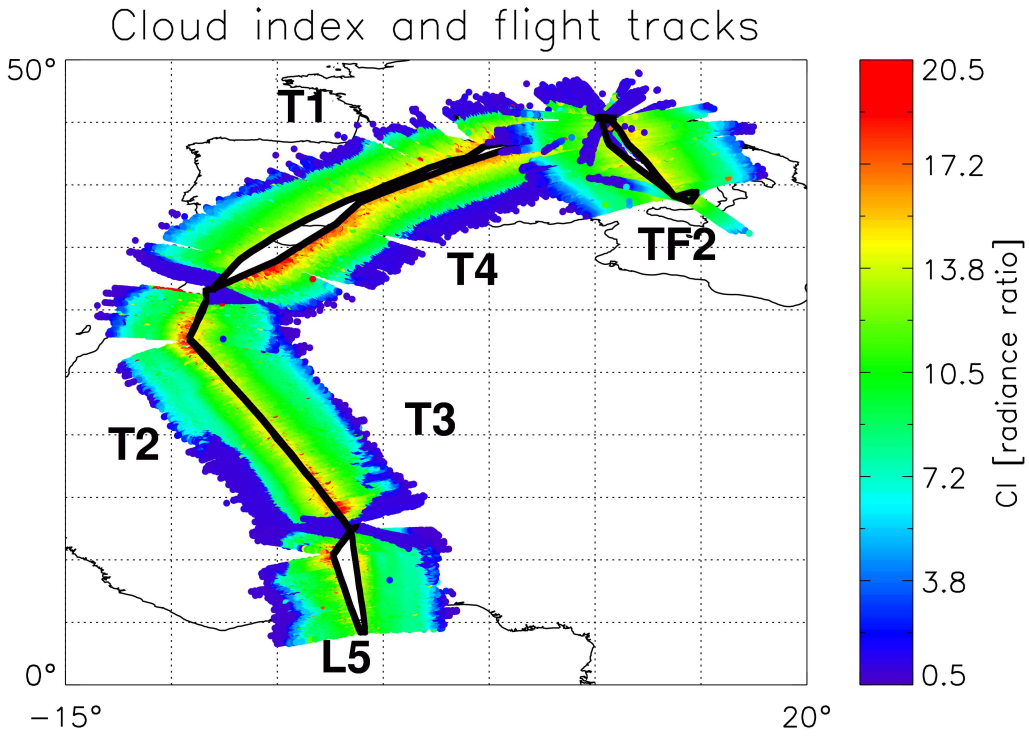

Figure 26: Overview over cloud index along flight tracks of all AMMA flights used for the trace gas retrieval.

Within the Special Observation Period of the AMMA Campaign and in cooperation with the Stratosphere-Climate links with emphasis On the UTLS-O3 (SCOUT-O3) project[8], ten M55-Geophysica flights took place (Silva dos Santos, 2008). CRISTA-NF measured successfully on all of these flights. Here, the data from the flights with least cloudy conditions and hence highest data quality for the trace gas retrieval are analyzed. These are the test flight,

[8]SCOUT-O3 is a project of the European Commission and has the aim to provide predictions about the chemistry-climate system with emphasis on the O_3 change in the lower stratosphere (SCOUT-O3, 2009).

Table 6: AMMA flights analyzed in this work

Abbr.	Date	Location	Main objective	Remark
TF2	2006/07/29	From and to Verona	Instrument test flight	Active attitude system used
T1	2006/07/31	Verona to Marrakech	Transfer flight	
T2	2006/08/01	Marrakech to Ouagadougou	Transfer flight	Detector temperature over 14.5K (first 1000s)
L5	2006/08/13	From and to Ouagadougou	CALIPSO[1] validation	Detector temperature over 14.5K (first 900s)
T3	2006/08/16	Ouagadougou to Marrakech	Transfer flight	
T4	2006/08/17	Marrakech to Verona	Transfer flight	Detector temperature over 14.5K (first 2500s)

[1]Cloud-Aerosol Lidar and Infrared Pathfinder Satellite Observation satellite (CALIPSO, 2009)

all transfer flights, and local flight number five, see Table 6. The Cloud index (see Section 2.2) from these flights is shown in Figure 26, giving an overview of the flight tracks and the viewing direction of CRISTA-NF.

4.2 Comparison to in situ measurements

As mentioned in Section 3.2 intercomparisons between retrieval results and in situ data are important to exclude systematic errors. Several in situ measurements were taken on M55-Geophysica during AMMA. Comparisons are presented for:

- Water vapor:

  Total water is measured with a high accuracy with the Fast In situ Stratospheric Hygrometer (FISH; Zöger et al., 1999). Since only gas-phase water can be compared and the FISH measures total water (including water droplets and ice crystals), only FISH measurements outside clouds are used for comparison.

- Temperature:

  If available, temperature measurements by the Thermo Dynamic Complex (TDC) from the Central Aerological Observatory (CAO) are used for comparison. As TDC data

is not available for the test flight and the second transfer flight, for these flights the M55-Geophysica avionic temperature measurements are used.

- Ozone:

  Ozone measured by the Fast Ozone ANalyzer (FOZAN; Yushkov et al., 1999) was used for comparisons. Data is available during L5, T3 and T4.

In situ data are not convoluted with the AVK for comparison because they are only available along the flight track. One would need data above and below the position of the in situ measurement position to consider the AVK. Because of the high measurement content and resolution of CRISTA-NF (see Section 3.2.4) this is expected to be of minor importance, especially for H_2O and temperature.

For water vapor the CRISTA-NF data are available up to about 15km altitude. Therefore only FISH measurements during ascent and descent of M55-Geophysica and, in addition, during the dives on flight TF2 and L5 can be compared. Temperature and ozone are compared along the flight track with the highest part of the CRISTA-NF profiles.

Figure 27 shows a cross section of the CRISTA-NF O_3 retrieval results for flight L5 (filtered and averaged as explained in Section 3.2.8). Along the flight track FOZAN O_3 measurements marked as colored line framed by black lines are shown. Generally, CRISTA-NF and FOZAN agree very well. Slight differences during the descent are likely due to the fact that FOZAN measurements and the nearest CRISTA-NF profiles are separated by several tenth of kilometers due to the limb scanning geometry.

Figure 28 displays the data for flight L5 as vertical profiles. In addition, the ECMWF O_3 values, which are used as a priori for the CRISTA-NF retrieval, are shown. The orchid diamonds give the mean value for every grid altitude of the CRISTA-NF result and error bars indicate averaged noise, total and smoothing errors. The CRISTA-NF O_3 values vary much more than the other data presented. This is presumably at least partly caused by existing horizontal O_3 variations between different profiles along the flight path (see for comparison also CLaMS O_3 in Appendix C.1, Figure 76). The mean CRISTA-NF O_3 corresponds well to the FOZAN measurements. Above 14 km the CRISTA-NF O_3 is somewhat lower and at

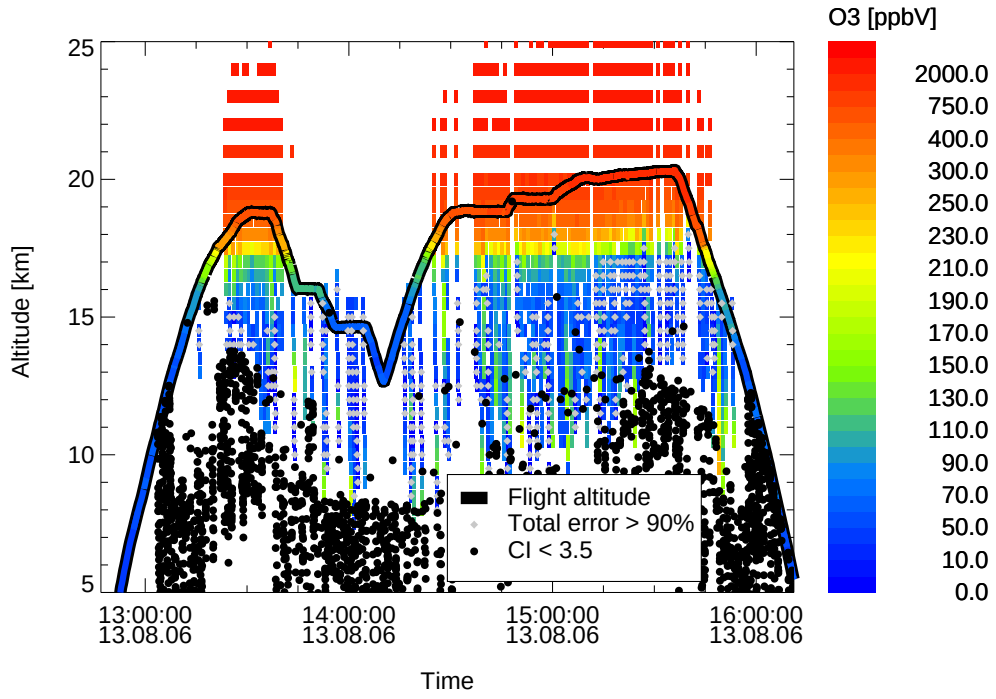

Figure 27: Cross section of CRISTA-NF O_3 mixing ratios and FOZAN measurements on 13 August (L5). The black line marks the flight altitude, the colors within the lines display the FOZAN measurements. Black dots: Cloud Index < 3.5, gray diamonds: Total error larger than 90%.

the same time, the ECMWF O_3 is rather too high compared to the FOZAN data. Since the FOZAN O_3 values are not convoluted with the AVK they should agree within the total and smoothing error of the retrieval. This is the case for most altitudes and hence indicates that the retrieval and its errors are reliable.

Comparisons for water vapor and temperature are shown in Section 4.4 for the test flight; FOZAN measurements are not available during that flight.

4.3 Comparison to CLaMS model results

The Chemical Lagrangian Model of the Stratosphere (CLaMS; McKenna et al., 2002a,b) is employed analyze dynamical and chemical processes in the stratosphere and their influence on stratospheric trace gases. The introduction of a hybrid vertical coordinate ($\zeta-$coordinate; Konopka et al., 2007) extended the range of application for CLaMS to the tropopause region and troposphere. Several studies demonstrated the capability of CLaMS by comparisons to

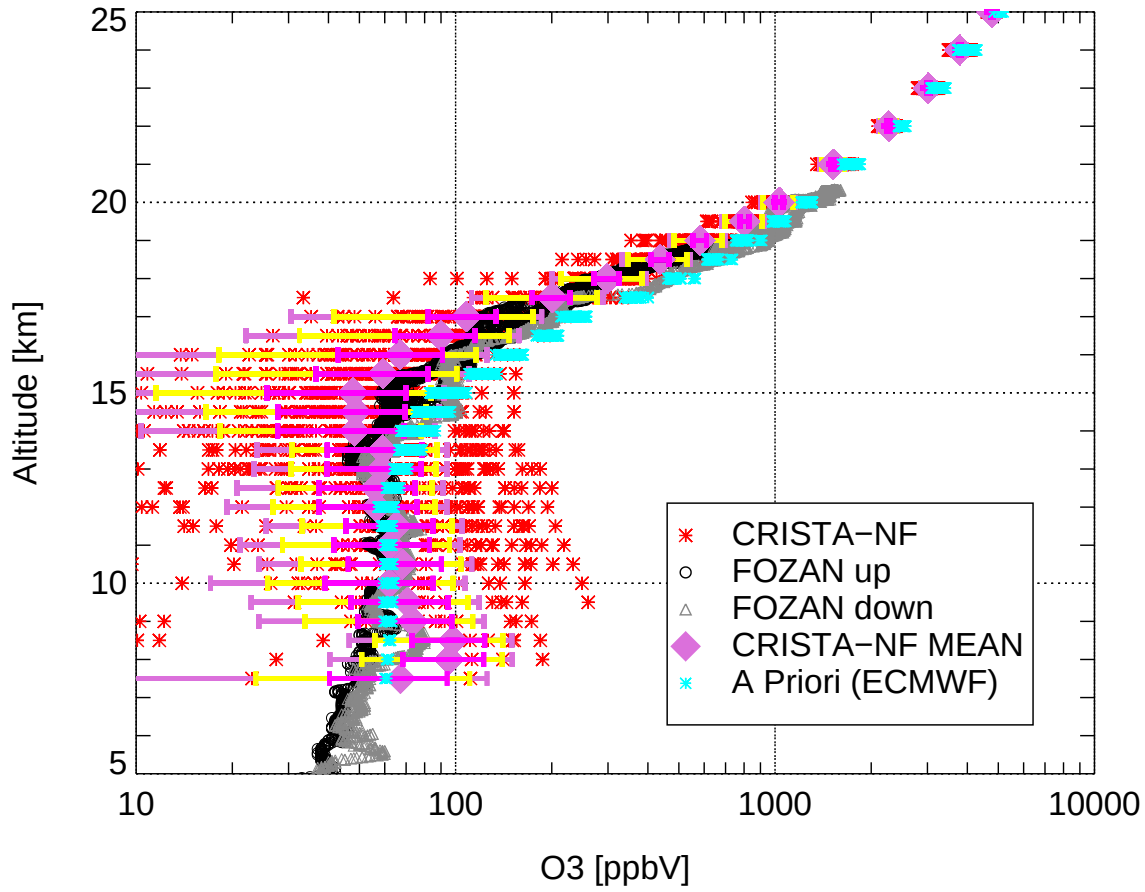

Figure 28: Profiles of measured O_3 on 2006/08/13 (L5). Red stars: CRISTA-NF (all profiles of flight L5); black and gray symbols: FOZAN measurements during ascent and descent of the airplane; orchid diamonds: Mean of CRISTA-NF measurements over the whole flight for each altitude of the retrieval grid; Error bars: Orchid: total error including smoothing, yellow: Total error without smoothing, pink: Noise error. Blue crosses: ECMWF O_3

remote sensing measurements, among them CRISTA (e.g. Khosrawi et al., 2005) and MIPAS (e.g. Vogel et al., 2008) and in situ data (e.g. Günther et al., 2008).

Two different CLaMS data sets were compared with CRISTA-NF retrieval results:

1. A climatological run provided by Paul Konopka:

   - Setup and resolution following Konopka et al. (2007). The HALOE climatology developed by Grooss and Russell (2005) was used for initialization and as boundary conditions.
   - Mean age: A tracer, whose source in the boundary layer increases linear with time, is defined. The mean age is calculated from the time lag between the time

where the tracer was released and the actual time(Waugh and Hall, 2002). MIPAS SF_6 observations are used for the upper boundary at θ =2500 K (Stiller et al., 2008; Konopka et al., in preparation, 2009).

2. A two month transient global run provided by Gebhard Günther:

   - Resolution: 70 km between 20 and 40° N, 100 km elsewhere
   - H_2O :
     ECMWF data used for initialization and boundary conditions. Lower and upper boundaries situated at ζ =200 K and ζ =500 K, respectively. Condensation and freezing based on cloud parameters by Krämer et al. (2008) and Schiller et al. (2008).
   - Other gases:
     Initialized from the climatological run.

CLaMS data are interpolated onto the CRISTA-NF grid, convoluted with the AVK (Equation 7) and filtered as explained in Section 3.2.8. Specific humidity, ice water content (IWC) (both with formation of cloud droplets at a relative humidity of 100%), cloud liquid water content (CLWC) and O_3 from the two-months CLaMS run are compared to CRISTA-NF H_2O, Clouds and O_3. For comparison with the CRISTA-NF retrieval results the specific humidity from CLaMS is converted to water vapor volume mixing ratio. The mean age of air from the climatological CLaMS run and backward trajectories are used to analyze the origin of observed air-masses. Trajectories are also used to correct for the time lag between the daily CLaMS data and the actual measurement time of CRISTA-NF. CLaMS results are presented in detail for the test flight in Section 4.4, the results for the other flights can be found in Appendix C.1.

4.4 AMMA test flight on 29 July 2006

4.4.1 Results and intercomparisons

The AMMA test flight was carried out on the 29 of July 2006. Figure 29 displays a three-dimensional view of the flight path and schematic representation of the CRISTA-NF measurement geometry. Black dots show spectra with a Cloud index below 3.5 on tangent points corrected for the result of the altitude retrieval and refraction. Colored symbols represent the CRISTA-NF PAN measurements positioned on the grid explained in Section 3.2.8. The vertical extent of these symbols denotes the vertical resolution[9].

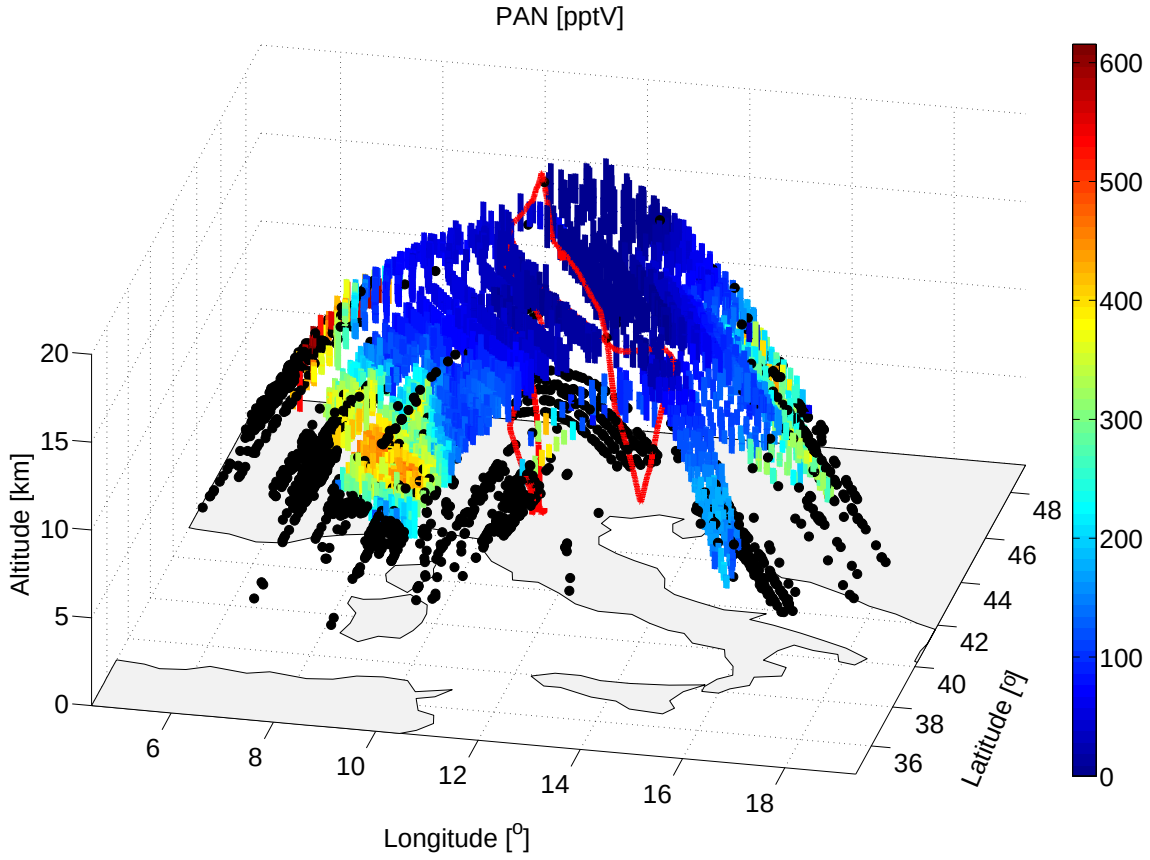

Figure 29: PAN as retrieved for the AMMA test flight on 29 of July 2006. Red line: Flight path, black dots: Cloud Index < 3.5.

Starting in Verona, the M55-Geophysica flew to the south-east. North of the coast of Sicily,

[9]The resolution depends on the retrieved variable (see Section 3.2.4) and is shown for PAN, here. The resolution of the other variables differ, it is e.g. better for H_2O and more coarse for O_3 .

after three short legs towards east, southwest and west the aircraft turned and returned to Verona. A dive down to about 9 km was performed on the two legs in westward direction. The view direction of CRISTA-NF is to the right of the aircraft, thus the measurements during the southeastward leg were taken over the Mediterranean Sea. On the way back to Verona they were taken above Italy and the Adriatic Sea. During the turn north of Sicily CRISTA-NF views towards southeast over Sicily and in northward directions during the dive. Few data could be analyzed during the dive because of increased aircraft movements and hence decreased data quality (causing the gap in the middle of the following Figures showing retrieval results).

Temperature

Figure 30 shows the result of the temperature retrieval as a cross section, spectra with a cloud index below 3.5, and in situ temperature measured by the avionic system of M55-Geophysica along the flight track. The M55-Geophysica flew at altitudes of 17-18 km before the dive, descents down to about 9 km during the dive, climbs up to about 18.5 km afterward and reaches nearly 21 km before the final descent. Figure 31 shows profiles of the CRISTA-NF temperatures (red stars), the in situ temperature (gray and black symbols) and ECMWF temperatures (blue crosses) for the whole flight. The temperatures measured in situ during ascent, dive and descent are colored light gray, dark gray and black, respectively.

All temperatures agree well with each other. The spread of the CRISTA-NF temperatures is slightly higher than the one of the in situ data and ECMWF data. The difference to the in situ data can be explained, because they are measured only along the flight path, see Figure 30). Hence, there is a large horizontal distance between most of the CRISTA-NF measurements and the in situ measurements for the same altitude. There is also a much larger area covered by CRISTA-NF measurements. The lowest temperature for each profile and thus the cold point tropopause is found at altitudes between 16 and 18 km during the whole flight. The minimum temperature along the flight path, about 205 K, is situated in the southern most profiles at about 16 to 17 km altitude. In this part of the flight also the highest observed temperatures are found below an altitude of about 10 km. In the northernmost part of the

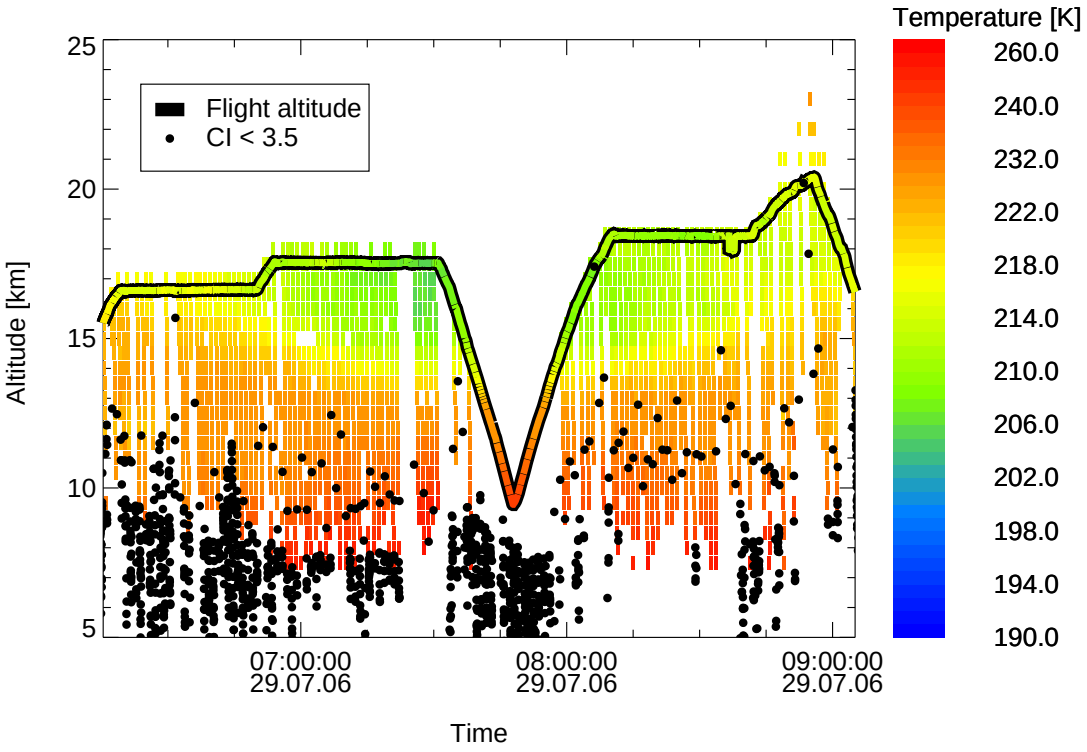

Figure 30: Cross section of CRISTA-NF temperatures together with M55-Geophysicas in situ avionic temperatures shown as colored line framed with black along the flight path for the test flight on 29 of July 2006. Black dots: Cloud Index < 3.5. Note nonlinear color scale.

flight, predominant during ascent and descent in the in situ data, a local minimum can be seen at a altitude of about 12 to 12.5 km. A 2D-field of interpolated ECMWF temperatures is shown in Figure 86, Appendix C.2 and agrees well with the temperature distribution of the CRISTA-NF temperatures.

Water vapor and clouds

Figure 32 shows the result of the water vapor mixing ratio (H_2O) retrieval (Panel a)) and a CLaMS simulation of H_2O (Panel b). The colored, black highlighted line shows the flight altitude with the FISH measurements as color code.

Large parts of the flight were cloud free down to an altitude of 8 km providing excellent conditions for trace gas retrievals. The colored rectangles show the result of the CRISTA-NF H_2O retrieval. Grey diamonds mark H_2O values with a total error over 90% (see Section 3.2.5 and 3.2.8). Almost all values above 12.5 km have errors exceeding 90%. An exception are

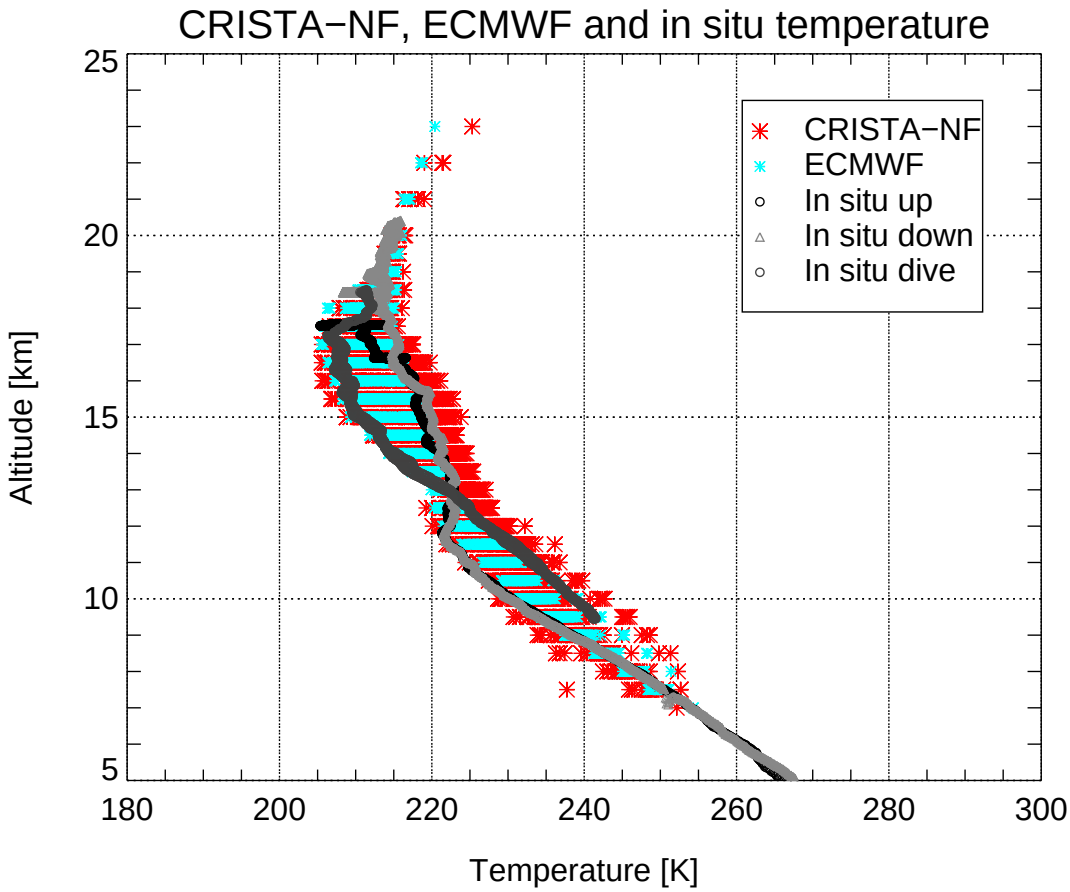

Figure 31: All profiles of CRISTA-NF temperature (red stars), in situ temperatures during ascent (light gray triangles), descent (black circles) and dive (dark gray circles) together with ECMWF temperatures (blue crosses) for the test flight on 29 of July 2006.

single, remarkably high water vapor values at altitudes of 13-14 km found in two isolated structures at about 7:00 and 8:30 UTC as well as enhanced H_2O mixing ratios in this altitude in the southernmost part of the flight, between 7:15-8:15 UTC. Below 12 km the H_2O mixing ratios are lowest in the southernmost part of the flight. The FISH measurement corresponds well to the nearest CRISTA-NF profiles during the dive. At the flight altitude water vapor has very low mixing ratios resulting in large relative errors of the CRISTA-NF data, because the H_2O emission at 784-785 cm^{-1} becomes hardly detectable (see Figure 6).

Panel b) shows H_2O and ice clouds (IWC $>$ 0) from the two-months CLaMS run (see Section 4.3). Ice clouds are marked with gray squares. There is only one liquid water cloud (LWC $>$ 0) in the CLaMS data at about 7:35 UTC marked as dark gray dot. Altogether,

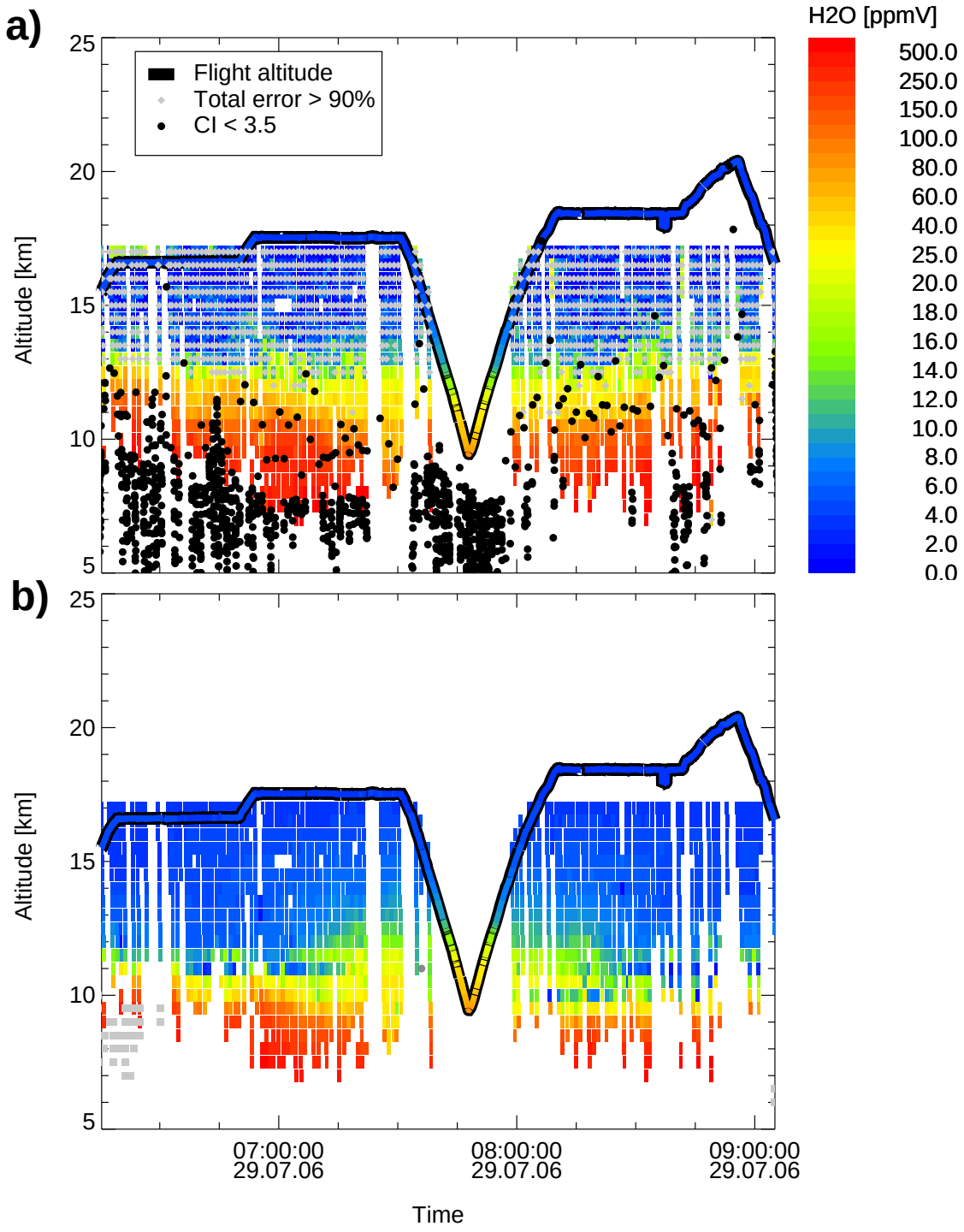

Figure 32: Test flight on 29 of July 2006: Panel a) Cross section of CRISTA-NF H_2O, black dots: Cloud Index < 3.5, gray diamonds: Total error >90%. Panel b) CLaMS H_2O interpolated on CRISTA-NF tangent point positions. Gray squares: IWC > 0, dark gray dot: LWC > 0. The flight path colored with FISH H_2O measurements and framed with black lines is shown in both panels. Note nonlinear color scale.

there are significantly fewer clouds in the CLaMS simulation than CRISTA-NF measurements indicate. One reason could be that clouds in CLaMS are only displayed, if they are situated at a grid point of the retrieval result whereas clouds indicated by CRISTA-NF can be situated anywhere along the LOS. The comparability of the clouds identified through the IWC in CLaMS to the CI of CRISTA-NF could be improved by interpolating the modeled cloud data onto the complete LOS to identify clouds (see e.g. Adams et al., 2009). During flight T4 a continuous cloud layer was present along most of the flight track (see Appendix C.1, Figure 83). Here CLaMS ice clouds reproduce the clouds seen with CRISTA-NF much better (see Appendix C.1, Figure 84).

At 12 to 13 km altitude there is an enhanced amount of water vapor mixing ratio in the southernmost part of the flight between about 7:15 to 8:15 UTC in the CLaMS data. This agrees in general with the CRISTA-NF results but the CLaMS H_2O mixing ratios are somewhat higher and more uniform in these altitudes. The structures of enhanced water vapor seen at about 7:00 and 8:30 UTC in the CRISTA-NF results above 12 km are not found in the CLaMS data. Below 12 km altitude the CLaMS water vapor mixing ratios are lower than the retrieved ones almost everywhere. As in the CRISTA-NF data, there is less water vapor in the southern part of the flight than in the northern part for the CLaMS data at lower altitudes. But for CLaMS this is the case for altitudes below 10 km and not up to 12 km as for CRISTA-NF.

Figure 33 shows the ECMWF water vapor interpolated onto the same grid as the CRISTA-NF results. The ECMWF values agree well with the CRISTA-NF results below 12 km, better than with the lower CLaMS water vapor. The enhanced water vapor values seen by CRISTA-NF and CLaMS above 12 km are not found in the ECMWF data. For ECMWF the water vapor is lowest in the south for all altitudes up to 14 km.

Figure 34 compares profiles of the different water vapor mixing ratios. Panel a) displays all CRISTA-NF and CLaMS values for the whole flight shown already in Figure 32. Panel b) only shows CRISTA-NF profile 76, one of the south viewing profiles over Sicily. This profile was chosen, because the tangent points are among the ones with the smallest horizontal distance

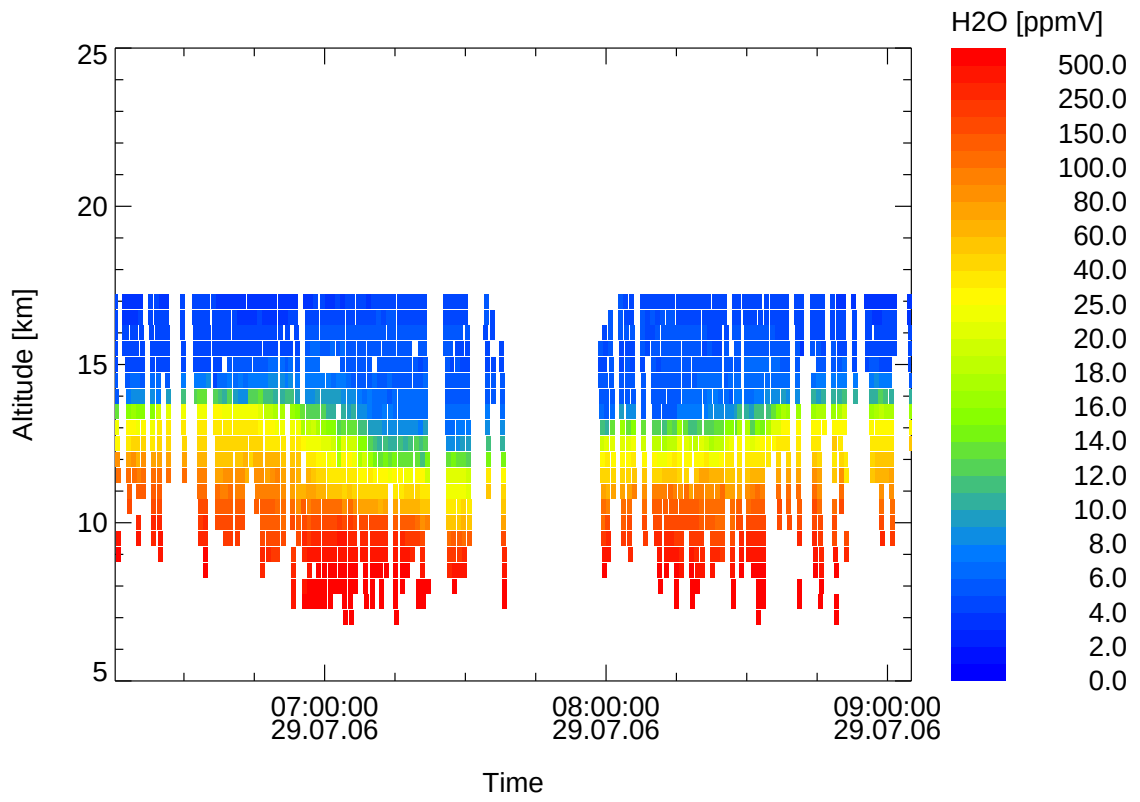

Figure 33: ECMWF water vapor interpolated onto CRISTA-NF tangent point positions for the test flight on 29 of July 2006, color coding like in Figure 32.

to the FISH in situ measurements during the dive.

From Panel a) it is obvious, that the CLaMS data (golden "X") are lower than all other data below about 12.5 km. The CRISTA-NF values (red crosses, mean for each grid altitude: orchid diamonds) agree better with the FISH measurements at lower altitudes, but above 12 km their errors reach 100% and they show a much larger variability than all other data. Still the mean water vapor for each grid altitude has a reasonable value up to 15.5 km. The CRISTA-NF data agree better with the FISH data (gray and black symbols) below 12 km than with the CLaMS data. This is a clear indication that the CLaMS data are too low at these altitudes. This might be due to an underestimation of convection, which is not resolved sufficiently in all cases in CLaMS (e.g. Walter, 2009).

That the CLaMS H_2O might be too low is also supported by the profile 76 shown in Panel b): During the dive the CLaMS values agree nearly exactly with the FISH measurement

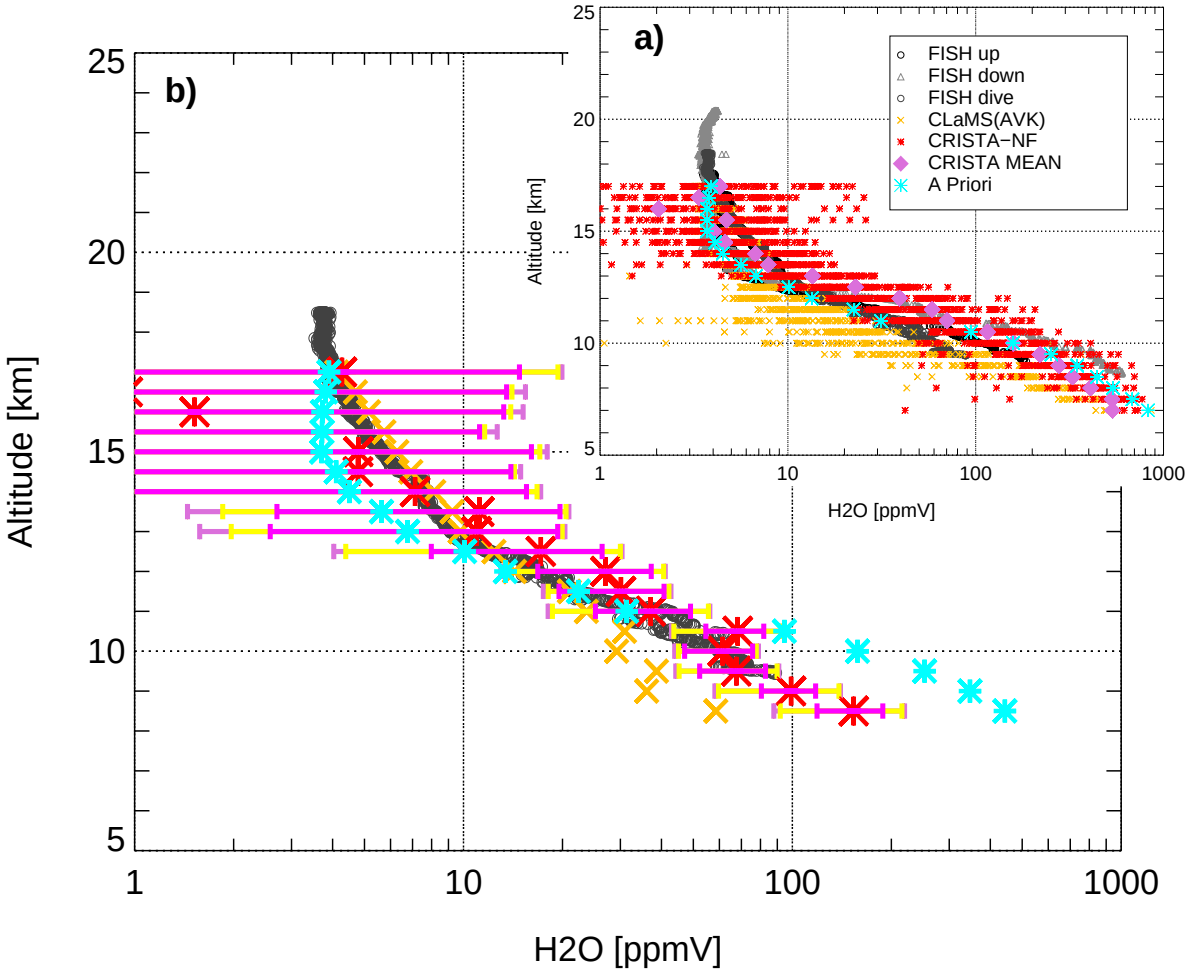

Figure 34: Intercomparison of water vapor profiles for the test flight on 29 of July 2006: a) All profiles b) profile 76 of CRISTA-NF (red stars), CLaMS (golden "X"), FISH (gray and black symbols) and MIPAS midlatitude climatology (a priori, blue stars). The CRISTA-NF mean profile is shown as orchid diamonds in Panel a). Averaged errors are shown for the CRISTA-NF data: Pink error bar: Noise error, yellow error bar: total error, orchid error bar: total error and smoothing error.

(dark gray symbols) above 11 km, but they are clearly lower below 11 km. In contrast, the differences between CRISTA-NF and FISH water vapor data increase at higher altitudes. For the CRISTA-NF data the averaged error bars are given: Pink is the noise error, yellow the total error without smoothing and orchid the total error including smoothing (see Section 3.2.5). Because they are convoluted with the AVK and interpolated on the same grid the CLaMS data should agree to the CRISTA-NF data within the total error without smoothing. This

is not the case below 12.5 km. The FISH H_2O measurements are not convoluted and there are differences between the horizontal positions of the CRISTA-NF tangent points and the FISH measurements. Hence, even larger differences than the total error with smoothing may be reasonable.

In almost all cases the difference between CRISTA-NF H_2O of profile 76 and FISH H_2O during the dive is smaller than the CRISTA-NF total and smoothing error. At the same time the distance of the tangent points to the flight path during the dive and hence to the FISH measurement positions are small. One might expect therefore that the differences rather decrease. The reason why this is not the case is the decrease of the strength of the spectral signature of H_2O relative to the contributions from other trace gases at 784–785 cm^{-1}, see Figure 6. Only up to about 12 km altitude the H_2O emission is dominant, above CO_2 and O_3 spectral signatures are stronger. Above about 15 km one can hardly identify the H_2O emission, leading to the large errors in the retrieval.

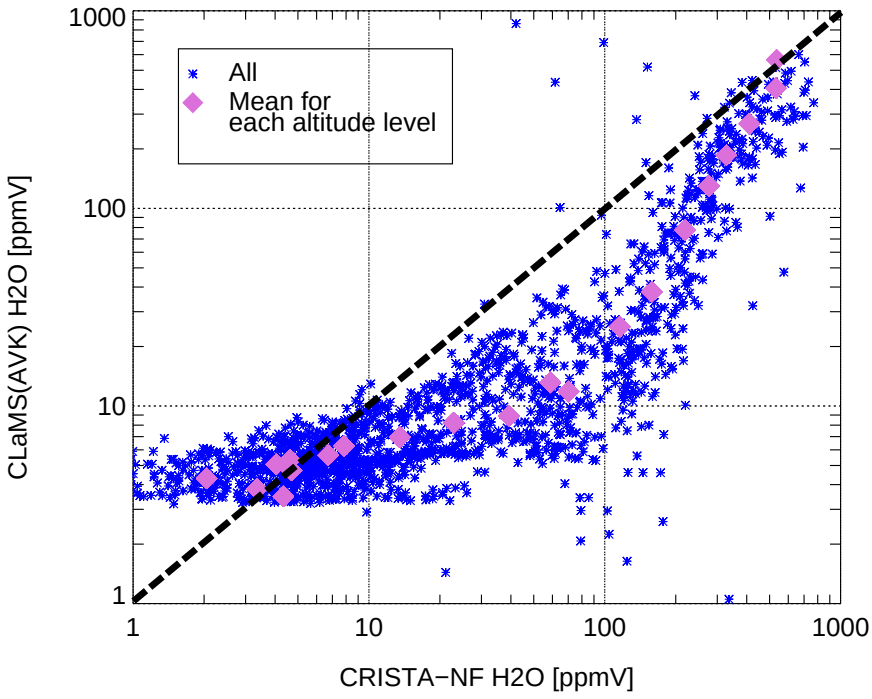

Figure 35: Scatter plot of CRISTA-NF and CLaMS water vapor for the test flight on 29 of July 2006.

Figure 35 shows a scatter plot of CRISTA-NF and CLaMS H_2O. There are two main differences: First, for water vapor values between 10 and 300 ppmV the CLaMS data are obviously lower. For mixing ratios above about 10 ppmV the CRISTA-NF water vapor mixing ratios can be considered to be reliable while CLaMS was developed mainly for stratospheric conditions and almost all H_2O mixing ratios above 10 ppmV are found in the troposphere during TF2. Second, there are nearly no CLaMS water vapor volume mixing rations lower than 3 ppmV while there are CRISTA-NF measurements down to zero. These CRISTA-NF H_2O measurements below about 10 ppmV are not significant and are certainly too low.

In summary, the CRISTA-NF results agree well with in situ measurements below 12 km altitude (i.e. where the water vapor volume mixing ratios are higher than 10 ppmV). At higher altitudes and lower mixing ratios, the retrieval errors become too large for the data to be significant. However, mean values over e.g. the whole flight are consistent with the in situ measurements up to about 15 km. For higher altitudes, a H_2O retrieval is hardly possible using the spectral line at about 784 cm^{-1}. This is already indicated in Figure 6 showing only a very weak water vapor contribution to the calculated radiance for 15 km altitude and above. There are stronger H_2O emissions within the spectral range covered by CRISTA-NF, but using them to analyze H_2O is beyond the scope of this work.

Ozone

The result for the O_3 retrieval is displayed in Figure 36 as a function of altitude (Panel a) and ζ-level (Panel b). In general, the O_3 mixing ratio increases with altitude. Air with low O_3 mixing ratios smaller than about 200 ppbV is found up to 12-13 km in the northern part of the flight track but up to 15-16 km in the southern part.

The most obvious structure in the retrieved ozone is a region of high volume mixing ratios ($>$ 200 ppbV) down to altitudes of 10 to 12 km (approximately $\zeta = 320$ K) before 7:00 and after 8:30 UTC, i.e. for the northern part of the flight track. Whereas in the southern part of the flight track volume mixing ratios down to 50 ppbV are found up to an altitude of about 15 km (approximately $\zeta = 380$ K), regions A1 and A2 in Panel b). The transition between low and high O_3 values is rather sharp above 13 km. Below, a "tongue" of moderate O_3 mixing

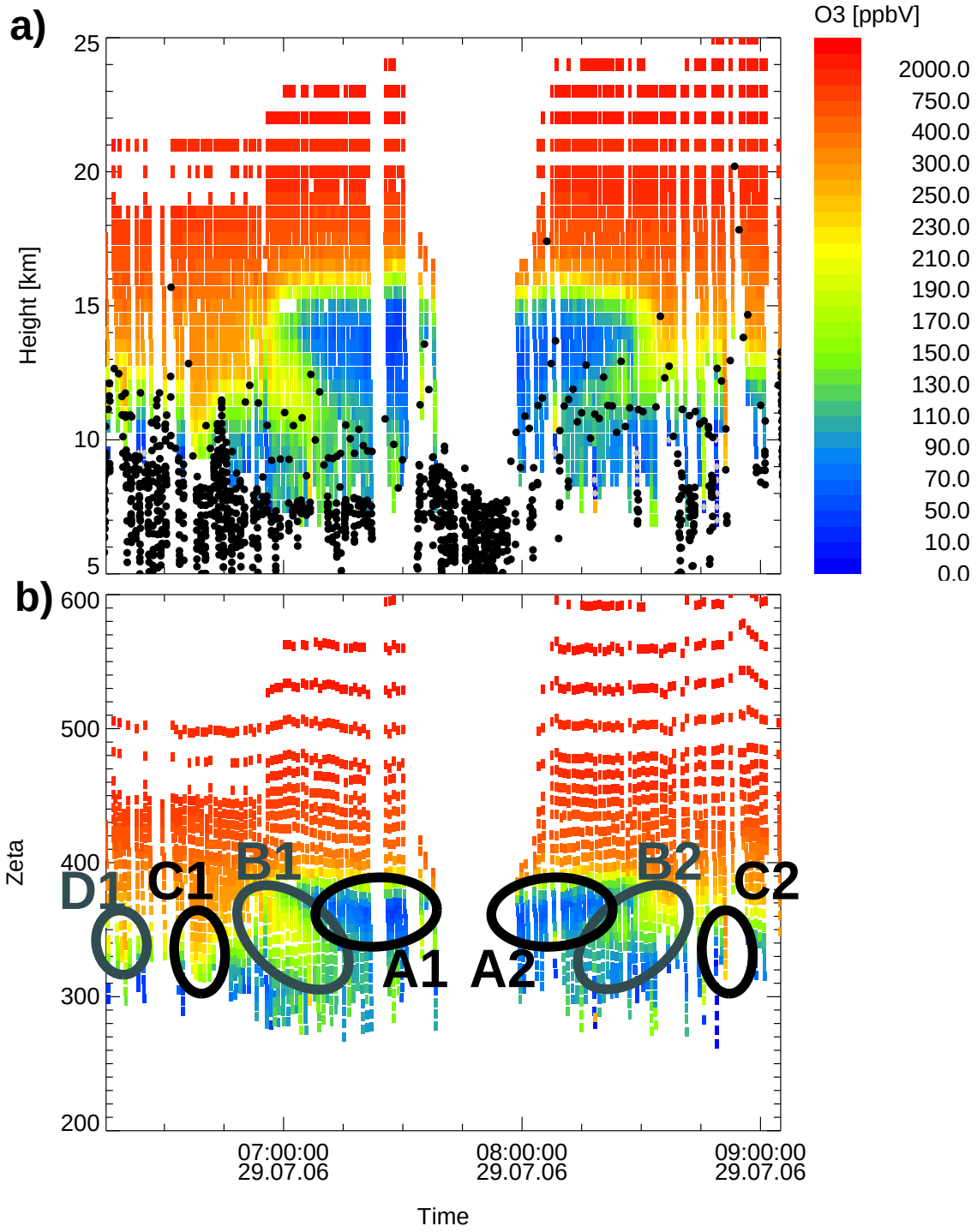

Figure 36: Cross section of CRISTA-NF O_3 volume mixing ratio plotted versus time and a) altitude and b) zeta for the test flight on 29 of July 2006. Black dots in a): Cloud Index < 3.5. Gray and black ellipses in Panel b) mark structures which are discussed in the text. Note nonlinear color scale.

ratios between 100 and 200 ppbV extends down to 8 km altitude, marked with B1 and B2. There are somewhat higher O_3 mixing ratios in B1 than in B2, but in general the structures marked with A and B are nearly symmetrical in both flight directions. In the first half of the flight there is a second O_3 maximum reaching down to below 10 km, at about 6:40 UTC, marked with C1. This is, if at all, only mirrored by a single profile at about 8:50 UTC in the second half of the flight (C2). Another region with enhanced O_3 is present directly in the beginning of the flight (D1), down to about 11 km. This is not found in the second half, presumably because the descent starts before.

The structures observed in the O_3 mixing ratios are significant compared to the retrieval errors. It is important to note that the low ozone values up to 15 km altitude are not part of an enclosed feature. Instead the aircraft is turning before 8:00 UTC, measuring the same structure a second time. This time the viewing direction is toward the northeast instead of south west. Comparing the structure found in the O_3 to the retrieved water vapor in Figure 32 shows that the isolated structures of enhanced H_2O observed at 7:00 and 8:30 UTC above 12 km coincide with the base of the O_3 "tongue".

The CLaMS and ECMWF O_3 mixing ratios are shown in Figure 37. ClaMS shows a very similar structure to CRISTA-NF in the ozone. However, the absolute values are somewhat higher than observed by CRISTA-NF, often outside the CRISTA-NF total errors. Further, the region of high O_3 mixing ratios above 200 ppbV extends lower down, below 10 km, in the CLaMS data. In the ECMWF analysis data no such distinct O_3 structure can be seen. Low O_3 values reach up to higher altitudes in the southern part of the flight but the whole transition is smoother and there is no O_3 "tongue". Before 7:00 and after 8:30 UTC the transition between low and high ozone is situated at the same altitude between 12 and 13 km, whereas its altitude is much more variable in the CLaMS data shown in Panel a) as well as in the CRISTA-NF data in Figure 32.

The scatter plot of CRISTA-NF and CLaMS O_3 presented in Figure 38 reveals that the O_3 values above 300 ppbV are in excellent agreement, while for lower mixing ratios CLaMS results are obviously higher.

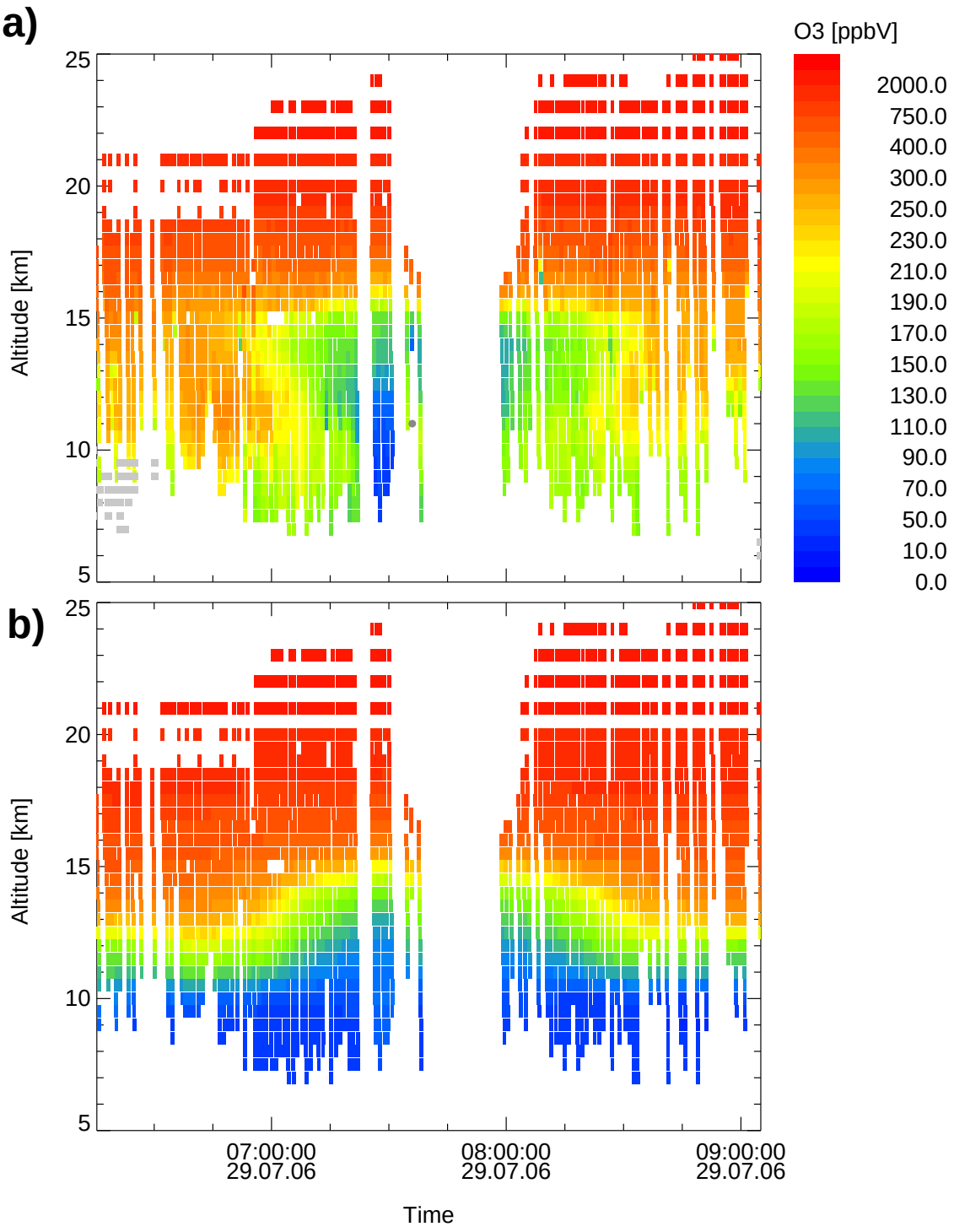

Figure 37: CLaMS (Panel a)) and ECMWF (a priori, Panel b)) O_3 mixing ratios interpolated onto CRISTA-NF tangent point positions for the test flight on 29 of July 2006. In Panel a) gray squares show CLaMS IWC > 0 and the dark gray dot a CLaMS LWC > 0, indicating ice and liquid water clouds, respectively. Note nonlinear color scale.

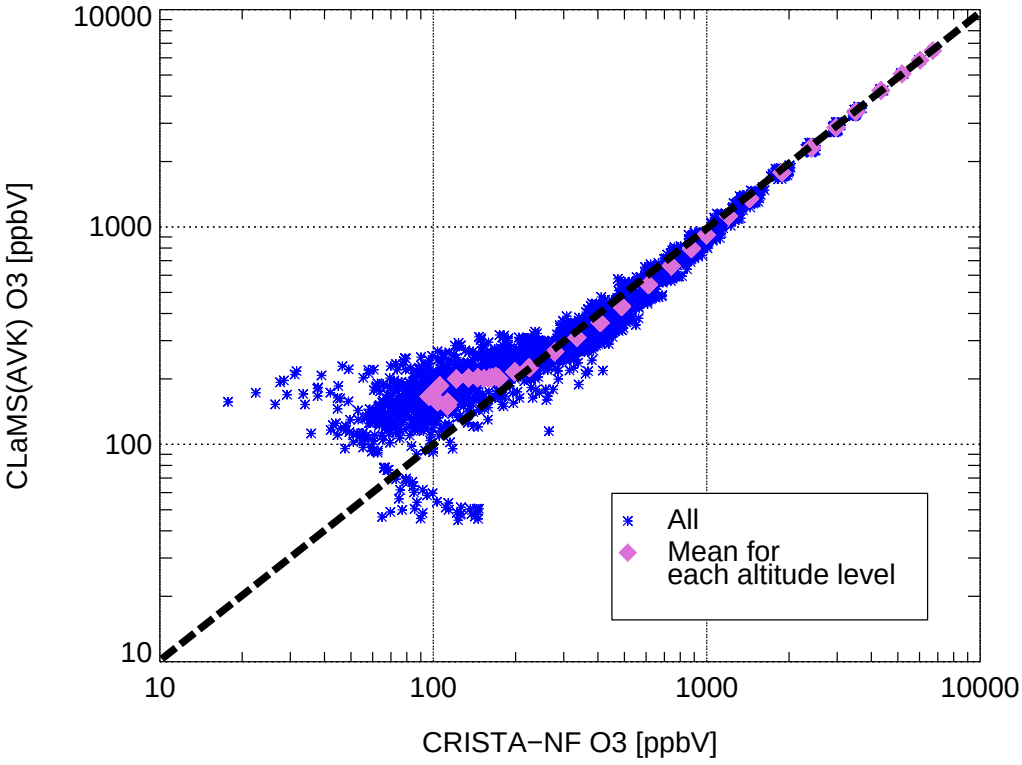

Figure 38: Scatter plot of retrieved CRISTA-NF and modeled CLaMS O_3 mixing ratios during the test flight on 29 of July 2006.

As mentioned before the probability is rather low that two isolated O_3 "tongues" have been measured on this flight. Instead the same extended structure is seen twice: Once during the measurement towards the southwest above the Mediterranean Sea and on the way back measuring towards north east above Italy and the Adriatic Sea. This is illustrated by plotting the CRISTA-NF O_3 values onto a map using the locations of the refracted tangent altitudes as positions in Figure 39. The O_3 distribution appears to be nearly symmetrical for both flight directions, indicating that it is one structure with several hundred kilometers horizontal extent.

The map of CLaMS O_3 values on the 350K ζ-Level in Figure 40 shows, that the flight path was crossing a transition between higher O_3 mixing ratios in the north and lower ones towards the south. This means that 350K ζ-Level transects the tropopause, i.e. the high O_3 mixing ratios in the north indicate rather air from the lowermost stratosphere, the lower

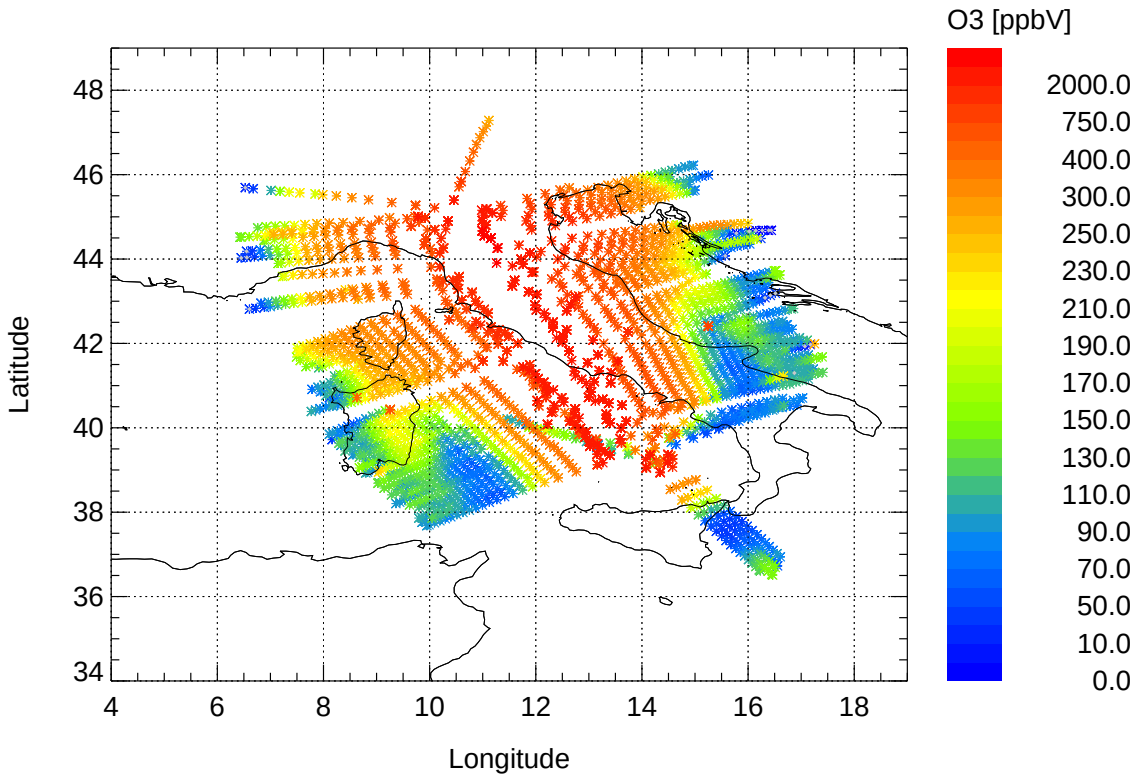

Figure 39: Map of the CRISTA-NF O_3 mixing ratios during the test flight on 29 of July 2006. Note nonlinear color scale.

O_3 mixing ratios in the south tropospheric air, as will be discussed in Section 4.4.2.

Other trace gases

The retrieval result for HNO_3 and PAN are shown in Figure 41. HNO_3 has a similar structure as O_3 for the southern part of the flight, while for the northern part the gradient between HNO_3 mixing ratios within air below and above about 12 km is not as strong as for O_3. PAN is a tracer originating from the troposphere and shows a totally different structure compared to O_3: In the southern part PAN mixing ratios of about 80 pptV are found up to 15.5 km altitude, in the northern part these values are rather located at 14 km. There is an isolated maximum at 7:15 and 8:15 UTC in the 14-15 km region with over 125 pptV PAN surrounded by air with lower PAN mixing ratios of about 90 pptV. Enhanced mixing ratios of PAN with over 150 pptV are also situated at the same location as the enhanced H_2O obvious in Figure 32 at 7:00 and 8:30 UTC between about 12 and 13.5 km.

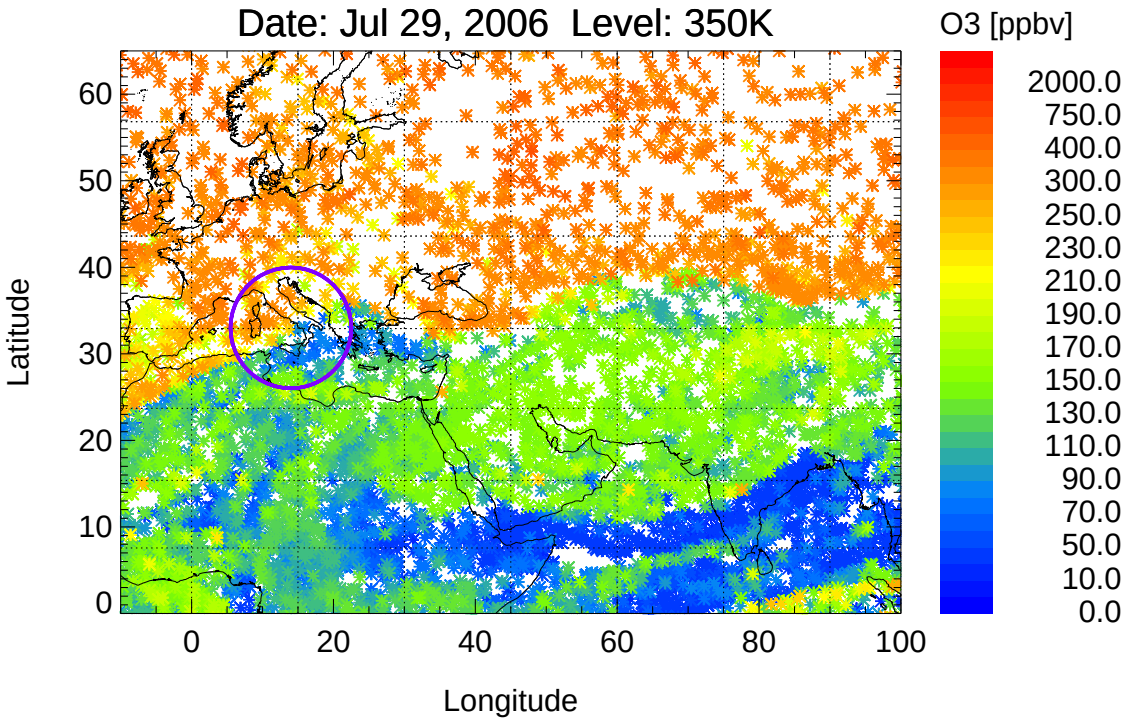

Figure 40: Horizontal distribution of CLaMS O_3 on the $\zeta = 350K$ (about 13 km altitude) level on 29 of July 2006 12:00. Note nonlinear color scale.

Figure 42 shows the retrieval result for CCl_4 and aerosol. They show similar, but much less distinct structures as PAN. CCl_4 and aerosol are both of tropospheric origin, too. CCl_4 has a much longer lifetime than PAN, whose lifetime is in the order of months in the upper troposphere (Talukdar et al., 1995). The lifetime of CCl_4 several tenth of years, (e.g. Volk et al., 1997 and Happell and Roche, 2003). The decrease of CCl_4 with altitude is therefore slower than for PAN and the differences between tropospheric and lower stratospheric values are smaller. This results in much less pronounced structures for CCl_4 than for PAN. For CCl_4 only in the last part of the flight measurements are taken at sufficiently high altitudes to detect the decrease at stratospheric altitudes.

For aerosol the structure is probably less clear as for PAN because it has the largest errors of all retrieved variables. It was also not well reproduced by the sequential retrieval (see Section 3.2.7). The structures found in O_3, HNO_3, and PAN, in contrast to the ones seen in

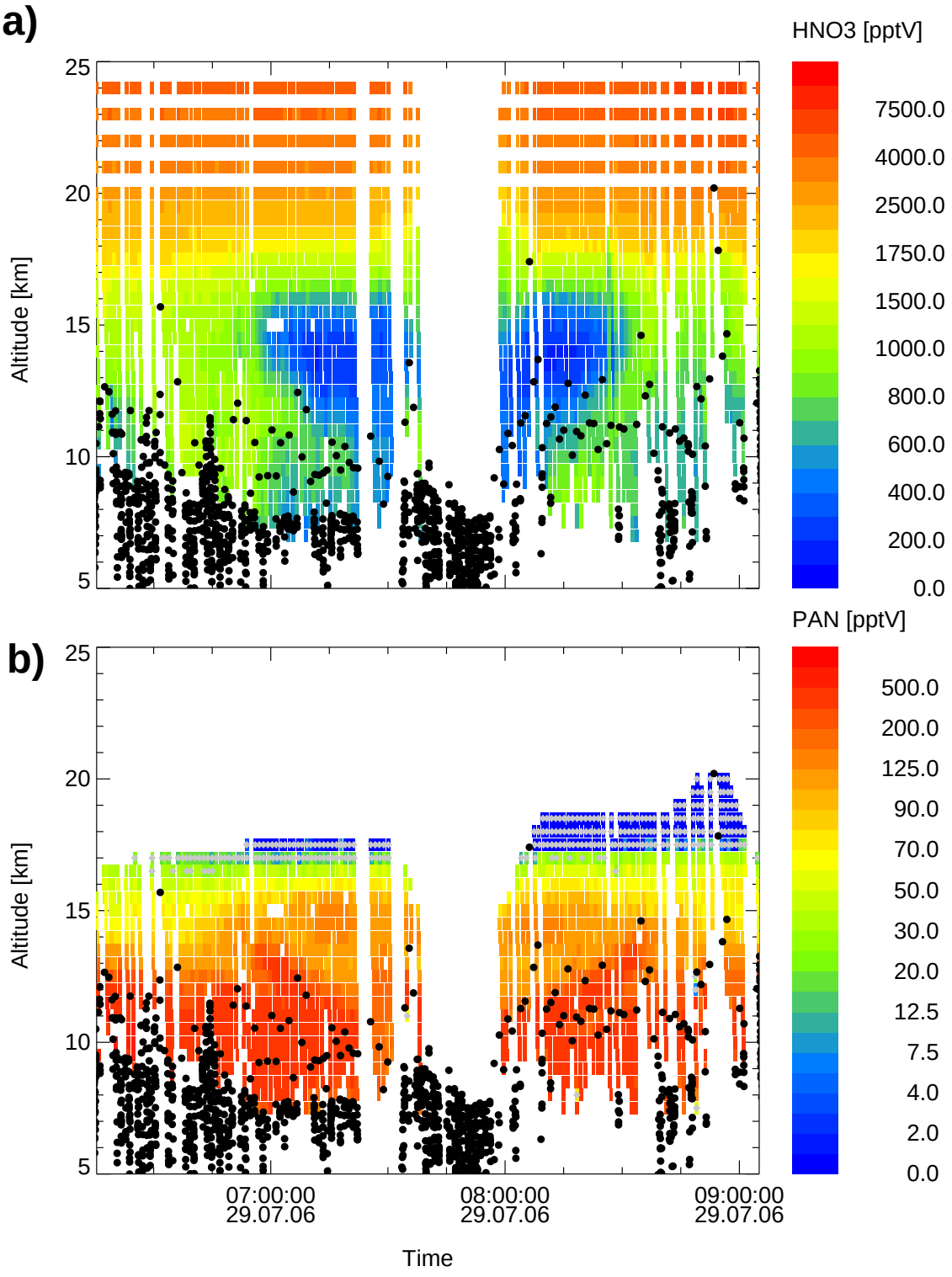

Figure 41: Cross section of CRISTA-NF HNO_3 (Panel a) and PAN (Panel b) for the test flight on 29 of July 2006. Black dots: Cloud Index < 3.5, gray diamonds: Total error $>90\%$. The PAN mixing ratios shown in Panel b) are the same as for the 3-D distribution shown in Figure 29 (color scale differs). Note nonlinear color scales.

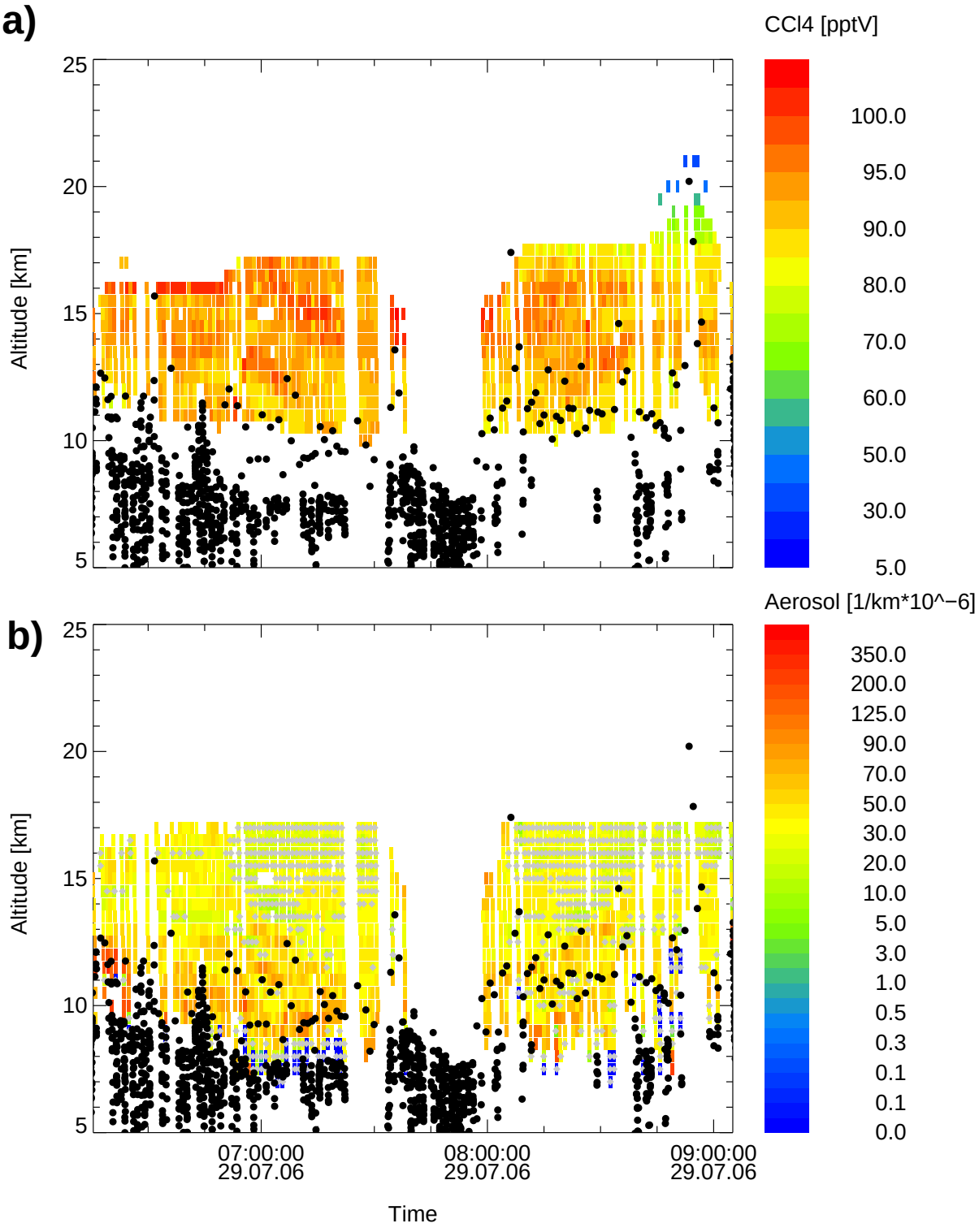

Figure 42: Cross section of CRISTA-NF CCl_4 (Panel a) and aerosol (Panel b) for the test flight on 29 of July 2006. Black dots: Cloud Index < 3.5, gray diamonds: Total error $>90\%$. Note nonlinear color scales.

the retrieval of Aerosol, H_2O and CCl_4, are significant for most profiles compared to the total and smoothing error for the respective species (not shown).

In summary, O_3 and the other retrieved trace gases show pronounced structures between approximately 10 and 15 km altitude. For O_3 the existence of this structure is reproduced by CLaMS but it seems to be not resolved in the ECMWF operational analysis data. In the southern part of the flight air with low O_3 and HNO_3 volume mixing ratios and at the same time enhanced amounts of PAN is found while it is the opposite for the northern part. This contrast is due to the different main origin of the trace gases. PAN has its source in the troposphere, O_3 and HNO_3 are, in contrast, mainly originating from the stratosphere. This indicates a transition between tropospheric and stratospheric air at these altitudes.

4.4.2 Discussion

The significant structures consistently observed in the CRISTA-NF trace gas cross sections of O_3, HNO_3 and PAN point to the fact that air-masses of stratospheric and tropospheric origin and mixing processes among them were observed. A common way to analyze such mixing processes are tracer-tracer correlations (e.g. Plumb and Ko, 1992, Volk et al., 1996). Figure 43 shows a scatter plot of O_3 versus PAN. The color code displays the appropriate altitude. PAN is originated in the troposphere only (Talukdar et al., 1995), while O_3 is mostly produced in the stratosphere. Therefore their gradients have an opposite sign at the tropopause, allowing to detect mixing, as explained by e.g Hoor et al. (2002) and Pan et al. (2007) for CO and H_2O in combination with O_3.

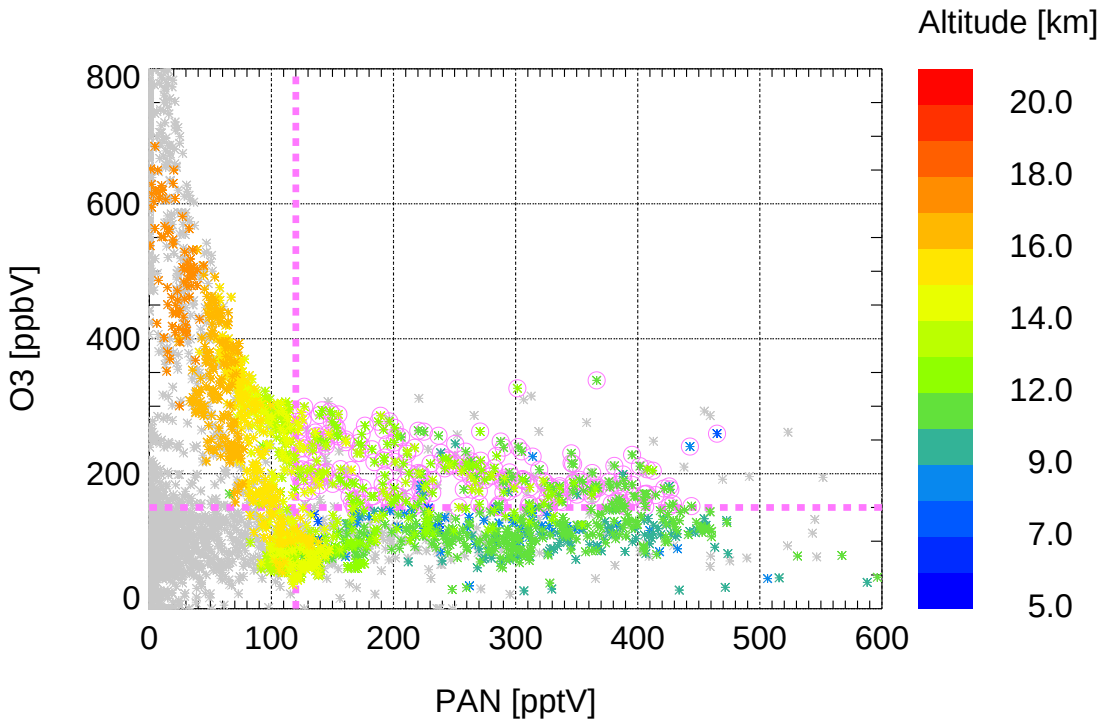

Figure 43: Scatter plot of CRISTA-NF O_3 versus PAN. Color scales display the altitude of the measured mixing ratios. Gray stars show values which did not pass the quality thresholds (see Section 3.2.8). Pink lines in Panel a) mark 150 ppbV O_3 and 120 pptV PAN. Measurements above both lines are marked with pink circles.

In this work, PAN is used instead of H_2O as tropospheric tracer because it could be retrieved reliably up to higher altitudes by CRISTA-NF. PAN is mainly originated from

pollution and therefore has its main sources close to the ground. Between the low PAN and high O_3 values above 14 km and the high PAN and low O_3 below 13 km there are intermediate values found between about 10 and 14 km. Such measurements with more than 150 ppbV O_3 and simultaneously more than 120 pptV PAN are marked with pink circles in Figure 43. They indicate mixing between tropospheric and stratospheric air. To some extent the field of view of CRISTA-NF may lead to an overestimation of mixing. For the altitudes where the mixing is observed the vertical resolution of PAN and O_3 is in most cases better than 3 km and often better than 2 km for O_3 and 1 km for PAN (see e.g. Figure 15).

The altitudes where intermediate PAN and O_3 mixing ratios occur, indicate a layer about 4 km wide with mixing between tropospheric and lowermost stratospheric air. It is similar to the one found by Pan et al. (2007) in connection with a tropopause fold on the cyclonic side of the polar jet in December 2005, using in situ measurements. Pan et al. (2007) observed a depth of the mixed air up to 5 km with rather low O_3 values with 100 ppbV also within the mixed air. For the CRISTA-NF measurements during flight TF2 the O_3 mixing ratios within the mixed air is significantly higher (up to 300 ppbV).

Figure 44 shows a scatter plot of HNO_3 versus O_3. The two species are positively correlated but one can distinguish two branches with tropospheric (blue and green) and stratospheric (green and other colors) air, respectively. Such branches can also be seen with the HNO_3 versus O_3 correlation described by Fairlie et al. (2007) in tropospheric and lower stratospheric air measured by high-frequency in situ observations from the DC8 during the Intercontinental Chemical Transport Experiment-North America in summer 2004. The slope of the stratospheric correlation observed by Fairlie et al. (2007) is similar to the one observed by CRISTA-NF above about 12 to 14 km. The tropospheric branch is more clearly separated and there are less stratospheric measurements in this in situ measurements, which reaches not higher up than about 12 to 13 km.

A similar structure to the one found here in the O_3 and HNO_3 mixing ratios (Figure 36 and 41a) was also described by Olsen et al. (2008) for High Resolution Dynamics Limb Sounder (HIRDLS) measurements. It has a much larger extent and was connected to an intrusion of

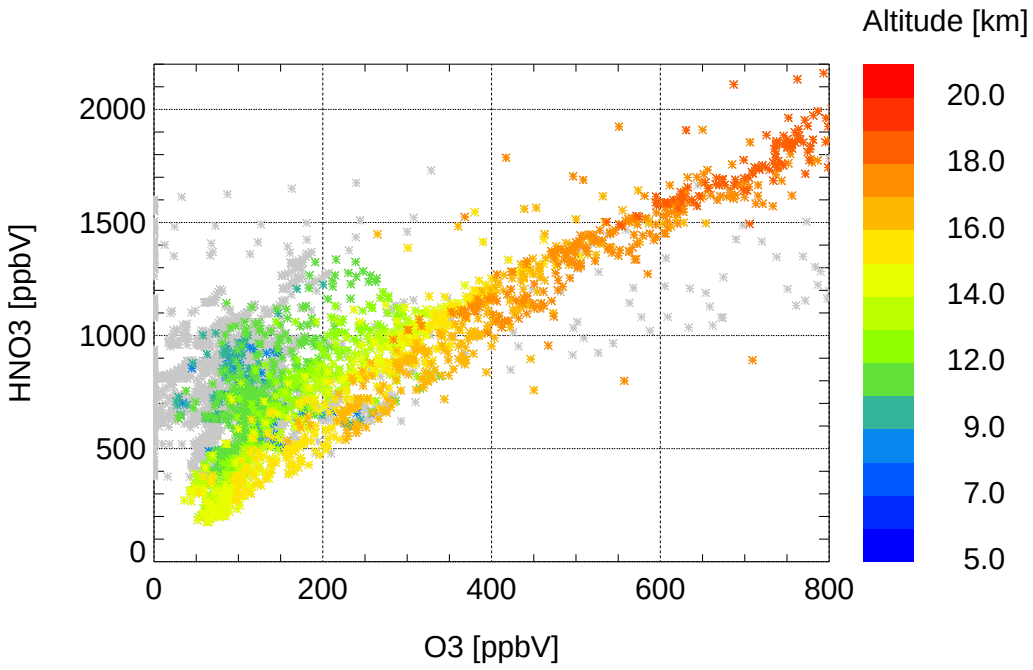

Figure 44: Scatter plot of CRISTA-NF HNO_3 versus O_3. Color scales display the altitude of the measured mixing ratios. Gray stars show values which did not pass the quality thresholds (see Section 3.2.8).

tropical lower stratospheric or upper tropospheric air into the high latitude lower stratosphere.

Figure 45a) presents a blowup of the O_3 distribution already displayed in Figure 36. The gray lines show the 1.5, 2 and 4 PVU surfaces as taken from ECMWF data, the black line shows the flight altitude. O_3 mixing ratios between 130 and 220 ppbV are marked with violet diamonds to emphasize the transition between tropospheric and stratospheric air. These are also shown in Panel b) together with the wind speed from ECMWF (golden contour lines) to identify the position of the subtropical jet, the cold-point tropopause from ECMWF temperatures (blue-green stars) and the lapsrate tropopause (at a lapsrate of 2 K/km; cyan squares) calculated from CRISTA-NF measurements. ζ-levels from CLaMS are shown as red contours. The measurements indicating mixed air based on O_3 and PAN mixing ratios from Figure 43a) are again marked as pink circles in Figure 45b).

The cold-point tropopause is situated at an altitude of 16 km or higher during the whole flight. It is determined from ECMWF data, because it is partly situated above the flight

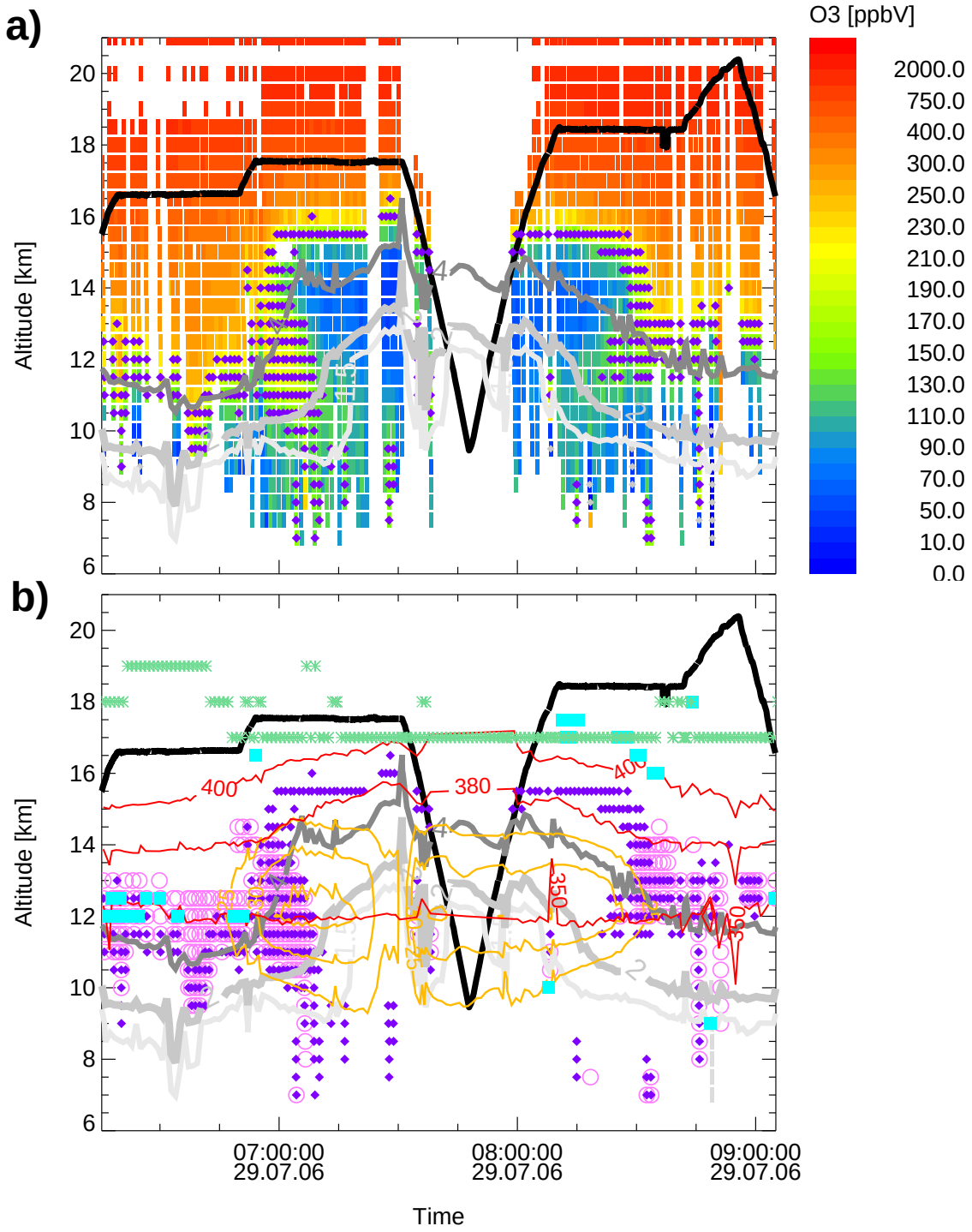

Figure 45: Excerpt of the CRISTA-NF O_3 cross section from Figure 36. Both Panels: Gray lines show the ECMWF potential vorticity at 1.5, 2 and 4 PVU, black line the flight track, violet diamonds show CRISTA-NF O_3 values between 130 and 220 ppbV. The Panel a) shows CRISTA-NF O_3 values as color coding. Panel b) shows ζ-level (CLaMS) as red contours, lapsrate tropopause from CRISTA-NF measurements (cyan squares), Cold-point tropopause from ECMWF temperatures (blue-green stars) and ECMWF wind speed (gold contours). Pink circles show positions, where the tracer-tracer correlation in Figure 43 indicates mixing.

altitude where CRISTA-NF temperatures are not passing the quality filters from Section 3.2.8. The lapsrate tropopause, on the other hand, is calculated from CRISTA-NF data to utilize the higher resolution. To detect it everywhere along the flight track an even higher resolution would be necessary.

The dynamical tropopause, often defined as the 2 PVU surface (e.g. Pan et al., 2007), is situated at about 10 km altitude in the northern part of the flight. During the southern part the 2 PVU surface is situated somewhat higher up, at about 13 km but still far below the cold point tropopause at 17 km. Even though no continuous lapsrate tropopause is resolved the profiles where it is detected indicate that it is situated somewhat above the 4 PVU surface. Like the dynamical tropopause but in contrast to the cold-point tropopause the lapsrate tropopause changes its altitude between the northern and the southern part of the flight.

In the north it is mainly found at about 12 km, in the south it seems to correspond to the cold-point tropopause at around 17 km altitude. The vertical and meridional wind speeds in the ECMWF data reveal, that the rise of the 2 PVU surface is situated just at the center of the subtropical jet. The air in the northernmost part of the flight above the lapsrate tropopause and the 4 PVU surface (corresponding to about 12 km altitude) belongs to the lowermost stratosphere, in accordance with the measured trace gas mixing ratios (especially the high O_3). In the southern part tropospheric air can be found up to an altitude of 15 km.

Shapiro (1980) described tropopause folds as mixing regions characterized by a chemical characterization between troposphere and stratosphere. The 2 PVU surface in the ECMWF data is not folded as sharply as one might expect in this case, but one should remember that the "tongue" seen in the CRISTA-NF O_3 is as well not resolved in the ECMWF data. Nevertheless, all PVU surfaces shown in Figure 45 rise at least 2 km, where the O_3 "tongue" is observed by CRISTA-NF. Also the relatively high O_3 values in the northern part of the flight (labeled with C1 and C2 in Figure 36) concur with decreasing altitudes of the shown PVU surfaces. In the ECMWF O_3 (Figure 37b) no corresponding structure is present. These results indicate that the CRISTA-NF measurements show a detailed cross section through a tropopause fold.

It certainly helped to resolve this structure by CRISTA-NF that the flight track was aligned nearly perpendicular to the fold, providing that the CRISTA-NF measurements also have a relatively high horizontal resolution and sampling in addition to the generally high vertical resolution. The resolution naturally can not be as high as the one provided by in situ measurements. However, the CRISTA-NF measurements have a higher resolution then most satellite data available for these altitudes today and provide, unlike in situ measurements, a two dimensional cross section. No in situ measurements deployed on the M55-Geophysica during this flight would be able to detect these structures without extensive flight maneuvers at lower altitudes, which would require some predictive knowledge of the structure.

Imaging spectrometers as the GLObal limb Radiance Imager for the Atmosphere (GLORIA; Riese et al., 2005, Friedl-Vallon et al., 2006), which is under development for the High Altitude and LOng range research aircraft (HALO) will provide an even better resolved view of such small scale structures. The next generation of infrared limb imaging satellites (see e.g. Riese et al., 2005 and ESA, 2008) like PRocesses Exploration through Measurements of Infrared and millimeter-wave Emitted Radiation (PREMIER) will provide a spectral and spatial resolution similar to CRISTA-NF with global coverage. This will offer the possibility to quantify the effect of small- and mesoscale processes on the total exchange between troposphere and stratosphere.

Tropopause folds are suspected to be one of the main mechanisms for cross-tropopause-transport (e.g. Shapiro, 1980 and Seo et al., 2008). Hoor et al. (2002) observed a greater depth of the mixing layer above the extra-tropical tropopause during summer and explained it with transport across the tropopause at the subtropical jet. Mixing between tropospheric and lower stratospheric air is observed to occur often in connection with tropopause folds. Figure 45 shows that the mixed air identified by the tracer-tracer correlation in Figure 43 is found at the northern side of the jet where the fold is situated at up to about 14.5 km altitude and ζ=380 K and at up to about 13 km further northwards in the lowermost stratosphere (above the dynamic and around the lapsrate tropopause).

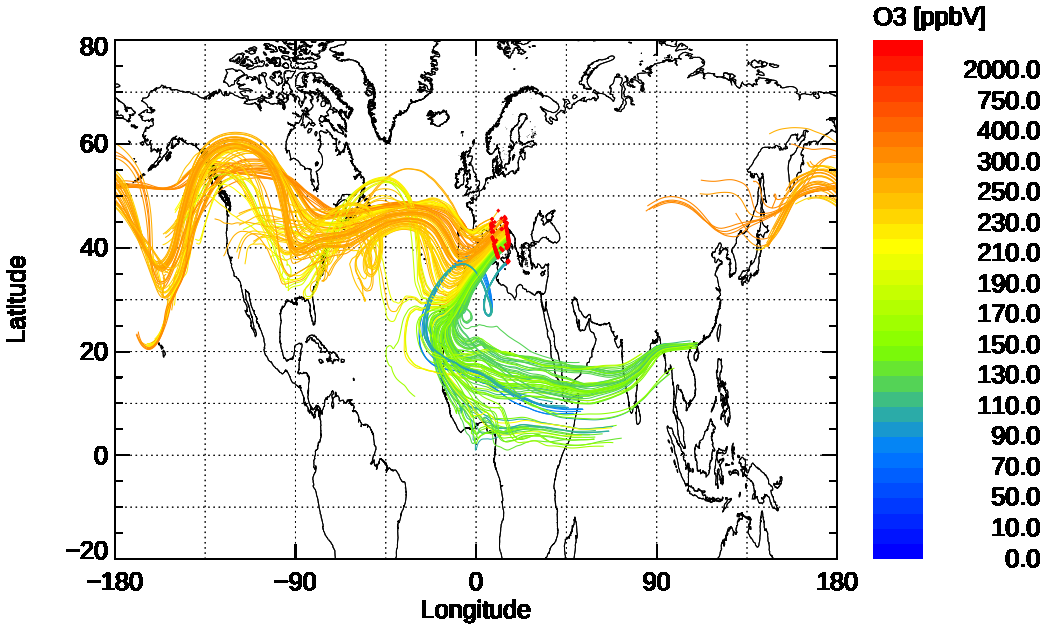

Figure 46: Map with 10 day backward trajectories from the TF2 CRISTA-NF grid positions between 350 and 360 K ζ. Color coding shows the CLaMS O_3 on the CRISTA-NF grid (without filtering) during the test flight. The flight track is marked with red diamonds.

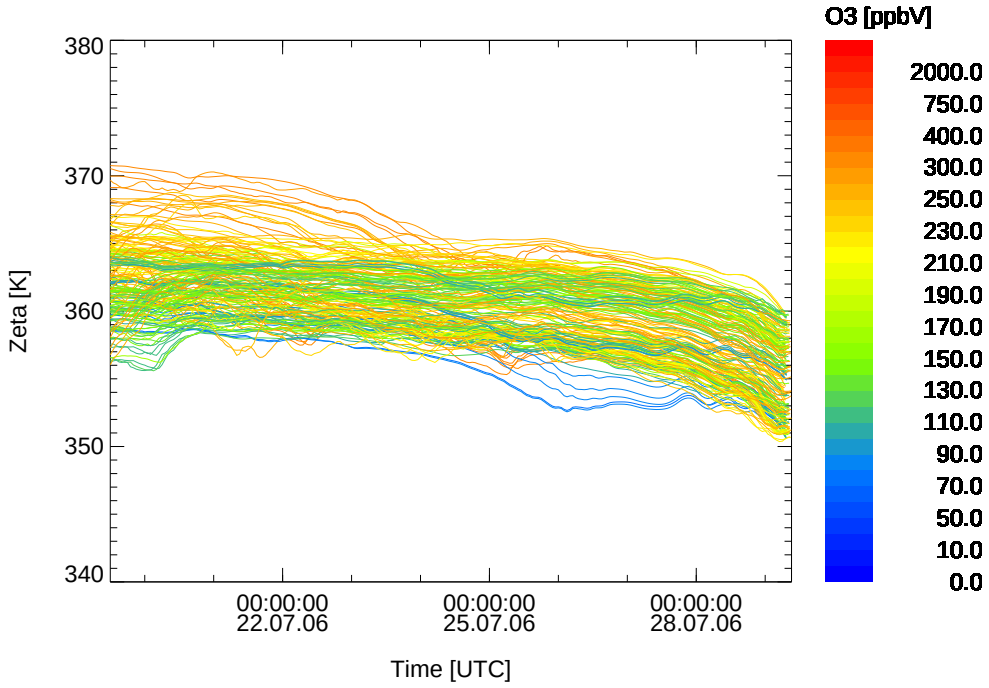

Figure 47: Vertical motion in ζ space of the backward trajectories from in Figure 46 plotted versus time.

To gain further insight into the origin and the fate of the air masses detected during the test flight trajectories are calculated with CLaMS. Figure 46 shows 10 days backward trajectories of all air parcels arriving at the CRISTA-NF grid positions between 350 and 360 K ζ (without filtering for resolution, measurement contribution and χ^2/m). For ζ between 350 and 360 K relatively low O_3 values are just found in the southern part of the flight. The trajectories reveal that nearly all air parcels with low O_3 volume mixing ratios under 200 ppbV originate in the region around the Asian monsoon anticyclone. In contrast, about all trajectories arriving in the northern part of the flight track with O_3 values over 200 ppbV come from westward directions along the subtropical jet.

The vertical motion of backward trajectories in ζ-Level is displayed in Figure 47 showing that they where at higher levels the days before the test flight. Further back, the ones with a higher O_3 mixing ratio are found at ζ-Level above 370 K. Most of the trajectories with lower O_3 values come from around 360 K and are sinking 2–5 K before the 29 of July. Generally the trajectories arriving at ζ-Level between 350 and 360 K with higher O_3 values seem to originate at higher ζ-Level compared to the ones with low O_3 mixing ratio.

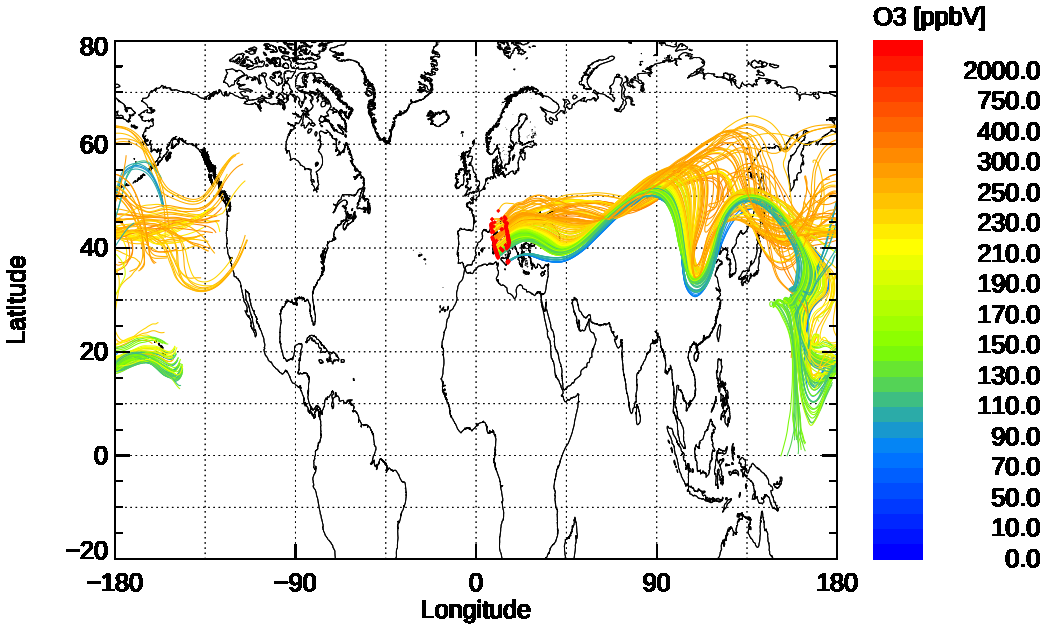

Figure 48: As Figure 46 but 10 day forward trajectories

Figure 48 displays forward trajectories for the same ζ interval over 10 days showing that the air-masses with low O_3 mixing ratios do not return into the flow around the Asian monsoon anticyclone, but follow the subtropical jet, like the ones with high O_3 values. Over Asia most of the trajectories arriving at high and low O_3 values, respectively, appear to be still separated. Few trajectories with high O_3 turn south over the Pacific Ocean. Most trajectories are sinking to ζ-Levels under 350 K during these 10 days (not shown).

The low O_3 and HNO_3 mixing ratios along with high PAN mixing ratios in the southern part of the flight also correspond well to the ACE-FTS observations of low O_3 and HNO_3 and high mixing ratios of tropospheric species within the Asian monsoon anticyclone (Park et al., 2008). They observe a strong isolation of the air within this anticyclone.

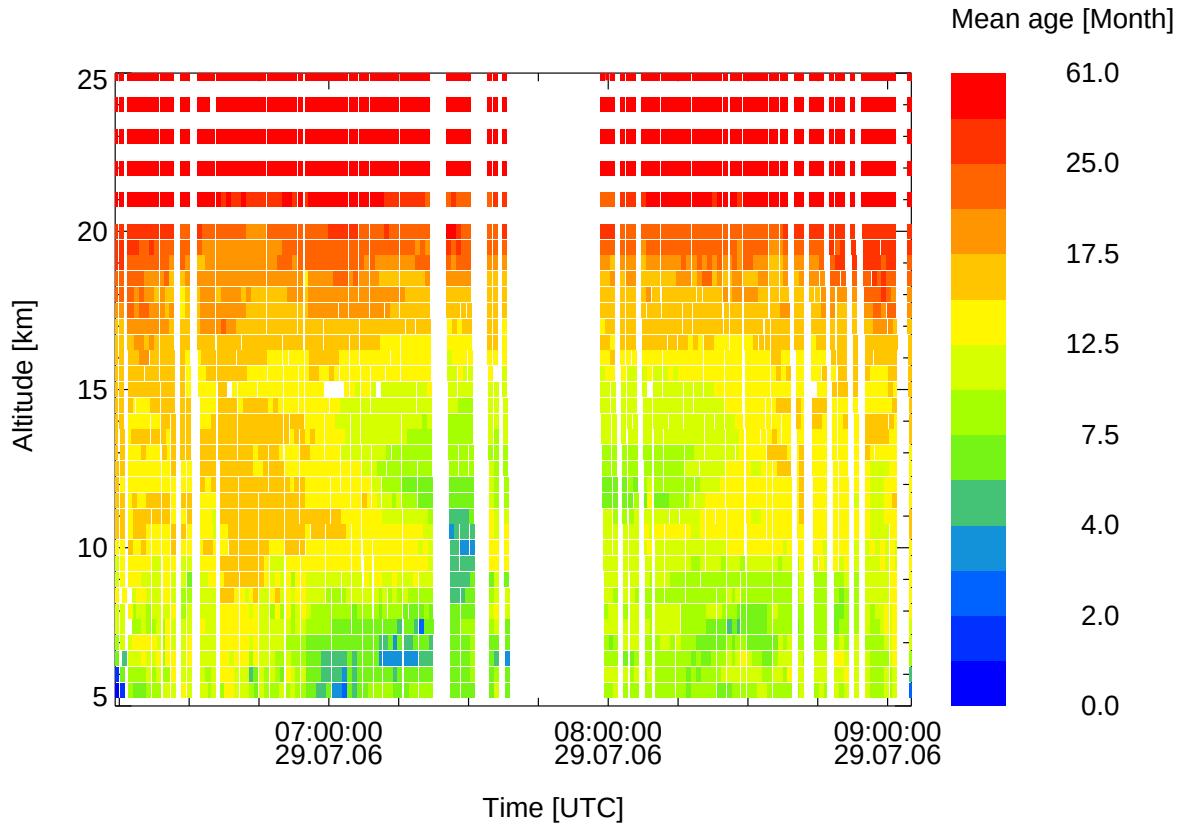

Figure 49: Cross section of mean age of air from the climatological CLaMS run interpolated on CRISTA-NF grid points.

A further measure for the origin of the air is the mean age (see Section 4.3). Figure 49 displays the mean age of air from the climatological CLaMS run. It indicates that in the

southern part of the flight track air with a mean age of less than about one year is found up to 15 km altitude. In the northern part young, tropospheric air is in most cases found only below 10 km.

In summary, the results of the AMMA test flight on 29 July 2006 shows that CRISTA-NF provides detailed measurements in the UTLS. The data obtained agree well with in situ measurements and modeled data from CLaMS. A tropopause fold, not well resolved by the ECMWF operational analysis was observed.

5 Summary and Outlook

This work concentrates on the analysis of measurements from the mid infrared spectrometers CRISTA-NF during the AMMA-SCOUT-O3 campaign, which took place in July and August 2006. Deployed on the high-altitude research aircraft M55-Geophysica it measured mid infrared radiance within an altitude range of about 5 to 21 km at maximum. The AMMA-SCOUT-O3 campaign consisted of a test flight over Italy and the Mediterranean Sea, four transfer flights via Marrakech to Ouagadougou and back and five local flights around Ouagadougou.

The retrieval code JURASSIC was utilized to retrieve atmospheric data from the 776 to 868 cm^{-1} detector channel of CRISTA-NF. Improvements of the forward model used and the thorough selection of the retrieval setup made it possible to retrieve altitude, temperature, H_2O, O_3, HNO_3, PAN, CCl_4, aerosol, and a radiometric offset simultaneously from the CRISTA-NF measurements. In addition, information about clouds along the flight track are available.

The accuracy of the forward model, required for the retrieval, was significantly increased by combining the Emissivity Growths Approximation, the Curtis Godson Approximation and a linear regression model as well as by including the computation of the H_2O continuum directly into the JURASSIC code.

The attitude determination of CRISTA-NF was improved by combining information from its own attitude monitoring system, which has a high time resolution, and the M55-Geophysica avionic system, which has a higher absolute accuracy. Due to the remaining uncertainty of the resulting attitude it was necessary to develop a retrieval setup, which can derive altitude and temperature simultaneously. This was achieved by using the radiance from nine spectral bands around 790 cm^{-1} and 840 cm^{-1} and utilizing the a priori knowledge of CFC-11 from HAGAR in situ measurements. At the same time this emphasizes the importance of good knowledge of the altitude in order to gain as much information as possible about the atmospheric quantities, i.e using CFC-11 measured in situ to be able to retrieve temperature and altitude implies that a CFC-11 retrieval is not possible.

Based on the improved attitude, the forward model correction and the new retrieval setup it is now possible to provide a CRISTA-NF level-2 data set for the AMMA transfer flights, the test flight and the fifth local flight. The retrieval results are available for these flights on a 500 m altitude grid with a vertical resolution varying between about 500 m and 3 km, depending on the retrieved variable and the sampling of the measured radiance, below the flight altitude of about 17 - 21 km. Measurement contribution and retrieval errors indicate a good data quality for H_2O (below about 12 km), temperature, CCl_4, and especially PAN, O_3, and HNO_3. Generally, CRISTA-NF data agreed well to the available in situ observations and a CLaMS simulation during the analyzed flights. Hence, CRISTA-NF data provides a detailed insight into the UTLS, measuring both trace gases of tropospheric and stratospheric origin. This allows to observe mesoscale processes, which have implications for the medium range weather forecast and ozone chemistry (WMO, 2006).

These level-2 data can form the basis to retrieve further atmospheric constituents and extend the H_2O retrieval to altitudes up to the observer altitude using the sequential retrieval on spectral intervals outside the 776 to 868 cm^{-1} region. Further improvements of the quality of the retrieved data can be achieved by using more detailed information for forward model parameters, e.g. from satellite measurements of $ClONO_2$ and CFCs. Additionally a more accurate in-flight wavelength calibration would be an asset.

A detailed analysis is performed for the test flight on the 29 of July 2005. Here, a sharp transition between tropospheric and stratospheric air was observed over the Mediterranean Sea, identified by strong gradients in O_3, HNO_3, and PAN. Its structure was reproduced by CLaMS simulations but was not as distinct in the ECMWF operational analysis data set.

It was identified to be caused by a small tropopause fold, which is not well resolved in the ECMWF data. CLaMS data made it possible to gain further information about the origin and the fate of the observed air masses. They indicate that the observed air originated on the one hand in the tropopause within the Asian monsoon anticyclone and on the other hand in the extratropical lowermost stratosphere along the subtopical jet. Tracer-tracer correlations between PAN and O_3 retrieved from the CRISTA-NF measurements show the presence of

mixed tropospheric and stratospheric air. This emphasizes that CRISTA-NF is capable of providing a detailed picture of the chemical composition in the UTLS with a higher resolution than today's satellites and a better coverage than in situ measurements.

To investigate the UTLS in such detail on a global scale could help to gain a better understanding of the whole atmosphere. This can be facilitated by future satellite instruments like PREMIER (ESA, 2008), which can provide a similar sampling and spectral resolution as CRISTA-NF and operate on a global scale.

A Appendix

A.1 CRISTA-NF

Table 7 lists the spectral ranges of all CRISTA-NF detectors in the calibrated spectra (level-1A data). The in-flight wavelength calibration is only available for some detectors. Therefore the spectral ranges available for data analysis can vary in the order of a few wavenumbers. There is also a small difference in the spectral range between forward and backward spectra. The spectral ranges listed here are based on the measured spectra of profile 76, TF2. They are similar, but not identically to the ones listed in Schroeder et al. (2009), which are based on the accuracy of the calibration.

Errors for the in-flight wavelength calibration for AMMA T3, detector L6 for forward and backward spectra are listed in Table 10.

Table 7: Detectors and spectral ranges available in level-1A data.

Detector channel	Approximate spectral range [μm]	Approximate spectral range [cm^{-1}]	In-flight wavelength calibration	Remark
HRS				
H1	11.39–10.74	878–931	no	
H2	11.88–11.25	842–889	yes[1]	
H3	12.18–11.53	821–867	no	Defective on flights TF2, L2, L5
H4	12.61–11.98	793–835	no	Calibration incomplete[2]
H5	12.89–12.25	776–816	T3	Defective on flights TF2, L2, L3 Empirical correction[3] apart from T3 and T4
H5R	12.89–12.25	776–816	yes[1]	Empirical correction[3] apart from T3 and T4
H6	6.72–6.39	1489–1565	no	
H7	13.72–13.05	729–766	no	
LRS				
L1	8.61–7.24	1161–1382	no	Review calibration[4]
L2	4.82–4.13	2076–2422	no	Defective on flights TF2, T1, T2, L1, L2, L3, L4, L5
L3	10.28–8.84	973–1131	no	
L5	11.78–10.38	849–963	T3	
L6	12.89–11.52	776–868	yes[1]	
L7	6.71–6.02	1490–1660	no	
L8	14.04–12.67	712–789	no	Review calibration[4]

[1] For flights TF2, T1, T2, L5, T3 and T4

[2] The post AMMA calibration with variable detector temperature could not be analyzed for H4 due to a failure of the detector before or during this calibration. The spectral range of H4 overlaps with H5R revealing that the radiance of H4 has large bias. Therefore it is not possible to use H4 without further correction.

[3] A change of the detector bias voltage before the back transfer (T3, T4) makes a correction for all other flights necessary, because the black body calibration is only valid for the new bias voltage (Schroeder, pers. com.).

[4] Artifacts in spectra measured with closed shutter. It might be possible to remove them with a reviewed black body or wavelength calibration.

A.1.1 Black body calibration

A black body calibration is necessary to translate the detector signals into radiance. This is described in detail by Kullmann (2006) and Schroeder et al. (2009) for CRISTA-NF and Ern et al. (2003) for CRISTA. The resulting instrumental errors from the post AMMA calibration for the detectors L5 and L6 used in this work are presented in Table 8, Appendix A.1. The Gain error is about 1% for the ISBs of both detectors (for radiance $< 0.0005\,\mathrm{W/(m^2 sr\,cm^{-1})}$ for L5 and $< 0.0015\,\mathrm{W/(m^2 sr\,cm^{-1})}$ for L6). The noise is divided by the square root of the number of spectral measurement points in each ISB and varies between 0.1 and 0.5%, depending on the ISB.

Usually these errors should be used as input to the retrieval. The noise is chosen larger than the result of the calibration, see Section 3.2.5. The offset was accidentally set too low for the L6 ISBs and too high for the L5 ISBs (0.0009 $[\mathrm{W/m^2 sr\,cm^{-1}}]$ for L5 and L6). This has next to no influence on the retrieval result for the main retrieval using L6, because

- it does not influence the retrieval errors of the other retrieved variables, because the offset is retrieved itself.
- it does not influence the result of the offset and the other retrieved variables because the retrieved offset is about one order of magnitude smaller than the one resulting from the calibration (see Section 3.2.6, Figure 23).
- the only significant influence can be seen on the resulting error for the offset.

This was tested on profile 94, flight AMMA T3. The influence of the larger offset error for the sequential retrieval using the L5 ISBs is also not expected to be large and it is not unusual, to choose a larger error for a retrieved variable.

Schroeder et al. (2009) showed that a black body calibration must account for the dependency of the detector signal on the detector temperature. The detectors have a nominal temperature of 13 K (Offermann et al., 1999) but have warmed up during some of the AMMA flights. Their sensitivity is temperature dependent the detectors were calibrated up to 14.5 K during the post AMMA calibrations. During some flights detector temperatures over 14.5 K

Table 8: Black body calibration errors for detector L5 and L6

ISB [cm^{-1}]	Offset [$W/m^2sr\,cm^{-1}$]	Gain [%]	Noise [%]
L5			
876–876.9	0.0006	1	0.21
878.1–879	0.0006	1	0.17
880.2–881.1	0.0006	1	0.08
L6			
777.8–778.7	0.0015	1	0.08
784–785	0.0015	1	0.13
787–790	0.0015	1	0.04
791–793	0.0015	1	0.05
794.1–795	0.0015	1	0.14
796.6–797.5	0.0015	1	0.14
832–832.9	0.0015	1	0.33
844.3–847.3	0.0015	1	0.10
863–864	0.0015	1	0.17

occurred (see Table 6). Data from these time periods need to be regarded with care because they are based on extrapolated calibration coefficients and in particular, the calibration errors are not reliable there.

Neighboring detector channels with overlapping radiance intervals are observed to display systematic differences, especially for the HRS spectrometer. Also between HRS and LRS channels with overlapping wavelength intervals differences exceeding the effects of the different resolution of the spectrometers have been observed (not shown). Therefore the radiometric offset (see Section 3.2) should be retrieved for each detector separately, or the joint retrieval of multiple atmospheric parameters should be limited to one detector.

A.1.2 Spectral resolution

To identify the emitters based on spectral signatures, an accurate wavelength calibration and knowledge about the spectrometer resolution is necessary. The resolution $\lambda/d\lambda$ of an Ebert-Fastie spectrometer is determined through the width of the entrance and the exit slit, the

diffraction of the grid and aberrations:

$$d\lambda = \frac{a}{nf} * \sqrt{s^2 + (F\lambda)^2 + b^2} \tag{8}$$

Where

- $F = 10$ is the F-Number
- $n = 1$ is the spectral order
- $a = 50\,\mu$m is the grating constant
- $s = 220\,\mu$m is the slit width
- $f = 50\,$cm is the focal length

for the detectors L6 and L5.

The spherical aberration b of the spectrometer mirror can be neglected (Nehls, 1991). Equation 8 results in $\lambda/d\lambda = 496$, for $\lambda = 12.5\,\mu$m($\nu = 800$ cm^{-1}) for both CRISTA and CRISTA-NF.

Another way to determine the resolution is to measure the width of a single spectral line. That was not done for CRISTA-NF, but for the CRISTA satellite instrument the resolution was estimated using in-flight observations of atmospheric emissions. For the channel corresponding to the channel L6 used in this work a value of $\lambda/d\lambda = 536$ for a reference wavelength of $\lambda = 12.5\,\mu$m was determined.

It was not possible to determine the resolution for CRISTA-NF trough in-flight information because that requires ideally detections of single spectral lines and an exact knowledge of tangent altitude and emitter abundances. Nevertheless, it was decided to use the value measured for the satellite instrument instead of the calculated one.

A.1.3 In-flight wavelength calibration

Two kinds of wavelength calibrations are performed for CRISTA-NF: A laboratory wavelength calibration, described in Kullmann (2006) and Schroeder et al. (2009) and a calibration using in-flight data.

For the in-flight wavelength calibration selected CRISTA-NF spectra measured during flight are compared to spectra calculated by RFM (see Section 3.1) and their difference is minimized. The wavelength is calculated by a quadratic fit (fit parameters a_0, a_1 and a_2) between the wavelength (λ) and the voltage representing the grid position (U_{gp}) (Kullmann, 2006):

$$\lambda(U_{gp}) = a_0 + a_1 \frac{U_{gp}}{1V} + a_2 \frac{U_{gp}^2}{1V^2}, \text{ with } [\lambda] = 1\ \mu\text{m}, \ [\text{U}_{\text{gp}}] = 1\ \text{V} \tag{9}$$

Spectra are measured by turning the grating. To distinguish the spectra from different turning directions, The terms forward and backward spectra are used. If a mean wavelength scale is used for both directions, this leads to a significant oscillation in the radiance of radiance profiles, because forward and backward spectra alternate in the measured profiles (see Figure 50). The right Panel shows the integrated radiance of the 844.3-847.3 cm^{-1} ISB obtained with a joint laboratory wavelength calibration for forward and backward spectra of profile 130 for flight AMMA TF2 minus an average profile of the whole flight. The difference from zero is due to variations of the atmosphere along the flight path. Oscillations are caused by the difference between forward and backward spectra.

To correct for this difference forward and backward spectra are separated during the wavelength calibration. This leads to a much smoother profile as obvious from Figure 50 (left Panel). Because derivations between the two types of spectra are still visible they are also separated during the retrieval to suppress additional noise. The drawback of this separation is that the vertical sampling is decreased by a factor of two.

The fit parameters a_0, a_1 and a_2 are determined for each flight and each detector is analyzed separately for forward and backward spectra[10]. For T3 a_0, a_1 and a_2 and their errors are shown in Table 9.

The resulting errors in wavelength and wavenumber are shown in Table 10. RFM is used to estimate the corresponding radiance errors caused depending on the ISB. Radiance errors

[10]Results of the in flight wavelength calibration are available for detector L6, H5R and H2 for the AMMA flights TF2, T1, T2, L5, T3 and T4 and for detector L5 for the flight T3

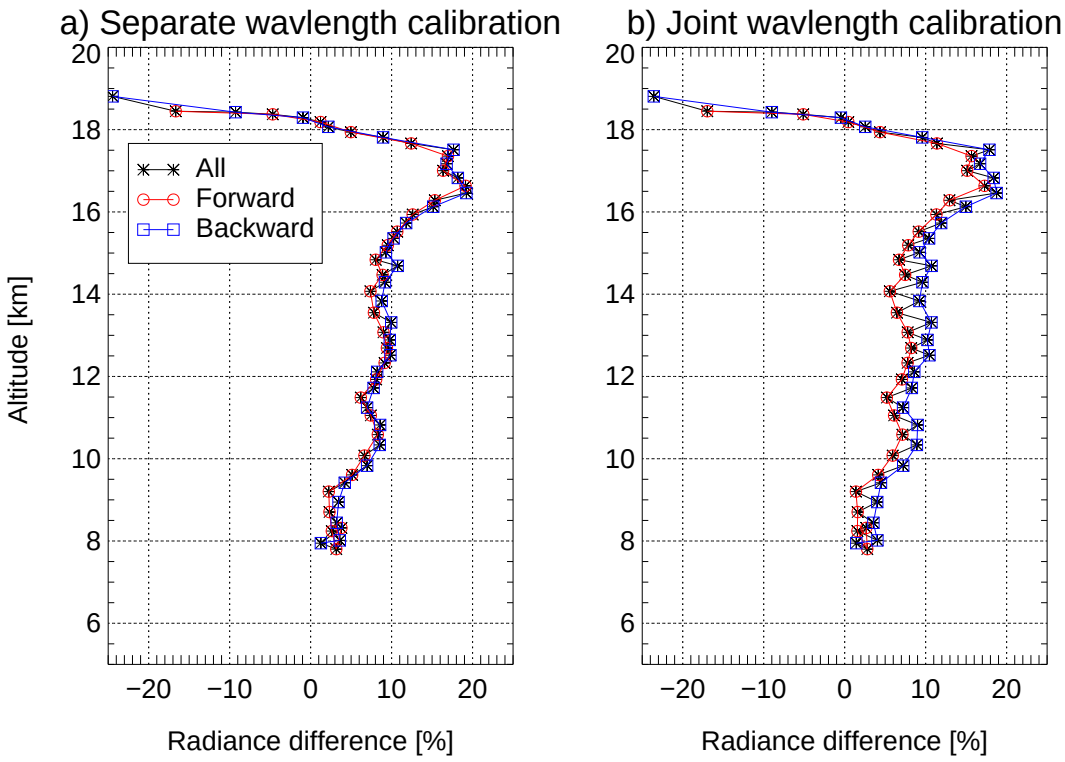

Figure 50: Radiance of the 844.3–847.3 cm^{-1} ISB recorded during AMMA flight TF2, profile 130, average profile subtracted. a) Separate in flight wavelength calibration for forward and backward spectra, b) joint laboratory wavelength calibration. Red line: Forward spectra, blue line: Backward spectra, black line: Combined profile with forward and backward spectra.

caused by spectral shifts depend on the shape of the spectra. If there are no large radiance difference even a large wavelength error only causes a small radiance error, but close to strong spectral signatures and peaks small wavelength shifts can cause large radiance errors. To estimate the radiance errors, spectra calculated with RFM were subtracted with shifted wavelength scales. The shift was done in both directions, the larger error is listed in the table.

Even with the in-flight wavelength calibration and separated forward and backward spectra, radiance errors of over 2% still occur for ISBs at the wavelength extremes of the detector. Even though the resulting radiance errors have a systematic reason they can vary with altitude because the shape of the spectra changes. Overall, the in-flight wavelength calibration and the separation of forward and backward spectra has decreased the errors significantly compared to the combined laboratory wavelength calibrations.

There are two possible reasons for these oscillations: First, for the CRISTA Satellite

Table 9: Fit parameters and their standard deviation for the in flight wavelength calibration for AMMA T3, detector L6 for forward (FW) and backward (BW) spectra according to equation 9.

	a_0 [μm]	a_1 [μm/V]	a_2 [μm/V^2]
FW	12.6582 ± 0.0007	0.2695 ± 0.0017	-0.0021 ± 0.0006
BW	12.6565 ± 0.0007	0.2698 ± 0.0009	-0.0016 ± 0.0002

Table 10: Errors for in flight wavelength calibration for AMMA T3, detector L6 for a) forward and b) backward spectra. Radiance errors are estimated based on a RFM calculation with an observation altitude of 20.2km and a tangent altitude of 12km.

a)	ISB [cm^{-1}]	$\Delta\lambda_{\mathrm{FW}}[\mu m]$	$\Delta\nu_{\mathrm{FW}}[cm^{-1}]$[11]	$\Delta\mathrm{Radiance}_{\mathrm{FW}}[\%]$
	777.8–778.7	0.00225	0.13610	0.33
	784–785	0.00135	0.08334	0.20
	787–790	0.00089	0.05534	0.09
	791–792	0.00055	0.03449	0.35
	794.1–795	0.00034	0.02141	0.03
	796.6–797.5	0.00016	0.01031	0.08
	832–832.9	0.00043	0.02955	0.18
	844.3–847.3	0.00166	0.11883	0.74
	863–864	0.00401	0.30309	2.04

b)	ISB [cm^{-1}]	$\Delta\lambda_{\mathrm{BW}}[\mu m]$	$\Delta\nu_{\mathrm{BW}}[cm^{-1}]$	$\Delta\mathrm{Radiance}_{\mathrm{BW}}[\%]$
	777.8–778.7	0.00145	0.08777	0.19
	784–785	0.00102	0.06303	0.13
	787–790	0.00079	0.04925	0.08
	791–792	0.00061	0.03850	0.39
	794.1–795	0.00050	0.03142	0.04
	796.6–797.5	0.00040	0.02510	0.20
	832–832.9	0.00002	0.00149	0.01
	844.3–847.3	0.00025	0.01773	0.11
	863–864	0.00089	0.06303	0.45

instrument is was observed, that detector relaxations (see also Section 3.2.5) have a different effect on forward and backward spectra (Riese et al., 1999a). Second, the detectors need a finite time to record the data each measured radiance corresponds to an integrated value

over a short wavelength and time interval. This can lead to a small difference between the wavelength scale for the spectra recorded during different scan directions.

A.1.4 LOS calibration

To allow to measure with a high vertical resolution in the atmosphere, CRISTA-NF contains an adjustable primary mirror. A calibration is necessary to link the voltage recording the mirrors position to the LOS of the telescope. The instrument is aligned into a horizontal position with a laser and a theodolite. The reference is a mirror cube permanently attached to the ZeSn-window flange. An infrared point source mounted on a height-adjustable table is detected with CRISTA-NF for different angles of the primary mirror. In this way the pointing direction of the mirror can be determined to better than $40'' \approx 0.011^o$. An LOS calibration was performed before and after each campaign. For AMMA-SCOUT-O3 there was a systematic difference smaller than the error of the calibration between these two calibrations. Therefore the result from a combination of data collected during both calibrations was used. For a detailed description of the LOS calibration see Kullmann (2006).

The airplane alignment must be added to the angle set by the mirror position to get the pointing direction of CRISTA-NF during flight.

A.1.5 The attitude monitoring system

To retrieve the vertical distribution of trace gases and temperature an exact pointing information is necessary. Although the pointing can in principle be retrieved from the measured radiance, it is desirable to know it as accurately as possible from an independent measurement in order to decrease the number of free parameters. The most important quantities to calculate the alignment of the line of sight of CRISTA-NF are the aircraft altitude, position and the attitude angles Φ (roll), Θ (pitch), and Ψ (yaw). Figure 51 shows these angles for definition following DIN 9300 (Fabeck, 1980).

There are two sources of pointing information:

- The M55-Geophysica Unit for Connection with Scientific Equipment (UCSE, MDB, 2002), provided, among others the following information:

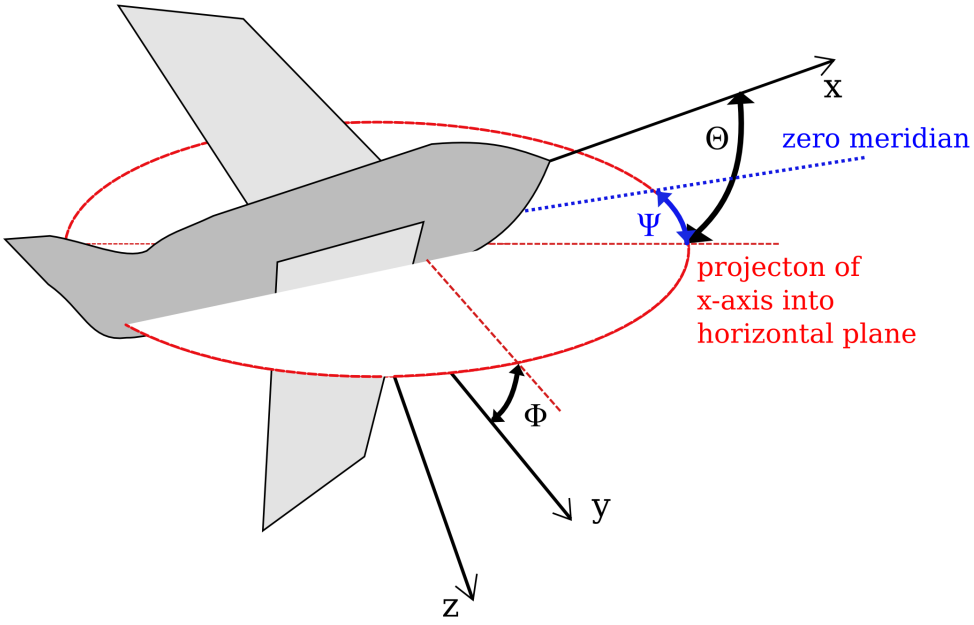

Figure 51: Attitude angles roll Φ, pitch Θ and yaw Ψ following DIN 9300. Figure based on Fabeck (1980).

  - Attitude angles:
    - Roll (Φ), pitch(Θ), standard deviation $\sigma \leq 0.05°$
    - Yaw (true heading, Ψ), $\sigma = 0.2°$
  - Two independently measured altitudes:
    - Pressure altitude (True Altitude), measurement error=75m
    - GPS altitude (Height upon MSL), measurement error=100m
  - Atmospheric pressure

- CRISTA-NFs AMS (Attitude Monitoring System), providing:
  - Inclinometer around x-direction
  - Accelerometers for x, y and z-direction
  - Gyros x-direction (SCOUT-O3 and AMMA) and y, z-direction (only AMMA)

A standard deviation of $\sigma = 0.05°$ corresponds to an altitude difference of about 330 m for an observer at 20 km and a roll angle of $\Phi = 3.5°$. The time resolution of the UCSE data is 1 Hz (5 Hz only on request), the one of the AMS data is about 28Hz for AMMA and 56Hz for SCOUT-O3. Despite the measurement errors given in MDB (2002) the two UCSE altitudes differ by up to 700m (Figure 52). Here, the height upon mean sea level (MSL) is used, since

it has proved to be more accurate by comparing the UCSE pressure with the interpolated ECMWF pressure for the two altitudes.

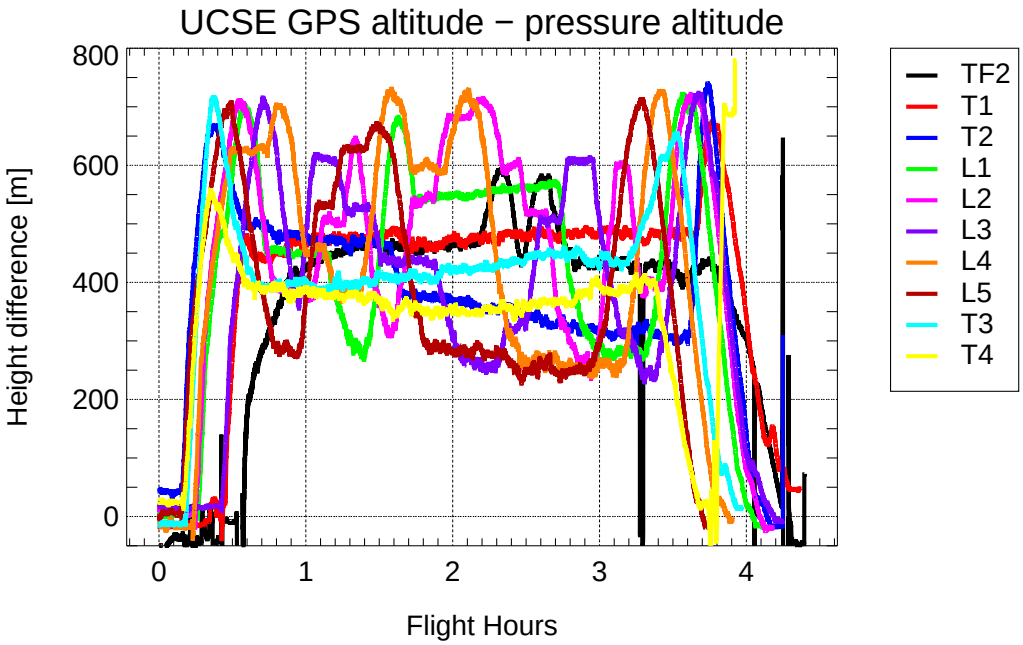

Figure 52: GPS altitude - pressure altitude for all AMMA flights.

The AMS data are used to calculate the roll angle with higher time resolution and to estimate the alignment of the instrument within the aircraft (see Appendix A.1.7)) and to correct the internal clock (see Section A.1.6).

A.1.6 Correcting the internal clock

The time is recorded with 218 Hz from the internal clock of CRISTA-NF and 1 Hz for M55-Geophysicas UCSE. The time recording of CRISTA-NF is subject to to different errors, time jumps (1.0s long) caused by an error in the data processing and a time delay which accumulates especially while the instrument is turned off. At first it is necessary to filter the time from these one second jumps.

Secondly, the time lag of the internal clock of CRISTA-NF compared to M55-Geophysica needs to be removed. To use the UCSE information on airplane position and pointing, an exact agreement between both clocks is required. To readjust the CRISTA-NF clock during the flights, the roll angle is used, since it is measured by both, UCSE and the CRISTA-NF AMS. Because of the inaccuracy of the AMS roll angle (see AppendixA.1.7) at first an estimate of the time offset is determined by comparing prominent features like sharp turns in the roll angle time series. With this approximated time offset a correction of the bearing angles is done as explained in Appendix A.1.7. With the corrected roll angle the correlation to the UCSE roll is maximized by varying the time lag for each profile. In this way it was possible to determine time offset better than 0.2 s for each profile. It was shown that it changed less than 0.5 s during most flights therefore a fixed time offset was chosen for each flight, see Table 12. Finally the attitude correction was repeated with the corrected time (see also Figure 56)

A.1.7 Correction of the pointing measurements

The attitude monitoring should fulfill two main requirements:

1. Give accurate information about the absolute positioning of the LOS
2. Allow to correct for movements whilst one spectrum is recorded or allow to exclude spectra recorded during large movements

To minimize the errors in the trace gas and temperature retrieval, it would be desirable to know the vertical pointing to better than 0.01^o with a time resolution higher than 5Hz, since one spectrum is measured in about one second. Neither the pointing information provided by M55-Geophysica nor the one from the CRISTA-NF AMS alone is sufficient to fulfill these requirements. But it is possible to improve the knowledge about the pointing by combining these two sources of information.

For the UCSE data the accuracy and especially the temporal resolution is too low. The CRISTA-NF AMS has an adequate temporal resolution, but there are other shortcomings: It is not possible to use inclinometers and acceleration sensors alone to determine the correct attitude during flight. Both instrument types measure the direction of the total acceleration. On ground in a not-accelerated object this is identical to the direction towards the center of gravity of the earth but in an aircraft additional accelerations are present during flight (see Figure 53). Especially during turns, where these accelerations are large, the attitude cannot be derived correctly from inclinometers and accelerometers. A gyrometer, in contrast, does not measure any absolute pointing but the change in angular velocity around the aircraft axes.

The effect of turns of the aircraft on inclinometers and accelerometers can also be seen Figure 54, where the roll angle recorded by the UCSE and the inclinometer and calculated from the accelerometer and the x-gyro[12] is displayed. The lower panel shows the difference between UCSE roll and the other angles. Inclinometer and accelerometer do not show the turn visible in the UCSE roll angle and the accelerometer is very noisy. The normalized,

[12]Here the integrated angular velocity around the x-axis ($\int \Omega_x dt$) is used, which is not exactly equal to the roll angle ($\Phi = \int \dot{\Phi} dt$), see equation 10. This integrated angular velocity is also used for the active attitude system (Appendix A.1.9).

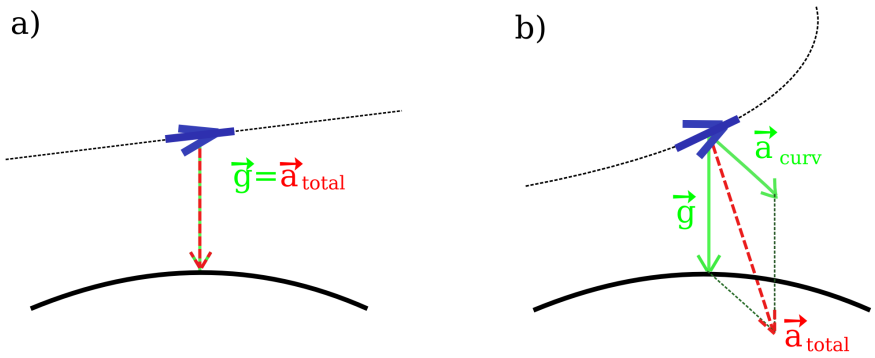

Figure 53: Vector of total acceleration measured from an aircraft during a) straight flight with constant velocity and b) a turn.

integrated gyro shows the turn but also a significant drift of about 2^o over this short time interval.

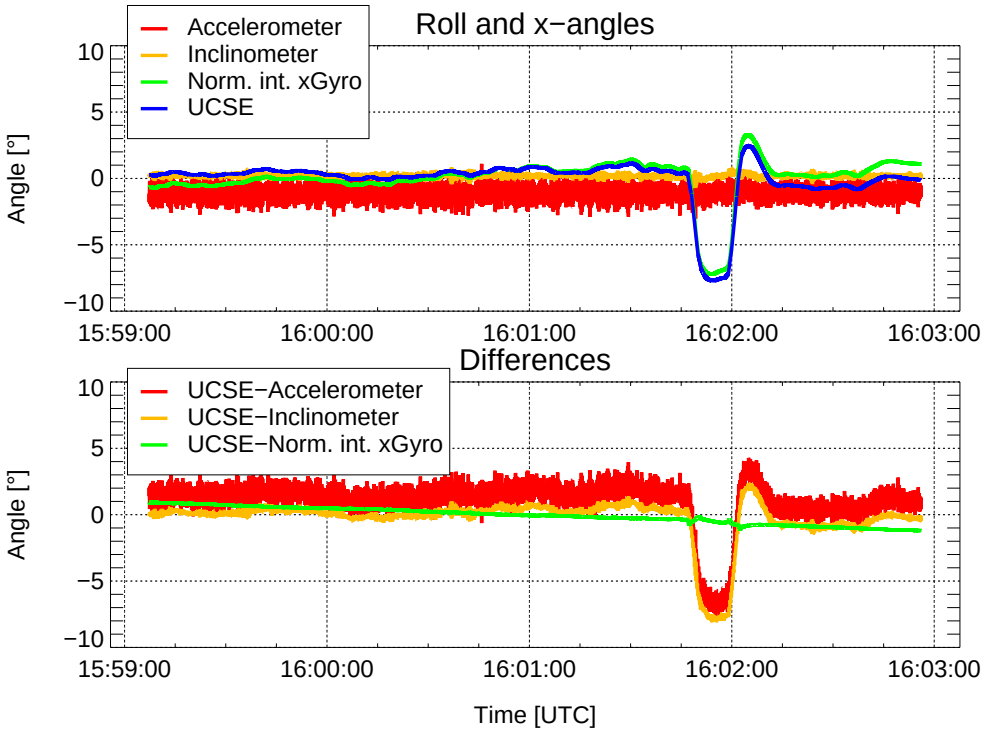

Figure 54: UCSE roll angle, CRISTA-NF AMS accelerometer, inclinometer and normalized gyro x-angle (upper Panel) and their differences (lower Panel) for a four-minute flight segment during the AMMA campaign on 2006/08/16 when an aircraft turn occurs at about 16:02 UTC.

Figure 55 shows the angles and their differences in pitch direction (or around the y-axis). There is no pitch inclinometer. The accelerometer is again very noisy and the drift of the

gyro is even larger as for the roll direction.

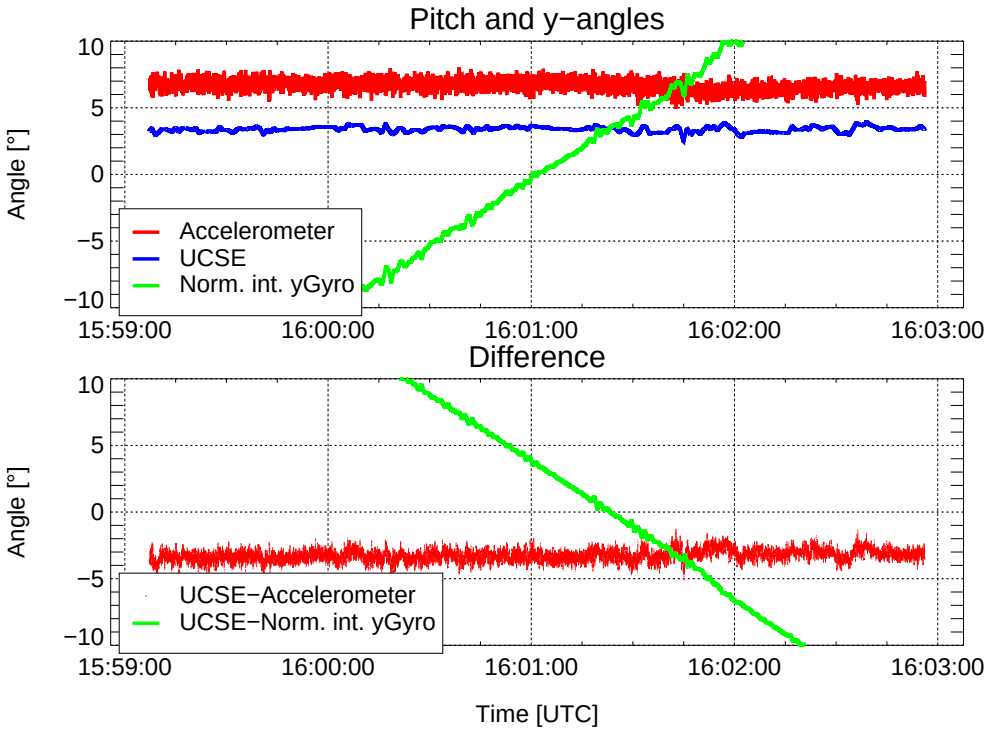

Figure 55: As Figure 54 but for UCSE pitch and the y-angle calculated from the accelerometer and the integrated y-gyro for the AMMA flight on 2006/08/16.

To calculate the exact attitude angles one would need gyrometers for all three axes and acceleration sensors for the same directions to get an absolute reference (ideally before the aircraft has started) and to compensate the drifts. The attitude angles could then be calculated employing the equations from Fabeck (1980):

$$\begin{aligned}
\text{Yaw}: \quad & \Psi = \int \dot{\Psi} \mathrm{d}t = \int [(\Omega_z \cos\Phi + \Omega_y \sin\Phi)/(\cos\Theta)] \mathrm{d}t \\
\text{Pitch}: \quad & \Theta = \int \dot{\Theta} \mathrm{d}t = \int [\Omega_y \cos\Phi - \Omega_z \sin\Phi] \mathrm{d}t \\
\text{Roll}: \quad & \Phi = \int \dot{\Phi} \mathrm{d}t = \int [\Omega_x + \Omega_z \tan\Theta \cos\Phi + \Omega_y \tan\Theta \sin\Phi] \mathrm{d}t
\end{aligned} \tag{10}$$

Since the UCSE attitude angles are expected to be more reliable than the AMS accelerometer, which shows noise and strong temperature dependence, it was chosen to calculate the high resolution attitude angles by combining the ones from UCSE interpolated onto the AMS temporal resolution with the information from the AMS roll gyrometer (see Figure 56). This

was done by recalculating the angular velocities from the UCSE attitude angles according to Fabeck (1980):

$$\begin{aligned}\Omega_x &= \dot{\Phi} - \dot{\Psi}\sin\Theta \\ \Omega_y &= \dot{\Theta}\cos\Phi + \dot{\Psi}\cos\Theta\sin\Phi \\ \Omega_z &= \dot{\Psi}\cos\Theta\cos\Phi - \dot{\Theta}\sin\Phi\end{aligned} \tag{11}$$

Then the angular velocity measured by the AMS x-gyro was adjusted to the angular velocity calculated from UCSE angles based on one minute means. The corrected attitude angles were finally calculated with this corrected angular velocities around the x-direction taking the starting value and the remaining directions from interpolated UCSE angular velocities. Figure 56 shows a scheme of the roll angle correction.

During the SCOUT-O3 campaign no AMS y- and z-gyros were available, therefore Ω_y and Ω_z were calculated from the UCSE angles. For the AMMA campaign, AMS y- and z-gyros were included but show spikes. These spikes are small but all aligned in the same direction (see Figure 57). Integrating these angular velocities would cause large errors for the resulting angles. Therefore UCSE Ω_y and Ω_z were used for AMMA, too.

The quality of the correction was estimated by the correlation, the mean and maximum difference between the UCSE Roll angle and the corrected angle and labeled with a flag[13] between 0 and 9.

Figure 59 shows a short sample of the corrected roll angle in comparison with the UCSE Roll angle and the correction flag for the AMMA flight T3 for a time interval, where the correction is problematic: Small movements are better resolved by the corrected angle, but at the same time it shows some significant drifts. In contrast Figure 58 shows a well corrected interval where the corrected angle follows the small turn more accurately than UCSE roll. Figure 60 summarizes the correction for the flight T3. With exception of the landing and starting period and strong turns a correction (flag > 3) can be obtained nearly all the time.

[13] 0: No correction possible, i.e. interpolated UCSE roll used, 1,2: No correction for parts of the profile, 3 and higher: Correction for the whole profile, 9: best correction (small differences and good correlation to UCSE roll indicating a period with few aircraft movements)

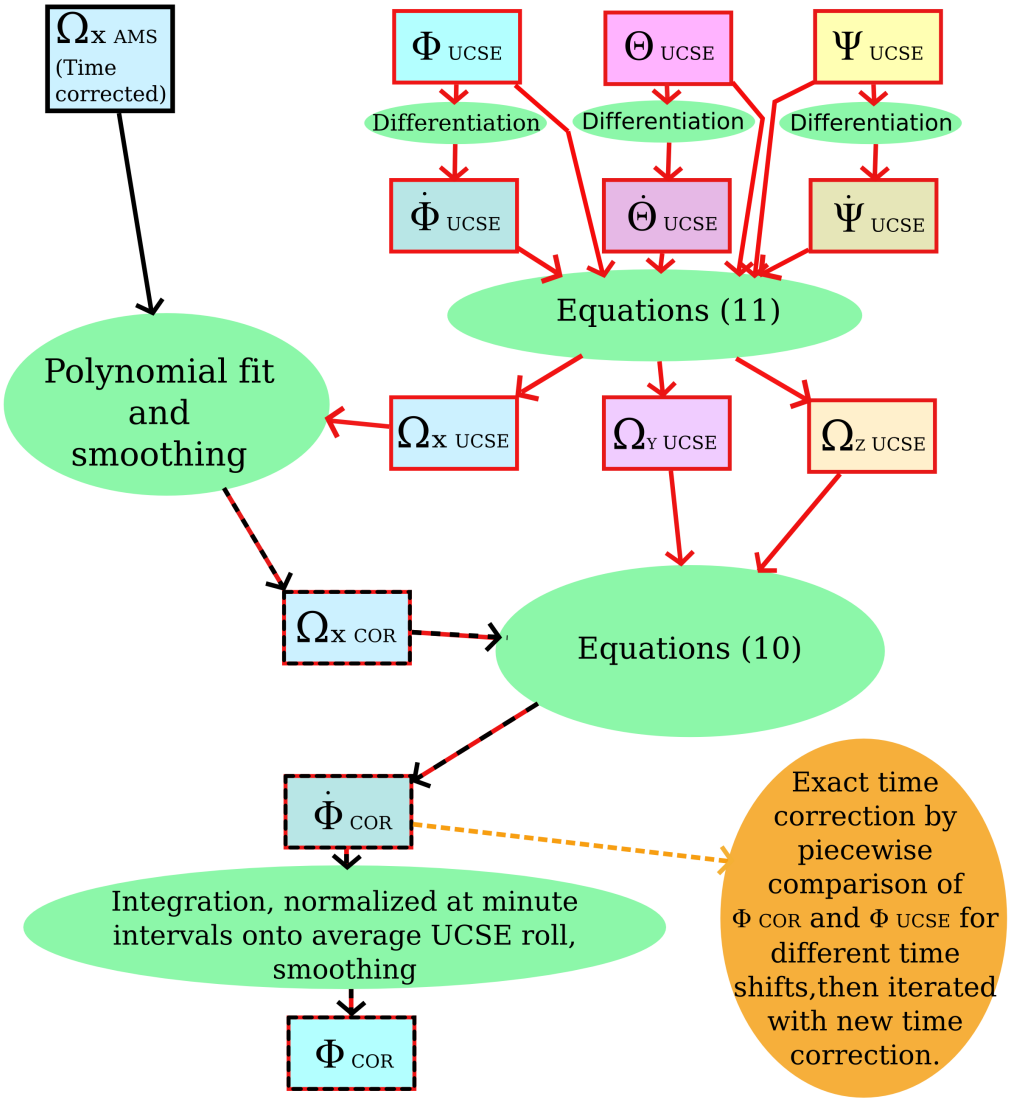

Figure 56: Scheme of the roll angle correction.

By combining the UCSE angles and the AMS x-gyro it was possible to largely improve the measurement of the aircraft movements, especially within each spectrum on time scales shorter than one second. However, it is important to remember that the AMS does not provide information about the absolute pointing, so the accuracy remains in the order $\sigma = 0.05^o$ as the UCSE angles. Therefore further corrections of the pointing using an altitude retrieval were necessary, see Section 3.2.6.

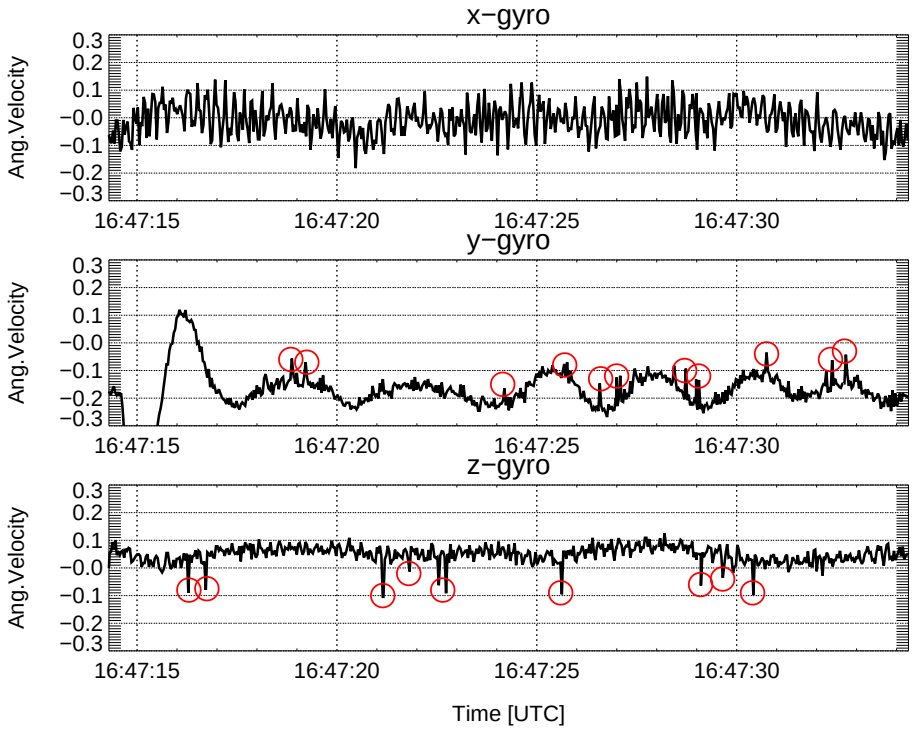

Figure 57: Spikes in gyro Ω_y and Ω_z during the AMMA flight on 2006/08/16.

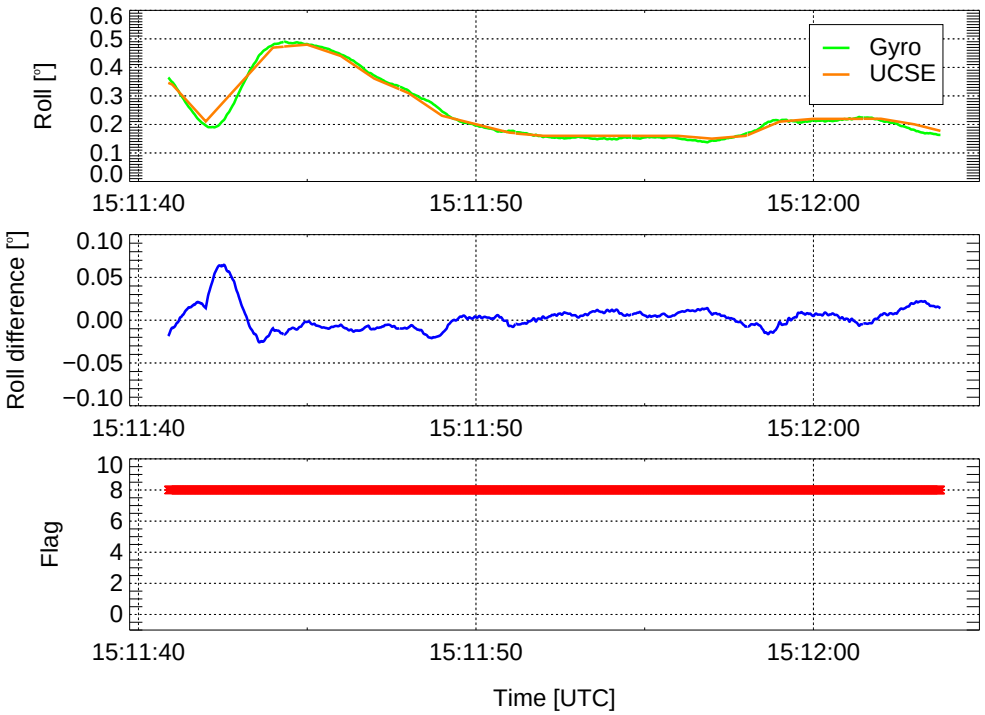

Figure 58: UCSE roll and corrected roll angle for an interval of about 20 seconds with a reliable correction.

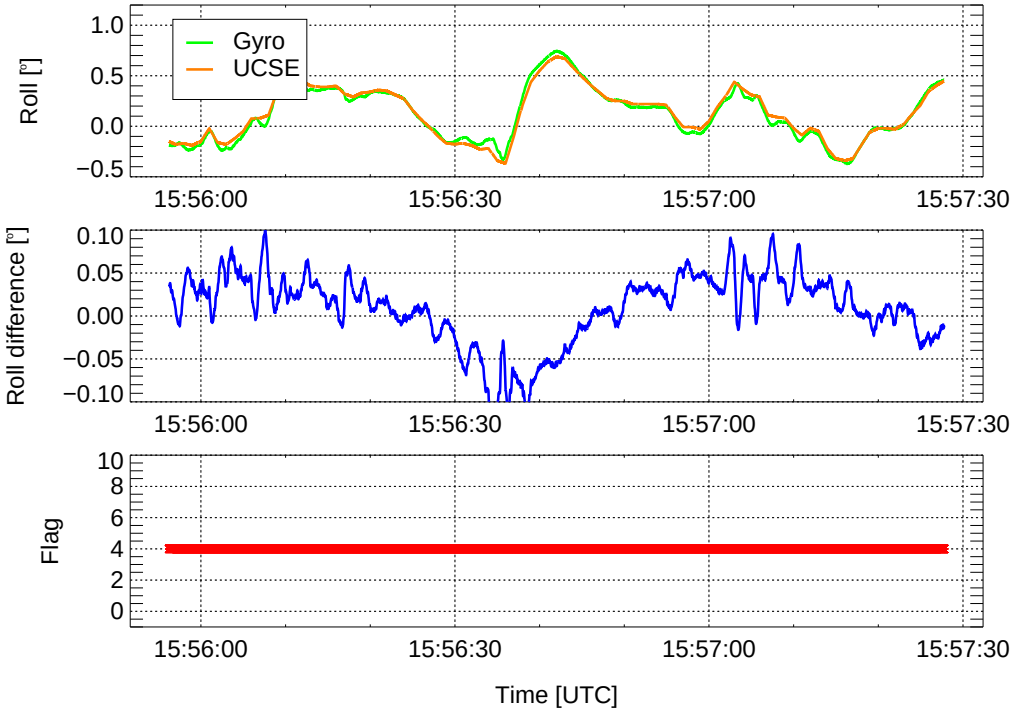

Figure 59: As Figure 58 for an interval of about 1.5 minutes.

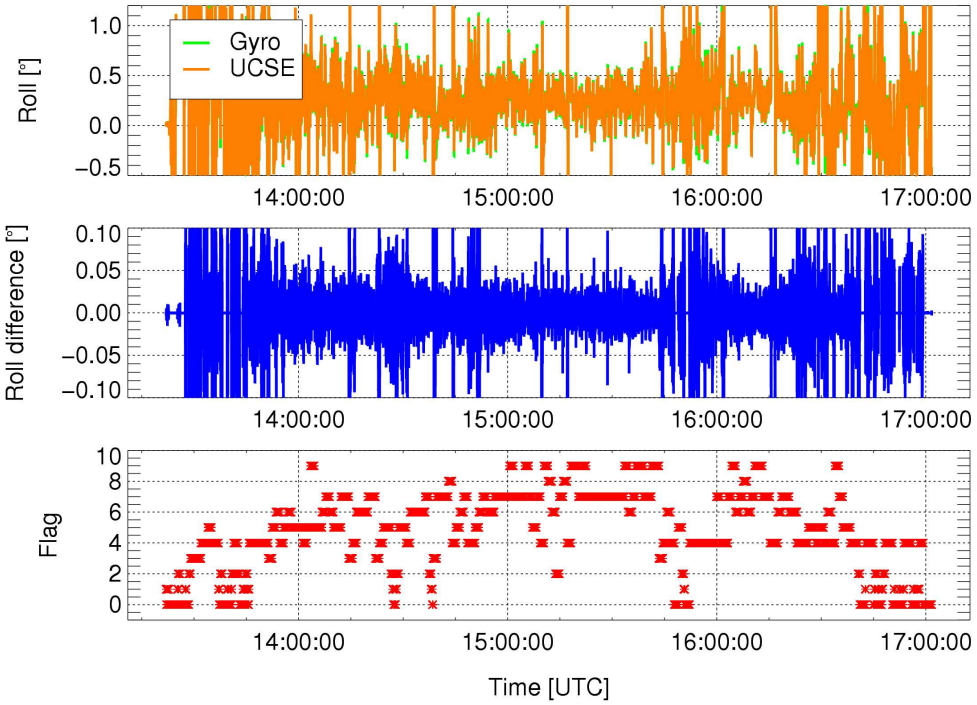

Figure 60: As figure 58 overview of the whole flight AMMA T3.

A.1.8 Offset angles

CRISTA-NF is attached to M55-Geophysica by 4 Enidine wire rope springs (WR16-200-08, Enidine, 2006). The springs are too stiff to affect the pointing, but the alignment of the instrument is not necessarily identically to the one of the aircraft and can change between different flights. Therefore the attitude angles calculated on ground from the AMS acceleration sensors and the inclinometer are compared to the UCSE attitude angles before the take-off, while the aircraft is at rest.

Table 11: Overview of time offsets and offset angles for all AMMA flights.

Flight	Date	Time diff.$[s]$	$\Phi_{\mathrm{INCL}} - \Phi_{\mathrm{UCSE}}[^o]$	$\Theta_A - \Theta_{\mathrm{UCSE}}[^o]$
TF2	2006/07/29	129.6126	-0.00441	-1.80695
T1	2006/07/31	151.7093	-0.03990	-1.75897
T2	2006/08/01	191.6676	0.02726	-1.75177
L1	2006/08/04	379.28066	-0.15938	-0.34046
L2	2006/08/07	877.63831	-0.05726	-0.43662
L3	2006/08/08	1040.8071	-0.13860	-0.45762
L4	2006/08/11	1542.3177	-0.05452	-0.56440
L5	2006/08/13	1855.1380	-0.12371	-0.55736
T3	2006/08/16	2349.0998	-0.15727	-0.63532
T4	2006/08/17	2398.1150	-0.16638	-0.71073

Figure 61 shows the offset of the roll angle for the AMMA test flight. Offset angles for roll and pitch direction for all AMMA flights are given in Table 12, the ones for all other CRISTA-NF flights can be found in Table 12. It is remarkable that the difference between roll offset angles of these intervals for some flights is large compared to the uncertainty of the UCSE and the gyrometer data (see Section A.1.5). In case several of these periods exist, as it is the case for most flights, a 22s mean from the one closest to take-off is chosen.

Generally, the roll and pitch offsets are given corresponding to the aircraft so that they must be corrected by the cosine of each other, transforming them into the coordinate system fixed to the Earth. This correction is less than 1% for roll and pitch angles smaller than 8° and is therefore omitted.

Table 12: Overview of time offsets and offset angles for the Testcampaign (TC5) and SCOUT-O3 flights.

Flight	Date	Time diff.$[s]$	$\Phi_{\mathrm{INCL}} - \Phi_{\mathrm{UCSE}}[^o]$	$\Theta_A - \Theta_{\mathrm{UCSE}}[^o]$
Testcampain				
TC5_1	2005/07/09	16.580	-0.09314	0.66994
TC5_2	2005/07/12	514.947	-0.09696	1.21003
SCOUT-O3				
T1	2005/11/04	580.887	-0.11230	-0.10323
T2	2005/11/04	620.711	-0.09972	0.46947
L2	2005/11/19	-21.308	-0.13170	-0.48292
L3	2005/11/23	183.866	-0.12545	-0.62027
L7	2005/11/30	4317.459	-0.16542	-0.64894
L8	2005/11/30	4367.699	-0.16879	-1.09092
L9$*^1$	2005/12/05	5192.772	-0.03386	-0.69101
T7	2005/12/09	5781.351	-0.16034	-0.89279
T8	2005/12/10	5822.645	-0.12597	-0.77286
T9	2005/12/13	5923.676	-0.15412	-1.31440
T10	2005/12/14	5962.917	-0.26914	-0.90023
T11	2005/12/16	6254.145	-0.16200	-1.31866
T12	2005/12/17	6295.326	-0.14561	-0.98397

$*^1$ CRISTA in M55-Geophysica bay 2

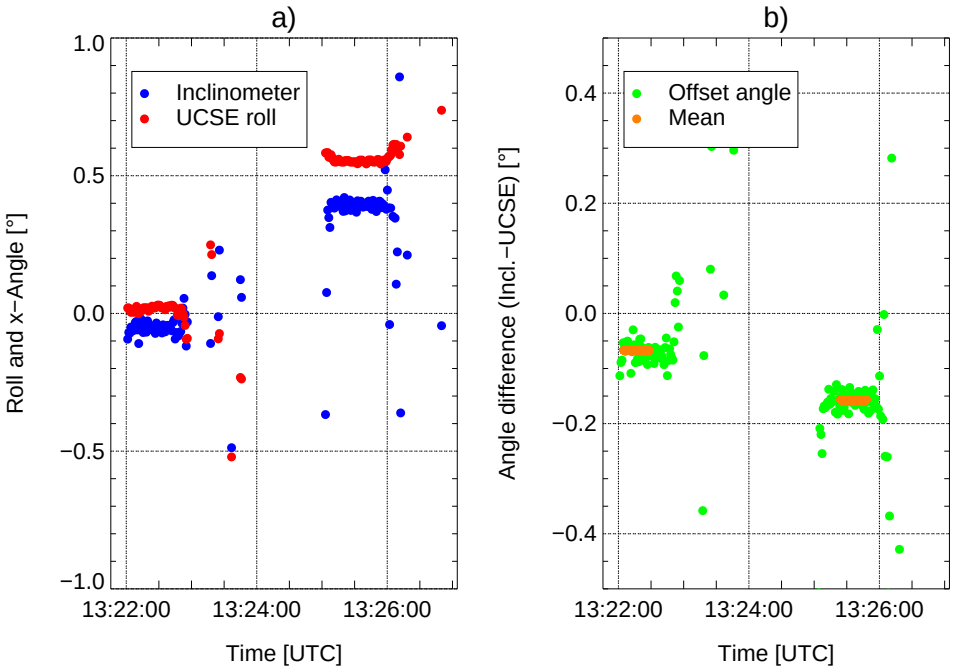

Figure 61: Inclinometer and UCSE roll angle (a) and offset angle (b) for the AMMA flight on 2006/08/16. Note that the scaling of the y-axes is different.

A.1.9 Active attitude system

During the AMMA test flight and some of the local flights the angle of the scanning mirror was used to compensate for the aircraft roll movements by a newly implemented active attitude system. The roll angle change was approximated by the x-gyro angular velocity. In this case the approximation is sufficient because the allowed scanning angles for the mirror were limited to $-0.5 - 4.0°$. The drift of the gyro can be neglected because the mirror position is reset to zero for the start of each new profile after about 70s (P. Knieling, personal communication). However large roll angle changes of the airplane, as they occur during turns (see Figure 54), can not be compensated for.

Figure 62 visualizes the stabilizing effect. The combined angle of airplane roll and the scanning mirror is shown for one profile and one spectrum of the AMMA test flight (blue, with active attitude system) and T1 (red, without active attitude system).

The active attitude system results in a more stable pointing while one spectrum is measured and a more uniform altitude spacing of the spectra in one profile. An example of this can be seen in Figure 63, where the upper Panel shows spectra recorded during one profile of flight TF2 (with active attitude system). The lower Panel shows spectra of a profile of AMMA T3, covering about the same altitude range but without active attitude system Since this system was tested the first time during the AMMA campaign it was used only on the test flight and the local flights 2 and 3. Due to a then unidentified problem not caused by the active attitude system it was deactivated for the remaining AMMA flights, unfortunately.

The higher stability is especially important on timescales of a second to prevent that different parts of one spectrum originate from different altitudes. In addition, a more equal distribution of spectra with altitude in one profile is also advantageous for the trace gas retrieval.

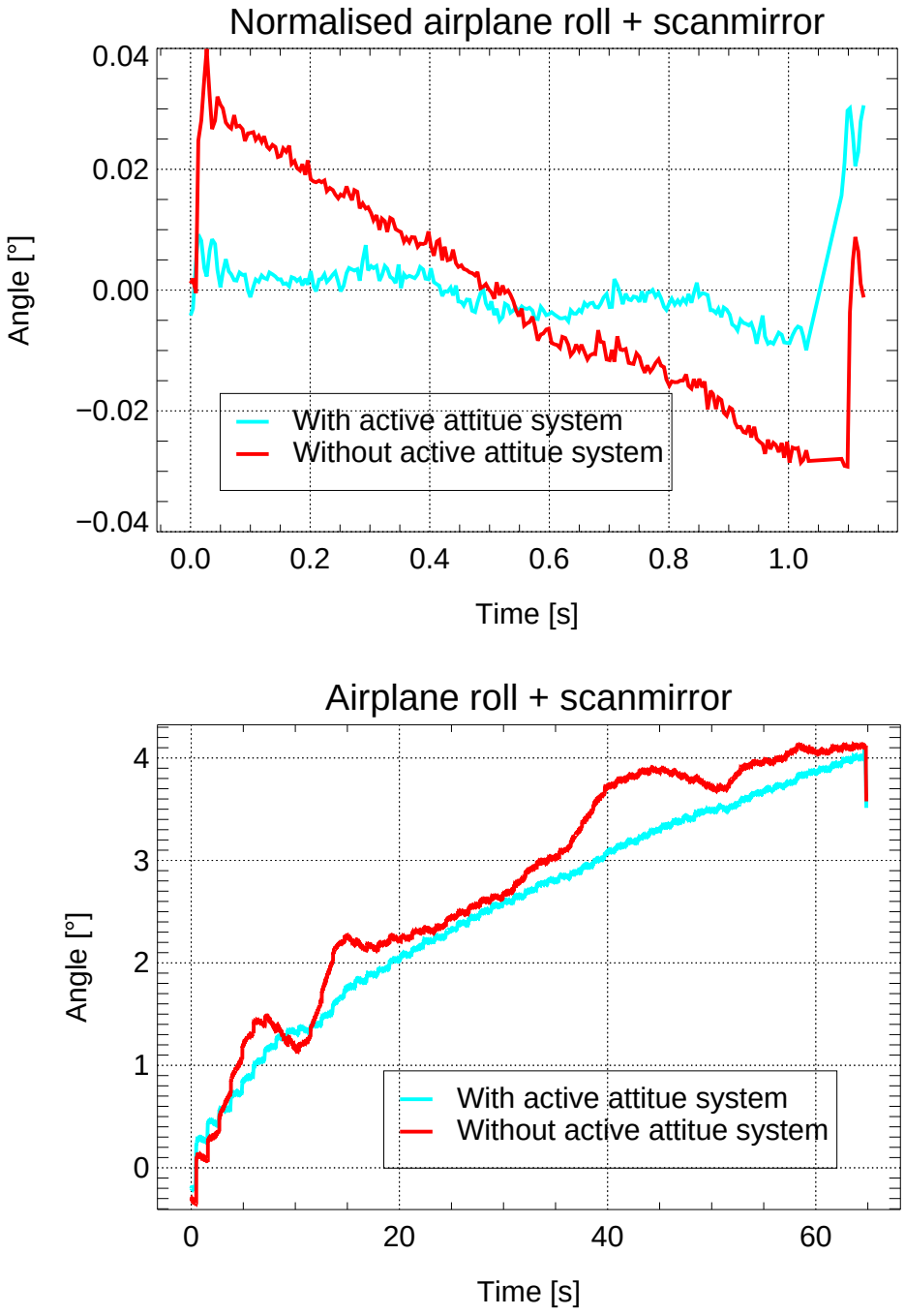

Figure 62: Combined angle out of airplane roll and primary mirror during one spectrum (top) and one profile (bottom) of AMMA test flight (with active attitude system) and transfer 1 (without active attitude system).

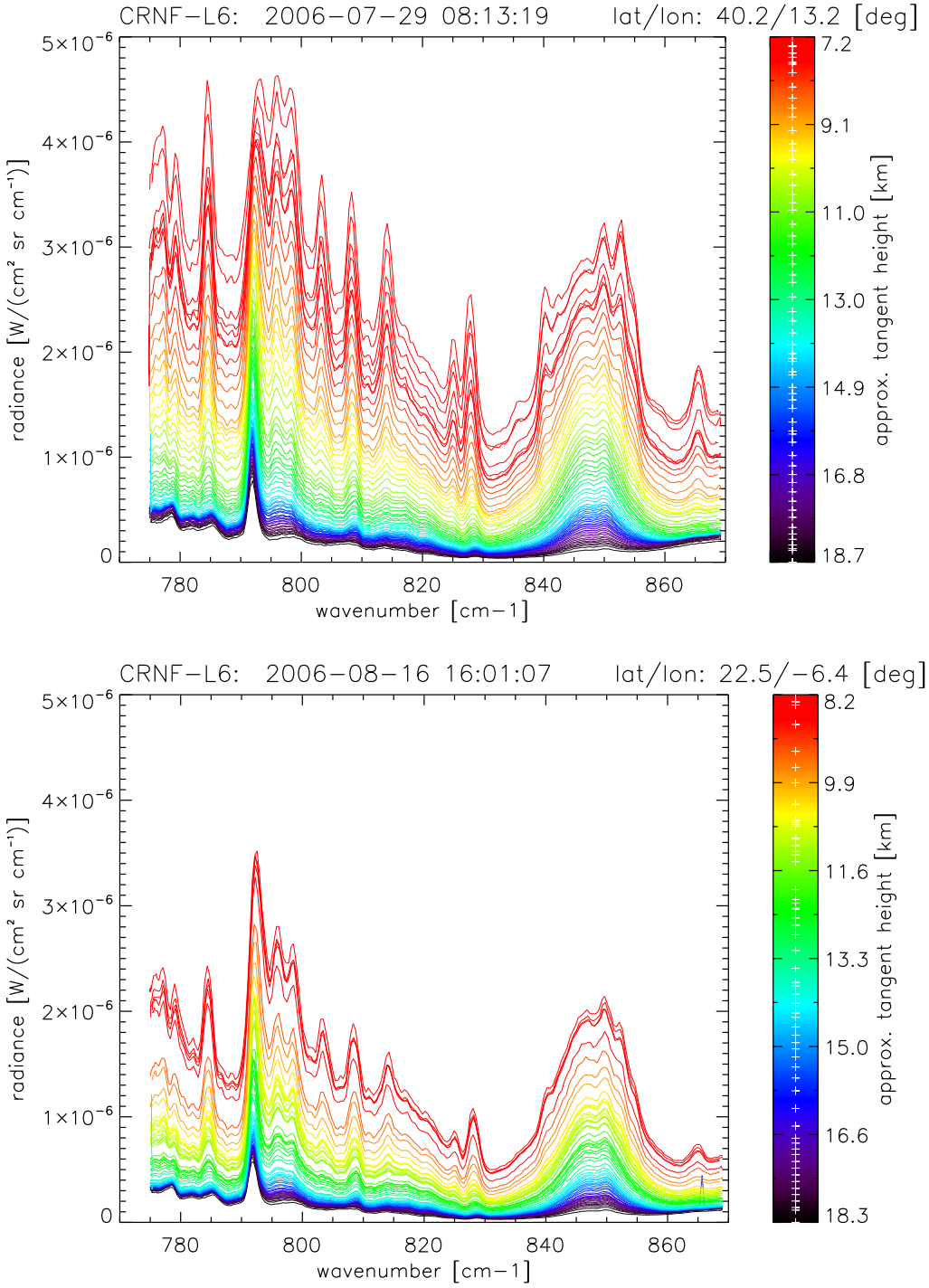

Figure 63: Spectra with active attitude system, profile 125 during AMMA test flight on 2006/07/29 (top) and spectra without active attitude system, profile 94 during AMMA flight T3 on 2006/08/16 (bottom).

B Appendix

B.1 The forward model

Figure 64 shows the difference between JFM and RFM based on a monochromatic approach without correction (Column 1), with H_2O continuum (Column 2), with EGA H_2O continuum (Column 3), with CGA H_2O continuum (Column 4), with a combination of radiance using EGA and CGA and H_2O continuum (Column 5), with a linear regression including EGA, CGA and the H_2O continuum for all L6 ISBs (Rows) used in the main retrieval setup (Setup C).

Implementation of the CGA in JFM

For the Curtis-Godson approximation (CGA) temperature and pressure are weighted by the emitters total column density along the LOS. For each emitter (ig), the Curtis-Godson column density ($u_{CGA,ig}$) is computed as the sum of the column density of this along the LOS:

$$u_{CGA,ig} = \sum_{ip=0}^{np} (u_{ip,ig}), \tag{12}$$

where ip is the index and np is the number of the segments along the LOS and $u_{ip,ig}$ is the column density of one segment of the LOS for one emitter. The Curtis-Godson temperature ($T_{CGA,ig}$) and pressure ($p_{CGA,ig}$) for each emitter and partial path are calculated with

$$T_{CGA,ig} = \frac{\sum_{ip=0}^{np} (u_{ip,ig} * T_{ip})}{u_{CGA,ig}}, \tag{13}$$

and

$$p_{CGA,ig} = \frac{\sum_{ip=0}^{np} (u_{ip,ig} * p_{ip})}{u_{CGA,ig}}, \tag{14}$$

where T_{ip} and p_{ip} are temperature and pressure of one segment (or point) along the LOS, respectively. $T_{CGA,ig}$ and $p_{CGA,ig}$ and $u_{CGA,ig}$ are then used to interpolate the emissivity $\epsilon_{CGA,ig}$ of the LOS from the emissivity look-up tables for each ISB and each emitter. If this is not done for the complete LOS, but for kip and $kip + 1$ LOS points (where $1 <= kip < np - 1$),

the result are two mean emissivities $\epsilon_{CGA,kip,ig}$ and $\epsilon_{CGA,kip+1,ig}$ whose difference is equal to the transmissivity along the reduced LOS multiplied by the emissivity of one additional segment:

$$\begin{aligned}\Delta\epsilon_{CGA,kip,ig} &= \epsilon_{CGA,kip+1,ig} - \epsilon_{CGA,kip,ig} \\ &= (1 - \tau_{CGA,kip+1,ig}) - (1 - \tau_{CGA,kip,ig}) \\ &= \tau_{CGA,kip,ig} - \tau_{CGA,kip+1,ig} \\ &= \tau_{CGA,kip,ig} * (1 - \tau_{CGA,ip+1,ig}) \\ &= \tau_{CGA,kip,ig} * (\epsilon_{CGA,ip+1,ig})\end{aligned} \tag{15}$$

To obtain the emissivity growth for all emitters ($\Delta\epsilon_{CGA,kip}$) the transmissivity for all emitters ($\tau_{CGA,kip}$) is calculated using the continuum approximation:

$$\tau_{CGA,kip} = \prod_{ig=0}^{ng} (\tau_{CGA,kip,ig}), \tag{16}$$

where ng is the number of emitters.

The Curtis-Godson radiance I_{CGA} is hence, similar as for the EGA explained in Hoffmann (2006) calculated iteratively by:

$$\begin{aligned}I_{CGA,kip+1} &= I_{CGA,kip} + D\epsilon_{CGA,kip} * \overline{B}_{ip+1} \\ &= I_{CGA,kip} + \tau_{CGA,kip} * \overline{B}_{ip+1} * (\epsilon_{CGA,ip+1}),\end{aligned} \tag{17}$$

where $\overline{B}_{ip+1}$ is the spectral mean of Planck function at one point of the LOS. In this way, the CGA also assumes a growth of emissivity along the LOS like the EGA, as also mentioned in Marshall et al. (1994). The difference is that the emissivity is interpolated from the tables for the whole LOS or intervals of the LOS. These intervals are treated like a homogeneous cell, using the Curtis-Godson mean of temperature and pressure (see Equations 13 and 14) over all LOS segments within them.

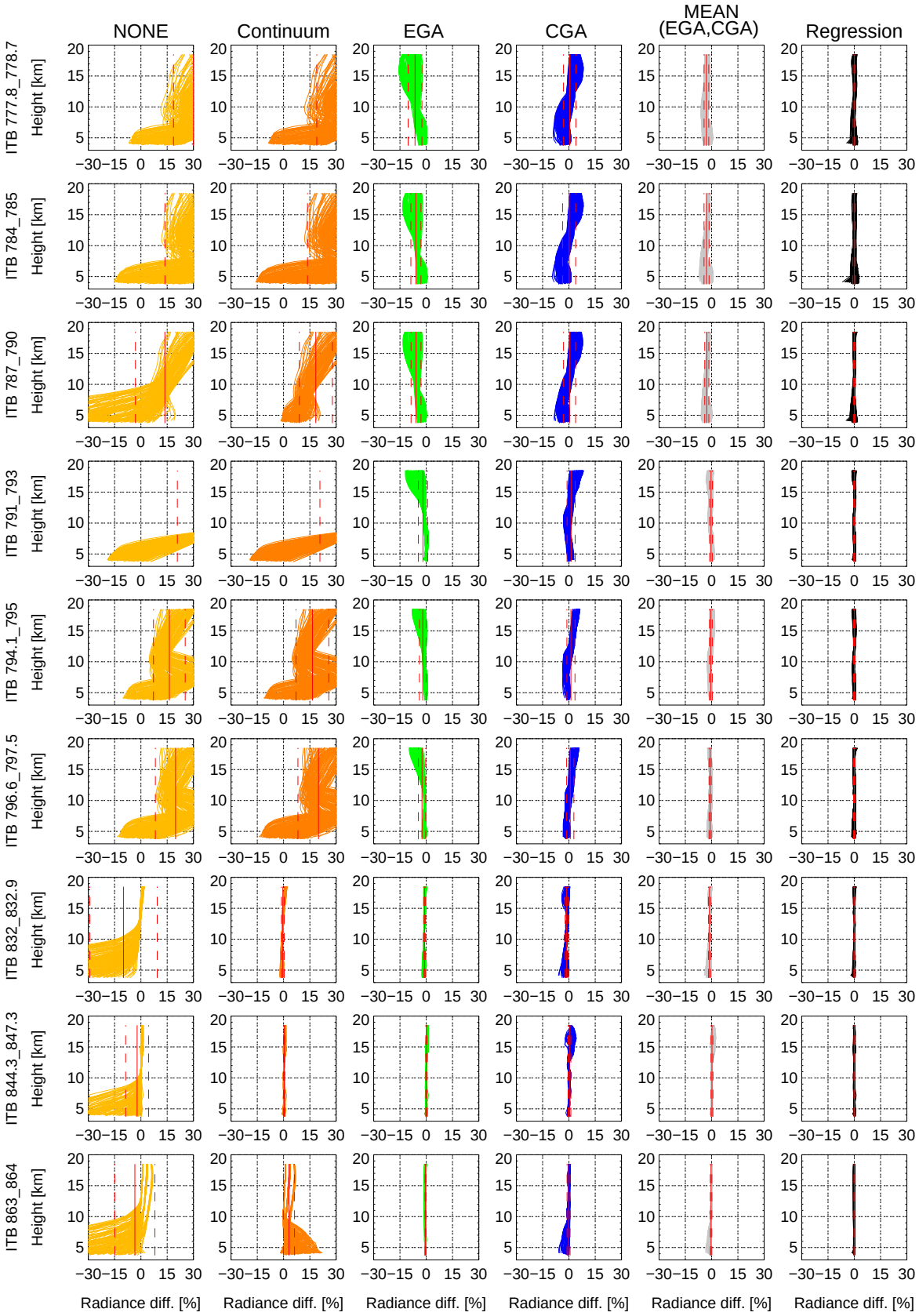

Figure 64: Percentage radiance difference between JFM and RFM calculation for 163 example atmospheres for all ISBs. Red lines: Mean, red dashed lines: Standard deviation.

For the regression, mean Curtis-Godson temperature (T_{CGA}) and pressure (p_{CGA}) weighted with the column density (u_{CGA}) of all emitters used for the regression are calculated:

$$u_{CGA} = \sum_{ig=0}^{ng} (u_{CGA,ig}),$$

$$T_{CGA} = \frac{\sum_{ig=0}^{ng} (u_{CGA,ig} * T_{CGA,ig})}{u_{CGA}}, \tag{18}$$

$$p_{CGA} = \frac{\sum_{ig=0}^{ng} (u_{CGA,ig} * p_{CGA,ig})}{u_{CGA}},$$

where ng is the number of emitters used for the regression.

B.2 JURASSIC

Percentage error components of the retrieval result for AMMA T3, profile 94 for H_2O , aerosol, O_3 , HNO_3 , CCl_4 and PAN. Corresponding absolute errors are shown in Section 3.2.5, Figures 17 and 18.

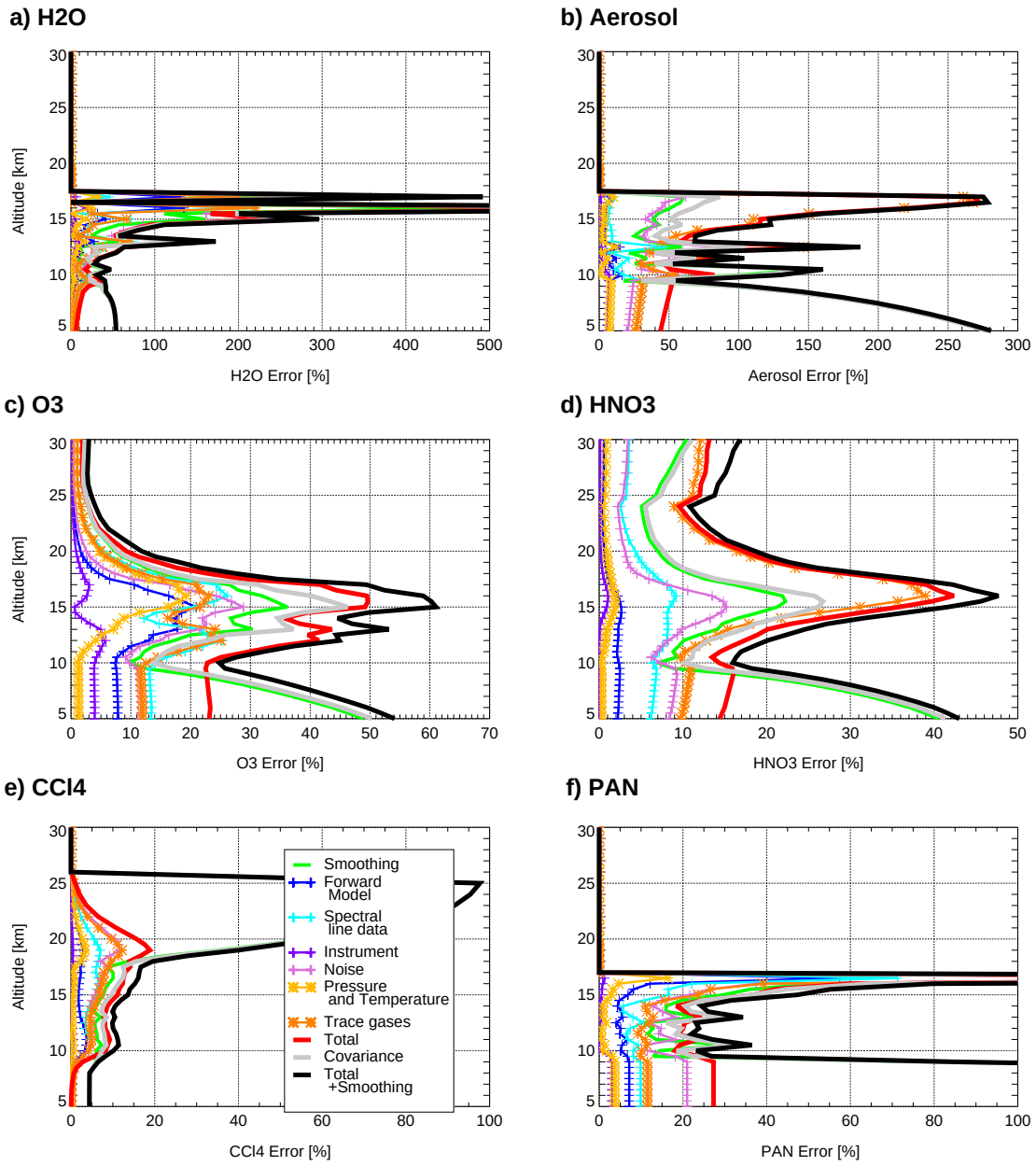

Figure 65: Estimated retrieval error components as in Figure 17 and 18, Section 3.2.5 but in percent. For a) H_2O , b) aerosol, c) O_3 , d) HNO_3 , e) CCl_4 and f) PAN retrieval.

C Appendix

C.1 AMMA transfer and fifth local flight

The following Figures show the results of the CRISTA-NF retrieval, comparisons to in situ data and CLaMS model results for the AMMA flights T1, T2, L5, T3 and T4.

C.1.1 AMMA T1

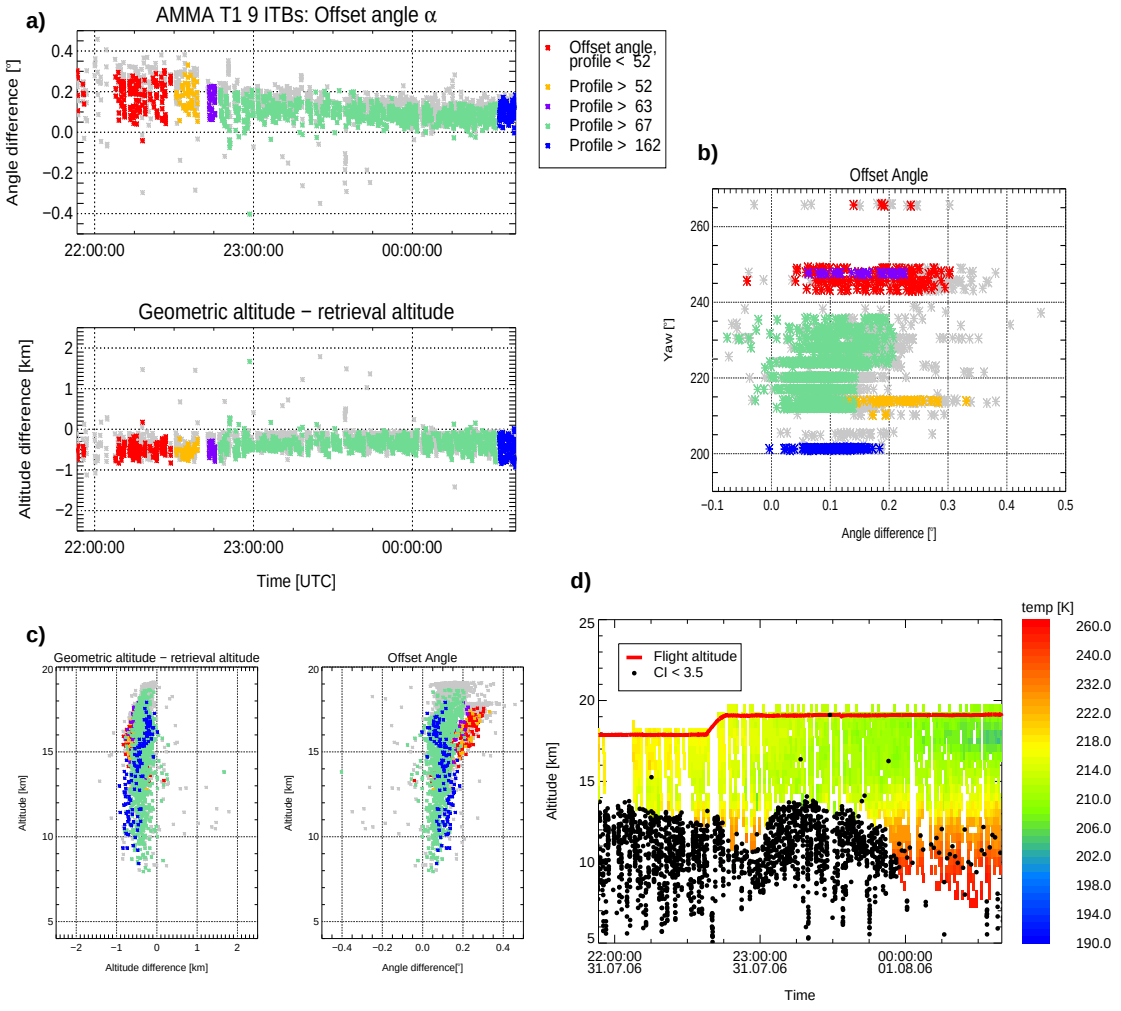

Figure 66: CRISTA-NF altitude and temperature retrieval results: a) Angle difference and height difference against time, b) angle difference against airplane yaw, c) angle difference and height difference against tangent point height. Grey stars: all values. Colored stars: $\chi^2 < 2$, measurement contend$> 98\%$ d) Result of temperature retrieval. Black dots: Cloud index < 3.5, corrected altitudes. Note nonlinear color scales.

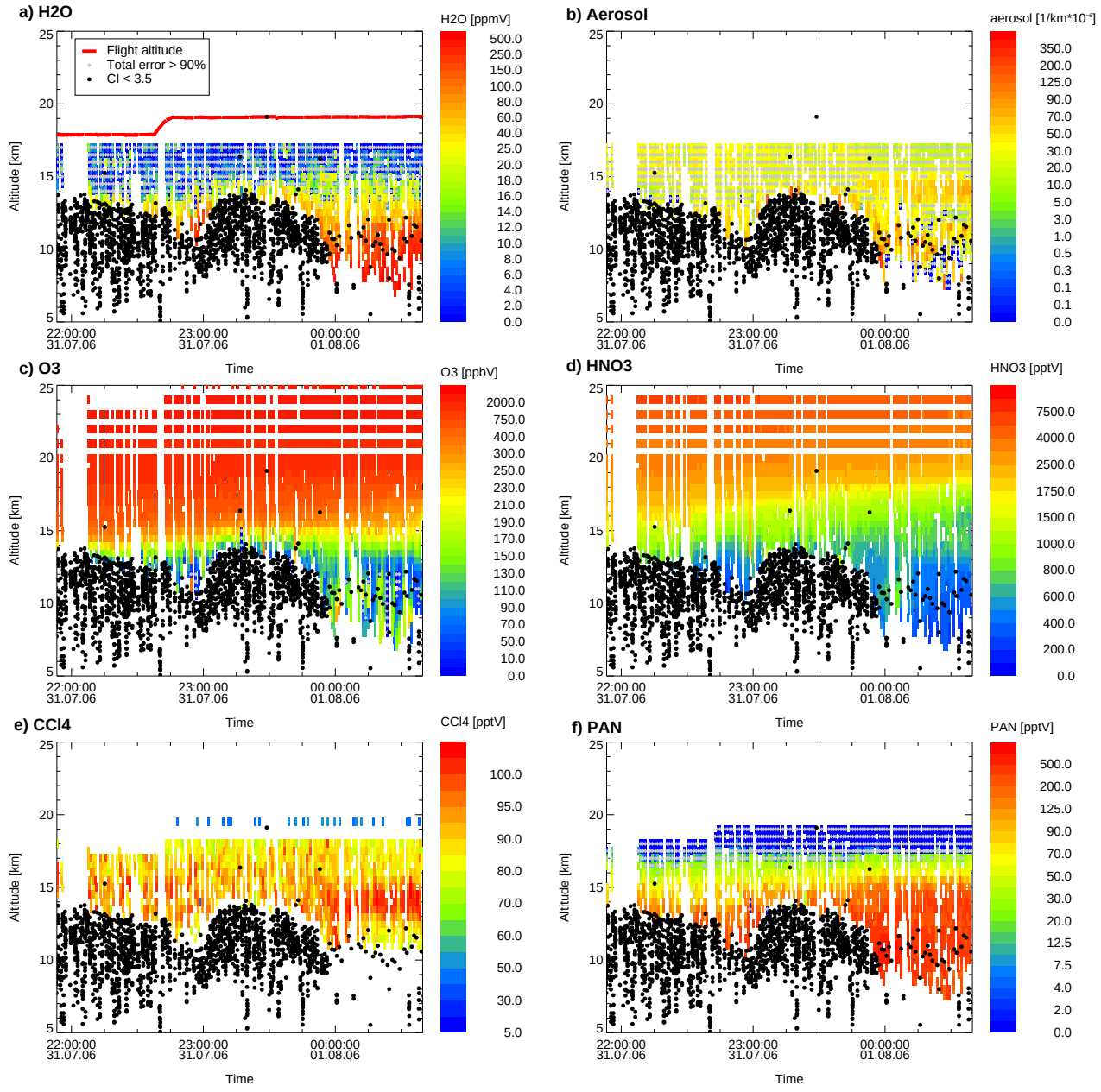

Figure 67: CRISTA-NF Retrieval results: a) H_2O , b) Aerosol, c) O_3 , d) HNO_3 , e) CCl_4 , f) PAN. Black dots: Cloud index < 3.5, corrected altitudes, grey diamonds: Total error (without smoothing) $> 90\%$. Note nonlinear color scales.

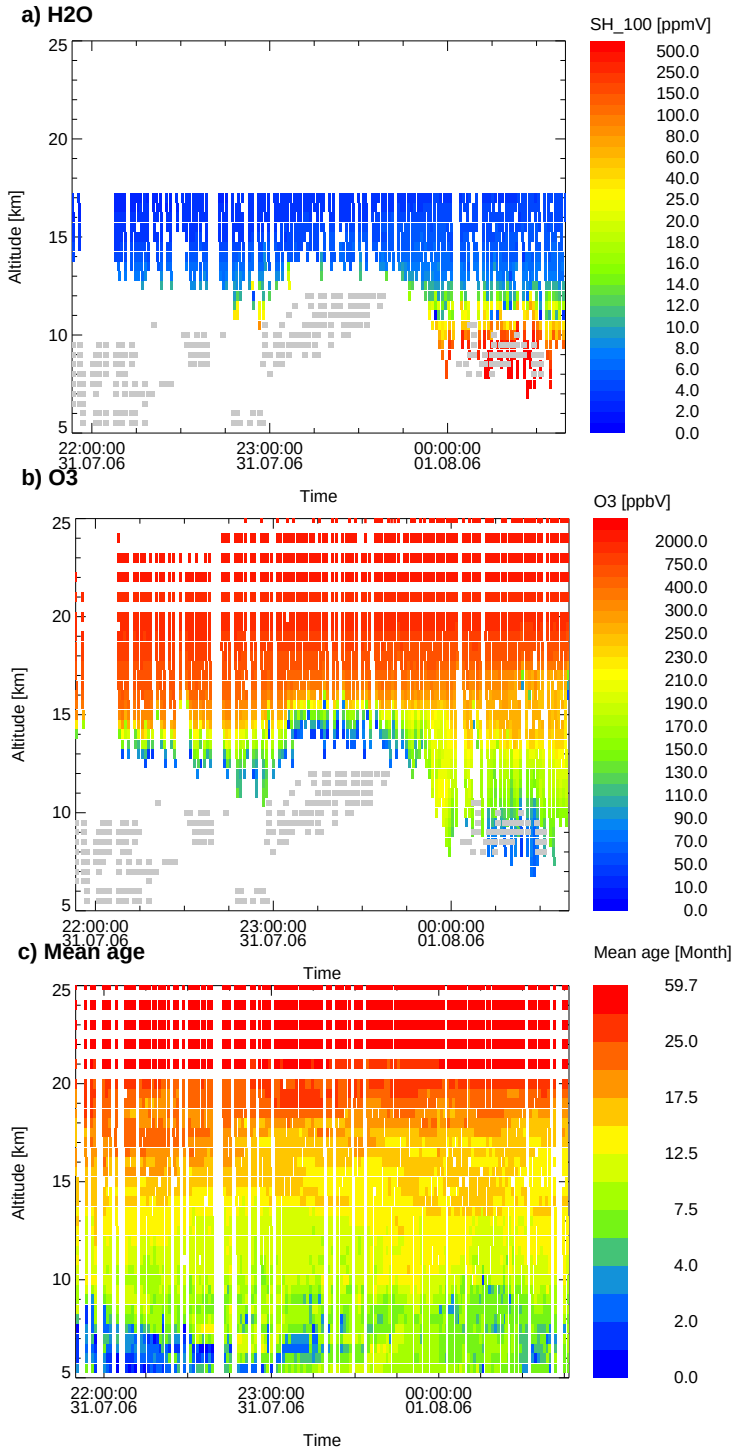

Figure 68: CLaMS results for AMMA T1: a) H_2O calculated from specific humidity with saturation at 100%, b) O_3 , c) Age of air. All interpolated onto CRISTA-NF grid. H_2O and O_3 Convoluted with CRISTA-NF AVK for corresponding variable and filtered as data in 67. Light grey squares: Ice clouds (IWC > 0). Note nonlinear color scales.

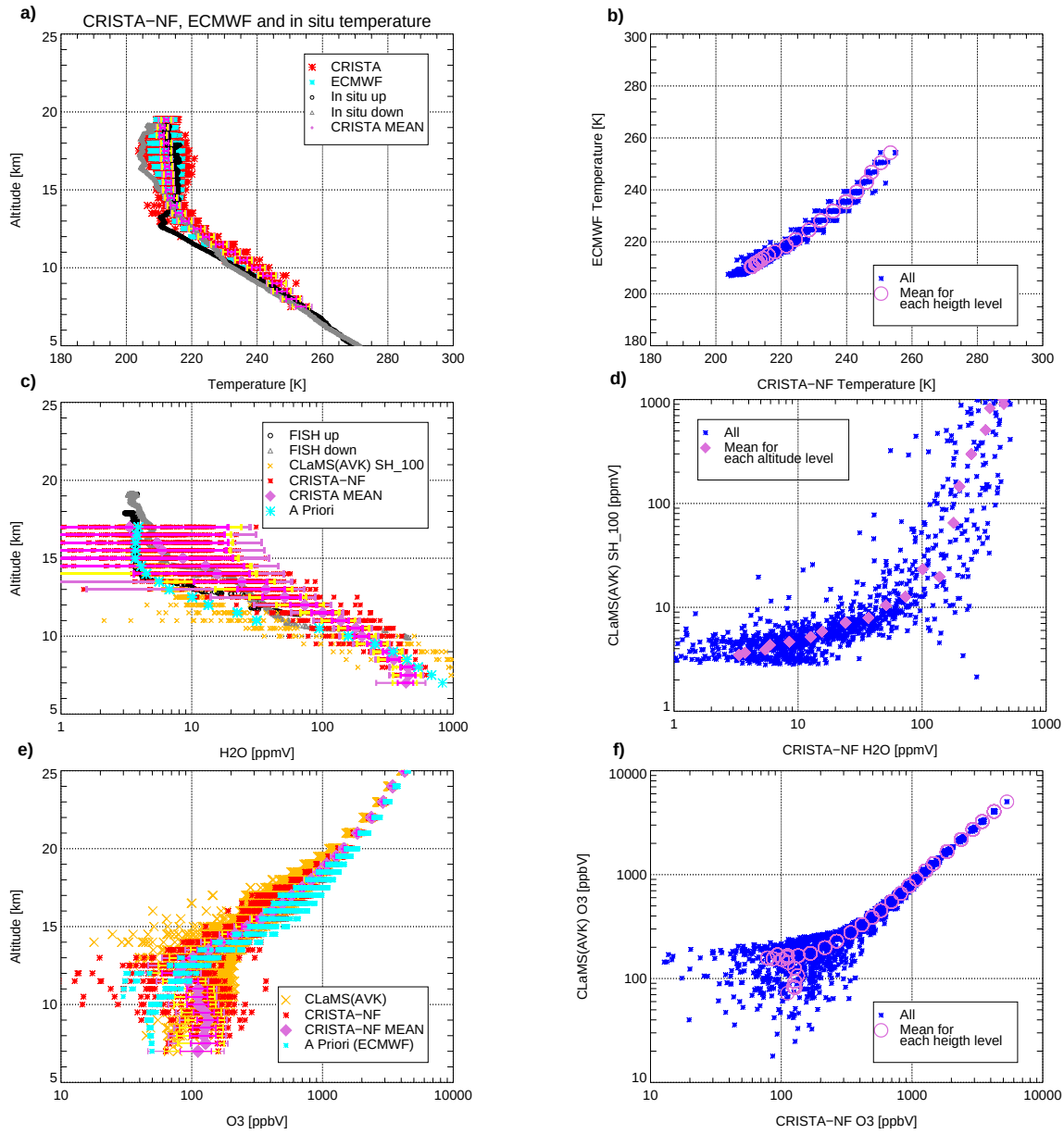

Figure 69: CRISTA-NF Retrieval results compared to in situ data, CLaMs and ECMWF analysis data: a) Temperature profile, b) temperature scatter plot, c)H_2O profile, d) H_2O scatter plot, e) O_3 profile, f) O_3 scatter plot.

C.1.2 AMMA T2

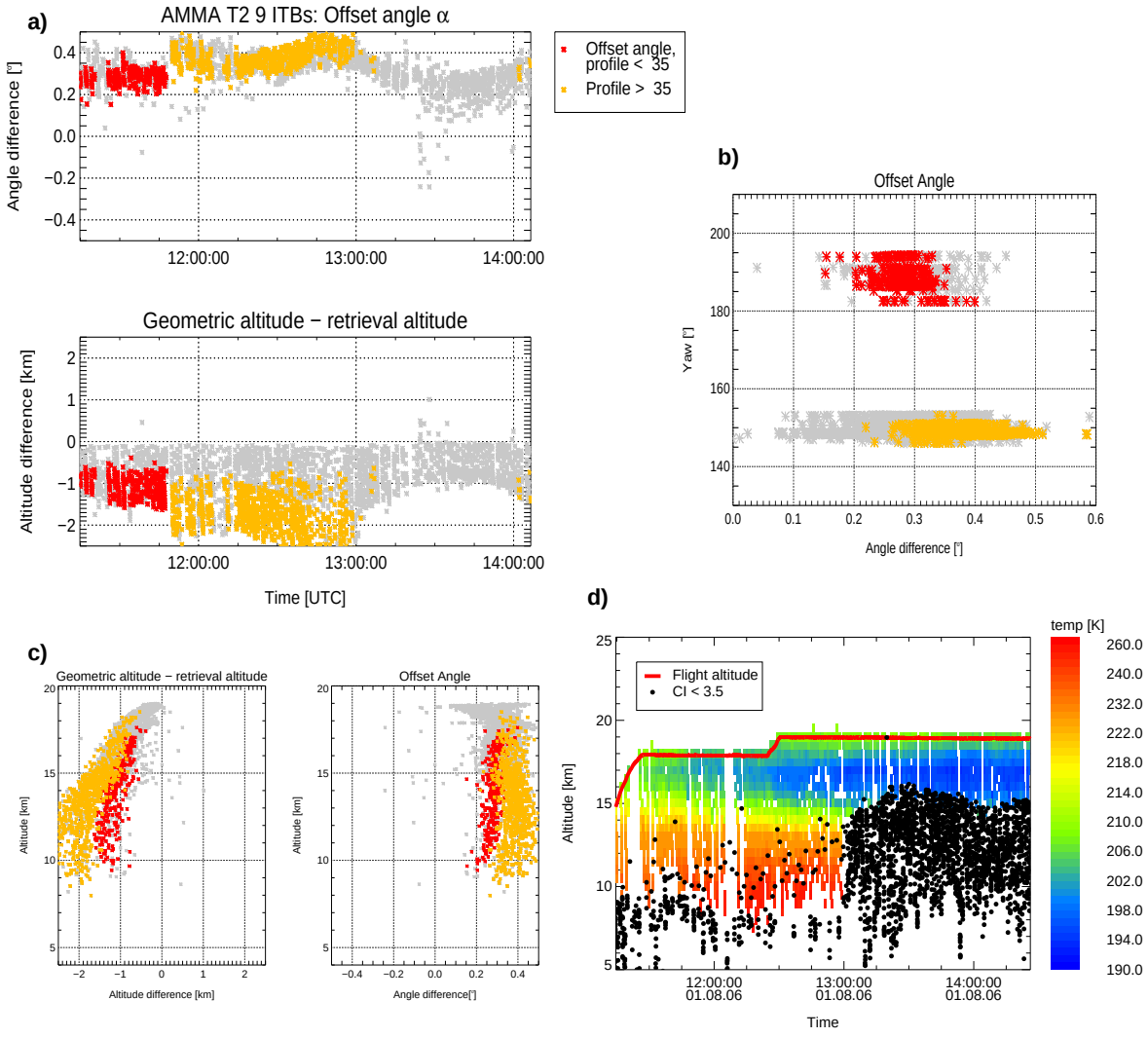

Figure 70: CRISTA-NF altitude and temperature retrieval results: a) Angle difference and height difference against time, b) angle difference against airplane yaw, c) angle difference and height difference against tangent point height. Grey stars: all values. Colored stars: $\chi^2 < 2$, measurement contend> 98% d) Result of temperature retrieval. Black dots: Cloud index < 3.5, corrected altitudes. Note nonlinear color scales.

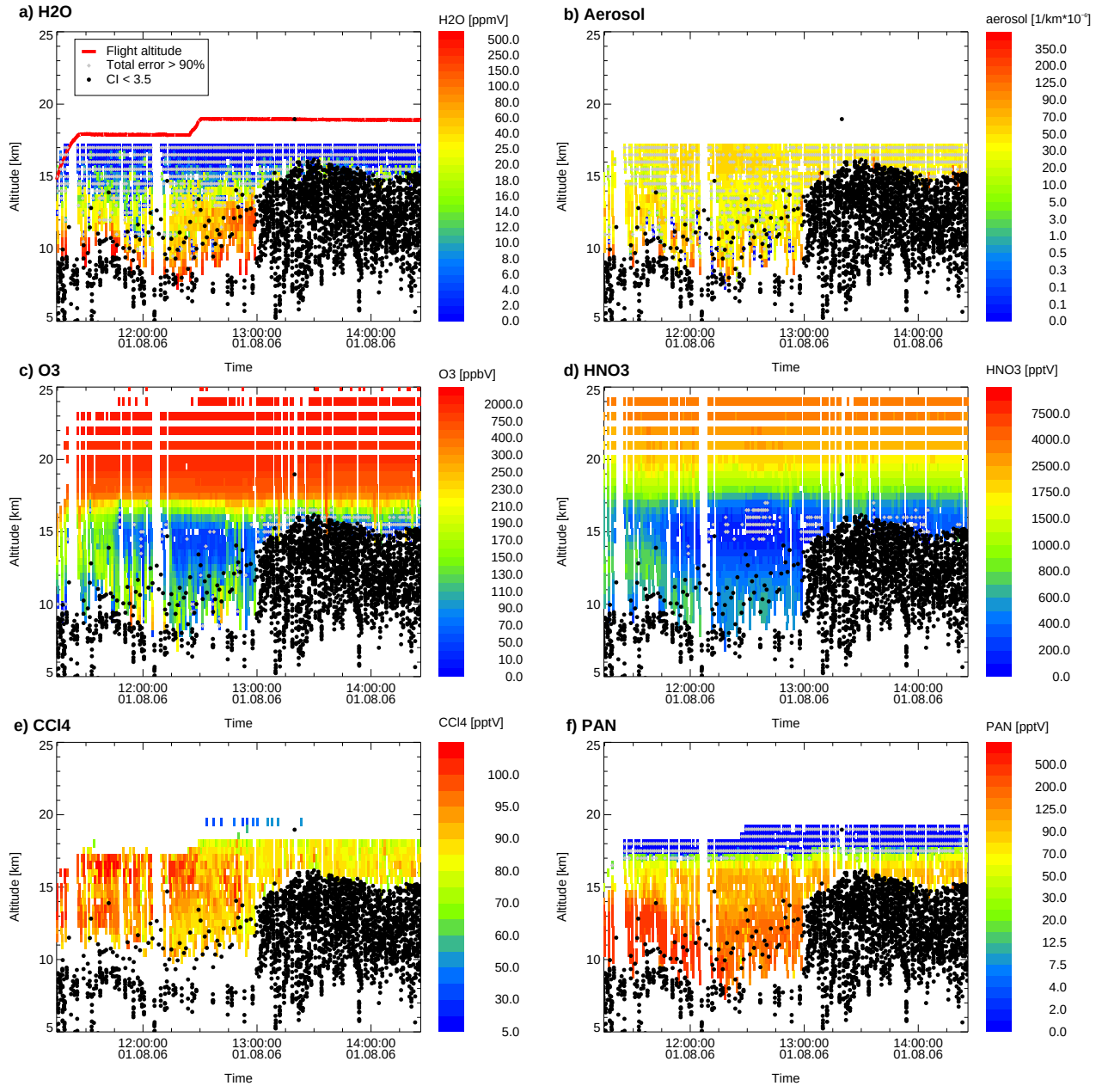

Figure 71: CRISTA-NF Retrieval results: a) H_2O , b) Aerosol, c) O_3 , d) HNO_3 , e) CCl_4 , f) PAN. Black dots: Cloud index < 3.5, corrected altitudes, grey diamonds: Total error (without smoothing) $> 90\%$. Note nonlinear color scales.

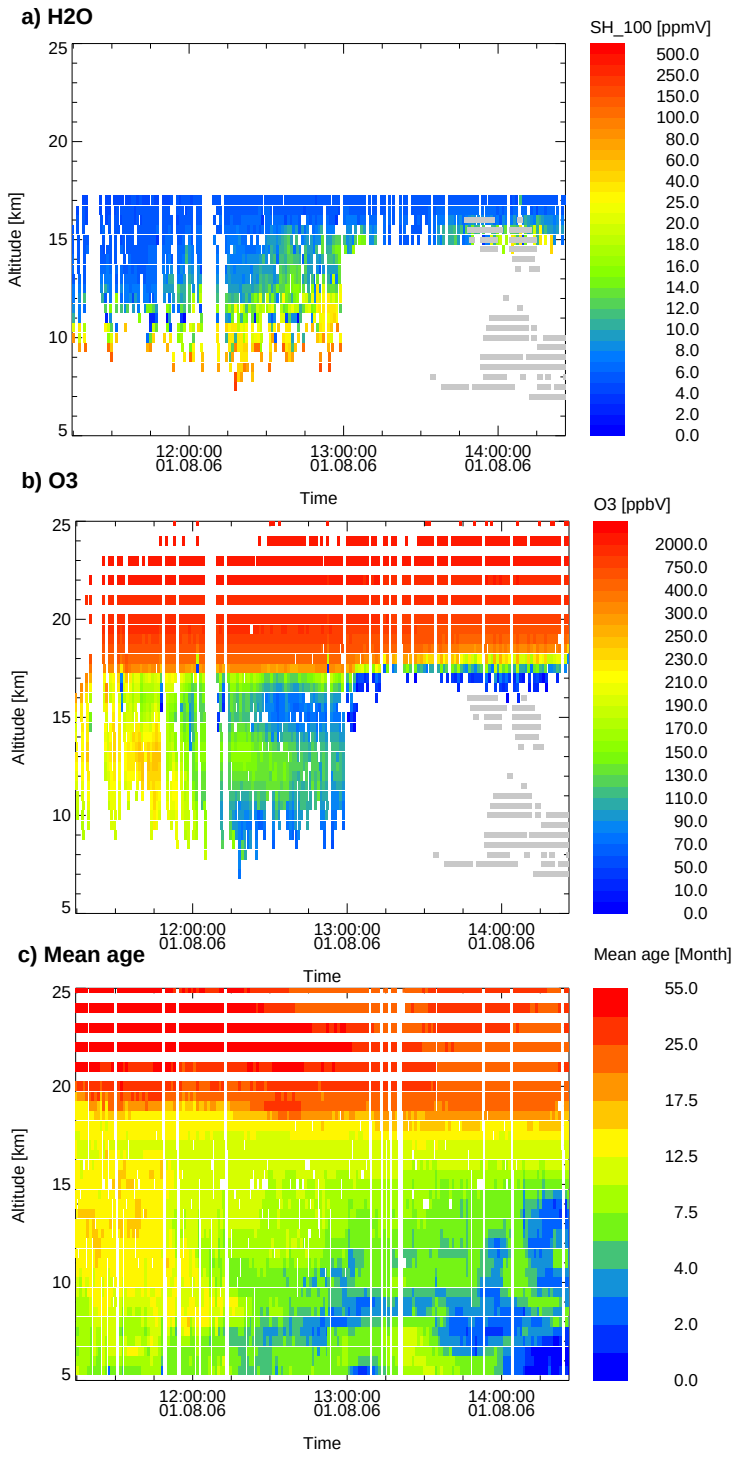

Figure 72: As Figure 68 but for CLaMs results for AMMA T2. Note nonlinear color scales.

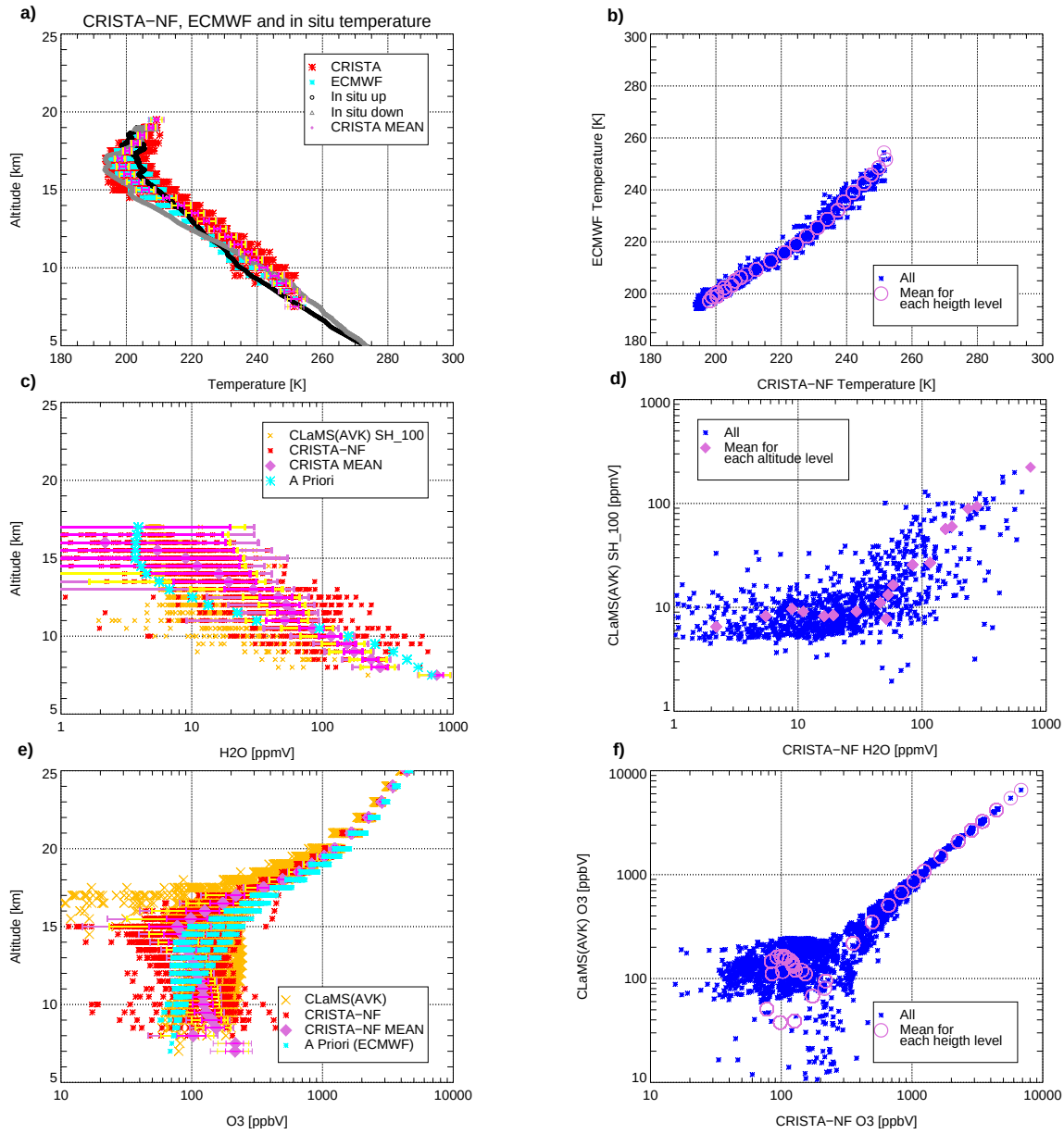

Figure 73: CRISTA-NF Retrieval results compared to in situ data, CLaMs and ECMWF analysis data: a) Temperature profile, b) temperature scatter plot, c)H_2O profile, d) H_2O scatter plot, e) O_3 profile, f) O_3 scatter plot.

C.1.3 AMMA L5

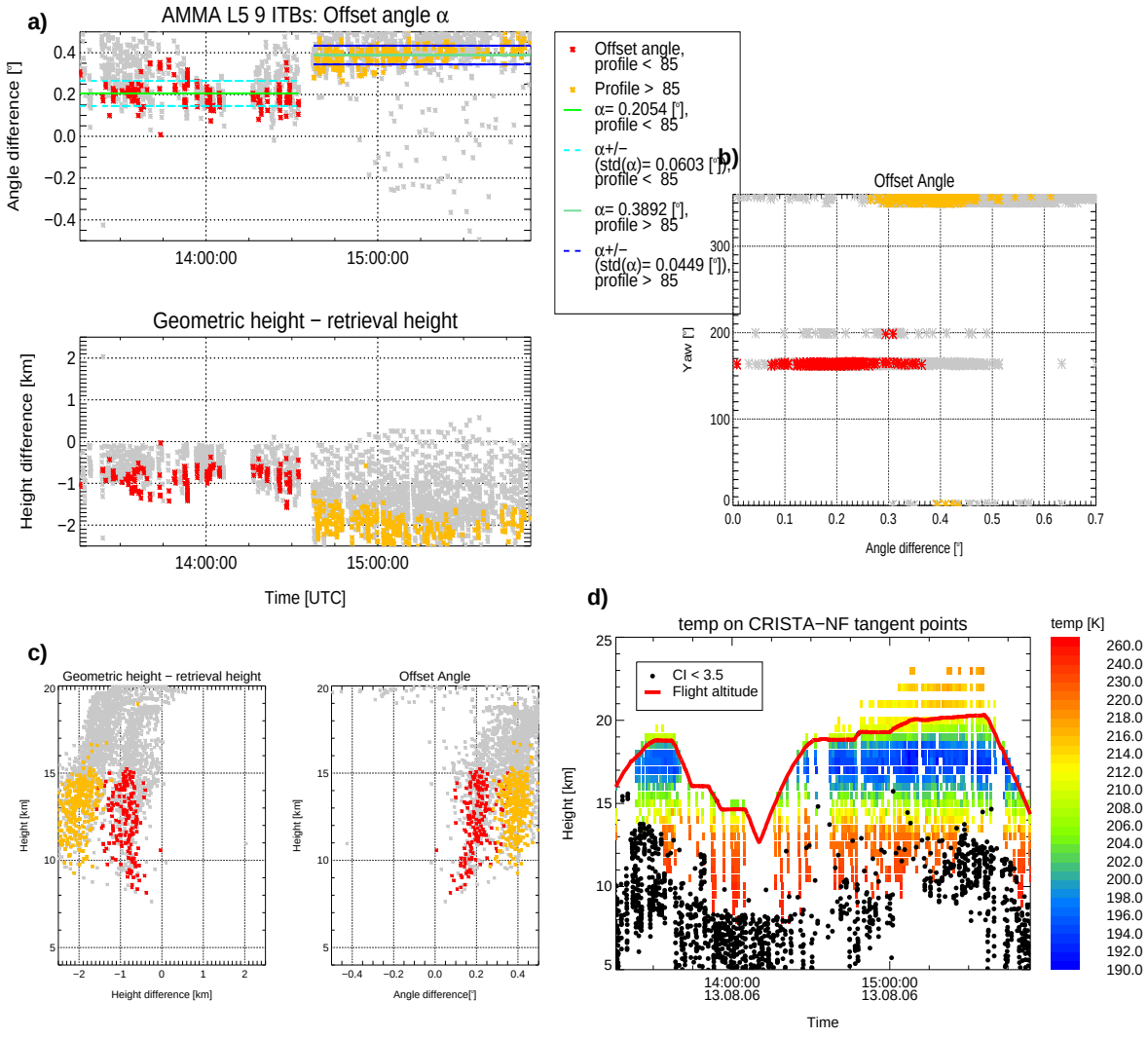

Figure 74: CRISTA-NF altitude and temperature retrieval results: a) Angle difference and height difference against time, b) angle difference against airplane yaw, c) angle difference and height difference against tangent point height. Grey stars: all values. Colored stars: $\chi^2 < 2$, measurement contend> 98% d) Result of temperature retrieval. Black dots: Cloud index < 3.5, corrected altitudes. Note nonlinear color scales.

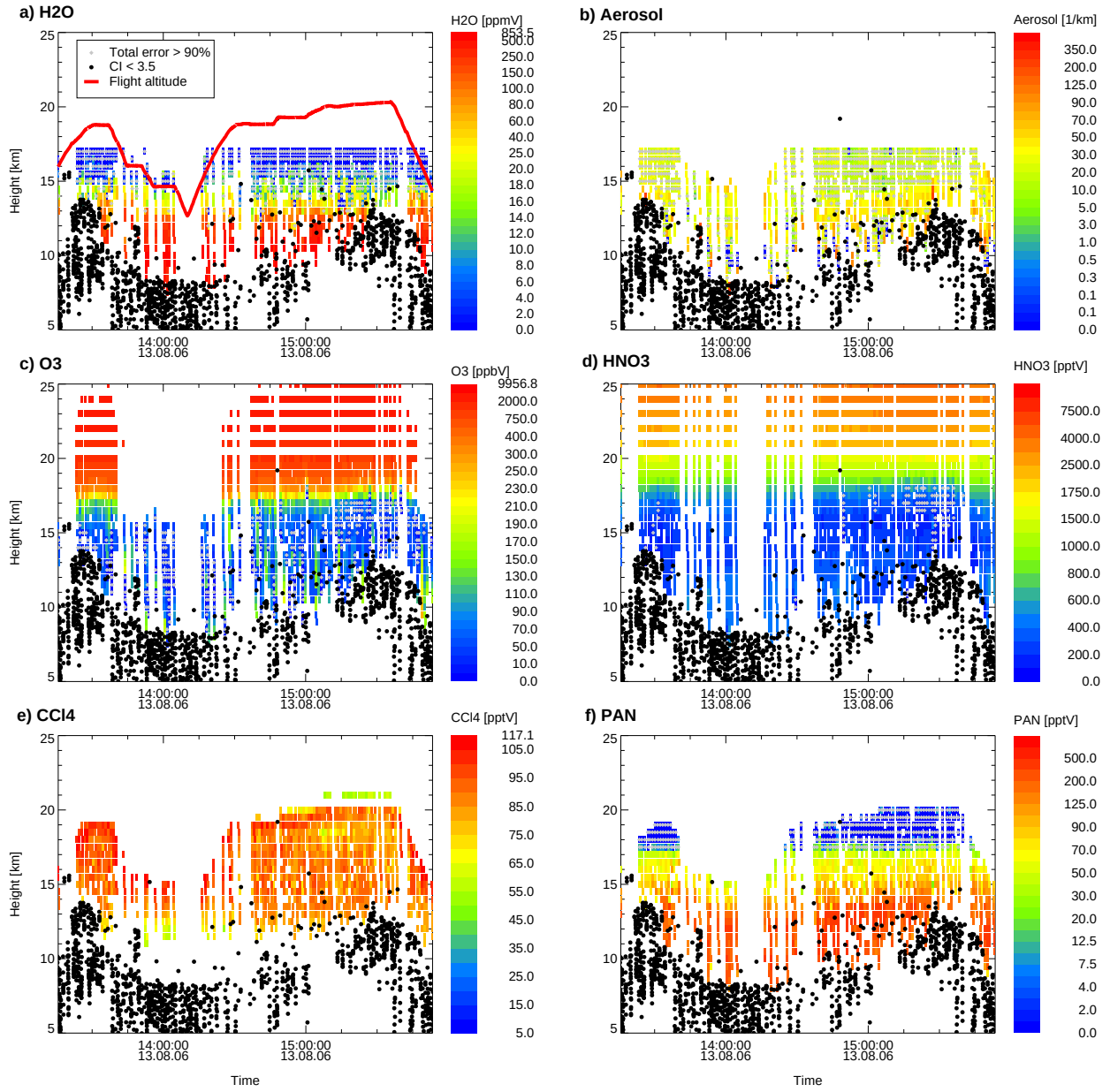

Figure 75: CRISTA-NF Retrieval results: a) H_2O , b) Aerosol, c) O_3 , d) HNO_3 , e) CCl_4 , f) PAN. Black dots: Cloud index < 3.5, corrected altitudes, grey diamonds: Total error (without smoothing) $> 90\%$. Note nonlinear color scales.

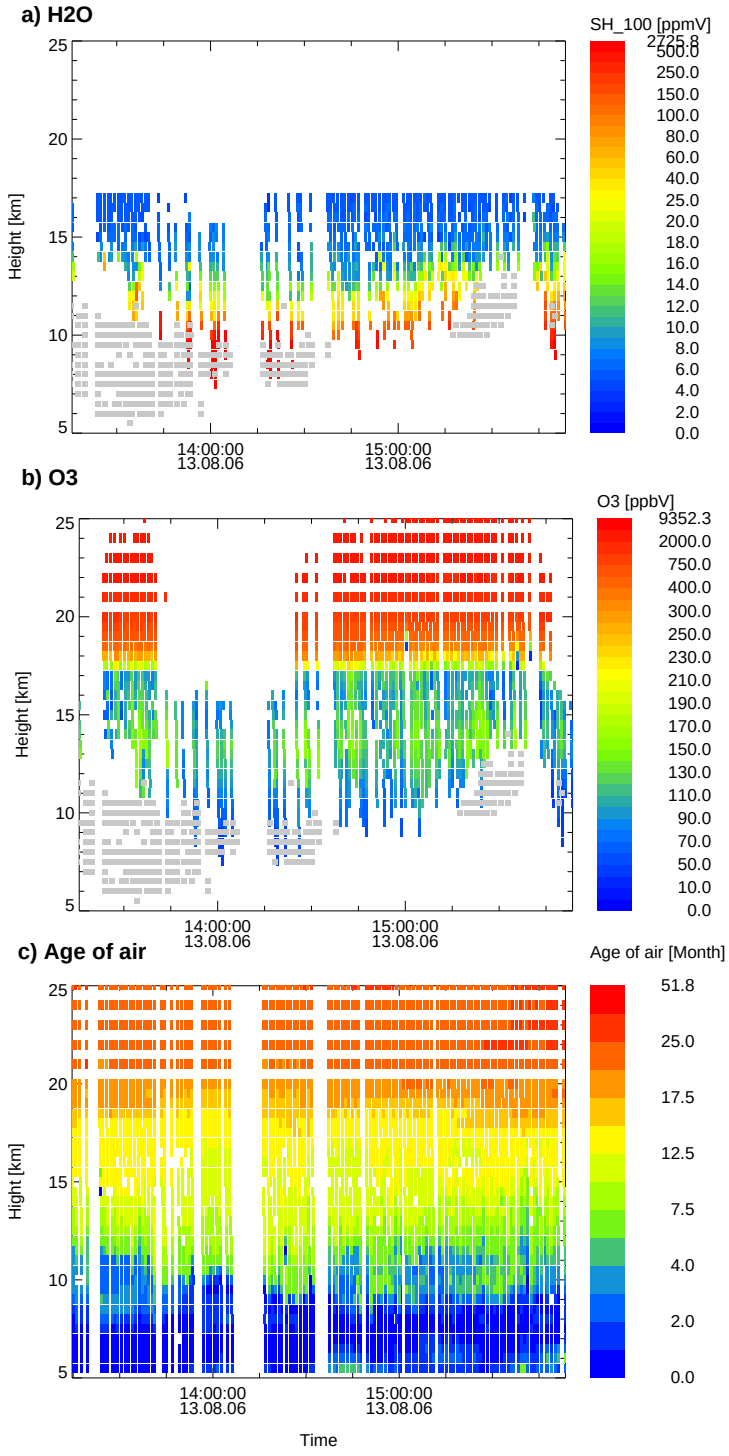

Figure 76: As Figure 68 but for CLaMs results for AMMA L5. Note nonlinear color scales.

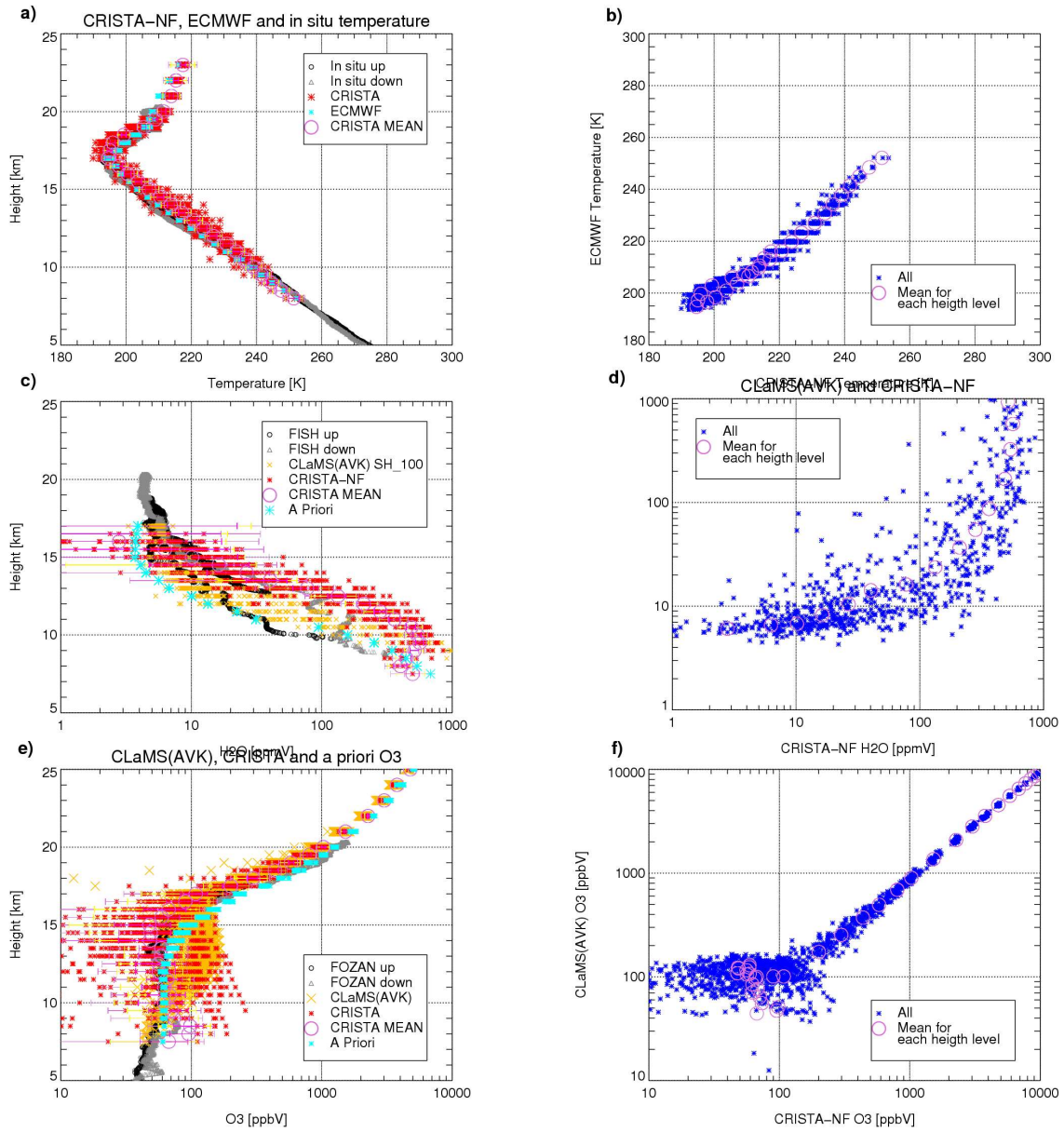

Figure 77: CRISTA-NF Retrieval results compared to in situ data, CLaMs and ECMWF analysis data: a) Temperature profile, b) temperature scatter plot, c)H_2O profile, d) H_2O scatter plot, e) O_3 profile, f) O_3 scatter plot.

C.1.4 AMMA T3

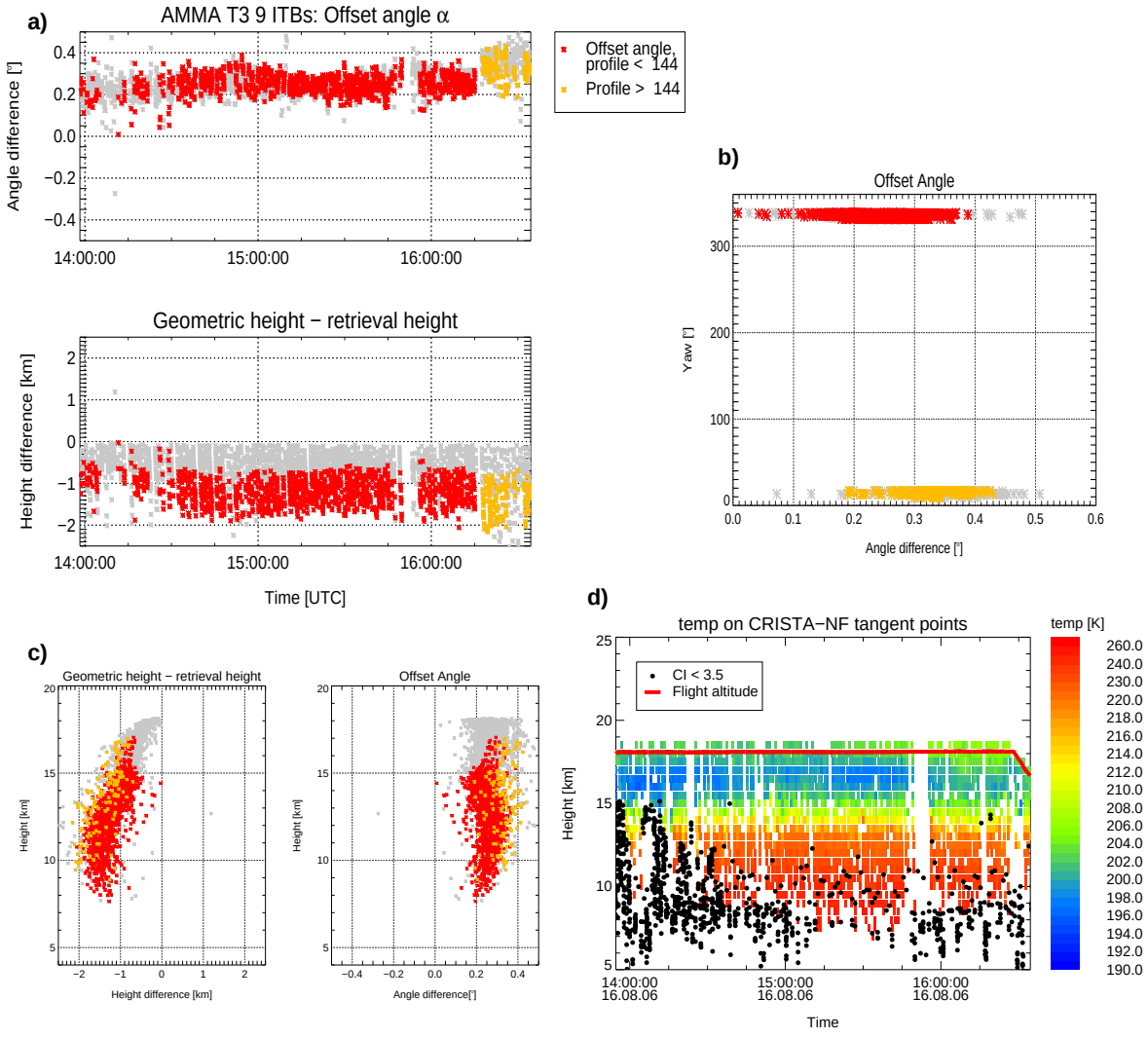

Figure 78: CRISTA-NF altitude and temperature retrieval results: a) Angle difference and height difference against time, b) angle difference against airplane yaw, c) angle difference and height difference against tangent point height. Grey stars: all values. Colored stars: $\chi^2 < 2$, measurement contend$>$ 98% d) Result of temperature retrieval. Black dots: Cloud index < 3.5, corrected altitudes. Note nonlinear color scales.

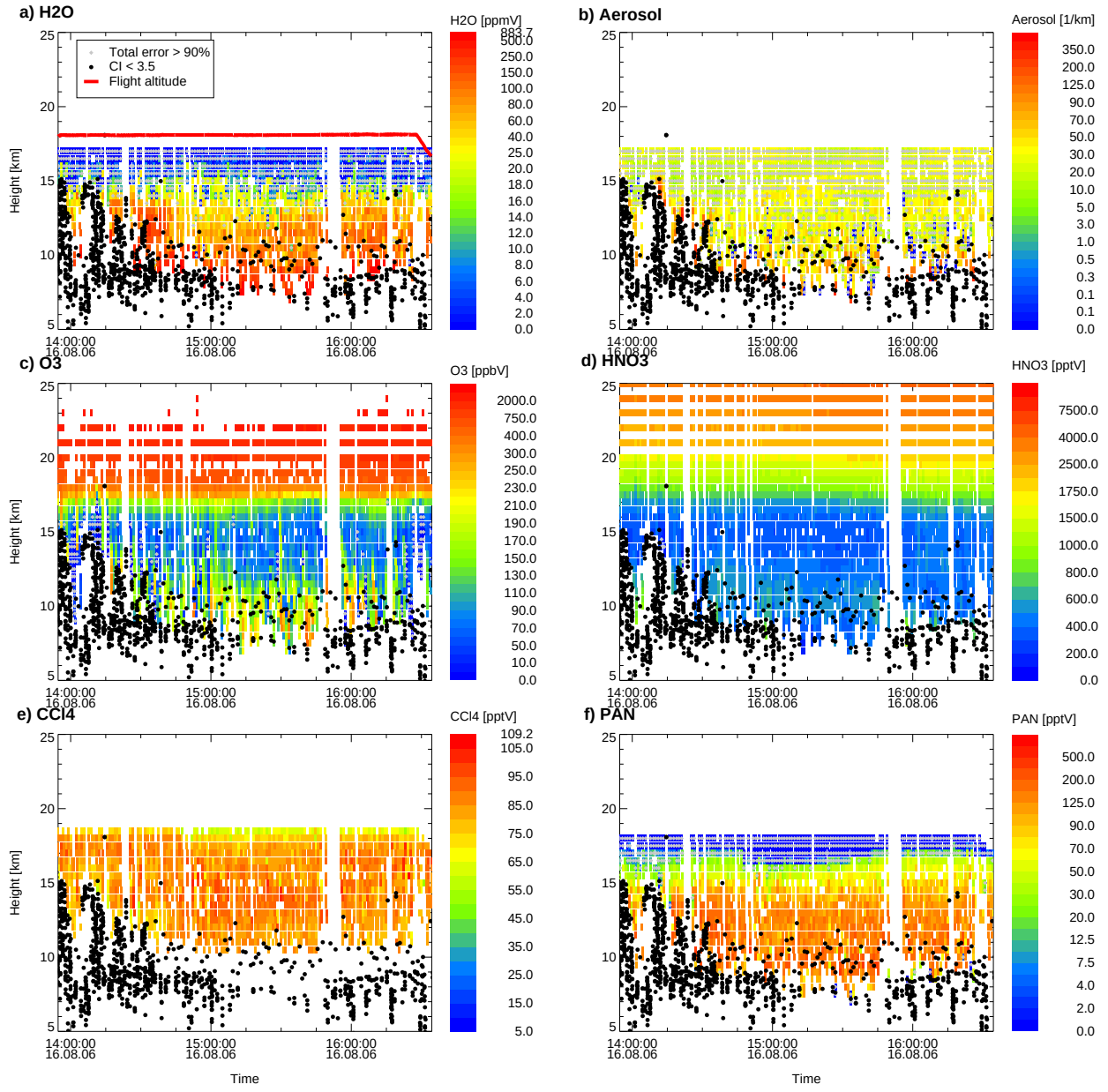

Figure 79: CRISTA-NF Retrieval results: a) H_2O , b) Aerosol, c) O_3 , d) HNO_3 , e) CCl_4 , f) PAN. Black dots: Cloud index < 3.5, corrected altitudes, grey diamonds: Total error (without smoothing) $> 90\%$. Note nonlinear color scales.

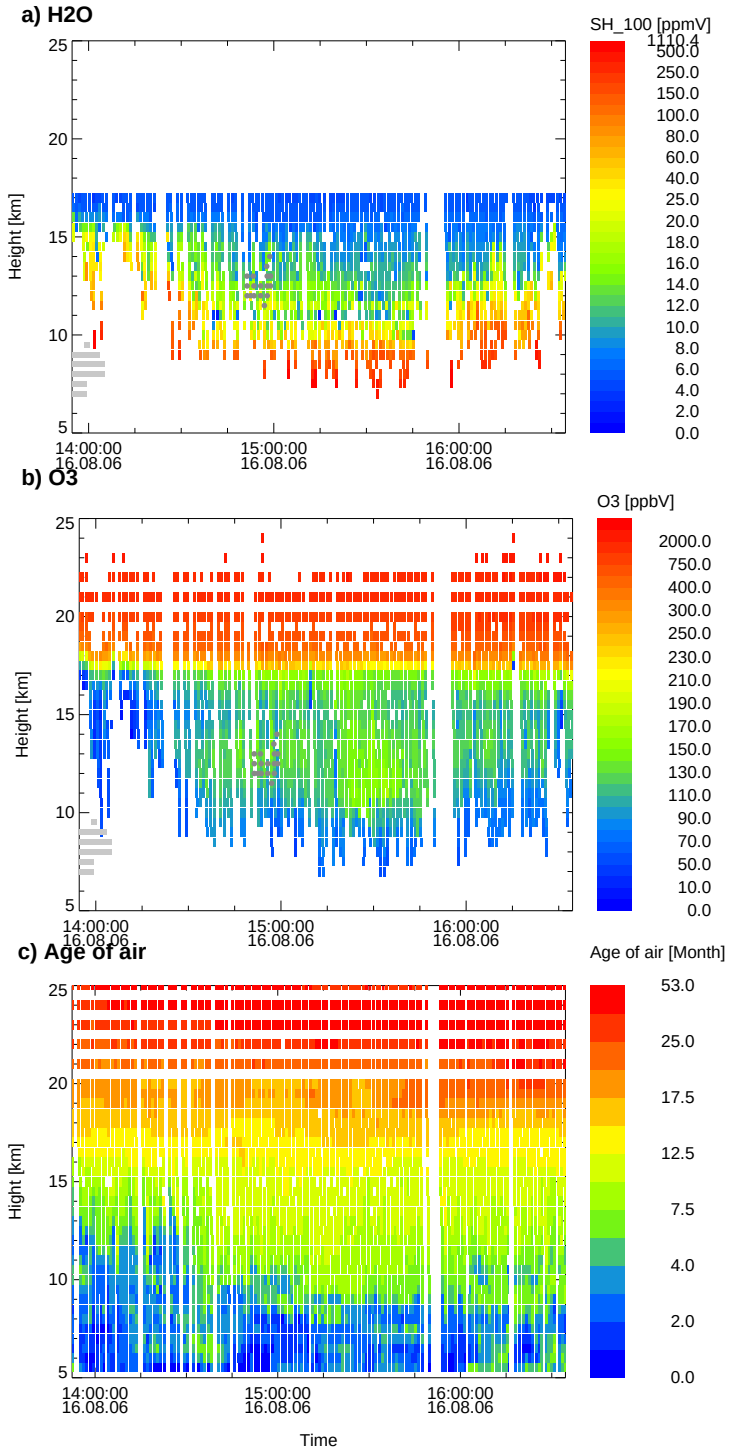

Figure 80: As Figure 68 but for CLaMs results for AMMA T3. Dark grey dots: Water clouds (LWC > 0). Note nonlinear color scales.

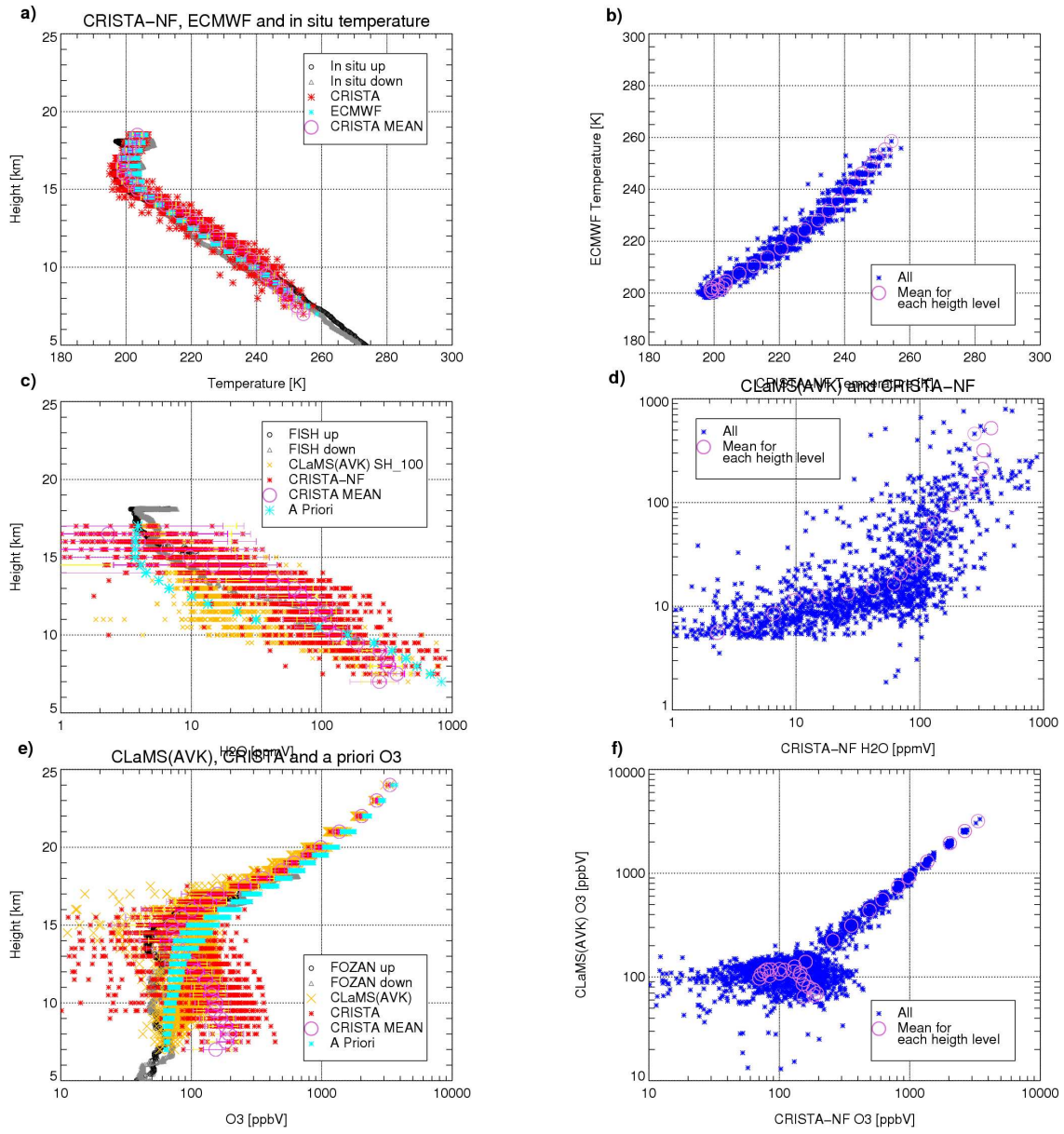

Figure 81: CRISTA-NF Retrieval results compared to in situ data, CLaMs and ECMWF analysis data: a) Temperature profile, b) temperature scatter plot, c)H_2O profile, d) H_2O scatter plot, e) O_3 profile, f) O_3 scatter plot.

C.1.5 AMMA T4

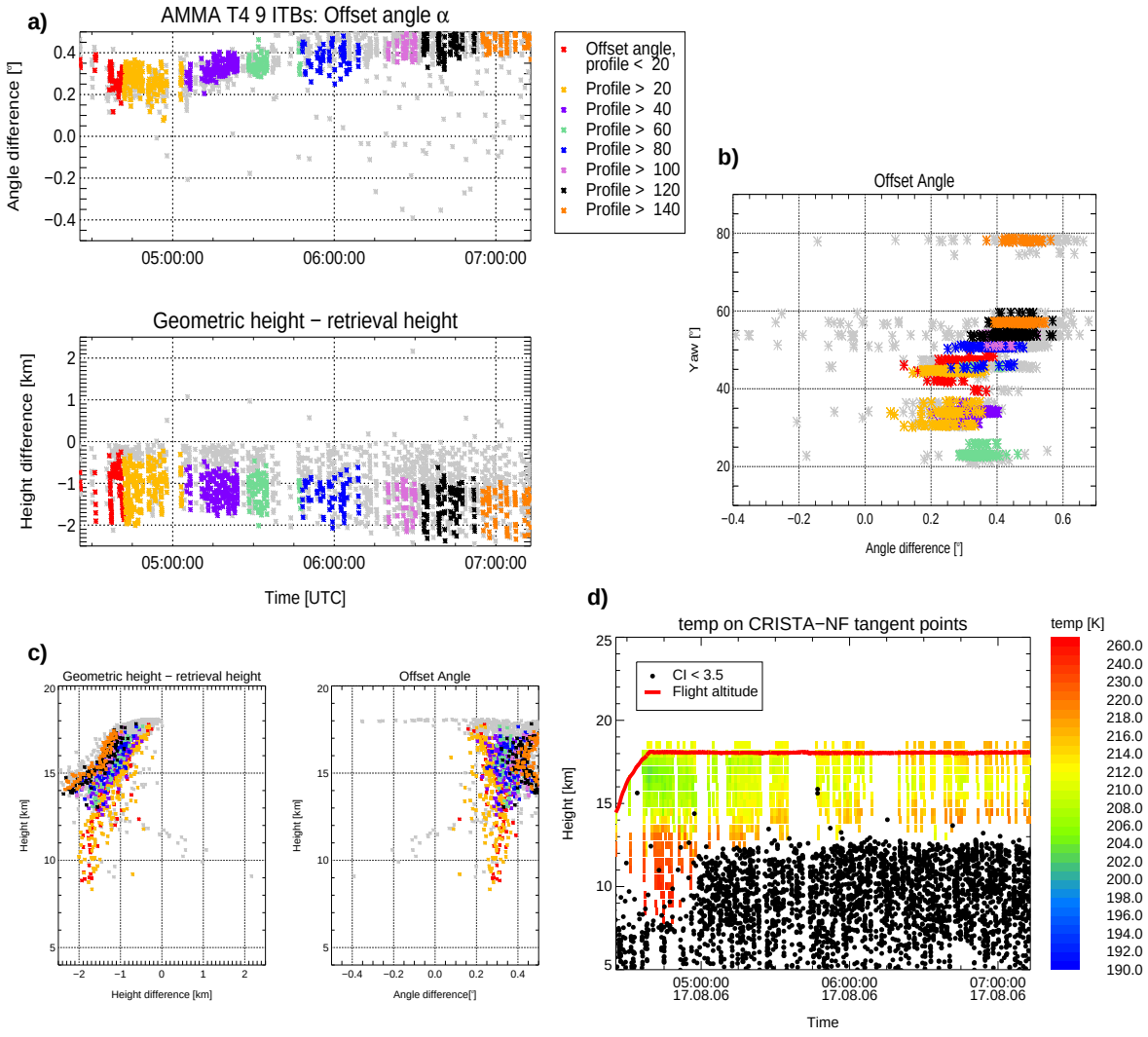

Figure 82: CRISTA-NF altitude and temperature retrieval results: a) Angle difference and height difference against time, b) angle difference against airplane yaw, c) angle difference and height difference against tangent point height. Grey stars: all values. Colored stars: $\chi^2 < 2$, measurement contend> 98% d) Result of temperature retrieval. Black dots: Cloud index < 3.5, corrected altitudes. Note nonlinear color scales.

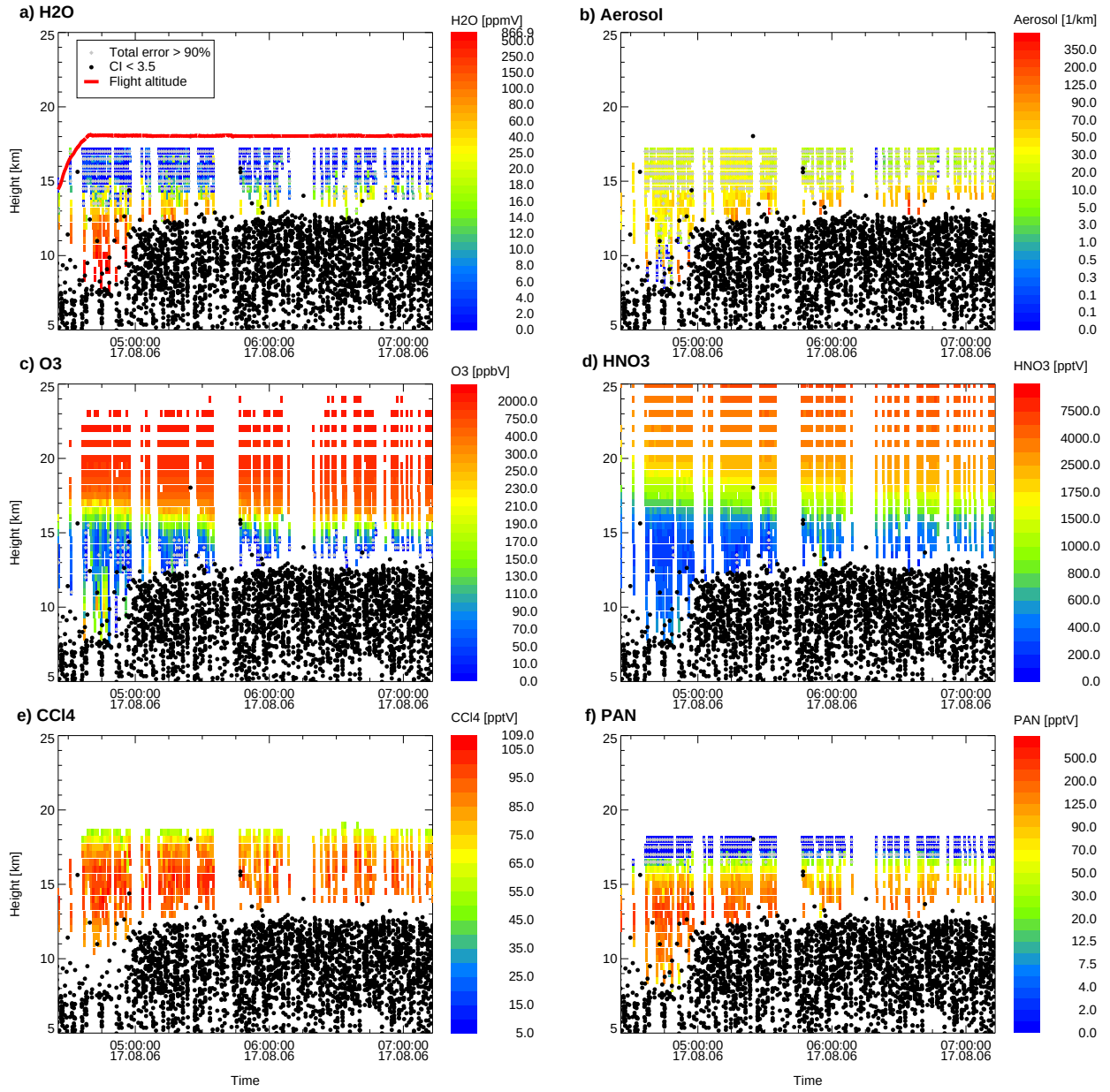

Figure 83: CRISTA-NF Retrieval results: a) H_2O , b) Aerosol, c) O_3 , d) HNO_3 , e) CCl_4 , f) PAN. Black dots: Cloud index < 3.5, corrected altitudes, grey diamonds: Total error (without smoothing) $> 90\%$. Note nonlinear color scales.

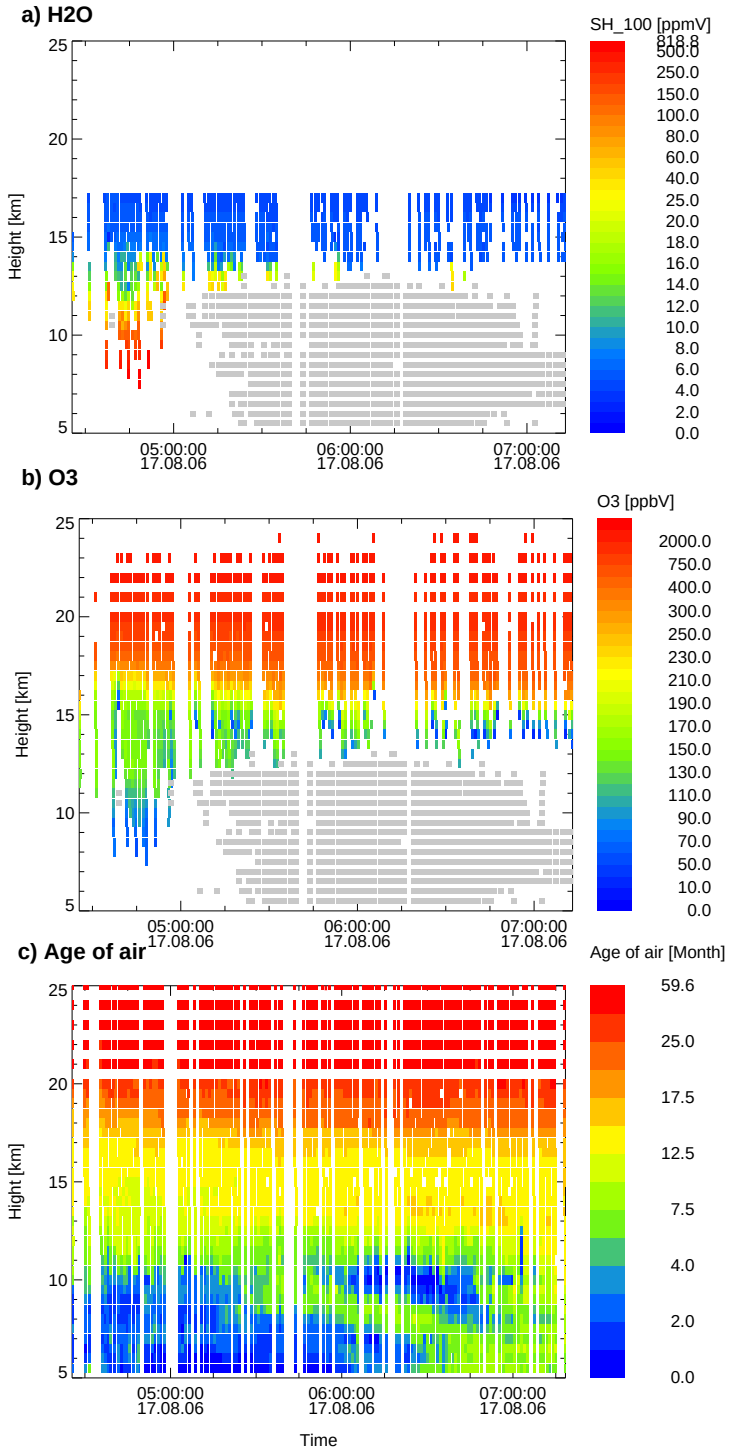

Figure 84: As Figure 68 but for CLaMs results for AMMA T4. Note nonlinear color scales.

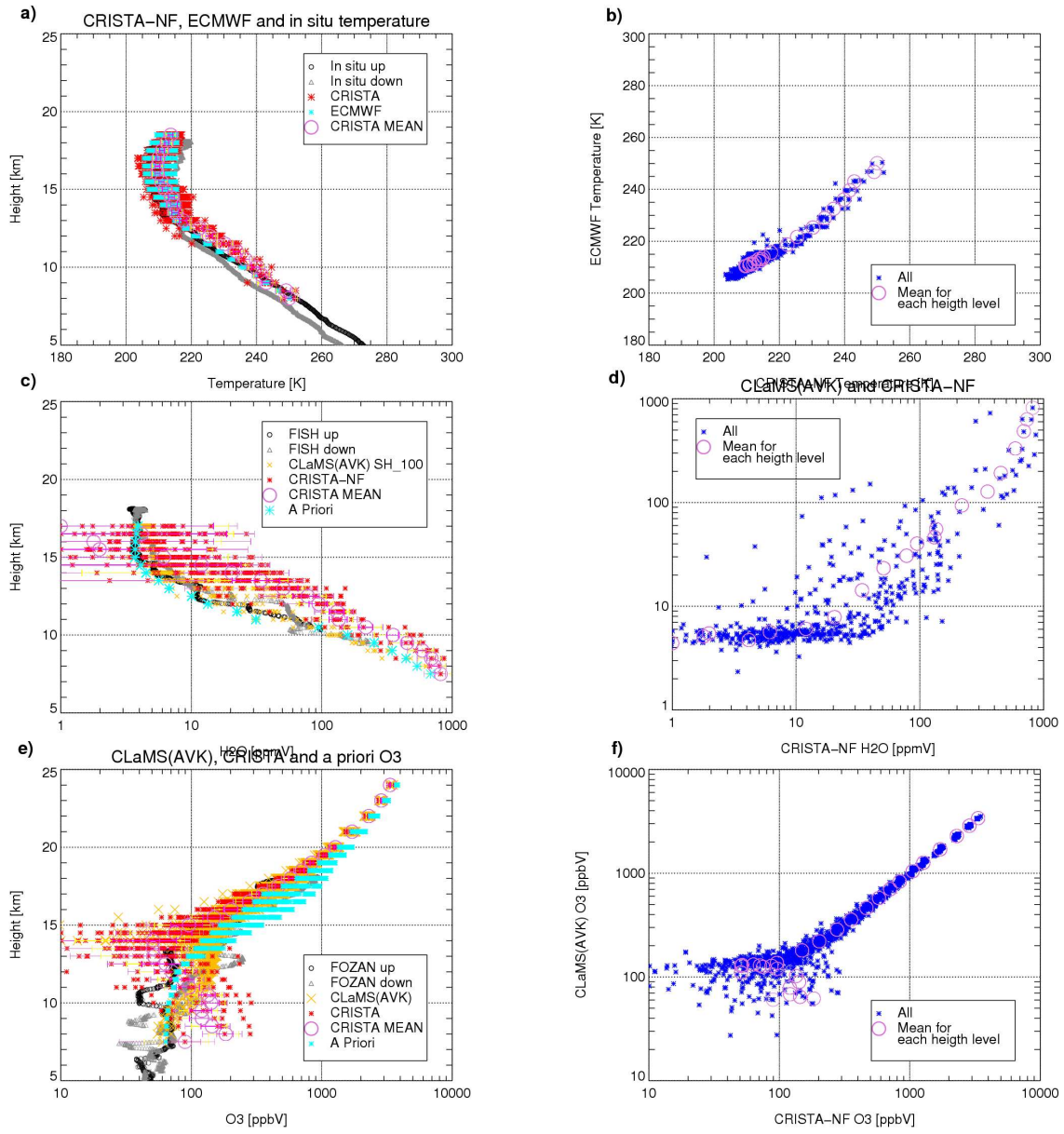

Figure 85: CRISTA-NF Retrieval results compared to in situ data, CLaMs and ECMWF analysis data: a) Temperature profile, b) temperature scatter plot, c)H_2O profile, d) H_2O scatter plot, e) O_3 profile, f) O_3 scatter plot.

C.2 ECMWF data

The following Figures show the ECMWF analysis data of potential vorticity, zonal, meridional and vertical wind speed, pressure, temperature, H_2O , and O_3 interpolated on the uncorrected geometric tangent points of CRISTA-NF for the AMMA flights TF2, T1, T2, L5, T3, T4. Temperature and O_3 are used as a priori for the CRISTA-NF retrieval.

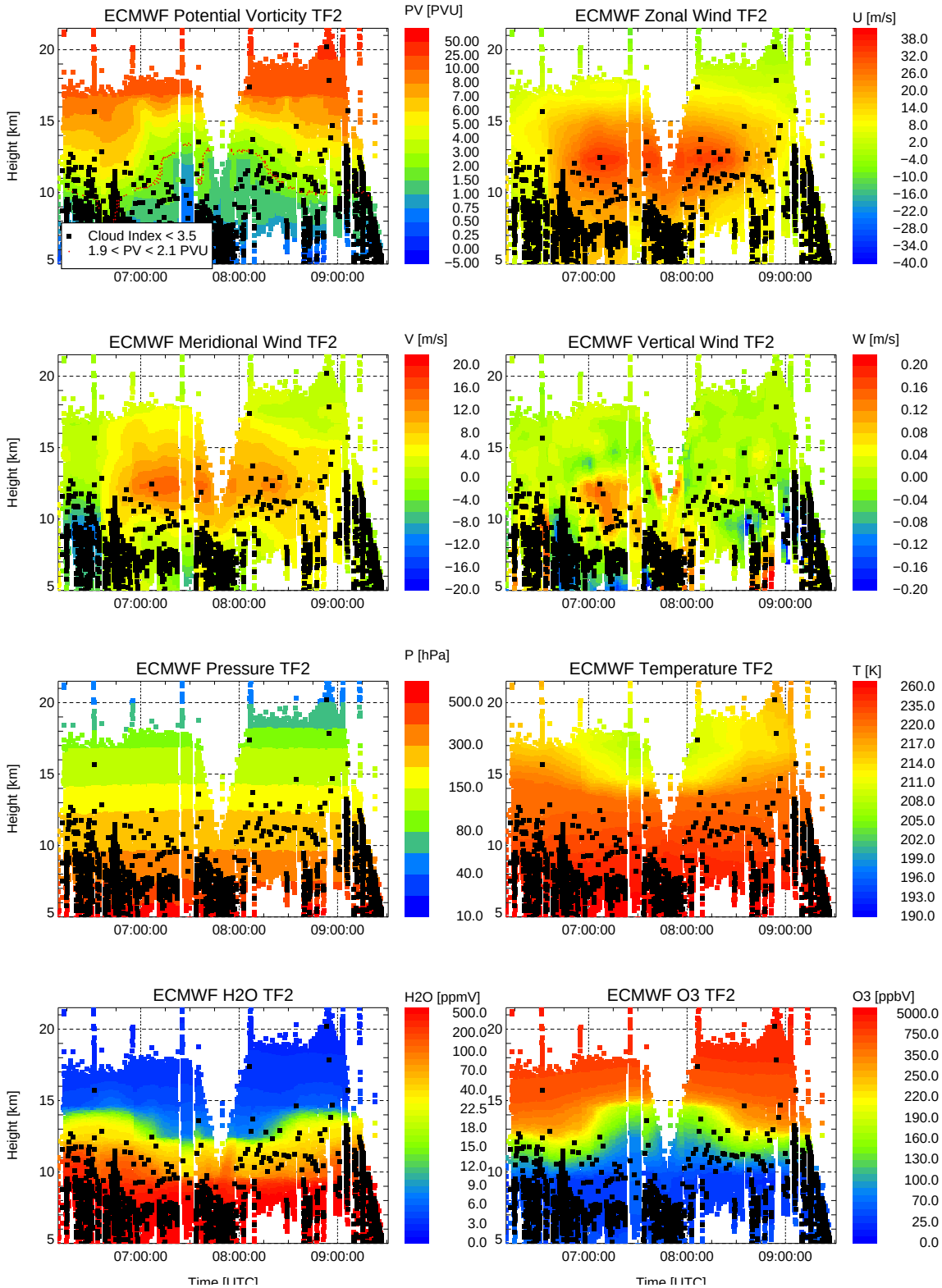

Figure 86: Cross section of ECMWF data on CRISTA-NF tangent points for TF2 on 2006/07/29. Black dots: Cloud Index < 3.5. Note nonlinear color scales.

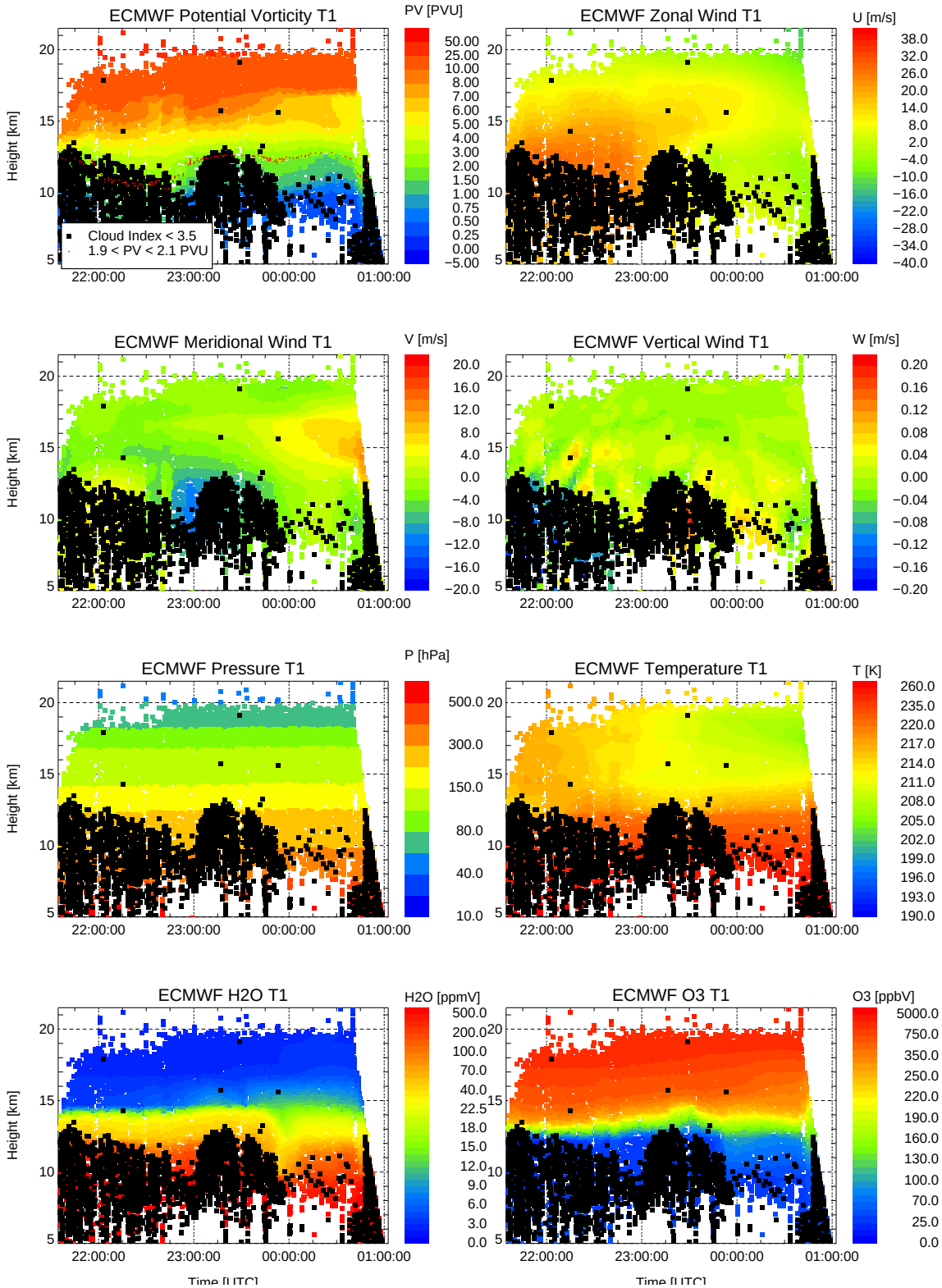

Figure 87: Cross section of ECMWF data on CRISTA-NF tangent points for T1 on 2006/07/31. Black dots: Cloud Index < 3.5. Note nonlinear color scales.

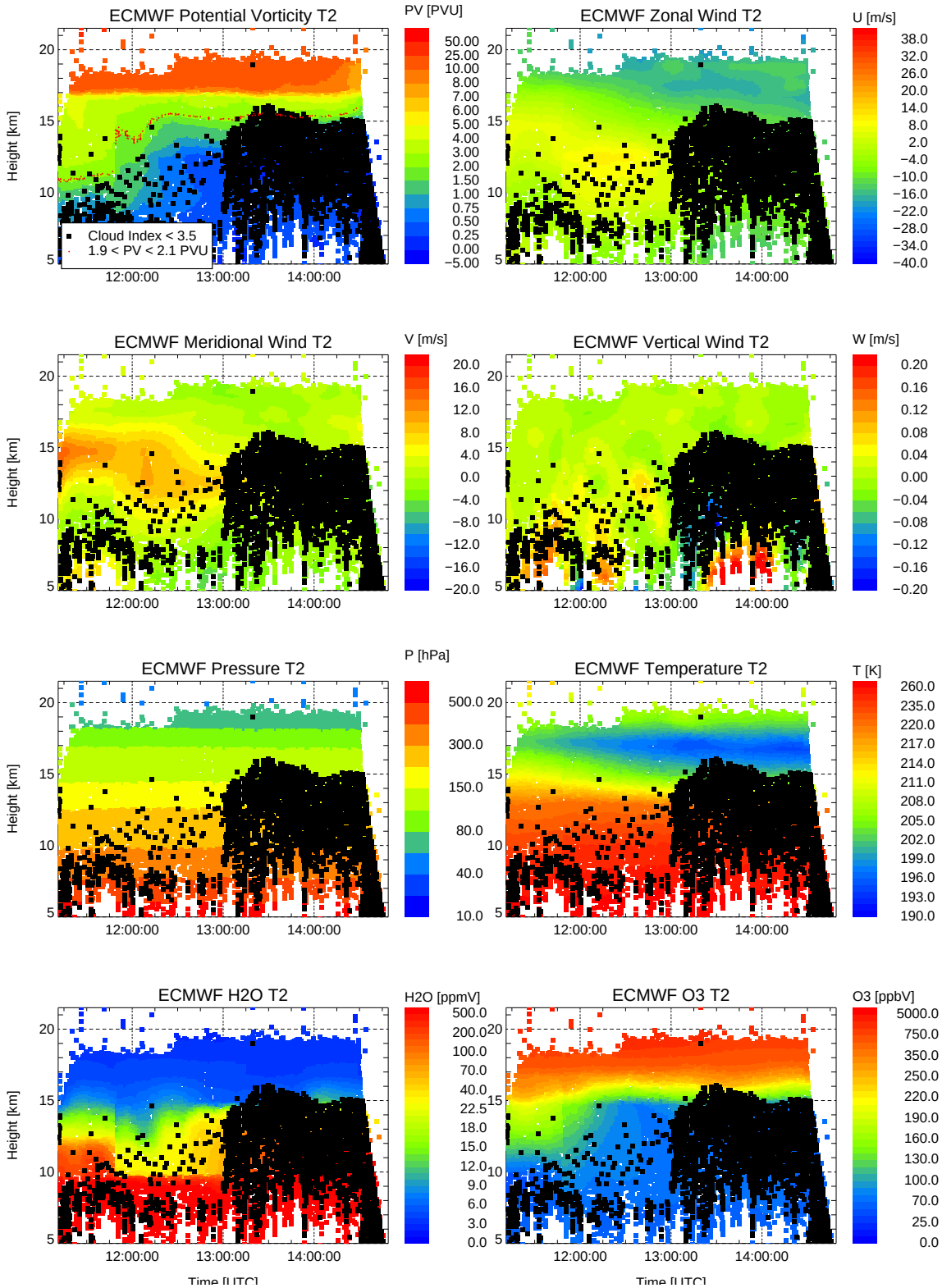

Figure 88: Cross section of ECMWF data on CRISTA-NF tangent points for T2 on 2006/08/01. Black dots: Cloud Index< 3.5. Note nonlinear color scales.

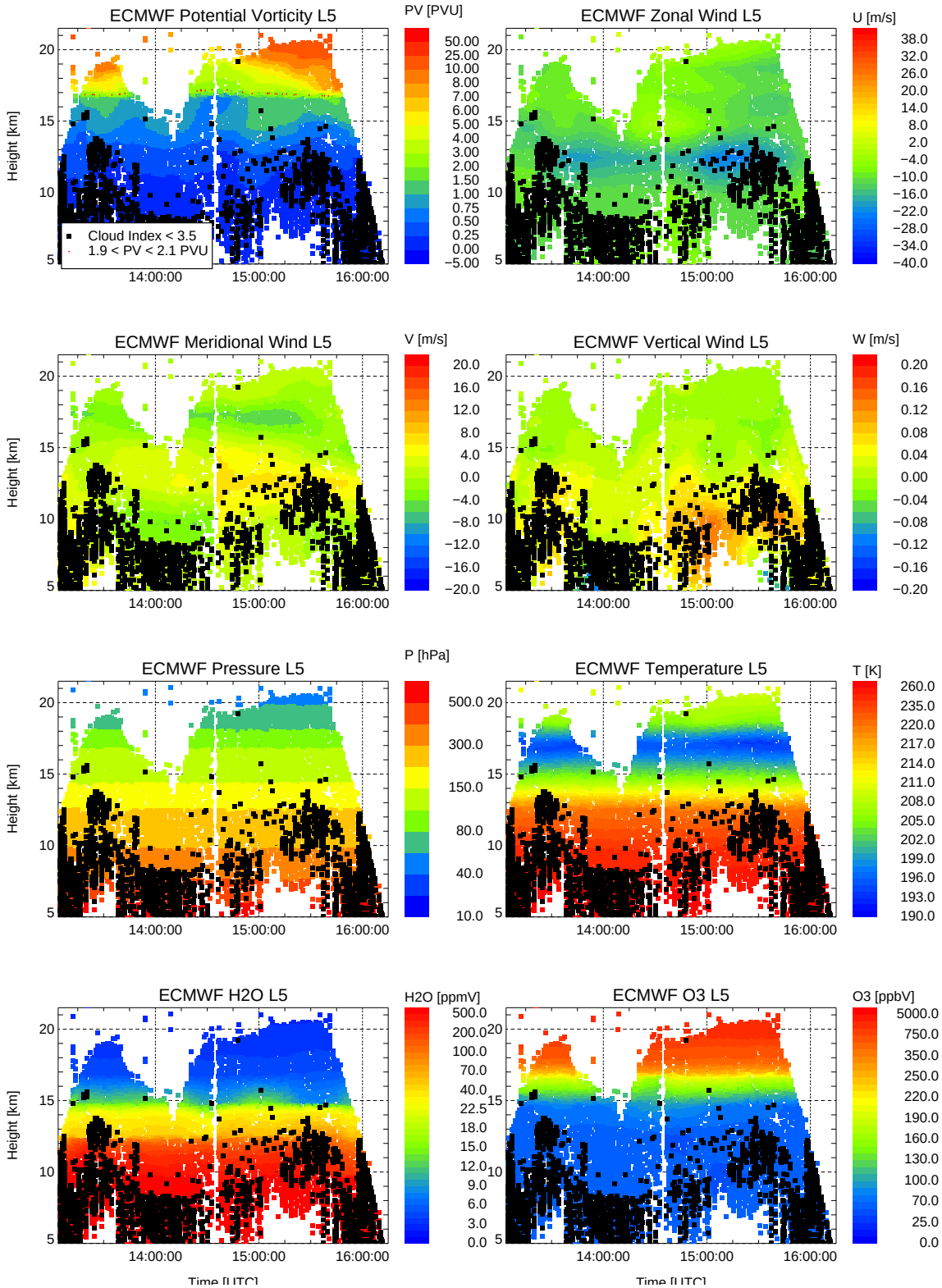

Figure 89: Cross section of ECMWF data on CRISTA-NF tangent points for L5 on 2006/08/13. Black dots: Cloud Index < 3.5. Note nonlinear color scales.

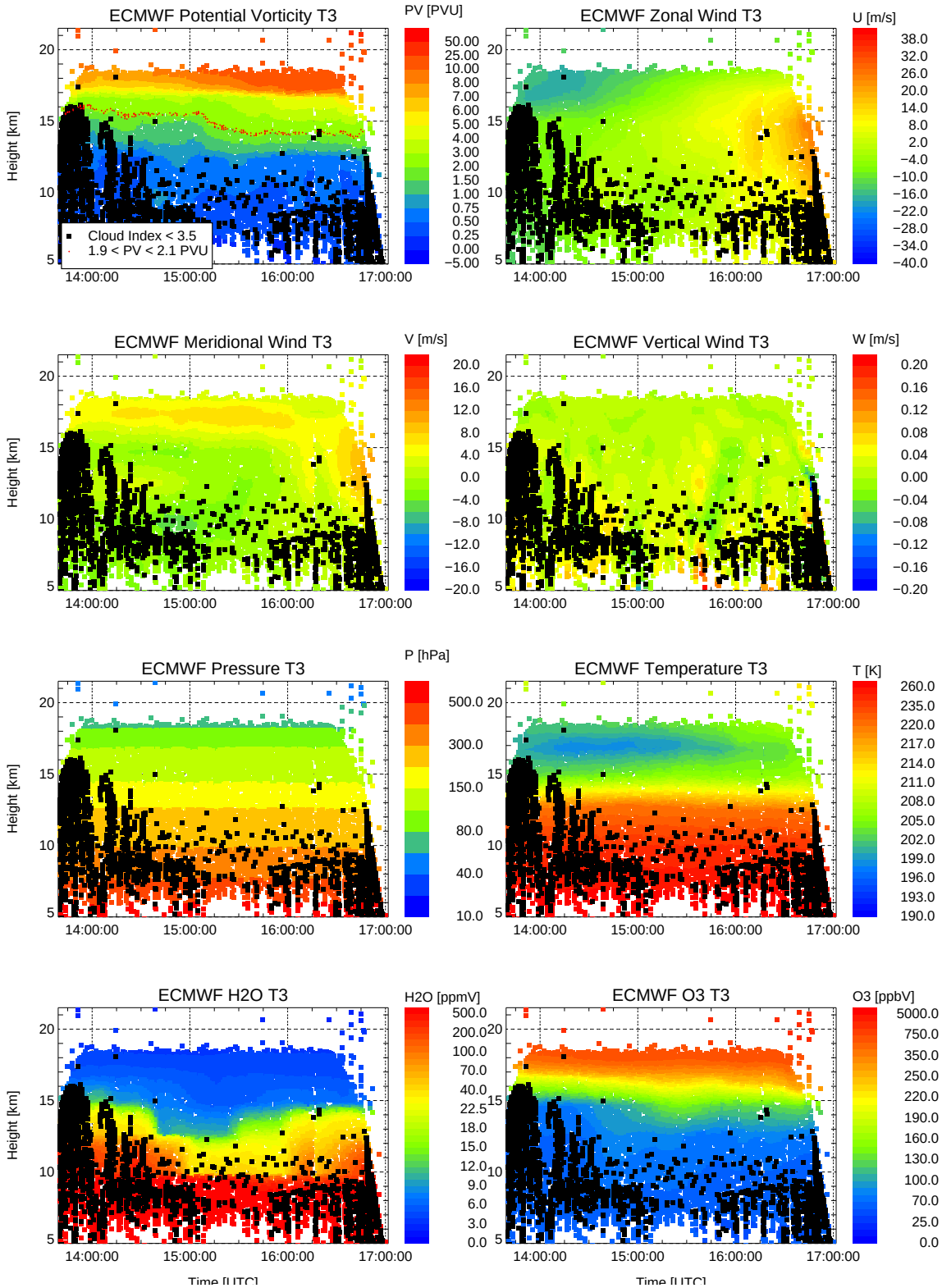

Figure 90: Cross section of ECMWF data on CRISTA-NF tangent points for T3 on 2006/08/16. Black dots: Cloud Index < 3.5. Note nonlinear color scales.

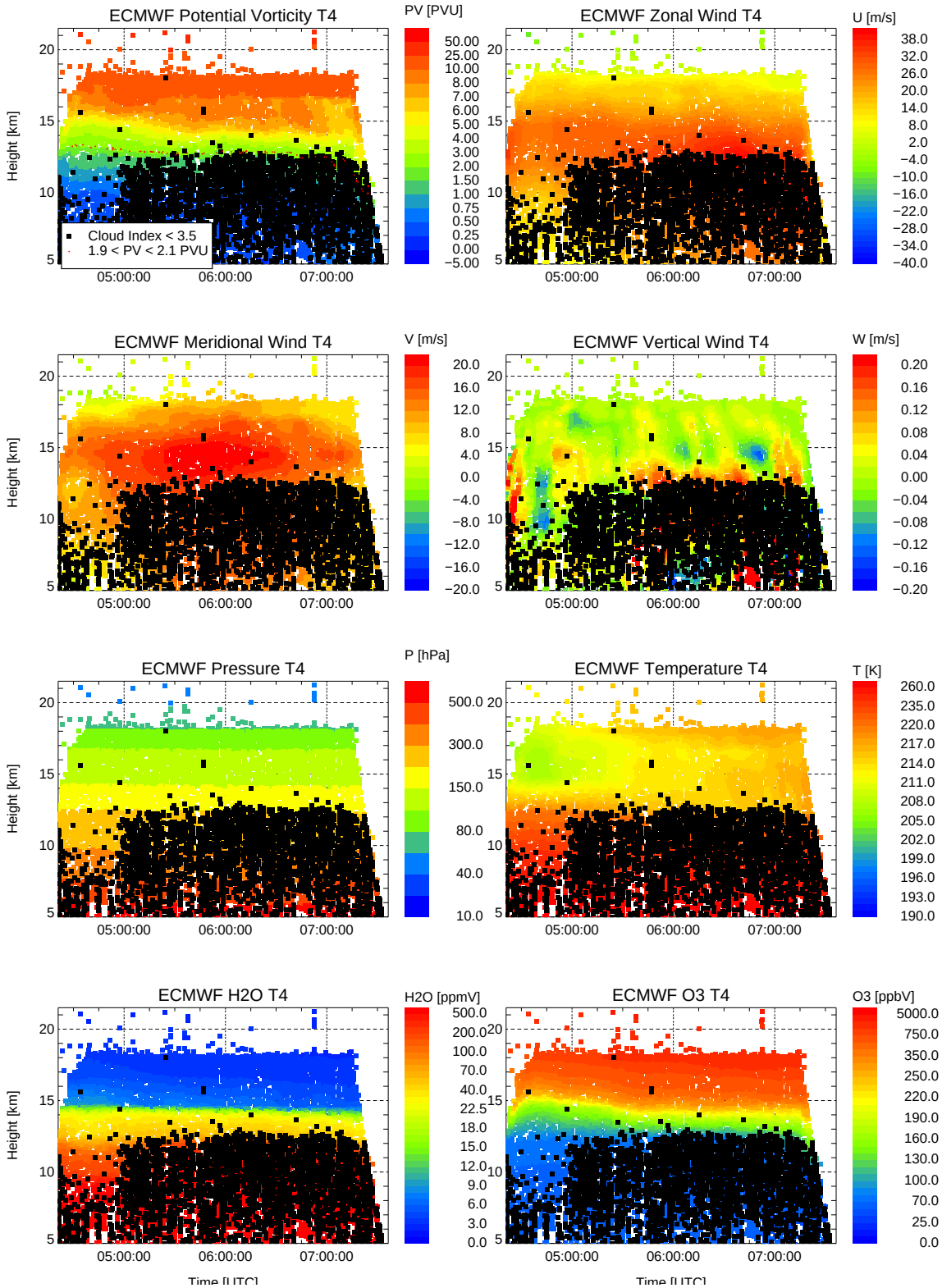

Figure 91: Cross section of ECMWF data on CRISTA-NF tangent points for T4 on 2006/08/17. Black dots: Cloud Index < 3.5. Note nonlinear color scales.

References

Adams, S., Spang, R., Preusse, P., and Heinemann, G.: "The benefit of limb cloud imaging for tropospheric infrared limb sounding", Atmos. Meas. Tech. Discuss., 2, 589-620, 2009

Allen, G., J.J. Remedios and K.M. Smith:"Low temperature mid-infrared cross-sections for peroxyacetyl nitrate (PAN) vapour", Atmos. Chem. Phys., 5, 3153–3158, 2005

Arndt, K.: "Spike Entfernung in IR Spektren des Fernerkundungs-Instruments CRISTA-NF mit Hilfe von Wavelets",Diplomarbeit, Fachhochschule Aachen, Fachbereich Physikalische Technik, 2006

Ballard, J., R.J. Knight, D.A. Newnham, J. Vander Auwera, M. Herman, G. Di Lonardo, G. Masciarelli, F.M. Nicolaisen, J.A. Beukes, L.K. Christensen, R. McPheat, G. Duxbury, R. Freckleton, K.P. Shine: "An intercomparison of laboratory measurements of absorption cross-sections and integrated absorption intensities for HCFC-22",Journal of Quantitative Spectroscopy and Radiative Transfer, 66, 109–128, 2000

Barthol, P.: "Das optische System des CRISTA-Experiments.", PhD thesis, Bergische Universität Gesamthochschule Wuppertal, 1994

Bernath, P. F., et al.: "Atmospheric Chemistry Experiment (ACE): Mission overview", Geophys. Res. Lett., 32, L15S01, 2005

Cloud-Aerosol Lidar and Infrared Pathfinder Satellite Observation (CALIPSO), http://www-calipso.larc.nasa.gov/, 2009

Chandrasekhar, S.: "Radiative Transfer", Dover, 1960.

Clough, S.A., M.W. Shephard, E.J. Mlawer, J.S. Delamere, M.J. Iacono, K. Cady-Pereira, S. Boukabara, P.D. Brown: "Short communication: Atmospheric radiative transfer modeling: A summery of AER codes", Journal of Quantitative Spectroscopy and Radiative Transfer, 91, 233–244, 2005.

Curtis, A. R.: "Discussion of 'A statistical model for water vapour absorption' by R. M. Goody", Quart. J. Roy. Meteorol. Soc., 78, 638–640, 1952.

Danielsen, E. F.: "A Dehydration Mechanism for the Stratosphere", Geophys. Res. Lett., 9(6), 605-608, 1982

Denman, K.L., G. Brasseur, A. Chidthaisong, P. Ciais, P.M. Cox, R.E. Dickinson, D. Hauglustaine, C. Heinze, E. Holland, D. Jacob, U. Lohmann, S Ramachandran, P.L. da Silva Dias, S.C. Wofsy and X. Zhang: "Couplings Between Changes in the Climate System and Biogeochemistry". In: Climate Change 2007: The Physical Science Basis. Contribution of Working Group I to the Fourth Assessment Report of the Intergovernmental Panel on Climate Change [Solomon, S., D. Qin, M. Manning, Z. Chen, M. Marquis, K.B. Averyt, M.Tignor and H.L. Miller (eds.)]. Cambridge University Press, Cambridge, United Kingdom and New York, NY, USA, 2007

Dinelli, B. M., Castelli, E., Carli, B., Del Bianco, S., Gai, M., Santurri, L., Moyna, B. P., Oldfield, M., Siddans, R., Gerber, D., Reburn, W. J., Kerridge, B. J., and Keim, C.: "Technical Note: Measurement of the tropical UTLS composition in presence of clouds using millimetre-wave heterodyne spectroscopy", Atmos. Chem. Phys., 9, 1191–1207, 2009

Dudhia, A.: "RFM Software User's Manual", Department of Atmospheric,Oceanic and Planetary Physics, University of Oxford, United Kingdom, http://www.atm.ox.ac.uk/rfm, 2004.

Dufour, G.,C. D. Boone and P. F. Bernath: "First measurements of CFC-113 and HCFC-142b from space using ACE-FTS infrared spectra", Geophys. Res. Lett., 32, L15S09, 2005.

Engel, A., Bönisch, H., Brunner, D., Fischer, H., Franke, H., Günther, G., Gurk, C., Hegglin, M., Hoor, P., Königstedt, R., Krebsbach, M., Maser, R., Parchatka, U., Peter, T., Schell, D., Schiller, C., Schmidt, U., Spelten, N., Szabo, T., Weers, U., Wernli, H., Wetter, T., and Wirth, V.: "Highly resolved observations of trace gases in the lowermost stratosphere and upper troposphere from the Spurt project: an overview", Atmos. Chem. Phys., 6, 283–301, 2006

Enidine: “Enidine Drahtseilfedern - Lösungen zur Energieabsorbtion und Vibrationsisolierung”, www.enidine.eu, 2006

Ern, M., D. Offermann, P. Preusse, K.-U. Grossmann, and J. Oberheide: “Calibration procedures and correction of detector signal relaxations for the CRISTA infrared satellite instrument”, Applied Optics, 42(9), 2003

European Space Agency: “PREMIER: Candidate Earth Explorer Core Missions - Reports for Assessment”, ESA SP-1313(5), Mission Science Division, ESA-ESTEC, Noordwijk, The Netherlands, ISSN 0379–6566, 121 pp., 2008

Fabeck, Wolf von: “Kreiselgeräte”, 1980.

Fairlie,T. D., M. A. Avery, R. B. Pierce, J Al-S., J. Dibb, and G. Sachse: “Impact of multiscale dynamical processes and mixing on the chemical composition of the upper troposphere and lower stratosphere during the Intercontinental Chemical Transport Experiment-North America”, J. Geophys. Res., 112, D16S90, 2007

Fastie, W. G.: “Ebert Spectrometer Reflections.”, Physics Today 4(1), 37–43, 1991

Fischer, H., F. G. Wienhold, P. Hoor, O. Bujok, C. Schiller, P. Siegmund, M. Ambaum, H. A. Scheeren, and J. Lelieveld: “Tracer Correlations in the Northern High Latitude Lowermost Stratosphere: Influence of Cross-Tropopause Mass Exchange”, Geophys. Res. Lett., 27(1), 97–100, 2000

Francis, G. L., D. P. Edwards, A. Lambert, C. M. Halvorson, J. M. Lee-Taylor, and J. C. Gille: “Forward modeling and radiative transfer for the NASA EOS-Aura High Resolution Dynamics Limb Sounder (HIRDLS) instrument”, J. Geophys. Res., 111, D13301, 2006

Friedl-Vallon, F., M. Riese, G. Maucher, A. Lengel, F. Hase, P. Preusse, R. Spang: “Instrument concept and preliminary performance analysis of GLORIA”, Advances in Space Research, 37(12), 2287–2291,2006

Glatthor, T., et al.: “Global peroxyacetyl nitrate (PAN) retrieval in the upper troposphere from limb emission spectra of Michelson Interferometer for Passive Atmospherc Sounding (MIPAS)”, Atmos. Chem. Phys., 7, 2775–2787, 2007.

Gille, J. C., and F. B. House: “On the inversion of limb radiance measurements, I, Temperature and thickness”, J. Atmos. Sci., 28, 1427–1442, 1971

Godson, W.L.: “THE COMPUTATION OF INFRARED TRANSMISSION BY ATMOSPHERIC WATER VAPOR”, J. Atmos. Sci., 12, 272–284, 1955:

Gordley, L. L., Russell III, J. M.: “Rapid inversion of limb radiance data using an emissivity growth approximation”, Appl. Optics, 20, 807–813, 1981.

Grooss, J.-U. and Russell III, J. M.: “Technical note: A stratospheric climatology for O3, H2O, CH4, NOx, HCl and HF derived from HALOE measurements”, Atmos. Chem. Phys., 5, 2797–2807, 2005

Grossmann, K. U., D. Offermann, O. Gusev, J. Oberheide, M. Riese, and R. Spang: “The CRISTA-2 mission”, J. Geophys. Res., 107(D23), 8173, 2002

Günther, G., Müller, R., von Hobe, M., Stroh, F., Konopka, P., and Volk, C. M.: “Quantification of transport across the boundary of the lower stratospheric vortex during Arctic winter 2002/2003”, Atmos. Chem. Phys., 8, 3655–3670, 2008

Happell J. D., and M. P. Roche: “Soils: A global sink of atmospheric carbon tetrachloride”, Geophys. Res. Lett., 30(2), 1088, 2003

Hervig, M. E., J. M. Russell III, L. L. Gordley, J. H. Park, and S. R. Drayson: “OBSERVATIONS OF AEROSOL BY THE HALOE EXPERIMENT ONBOARD UARS: A PRELIMINARY VALIDATION”, Geophys. Res. Lett., 20(12), 1291–1294, 1993

Hoffmann, L.: “Schnelle Spurengasretrieval für das Satellitenexperiment Envisat MIPAS”,PhD thesis, University of Wuppertal, 2006.

Hoffmann, L., Kaufmann, M., Spang, R., Mller, R., Remedios, J. J., Moore, D. P., Volk, C. M., von Clarmann, T., and Riese, M.: "Envisat MIPAS measurements of CFC-11: retrieval, validation, and climatology", Atmos. Chem. Phys., 8, 3671–3688, 2008.

Hoffmann, L., M. J. Alexander: "Retrieval of Stratospheric Temperatures from AIRS 1 Radiance Measurements for Gravity Wave Studies", J. Geophys. Res., in press, 2009

Hoffmann, L., Weigel, K., Spang, R., Schroeder, S., Arndt, K., Lehmann, C., Kaufmann, M., Ern, M., Preusse, P., Stroh, F., Riese, M.: "CRISTA-NF measurements of water vapor during the SCOUT-O3 Tropical Aircraft Campaign",Adv. Space Res.,43(1),74–81, 2009.

Holton, J. R., P. H. Haynes, M. E. McIntyre, A. R. Douglass, R. B. Rood, and L. Pfister: "Stratosphere-Troposphere Exchange", Rev. Geophys., 33(4), 403–439, 1995

Hoor, P., H. Fischer, L. Lange, J. Lelieveld, and D. Brunner: "Seasonal variations of a mixing layer in the lowermost stratosphere as identified by the CO-O3 correlation from in situ measurements", J. Geophys. Res., 107(D5), 4044, 2002

Kiefer, M., von Clarmann, T., Grabowski, U., De Laurentis, M., Mantovani, R., Milz, M., and Ridolfi, M.: "Characterization of MIPAS elevation pointing", Atmos. Chem. Phys., 7, 1615–1628, 2007

Kaufmann, M., O. A. Gusev, K. U. Grossmann, R. G. Roble, M. E. Hagan, C. Hartsough, and A. A. Kutepov: "The vertical and horizontal distribution of CO2 densities in the upper mesosphere and lower thermosphere as measured by CRISTA", J. Geophys. Res., 107(D23), 8182, 2002

Keim, C.: "Entwicklung und Verifikation der Sichtlinienstabilisierung für MIPAS auf dem hochfliegenden Forschugsflugzeug M55 Geophysica", Forschungszentrum Karlsruhe in der Helmholtz-Gemeinschaft, Wissenschaftliche Berichte, FZKA 6729, 2002.

Khosrawi, F., Groo, J.-U., Müller, R., Konopka, P., Kouker, W., Ruhnke, R., Reddmann, T., and Riese, M.: "Intercomparison between Lagrangian and Eulerian simulations of the

development of mid-latitude streamers as observed by CRISTA", Atmos. Chem. Phys., 5, 85–95, 2005

Konopka, P., Guenther, G., Müller, R., dos Santos, F. H. S., Schiller, C., Ravegnani, F., Ulanovsky, A., Schlager, H., Volk, C. M., Viciani, S., Pan, L. L., McKenna, D.-S., and Riese, M.: "Contribution of mixing to upward transport across the tropical tropopause layer (TTL)", Atmos. Chem. Phys., 7, 3285–3308, 2007

Konopka, P., M. Park, J.-U. Grooss, G. Günther, R. Walter, F. Ploeger, R. Müller and, Randel W. J.: "The seasonality of the composition of air in the TTL",in preparation, 2009

Krämer, M., C. Schiller, H. Ziereis, J. Ovarlez, and H. Bunz: "Nitric acid partitioning in cirrus clouds: the role of aerosol particles and relative humidity", Tellus: Series B 58, 2, 141–147, 2006

Krämer, M., Schiller, C., Afchine, A., Bauer, R., Gensch, I., Mangold, A., Schlicht, S., Spelten, N., Sitnikov, N., Borrmann, S., de Reus, M., and Spichtinger, P.: "Ice supersaturations and cirrus cloud crystal numbers", Atmos. Chem. Phys. Discuss., 8, 21089–21128, 2008

Küll, V.: "Dynamik und Photochemie in der Stratosphäre: Spurengasmessungen des CRISTA Experiments",PhD thesis, University of Wuppertal, 2002.

Kullmann, A., M. Riese, F. Olschewski, F. Stroh, K.-U. Grossmann: "Cryogenic Infrared Spectrometers and Telescopes for the Atmosphere - New Frontiers", Proceedings of SPIE, 5570, 423–432, 2004.

Kullmann, A.: "Ein flugzeugetragenes kryogenes Infrarotspektrometer zur Fernerkundung klimarelevanter Spurengase im Tropopausenbereich",PhD thesis, University of Wuppertal, 2006.

Laube, J.C., A. Engel, H. Boenisch, T. Moebius, D. R. Worton, W. T. Sturges, K. Grunow and U. Schmidt: "Contribution of very short-lived organic substances to stratospheric chlorine and bromine in the tropics - a case study", ACPD, 8, 8491–8515, 2008.

Marshall, B.T., L.L. Gordley and D.A. Chu: "BANDPACK: Algorithms for modelling broadband transmission and radiance", Journal of Quantitative Spectroscopy and Radiative Transfer, 52(5),581–599, 1994

Massie, S.T., P.L. Bailey, J.C. Gille, E.C. Lee, J.L. Mergenthaler, A.E. Roche, J.B. Kumer, E.F. Fishbein, J.W. Waters, and W.A. Lahoz: "Spectral Signatures of Polar Stratospheric Clouds and Sulfate Aerosol", J. Atmos. Sci., 51, 3027–3044, 1994

May, R.D. and R.R. Friedl: "Integrated band intensities of HO2NO2 at 220 K",Journal of Quantitative Spectroscopy and Radiative Transfer, 3, 257–266, 1993

McDaniel, A.H., C.A. Cantrell, J.A. Davidson, R.E. Shetter and J.G. Calvert: "The Temperature Dependent, Infrared Absorption Cross-Sections for the Chloroflourocarbons: CFC-11, CFC-12, CFC-13, CFC-14, CFC-22, CFC-113, CFC-114 and CFC-115", Journal of Atmospheric Chemistry, 12, 211–227, 1991

McKenna, D. S., P. Konopka, J.-U. Grooss, G. Guenther, R. Mueller, R. Spang, D. Offermann, and Y. Orsolini (2002): "A new Chemical Lagrangian Model of the Stratosphere (CLaMS) 1. Formulation of advection and mixing", J. Geophys. Res., 107(D16), 4309, 2002

McKenna, D. S., J.-U. Grooß, G. Guenther, P. Konopka, R. Mueller, G. Carver, and Y. Sasano: "A new Chemical Lagrangian Model of the Stratosphere (CLaMS) 2. Formulation of chemistry scheme and initialization", J. Geophys. Res., 107(D15), 4256, 2002

MYASISHCHEV DESIGN BUREAU: "High-altitude M55 Geophysica aircraft", Investigators Handbook, 2002.

Murcray, D. G., T. G. Kyle, F. M. Murcray, and W. J. Williams: "Nitric Acid and Nitric Oxide in the Lower Stratosphere", Nature, 218, 78,1968

Nehls, S.: "Entwicklung und Tests von Komponenten für die CRISTA - Optik", Diplomarbeit, University of Wuppertal, 1991

Nemtchinov, V. and P. Varanasi: "Thermal infrared absorbtion cross-sections of CCl4 needed for atmospheric remote sensing",Journal of Quantitative Spectroscopy and Radiative Transfer, 82, 473-481,2003

Offermann, D., K.-U. Grossmann, P. Barthol, P. Knieling, M. Riese and R. Trant: "Crypgenic Infrared Spectrometers and Telescopes for the Atmosphere (CRISTA) erxperiment and middle atmosphere variability", J. Geophys. Res., 104(D13), 16311–16325, 1999

Offermann, D., B. Schaeler, M. Riese, M. Langfermann, M. Jarisch, G. Eidmann, C. Schiller, H. G. J. Smit, and W. G. Read: "Water vapor at the tropopause during the CRISTA 2 mission", J. Geophys. Res., 107(D23), 8176, 2002

Olsen, M. A., A. R. Douglass, P. A. Newman, J. C. Gille, B. Nardi, V. A. Yudin, D. E. Kinnison, and R. Khosravi: "HIRDLS observations and simulation of a lower stratospheric intrusion of tropical air to high latitudes", Geophys. Res. Lett., 35, L21813,2008

Pan, L. L.,K. P. Bowman, M. Shapiro, W. J. Randel, R. S. Gao, T. Campos, C. Davis, S. Schauffler, B. A. Ridley, J. C. Wei, C. Barnet: "Chemical behavior of the tropopause observed during the Stratosphere-Troposphere Analyses of Regional Transport experiment", J. Geophys. Res., 12, D18110, 2007

Park, M., Randel, W. J., Emmons, L. K., Bernath, P. F., Walker, K. A., and Boone, C. D.: "Chemical isolation in the Asian monsoon anticyclone observed in Atmospheric Chemistry Experiment (ACE-FTS) data", Atmos. Chem. Phys., 8, 757–764, 2008

Plumb, R. A., and M. K. W. Ko: "Interrelationships between mixing ratios of long-lived stratospheric constituents", J. Geophys. Res., 97, 10145–10156, 1992

Preusse, P.: "Vorbereitung der Eichung der CRISTA-Spektrometer", Diplomarbeit, WU D 94-45, Bergische Univ.-Gesamthochschule Wuppertal, Wuppertal, Germany, 1995

Preusse, P., A. Doernbrack, S. D. Eckermann, M. Riese, B. Schaeler, J. Bacmeister, D. Broutman, and K. U. Grossmann: "Space based measurements of stratospheric mountain

waves by CRISTA: 1. Sensitivity, analysis method, and a case study", J. Geophys. Res., 107(D23), 2002

Purser, R.J. and H.L. Huang:"ESTIMATING EFFECTIVE DATA DENSITY IN A SATELLITE RETRIEVAL OR AN OBJECTIVE ANALYSIS",J. Appl. Meteorol., 32(6), 1092–1107, 1993

Redelsperger, J.-L., C. D. Thorncroft, A. Diedhiou, T. Lebel, D. J. Parker J. Polcher: "AFRICAN MONSOON MULTIDISCIPLINARY ANALYSIS", Bulletin of the American Meteorological Society, 87(12), 1739–1746, 2006

Remedios, J. J., Allen, G., Waterfall, A. M., Oelhaf, H., and Kleinert, A.: "Detection of organic compound signatures in infra-red, limb emission spectra observed by the MIPAS-B2 balloon instrument", Atmos. Chem. Phys., 7, 1599–1613, 2007

Remedios, J. J., Leigh, R. J., Waterfall, A. M., Moore, D. P., Sembhi, H., Parkes, I., Greenhough, J., Chipperfield, M., Hauglustaine, D.: "MIPAS reference atmospheres and comparisons to V4.61/V4.62MIPAS level 2 geophysical data sets", ACPD, 7, 9973–10017, 2007.

Riese, M., R. Spang, P. Preusse, M. Ern, M. Jarisch, D. Offermann, and K. U. Grossmann: "Cryogenic Infrared Spectrometers and Telescopes for the Atmosphere (CRISTA) data processing and atmospheric temperature and trace gas retrieval",J. Geophys. Res., 114(D13), 16349–16367, 1999a

Riese, M., X. Tie, G. Brasseur, and D. Offermann: "Three-dimensional simulations of stratospheric trace gas distributions measured by CRISTA", J. Geophys. Res., 104, 16419–16435, 1999b

Riese, M., F. Friedl-Vallon, R. Spang, P. Preusse, C. Schiller, L. Hoffmann, P. Konopka, H. Oelhaf, Th. von Clarmann, M. Hopfner: "GLObal limb Radiance Imager for the Atmosphere (GLORIA): Scientific objectives", Advances in Space Research, 36(5), 989–995, 2005

Rodgers, C. D.:"Inverse Methods for Atmospheric Sounding: Theory and Practice",World Scientific, 2000.

Rothman,L.S., D. Jacquemart, A. Barbe, D. Chris Benner, M. Birk, L.R. Brown, M.R. Carleer, C.Chackerian Jr., K. Chance, L.H. Coudert, V. Dana, V.M. Devi, J.-M. Flaud, R.R. Gamache, A. Goldman, J.-M. Hartmann, K.W. Jucks, A.G. Maki, J.-Y. Mandin, S.T. Massie, J. Orphal, A. Perrin, C.P. Rinsland, M.A.H. Smith, J. Tennyson, R.N. Tolchenov, R.A. Toth, J. Vander Auwera, P. Varanasi, G. Wagner: "The HITRAN 2004 molecular spectroscopic database",Journal of Quantitative Spectroscopy and Radiative Transfer, 96, 139–204, 2005

Schiller, C., M. Kraemer, A. Afchine, N. Spelten, and N. Sitnikov, "Ice water content of Arctic, midlatitude, and tropical cirrus", J. Geophys. Res., 113, D24208, 2008

Schroeder, S. E., A. Kullmann, P. Preusse, F. Stroh, K. Weigel, M. Ern, P. Knieling, F. Olschewski, R. Spang, M. Riese: "Radiance calibration of CRISTA-NF", Adv. Space Res., accepted, 2009

Stratospheric-Climate Links with Emphasis on the Upper Troposphere and Lower Stratosphere (SCOUT-O3), http://www.ozone-sec.ch.cam.ac.uk/scout_o3/, 2009

Seo, K.-H., and K. P. Bowman: "Lagrangian estimate of global stratosphere-troposphere mass exchange", J. Geophys. Res., 107(D21), 4555, 2002

Shapiro, M. A.: "Turbulent mixing within tropopause folds as a mechanism for the exchange of chemical constituents between the stratosphere and troposphere", J. Atmos. Sci., 37(5), 994–1004, 1980

Silva dos Santos, F. H.: "Hydratation und Dehydratation in der tropischen Tropopausenschicht",PhD thesis, University of Wuppertal, 2008.

Spang, R., G. Eidmann, M. Riese, D. Offermann, P. Preusse, L. Pfister, and P.-H. Wang: "CRISTA observations of cirrus clouds around the tropopause", J. Geophys. Res., 107(D23), 8174, 2002

Spang, R., Hoffmann, L., Kullmann, A., Olschewski, F., Preusse, P., Knieling, P., Schroeder, S., Stroh, F., Weigel, K., Riese, M.: "High resolution limb observations of clouds by the CRISTA-NF experiment during the SCOUT-O3 tropical aircraft campaign", Adv. Space Res.,2008.

Stefanutti, L., L. Sokolov, S. Balestri, A.R. MacKenzie, and V. Khattatov: "The M-55 Geophysica as a Platform for the Airborne Polar Experiment.", Journal of Atmospheric & Oceanic Technology, 16(10), 1999

Stiller, G. P., von Clarmann, T., Höpfner, M., Glatthor, N., Grabowski, U., Kellmann, S., Kleinert, A., Linden, A., Milz, M., Reddmann, T., Steck, T., Fischer, H., Funke, B., Lopez-Puertas, M., and Engel, A.: "Global distribution of mean age of stratospheric air from MIPAS SF6 measurements", Atmos. Chem. Phys., 8, 677–695, 2008

Talukdar, R. K., J. B. Burkholder, A.-M. Schmoltner, J. M. Roberts, R. R. Wilson, and A. R. Ravishankara: "Investigation of the loss processes for peroxyacetyl nitrate in the atmosphere: UV photolysis and reaction with OH", J. Geophys. Res., 100(D7), 14163–14173, 1995

Toon, O. B., P. Hamill, R. P. Turco, and J. Pinto: "Condensation of HNO3 and HCl in the Winter Polar Stratospheres", Geophys. Res. Lett., 13(12), 1284–1287, 1986

Trenberth, K.E., P.D. Jones, P. Ambenje, R. Bojariu, D. Easterling, A. Klein Tank, D. Parker, F. Rahimzadeh, J.A. Renwick, M. Rusticucci, B. Soden, and P. Zhai: "Observations: Surface and Atmospheric Climate Change". In: Climate Change 2007: The Physical Science Basis. Contribution of Working Group I to the Fourth Assessment Report of the Intergovernmental Panel on Climate Change [Solomon, S., D. Qin, M. Manning, Z. Chen, M. Marquis, K.B. Averyt, M. Tignor, and H.L. Miller (eds.)]. Cambridge University Press, Cambridge, United Kingdom and New York, NY, USA, 2007

Varanasi, P. and V. Nemtchinov: "Thermal infrared absorbtion ceofficients of CFC-12 at

atmospheric conditions",Journal of Quantitative Spectroscopy and Radiative Transfer, 51, 679–687,1994

Vogel, B., Konopka, P., Grooss, J.-U., Müller, R., Funke, B., Lopez-Puertas, M., Reddmann, T., Stiller, G., von Clarmann, T., and Riese, M.: "Model simulations of stratospheric ozone loss caused by enhanced mesospheric NOx during Arctic Winter 2003/2004", Atmos. Chem. Phys., 8, 5279–5293, 2008

Volk, C.M., Elkins, J.W., Fahey, D.W., Salawitch, R.J., Dutton, G.S; Gilligan, J.M; Proffitt, M.H., Loewenstein, M., Podolske, J.R., Minschwaner, K., Margitan, J.J., Chan, K.R.: "Quantifying transport between the tropical and mid-latitude lower stratosphere",SCIENCE, 272 (5269), 1763–1768,1996

Volk, C. M., J. W. Elkins, D. W. Fahey, G. S. Dutton, J. M. Gilligan, M. Loewenstein, J. R. Podolske, K. R. Chan, and M. R. Gunson: "Evaluation of source gas lifetimes from stratospheric observations", J. Geophys. Res., 102(D21), 25543–25564, 1997

von Clarmann T., S.Ceccherini, A. Doicu, A. Dudhia, B. Funke, U. Grabowski, S. Hilgers, V. Jay, A. Linden, M. Lopez-Puertas, F.J. Martin-Torres, V. Payne, J. Reburn, M. Ridolfi, F. Schreier, G. Schwarz, R. Siddans, T. Steck: "A blind test retrieval experiment for infrared limb emission spectrometry", J. Geophys. Res., 108(D23), 4746, 2003

von Clarmann, T.: "Validation of remotely sensed profiles of atmospheric state variables: strategies and terminology", Atmos. Chem. Phys., 6, 4311–4323, 2006

Wagner, G. and M. Birk: "New infrared spectroscopic database for chlorine nitrate",Journal of Quantitative Spectroscopy and Radiative Transfer, 82, 443–460, 2003

Walter, R.: "Chemie und Transport in der Tropopausenregion: CLaMS-Simulationen im Vergleich mit In-situ- und Satellitenmessungen",PhD thesis, University of Wuppertal, 2009

Waugh, D., and T. Hall: "Age of stratospheric air: Theory, observations, and models", Rev. Geophys., 40(4), 1010, 2002

Weinreb, M. P. und A. C. Neuendorfer: "Method to Apply Homogeneous-path Transmittance Models to Inhomogenous Atmospheres", J. Atmos. Sci., 30, 662–666, 1973.

Werner, A., C. M. Volk, E. V. Ivanova, T. Wetter, C. Schiller, H. Schlager, and P. Konopka: "Quantifying transport into the Arctic lowermost stratosphere", ACPD, 9, 1407–1446, 2009

WMO: "Scientific assessment of ozone depletion: 2006", Report No. 50, 572 Geneva, Switzerland, 2007

Yushkov V., A. Oulanovsky, N. Lechenuk, I. Roudakov, K. Arshinov, F. Tikhonov, L. Stefanutti, F. Ravegnani, U. Bonafe, T. Georgiadis: "A chemiluminescent analyzer for stratospheric measurements of the ozone concentration (FOZAN)",JOURNAL OF ATMOSPHERIC AND OCEANIC TECHNOLOGY, 16(10), 1345–1350, 1999

Zoeger, M., A. Afchine, N. Eicke, M.-T.Gerhard, E. Klein, D. S. McKenna, U. Moerschel, U. Schmidt, V. Tan, F. Tuitjer , T. Woyke, and C. Schiller: "Fast in situ stratospheric hygrometers: A new family of balloon-borne and airborne Lyman photofragment fluorescence hygrometers", J. Geophys. Res., 105(D1), 1807–1816, 1999

D Acknowledgments

At first I want to thank Prof. Dr. Martin Riese who supported me and made this work possible. My special thanks go to Dr. Peter Preusse and Dr. Fred Stroh for their support and supervision of my work. Special thanks also to Dr. Lars Hoffmann for providing the fast forward model and the retrieval software, and for helping me through the jungle of JURASSIC.

There are many people, who made CRISTA-NF and its measurements possible, both at the Forschungszentrum Jülich and at the University of Wuppertal. I like to thank them all, especially Karina Arndt, Dr. Andreas Kullmann, Sebastian Schröder, Dr. Reinhold Spang, and all other members of the satellite group, who supported me during the data analysis, as well as Hans-Peter Heuser, Peter Knieling, Friedhelm Olschewski, Axel Schönfeld, and Vicheith Tan for there work during calibrations and measurement preparations.

The AMMA-SCOUT-O3 measurement campaign was facilitated by the European Commission and to the EC Integrated Project SCOUT-O3 (505390-GOCE-CT-2004) and AMMA. Based on a French initiative, AMMA was built by an international scientific group and is currently funded by a large number of agencies, especially from France, the United Kingdom, the United States, and Africa. It has been the beneficiary of a major financial contribution from the European Communities Sixth Framework Research Program. Many thanks also to the team and pilots of the Myasishchev Design Bureau for making the M55-Geophysica flights possible.

I like to thank Dr. Anu Dudhia for providing the MIPAS Reference Forward Model and his help to include the HITRAN2004 line mixing. For providing other observation data for comparisons and retrieval support I like to thank Thomas Gulde for the MIPAS data, Dr. Fabrizio Ravegnani and Dr. Vladimir Yushkov for the FOZAN data, Dr. Cornelius Schiller for the FISH data, and Prof. Dr. Michael Volk for the HAGAR data.

Further, I like to thank the CLaMS Team, e.g. Nicole Thomas, Dr. Jens-Uwe Grooß, Dr. Gebhard Günther, Dr. Paul Konopka, Dr. Rolf Müller and Robert Pommerich, who provided and explained the CLaMS simulations and tools for the comparison with the CRISTA-NF data.

IDL and Matlab were used for data analysis and visualization of the data. My special thanks go to all people at the ICG-1, who helped me with IDL, wikis and general misbehavior of the computer, especially Verena Alishahi and Reimar Bauer.

Many thanks to Anne Kunz and Nicole Spelten for the good company and the choicely decoration of the office. I also like to thank all the others, who make the ICG-1 such a great place to work, especially the colleagues sharing their coffee braek with me. My family and friends I owe thanks for there support and encouragement.

At the end I like to thank anybody whom I might have forgotten to thank before.